University of Southern Queensland
Faculty of Health, Engineering and Sciences

Glass Surface Contamination Sensor System: Design and Verification

A dissertation submitted by

Kane Hilmer

In fulfilment of the requirements of

Course ENG4111/4112 – Research Project

towards the degree of

Bachelor of Engineering (Electrical & Electronic)

Submitted: September, 2023

ABSTRACT

Contamination on glass surfaces, including that found on photovoltaics (PV), results in significant reductions in power generating capacity, and requires regular cleaning maintenance. This project develops a sensor system that could be integrated into the construction of a PV module. The sensor can provide information about the quantity of contamination on a glass surface. Research conducted showed that the properties of interest of typical contaminants found on PV modules could be systematically measured via relative permittivity and temperature. Electrodes bonded to the rear of the glass surface are used to develop a capacitance change due to the contamination on the front surface. RTD temperature measurements provide contaminant temperature and additional information. Processing of the capacitance and temperature measurement information is proposed for use in determining surface contamination. FDM simulation of a surface contamination sensor embedded into a PV module is discussed and implemented prior to conducting extensive simulations to verify the operation and optimise the sensor electrode dimensions. A physical analogue is designed and FDM simulations are performed using a PCB, prior to fabrication. An interfacing circuit is included for verifying the PCB Sensor functionality. Testing of the PCB Sensor element is completed using various contaminants, with LCR Meter and VNA measurements determining the characteristics of the sensor element for comparison to the FDM simulation results. The interface circuit and combined sensor system were also tested, with the results of all testing showing that the measurement of contamination using the electrode on glass method is viable, and that contamination on a glass surface is measurable. Future design and development with additional testing will support the full-scale integration into a PV module.

University of Southern Queensland
Faculty of Health, Engineering and Sciences
ENG4111/ENG4112 Research Project

Limitations of Use

Certification of Dissertation

I certify that the ideas, designs and experimental work, results, analyses and conclusions set out in this dissertation are entirely my own effort, except where otherwise indicated and acknowledged.

I further certify that the work is original and has not been previously submitted for assessment in any other course or institution, except where specifically stated.

[redacted]

Kane Hilmer
September 2023

ACKNOWLEDGEMENTS

I would like to thank my wife, Vera, for her unwavering support through not only my dissertation, but my university career. It has been a journey that I could not have completed without her.

I would also like to thank my supervisor Andrew Maxwell for his guidance and mentorship. Andrew has provided feedback on my work and I am grateful for his expertise and support.

TABLE OF CONTENTS

LIST OF TABLES

LIST OF FIGURES

ABBREVIATIONS

HMI - Human Machine Interface
PV - Photo Voltaic
SEM -Scanning Electron Microscope
ITO - Indium Tin Oxide
PET - Polyethylene Terephthalate
COP - Cyclic Olefin Polymer
IC - integrated circuit
ADC - Analogue to Digital Converters
DSP - Digital Signal Processing
SoM - System on Module
FDM - Finite Difference Method
2D - Two-Dimensional
3D - Three-Dimensional
VNA – Vector Network Analyser
PCB – Printed Circuit Board
SMD – Surface Mount Device
DSO – Digital Storage Oscilloscope
GPU – Graphics Processing Unit

1. Introduction

1.1. Background

The energy demands of the world are ever-increasing, and renewable energy plays a vital role in meeting these demands. A large component of the renewable energy generation across the globe is from Photo Voltaic (PV) installations, or ‘solar panels’.

PV installations accounted for the largest global investment in any energy sector in 2022, with US$200b spent (IEA 2022). Given the large investment and a reliance on PV installations to produce energy, installations must produce energy as efficiently as possible; not doing so has both environmental and financial implications.

Terrestrial PV installations use solar radiation reaching the earth’s surface of the module. Thus, any obstructions in the path, such as clouds, dust, debris, bird droppings or organic materials, reduce the radiation available to the PV module to produce energy. These obstructions contaminate the surface of the PV module and either absorb or reflect solar radiation, thereby reducing the PV module output. The reduction in output varies depending on the type, quantity and deposit method (Julius et al. 2015).

Unfortunately, natural cleaning processes of rain and wind do not always ensure the PV module glass surface is free from contamination, with build-up of contamination occurring across the surface, along with concentrations at the frame edges. Mechanical cleaning is typically required to remove the contamination and restore the module to its maximum energy output.

Operators of commercial power generating installations use cleaning systems that may include autonomous or manual regimes based on localised information from a dedicated sensor in a larger array or the elapse of a specific time period to prompt manual cleaning. Neither of these options allow for flexible and efficient approaches to cleaning the modules. Instead, it is proposed that a per-module contamination sensor would allow operators of PV modules to make data-driven decisions on the period of cleaning operations, maximising the energy output of the PV module(s) while managing the cleaning expenses based on past and expected performance.

The sensing of contamination on a glass surface extends beyond PV, with any application that uses glass to provide the transmission of solar radiation having a possible application. Solar hot water, skylights, windows etc, particularly where access or monitoring of the surface is difficult may benefit from surface contamination sensing.

1.2. Summary of Overall Approach

This dissertation aims to investigate and design a sensor system that may be integrated into the construction of PV modules to estimate the quantity of contamination on the glass surface.

Contained is a Literature Review chapter, which provides an overview of existing knowledge for the effects of PV soiling and the energy production and financial impacts of module soiling. Existing techniques and systems for PV soiling are also reviewed along. Properties of contaminants that are able to be used for detection along with the methods of detection are explored.

The Methodology chapter outlines the development of a proposed sensor, where the physical attributes of the contamination material detection are investigated. The properties of interest are established, before being analysed for the measurements that are to be taken for successful measurement of the surface contamination. Similarities to existing touch technologies used in computer and mobile phone interfacing are selected. The system is defined so that the proposed sensor may be simulated.

The Simulation chapter establishes the technique of Finite Differences that is used to generate a mathematical model for the sensor system accounting for the physical properties of interest, as established in the Methodology chapter. The simulation theory is expanded and developed so that the physical properties of the sensor are optimised for multiple material contaminants with multiple deposit methods. The simulation model is verified through both the logical testing and comparison to known mathematical models for solid dielectric models. Performance and accuracy are calculated with node quantity and simulation time reaching a satisfactory compromise.

The physical parameters for the sensor, including the range of electrode widths and spacings, and the physical parameters of the PV moule are defined for the simulation prior to conducting multiple simulations.

The Simulation Results section presents the data resulting from the multiple FDM simulation completed. Results are analysed prior to the normalisation of the results, to find the optimal electrode dimensions.

Once the sensor physical systems are optimised, an additional series of simulations is completed to establish the performance of the chosen physical dimensions.

The PV Sensor Design chapter outlines the physical design and parameters of the simulated sensor based on simulation outputs and proposes a solution for integration into a PV module.

A physical model is developed in Prototype Sensor System, with a PCB based sensor simulated, designed, fabricated, and constructed. An interfacing circuit for use with the PCB Sensor is also simulated, designed, fabricated, and constructed to allow the measurement system to be tested.

The Test & Data Collection chapter details the test methodology, equipment used, procedure and data collection for the sensor system components. The results for each contaminant used in the testing of the PCB Sensor and Prototype Interface are given separately and as a combined sensor system.

Testing results are summarised in the Results Summary chapter, where tabulated data is available for each test performed.

The Discussion/Improvements chapter combines a summary of the process, results, and recommendations, as well as the challenges faced during the writing of this dissertation.

A Conclusion chapter is included to summarise the contents of this dissertation and close out the report.

References and Appendices containing additional information are available at the end of the document.

2. Literature Review

This chapter provides a broad overview of existing literature on the effect of soiling of PV surfaces on PV energy output, as well as the materials typically found in the soiling media. It will also explore the available literature on measurement systems, from a wider perspective to a more focused review of the technologies currently used to detect objects physically contacting a surface, and how they may be leveraged in the development of a glass plate surface contamination sensor. The Measurement Process Algorithm section refers to the technical components in this chapter for consideration into the sensor design.

2.1. The Impact of Contamination on PV Performance

Evidence suggests that there is a 16% to 29% improvement in electrical output performance of a PV module due to the removal of soiling (Julius et al. 2015). Further, performance degradation due to the buildup of dust and soiling can be counteracted by regular cleaning (Julius et al. 2015). Finally, they also correlate performance degradation with characteristics of the soiling, including the transmittance, coverage thickness (density) and particle size and shape.

Complementing research from Julius et al. (2015), Yusuf et al. (2020) extends the correlation of soiling to transmittance and power reduction in PV output. Analysis of 13 soiling media, each deposited in wet and dry formats, was conducted by Yusuf et al. (2020), with findings indicating that all soiling media reduced the power output of the PV module, with the wet deposition method resulting in the largest reductions in power output for all contaminant media types. In a review of similar studies, Yusuf et al. (2020) concludes that contamination on a PV module results in significant reductions in PV output performance regardless of contamination media type and quantity or density.

A selection of media tested in Julius et al. (2015), and the described methods of deposition from Yusuf et al. (2020) will be used in the design and verification of the developed soiling sensor for this dissertation.

Additional research has shown that unevenly distributed soiling, which is typical of a real-world PV installation, also significantly affects the electrical power output of a PV module. Gostein et al. (2015) found that concentrations of soiling along the lower portion of the PV module surface, where a limited number of cells are soiled, reduces the power output by 9.6%. This evidence suggests that the location of a sensor mounted within a PV module would influence the amount of soiling the sensor is potentially exposed to. The development of the sensor in this research will be considered with the area available within a typical PV module a large influence on the design.

2.2. The Financial Impact of PV Soiling

The financial impact of PV soiling is a determinant of cleaning frequency. An equation for time between cleaning based on a linear soiling deposition, fixed cleaning costs and electricity price has been developed by Abu-Naser (2017).

$$\widehat{N} = \sqrt{\frac{2P}{\alpha s i \beta}} \tag{2-1}$$

Where: P is the cost of cleaning, α is the average daily losses in conversion efficiency, s is the average sun hours per day, i is the installed PV capacity, β is the price per kWh.

This equation shows that operators of PV systems need to evaluate the cost of cleaning compared to the increase in performance, and hence financial gain. This project aims to support operators to make evidence-based cleaning frequency decisions, based on data on the level of the soiling of the PV modules.

The impact of soiling on PV performance is widely understood by operators of PV modules. Detection of soiling on the surface of PV modules has been researched and commercialised prior to this research project. Techniques described in papers by Smestad et al. (2020) and Korevaar et al. (2017) use optical detection methods focusing on light transmission to determine soiling level. However, both methods require additional hardware (cameras, processing etc) to perform the measurement of potential soiling experienced by adjacent PV modules, which is a barrier to their adoption. An additional technique to detect contaminants on designed PV farms using imaging from spacecrafts has also been explored (Supe et al. 2020). However, the area of detection and modelling for the detection of soiling requires large surface areas and specific data for analysis.

2.3. Sensors

Variables measured by sensors may include physical properties such as temperature, pressure, force, density, humidity, displacement/strain. They may produce passive or active electrical outputs, mechanical outputs thermal or optical outputs (Bentley 2005). The physical property common to all soiling medias will need to be evaluated to evaluate the best used for sensing of the soiling. The sensor output will require modification to an appropriate signal for analysis/presentation and integration into a management system.

With the soiling to be measured physically resting on the surface of the glass plate, various similarities to existing devices for detecting its presence are clear. Detecting objects approaching or touching a surface is a commonplace technology by modern standards, with the advent of touch sensitive devices becoming synonymous with mobile communication devices, computers, home appliances as a Human-Machine Interface (HMI) well as in commercial and industrial applications for process control. Typically, however the object being detected is of significant mass or moisture content to allow for detection.

2.4. Contaminants

The studies conducted by Julius et al. (2015) and Yusuf et al. (2020) both directly measure the electrical performance of PV modules contaminated by real-world and also laboratory generated contamination.

The studies characterise the contamination used with various properties measured including:

- Particle shape
- Particle size
- Particle surface roughness
- Density
- Spectral transmissibility
- Deposition method
- Chemical composition

Both Yusuf et al. (2020) and Julius et al. (2015) utilised a Scanning Electron Microscope (SEM) to study the contamination material under test, while also conducting spectral transmissibility over the range of 250-1250nm and 300-1100nm respectively. Both studies demonstrate that spectral transmission has the greatest negative impact on PV performance. This is because contamination blocks transmission of light to the PV module itself, and therefore results in reduced power output.

As listed above, the deposit method of the contamination also influences power output. Yusuf et al. (2020) demonstrates that this power output reduction is due to decreases in spectral transmissibility because of soiling. That is, the wet deposition of all tested contaminants resulted in significant transmission degradation of up to 100%. This suggests that a compaction of particles during wet deposition, forming an opaque layer, blocks further light from passing through the contamination.

Particle size, shape and roughness were also contributing factors, as smaller particles allowed for greater compaction and therefore reduced transmissibility (Yusuf et al. 2020). Additional research from a site near Perth in Western Australia shows that with increasing dust density an approximately logarithmic decrease in spectral transmittance was observed.

The effect of the contamination (dust/particulates) was also compared over three PV module cell types, Polycrystalline Silicone, Monocrystalline Silicone and Amorphous Silicone, all showing comparable susceptibility to the effects of contamination (Julius et al. 2015). This dust was also analysed, and found to consist of 67.34% clay, 22.34% of very fine silt and the remaining in progressively larger particles (Julius et al. 2015).

Laboratory testing of PV module power degradation using two deposition methods (wet and dry) shows that all contaminants result in PV power output degradation, with wet deposition resulting in the most significant degradation of power output Yusuf et al. (2020). Table 1 shows these results:

Table 1: Contaminant PV Power Degradation (Yusuf et al. 2020)

	Power degradation %		
Contaminant	**Dry**	**Wet**	**Density (g/m²)**
ASH	23	94	1289.94
BIRD DROPPING	30	76	958.58
CARPET DUST	7	91	609.47
CEMENT	8	96	1964.50
CHARCOAL	35	96	923.08
CLAY	10	94	2621.3
COARSE SAND	11	61	3218.93
LATERITE	9	95	2426.04
LOAM	12	96	3011.83
SALT	8	68	2846.04
SANDY SOIL	13	95	2384.62
STONE DUST	10	92	2751.48
WOOD DUST	12	95	609.47

2.5. Current PV Soiling Detection Methods

Techniques currently used to detect PV cleanliness are discussed in Smestad et al. (2020) and Gostein et al. (2015) as ‘soiling stations’ which use a pair of PV modules. One of the PV modules in the pair is cleaned regularly, while the other PV module is left to soil naturally. The power output, or short circuit current of the pair of PV modules is compared, and the difference indicates the possible effect of soiling. The result is extrapolated for surrounding PV modules. However, a limitation of this method is that soiling stations require regular cleaning to be effective and provide only a local indication of soiling.

Localised soiling, such as around frame edges on PV modules, may not always be detected by ‘soiling station’ methods (Gostein et al. 2015). For example, if soiling accumulates in the lower areas of PV modules, obstructing individual cells, a power output reduction occurs due to a decrease in the individual contaminated cell output voltage due to the series electrical connection of the cells. However, the cell may maintain a short circuit current, leading to no detection of contaminations with the use of a traditional soiling station.

Thus, the paper suggests that detection of contamination in smaller areas, specifically lower areas of mounted PV modules where contamination accumulation can occur, may have significant benefit to the performance of a PV module (Gostein et al. 2015).

2.6. Environment

PV modules experience full environmental extremes of complete exposure to all elements when installed, such as: rain, snow, wind, sun and contamination. In addition, they are often installed into areas which are not easily accessed for regular maintenance of a traditional soiling sensor. Temperatures of the PV surface can reach 40°C above ambient temperature, creating a hostile environment (Ozemoya et al. 2013).

As a result, the development of a sensor that does not require a reference to be regularly maintained and which detects the presence of contamination would be beneficial. A sensor which can indicate an increasing level of contamination such that an informed cleaning regime can be undertaken is the goal of this research.

2.7. Contaminant Properties – Relative Permittivity

Of the reviewed literature, the contaminants listed in Table 1 Contaminant PV Power Degradation (Yusuf et al. 2020) were analysed for properties that were possible to measure through a glass surface. The Relative Permittivity (ε_r) was identified as a property suitable for measurement, as no physical contact with the contamination material is required to measure it.

Relative Permittivity, or Dielectric Constant is defined as the ratio of the material permittivity to that of free space:

$$\varepsilon_r = \frac{\varepsilon}{\varepsilon_0} \qquad 2\text{-}2$$

Where ε *is the absolute permittivity of the material and* ε_0 *is the permittivity of free space, with a magnitude of 8.8572 pF* m^{-1}*.*

Permittivity of a material is a function of measurement frequency, and material properties and results in complex permittivity (Spain & Venkatanarayanan 2014):

$$\varepsilon_r^* = \varepsilon_r' + j\varepsilon_r'' \qquad 2\text{-}3$$

Where:

$$\varepsilon_r' = \varepsilon_\infty + \frac{\varepsilon_s - \varepsilon_\infty}{1 + \omega^2 t^2} \qquad 2\text{-}4$$

$$\varepsilon_r'' = \varepsilon_\infty + \frac{(\varepsilon_s - \varepsilon_\infty)\omega\tau}{1 + \omega^2 \tau^2} \qquad 2\text{-}5$$

Where: ε_r' *is the real permittivity.* ε_r'' *is the complex permittivity.* ε_s *is the permittivity at low frequencies.* ε_∞*is the permittivity at high frequencies.* τ *is the relaxation time of the material.*

Complex permittivity is shown to relate to losses in the material with the dissipated energy being defined as the dissipation factor:

$$\varepsilon_r^* = \varepsilon_r' + j\varepsilon_r'' \tan(\delta) = \frac{\varepsilon_r'}{\varepsilon_r''} \qquad 2\text{-}6$$

Nelson (2005) shows a relationship between material density and permittivity, while Jesch (1978) and Ellison et al. (2017) showed that the permittivity of the substances in Table 2 were relatively constant for frequencies within the Ionic and Dipolar frequency regions of the materials. Hewlett-Packard Company (1992) demonstrates this with the plot of real and complex permittivity vs the frequency in Figure 1.

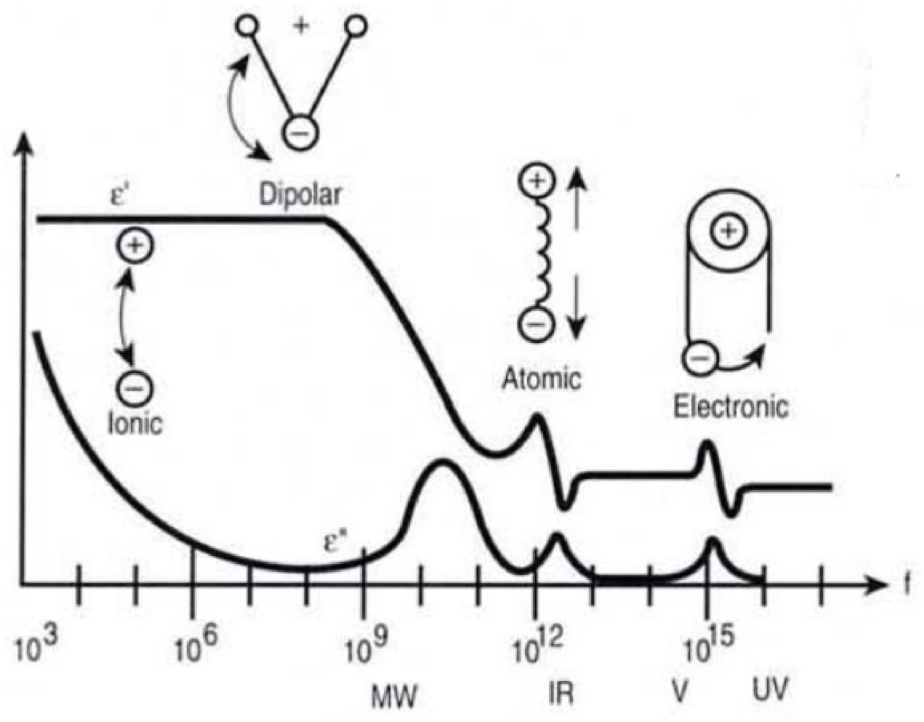

Figure 1 Frequency Of Dielectric Mechanisms (Hewlett-Packard Company 1992)

Table 2: Permittivity of Select Materials

Contaminant	$\varepsilon'/\varepsilon_r$	f(MHz)	Source
ASH	~60000	0.010-0.1	Raghavendra et al. (2002)
CEMENT	6-14	40	Al-Qadi (1995)
CHARCOAL	~7	500	Ellison et al. (2017)
CLAY-0% Water	2.717	300	Jesch (1978)
CLAY-7% Water	6.03	300	Jesch (1978)
CLAY-14% Water	10.676	300	Jesch (1978)
LATERITE	10-40	100	Xu et al. (2022)
LOAM - 0% Water	2.34-2.77	300	Jesch (1978)
LOAM - 5% Water	4.45-5.96	300	Jesch (1978)
LOAM - 10% Water	8.72-9.15	300	Jesch (1978)
SALT	6.6	-	Bramley (1928)
SAND - 0% Water	2.70	300	Jesch (1978)
SAND - 8% Water	6.96	300	Jesch (1978)
SAND - 14% Water	10.46	300	Jesch (1978)
STONE DUST	4-15	-	Martinez and Byrnes (2001)
WOOD DUST	~2	500	Ellison et al. (2017)
BIRD DROPPINGS	No data found in the literature.		
CARPET DUST	No specific information available.		

The relative permittivity of the materials used by Yusuf et al. (2020) in the study of PV performance has been summarised in Table 2, with the frequency of test and information source also listed. In the case of Bird Droppings and Carpet Dust, the variability of the material resulted in no reliable relative permittivity figure being found in the literature.

In addition to the materials tested in Yusuf et al. (2020), the typical materials used in a PV module construction were found:

Table 3 Dielectric Properties of PV Module Construction Materials

Material	**$\varepsilon'/\varepsilon_r$**	**f(MHz)**	**Source**
Low Iron Glass	~4	100	Amara et al. (2019)
EVA	2.5-3	100	Rahaman et al. (2012)

2.8. Contaminant Properties-Density

Wet deposition of contamination demonstrates a significant reduction in PV power production (Yusuf et al. 2020). This is because the wet deposition method produces a denser contamination due to the compaction of the particles that constitute the contamination. The increase in density results in less optical transmissibility, reducing the available energy transmission to the PV cells, thereby reducing power production.

Density of the contamination material is investigated for detectable property changes. Nelson (2005) discusses the density-permittivity relationship of powdered and granular materials before conducting an experiment to test. Coal, limestone, and a limestone-coal mixture were tested, demonstrating a relationship between the density of the two states (air-particle and solid) of the material to the permittivity of the states.

Utilising the Landay, Lifshitx and Looyenga (LLL) equation:

$$\varepsilon^{\frac{1}{3}} = v_1(\varepsilon_1)^{\frac{1}{3}} + v_2(\varepsilon_2)^{\frac{1}{3}} \tag{2-7}$$

Where: ε is complex permittivity, v_1 ε_1 and v_2 ε_2 are volume fractions and permittivity of the materials.

Nelson (2005) derived that the complex permittivity of selected particles in an air mixture could be closely approximated using:

$$\varepsilon_b = \left[\frac{\left((\varepsilon_a)^{\frac{1}{3}} - 1\right)\rho_b}{\rho_a} + 1\right]^3 \qquad 2\text{-}8$$

Where: ε_a *and* ε_b *are complex permittivity of the air-particle mixture.* ρ_a *and* ρ_b *mixture density respectively.*

It is shown that the permittivity of the material mixture increases with increased density.

Sihvola (2000) discusses the theoretical application of the Maxwell-Garnett mixing rule in determining the effective dielectric properties of discreet, spherical inclusion heterogeneous materials, including those with complex permittivity.

$$\varepsilon_{eff} = \varepsilon_e + 3f\varepsilon_e \frac{\varepsilon_i - \varepsilon_e}{\varepsilon_i + 2\varepsilon_e} \qquad 2\text{-}9$$

Where: ε_{eff} *is the effective complex permittivity.* ε_e *is the complex permittivity of the environment.* ε_i *is the complex permittivity of inclusions.* f *is the volume fraction, with* $0 \leq f \leq 1$.

The outcome of this rule shows that as the composition of a mixture of dielectric materials changes, the effective permittivity of the mixture moves towards the permittivity of the main mixture constituent.

For complex mixtures made from multiple materials with different permittivity values or with lossy dielectric materials, Sihvola (2000) expands, showing that conductivity of mixtures with conductive materials with volume fractions less than unity are dependent on the measurement frequency and approach 0 as frequency approaches 0 Hz (DC).

For the contaminants listed in Table 1: Contaminant PV Power Degradation (Yusuf et al. 2020) the composition of the mixtures is likely to be simple, with the mixture consisting of the material and either air or water. It is probably that the dry deposition method results in a lower deposition density, while a wet deposition initially creates a mixture where air between particles is replaced with water. Thus, the mixture effective permittivity will be changed during this stage.

As water is removed from the contaminant-water mixture, the density of the contaminant material tends to increase from the dry deposition, with the volume fraction f increasing towards 1. The resulting change in effective permittivity is towards the properties of the contaminant alone.

Both the increase in contaminant density and the change in mixture composition are shown to alter the effective permittivity of the contamination material.

2.9. PV Module Construction

The construction of typical Polycrystalline and Monocrystalline PV modules consists of a low-iron glass front of thickness between 2 and 3.2mm. The front glass faces the sun and is subject to the contamination of interest. A extruded anodised aluminium frame that surrounds the glass front panel is also typical of many PV modules (Figgis et al. 2023).

The PV cells are typically encapsulated in Ethelene Vinyl Acetate (EVA) with a backing sheet of three classes, all consisting of layers of polymers (Buerhop-Lutz et al. 2021). The PV cells are interconnected with conductive electrodes which are also encapsulated. A diagrammatic representation is shown in Figure 2 Typical PV construction.

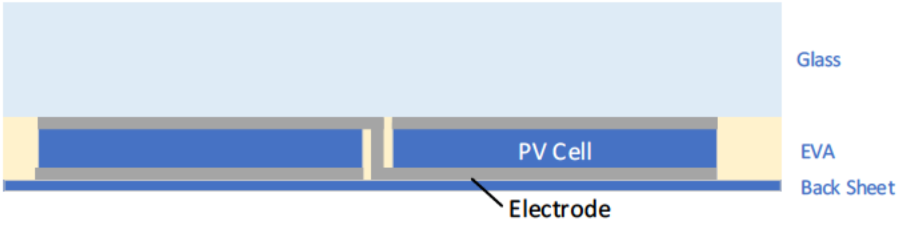

Figure 2 Typical PV construction

2.10. Glass Surface Detection Technologies

Similarities between detecting contamination on a glass surface and touch panel technologies are due to the similar physical characteristics and construction. Where touch panel technologies allow for the detection of fingers, stylus or other objects which cause a capacitance change at precise coordinates to interact with the device, a contamination sensor need only determine the amount of contamination and does not require location information.

Resistive, Acoustic, Optical and Capacitive are touch panel technologies that are described in Nam et al. (2021) each with distinctive detection methods and properties which were considered for the application to the sensor system.

2.10.1. Resistive

Resistive touch panels rely on the object physically pressing the touch interface to create an electrical circuit between two conductive layers within the touch panel interface. The output of the touch panel is a proportional resistance that a controller can interpret as coordinates and perform appropriate interactions with the user. Multiple variations of output configurations exist, with two common configurations shown in Figure 3. Resistive touch panels require a relatively large amount of physical force to actuate and can have poor durability (Nam et al. 2021).

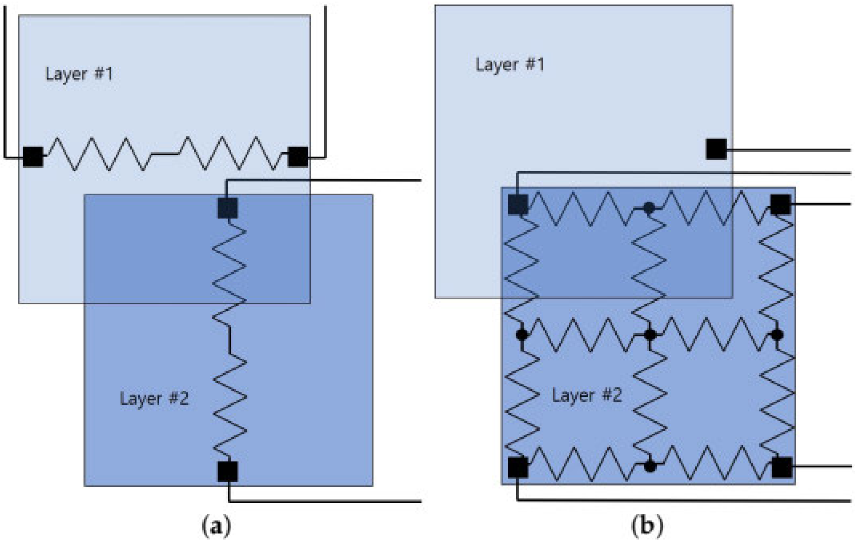

Figure 3 Resistive Touch Panel Architectures (Nam et al. 2021, p. 4)

Resistive touch panel technology is not suitable for detecting surface contamination, as the physical force required is not obtainable in the application of a surface contamination sensor.

2.10.2. Acoustic

Acoustic touch panels use Surface Acoustic Wave (SAW) technology. Transmitters and receivers of the surface waves are placed on the edge of the glass surface, in an X & Y axis configuration. Waves are reflected internally, and when a touch occurs, it is interpreted by attenuation in the acoustic wave propagation for both axes. A diagrammatic representation of an acoustic touch panel is shown in Figure 4.

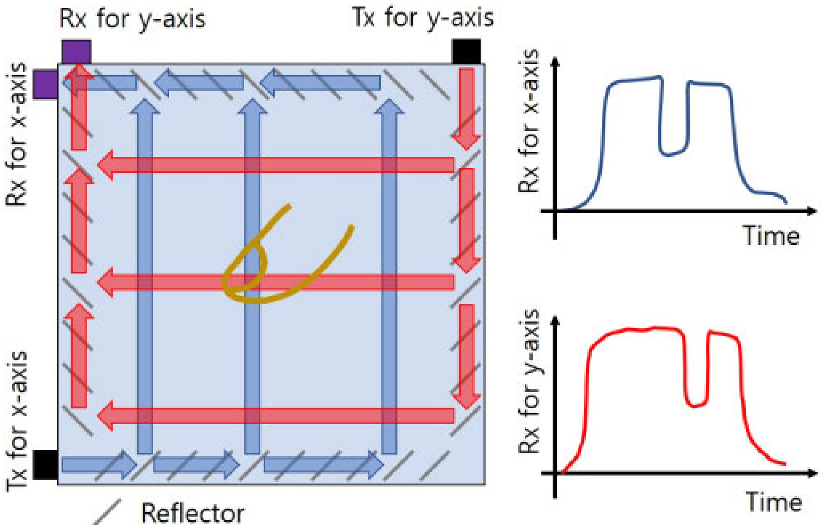

Figure 4 Acoustic Touch Panel (SAW) (Nam et al. 2021, p. 5)

Acoustic touch panels require only average touch force of an object that can absorb acoustic energy. Acoustic touch panels have the best durability out of the four variations of touch technology; they also offer good contamination resistance. Acoustic touch panels have average touch diversity allowing them to only detect distinct single touches (Nam et al. 2021).

However, given that acoustic touch panels require vibration absorbing materials to function, they are not suitable for detecting surface contamination. This is due to the contamination material not having sufficient mass or damping properties to absorb the acoustic energy.

2.10.3. Optical

Optical touch panels use similar methodology to acoustic panels to detect touch inputs, with transmitted light being disrupted or reflected by a touch input. Optical touch panels have high touch diversity and use light touch force. However, they do require multiple transmitters and receivers to be placed at the edge of the glass panel or sensors to detect a touch input reflecting or directing light from the surface of the glass panel (Nam et al. 2021). A diagrammatic representation of an optical touch panel is shown in Figure 5.

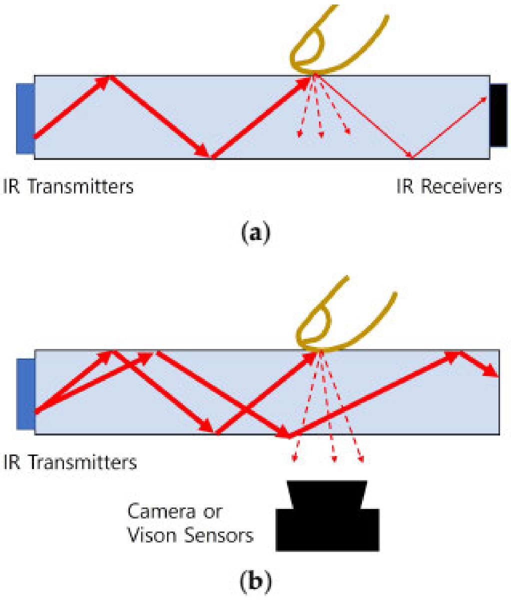

Figure 5 Optical Touch Methodologies (Nam et al. 2021, p. 6)

The use of optical energy and camera or visual sensors limits the suitability of optical touch technology for integration into a PV module. Maxwell (2007) shows that diffusers are used to allow the operation of the optical touch panels, which reduce the light passing through the panel. This property alone eliminates optical touch form use in PV modules due to the reduced PV performance from limiting the solar energy. In addition, the durability and packaging of sensors for exposure to environmental conditions are limiting factors.

2.10.4. Capacitive

Capacitive touch technologies are split into two sensing schemes, surface-capacitance and projected-capacitance, with projected-capacitance sensing also being split into self-capacitance and mutual capacitance architectures (Nam et al. 2021).

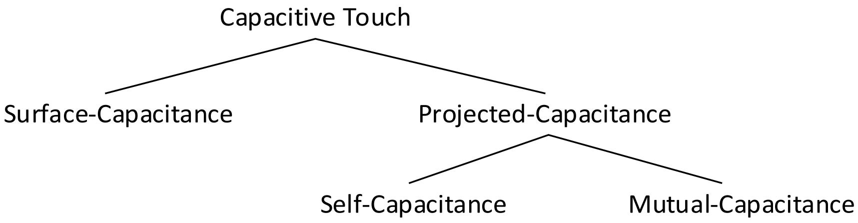

Figure 6 Capacitive Touch Technologies

Surface Capacitance

The Surface-Capacitance method uses a single conductive internal layer that is fed with a synchronised AC voltage from multiple points on the conductive layer. The touch input is sensed by the object introducing additional capacitance at the point of touch, which modifies the current between the feed points. The change in current allows for the calculation of the point of the added capacitance.

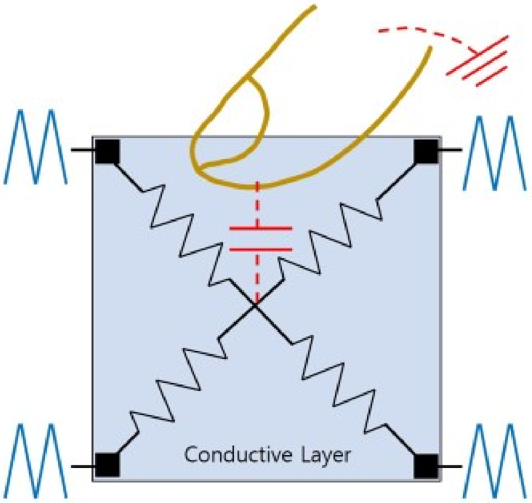

Figure 7 Surface-Capacitive Methodology (Nam et al. 2021)

A representation of a Surface-Capacitance touch detection is shown in Figure 7.

Projected Capacitance

Projected-Capacitance methods use multiple internal conductive paths configured so that they can be ‘scanned’ to find the coordinates of a touch input. The two methods of Self-Capacitance and Mutual-Capacitance differ in the application of the scanning technique.

Self Capacitance

The Self-Capacitance method senses a touch input by detecting a capacitance change between conductive paths or pad and ground. Individual sensor pads or a grid of sensor conductive paths may be used. The grid methodology estimates location by using both X & Y conductive paths that exist in a Self-Capacitance touch sensor panel, which are scanned so that the coordinates of the touch are estimated. Figure 8 illustrates the X & Y conductive paths, and the capacitance added as the result of a touch input (Nam et al. 2021). Individual sensor pads may also be utilised as discrete input locations, which require scanning individually. (Walker 2014).

The Self-Capacitance method can suffer from ‘ghost touches’ when multiple touch inputs exist in a X & Y grid configuration and can be made into a single layer of conductive elements. However, Self-Capacitance methods are more susceptible to noise over other methods (Walker 2014; Nam et al. 2021).

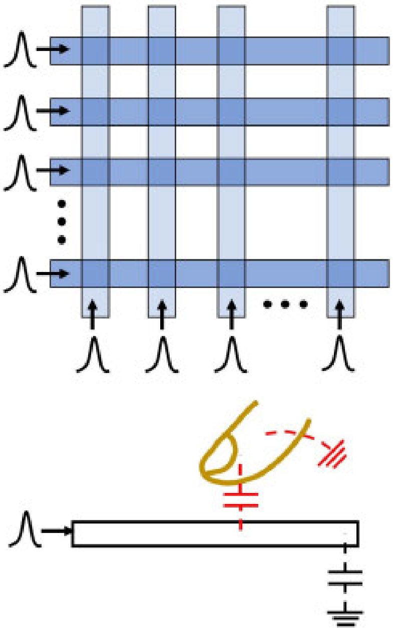

Figure 8 Self-Capacitance Method (Nam et al. 2021, p. 6)

Mutual-Capacitance

The Mutual-Capacitance method is similar to a Self-Capacitance method with both X & Y conductive paths; however, the scanning is completed by measuring the capacitance between X & Y conductive paths, not exclusively to ground. Figure 9 demonstrates this graphically, by showing the change in capacitance between X & Y paths, introduced by the finger model (Nam et al. 2021).

Adding a touch input introduces additional capacitance between the X & Y conductive paths, allowing for the determination of the location of the touch, or multiple touches. A model of capacitances that are present in a system is expanded by Walker (2014) to show how multiple mutual capacitances exist in a functioning system. Figure 10 is reproduced from Walker (2014) demonstrating the capacitances that exist between the various components of an LCD touch panel, and demonstrates the complex interaction between conductors and sources.

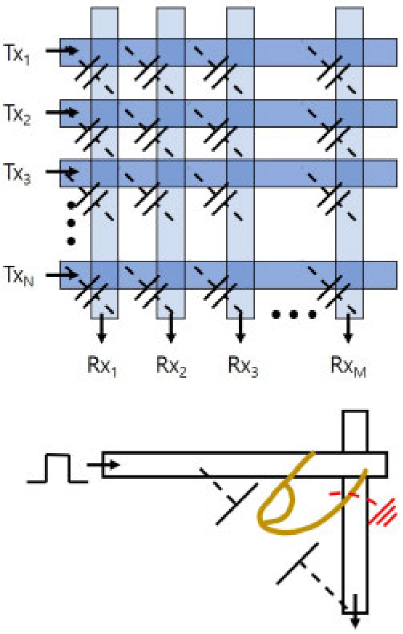

Figure 9 Mutual Capacitance Method (Nam et al. 2021, p. 6)

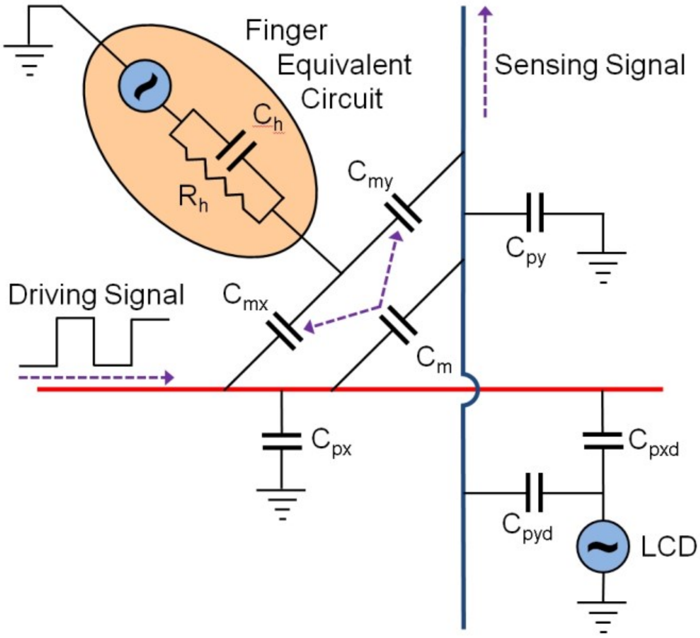

Figure 10 Mutual Capacitance Model for LCD (Walker 2014)

All capacitive touch technologies suffer from environmental and operational electronic interference due to electric field disruption and capacitive coupling. The presence of signals in the form of LCD switching noise, shown in Figure 10 as C_{pxd} and C_{pyd} and other noise external to the touch panel, can influence the sensing of a capacitance change (Nam et al. 2021). Noise is also a limiting factor in touch technology’s ability to recognise the degree of a touch, its location or exclude non-valid touches.

Various techniques have been developed for improvements in the Signal to Noise Ratio (SNR) of capacitive touch technologies. Active guard circuits, digital filtering, accumulation output pulses, differential charge amplifiers and delta-sigma analogue to digital converters have been used to improve the SNR. Sample timing and variable frequencies are also used so that the scanning of a touch input is conducted around the synchronisation pulses of an LCD (Walker 2014; Nam et al. 2021).

Self-Capacitance and Mutual-Capacitance methods are similar in function, where the latter is better for multiple-touch detection. Both utilise conductive electrodes on the underside of the panel surface, insulating the touch input from the conductive paths. Only the change in capacitance between the touch sensor conductive paths of the touch sensor are used to determine the location of the touch in the mutual capacitance method (Nam et al. 2021).

2.11. Touch Panel Construction

Construction of commercial touch panels is typically completed in two main categories: Transparent and Opaque. Opaque touch is used in interfaces such as notebook touchpads and are typically constructed as two layer projected capacitance techniques (Walker 2014).

Transparent touch panels that use projected-capacitance touch sensing all feature a multi-layer construction with a glass surface as the user interface. Soda-lime glass is typically used and can range from 0.3mm through 3mm in thickness (Barrett & Omote 2010; Walker 2014).

A transparent conductor, Indium Tin Oxide (ITO) is typically bonded to a thin film layer for use as electrodes. The ITO layer(s) are bonded to glass, Polyethylene Terephthalate (PET) or Cyclic Olefin Polymer (COP) that forms the remaining layers of the touch panel (Barrett & Omote 2010; Walker 2014). An example of touch sensor panel layering is shown in Figure 11 Example Touch Panel Layers.

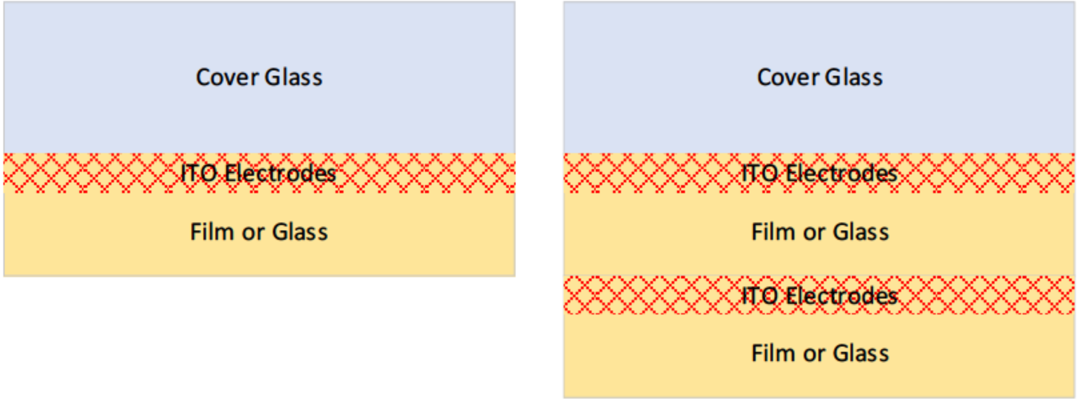

Figure 11 Example Touch Panel Layers

The dielectric constant and thickness of the cover glass influences the sensitivity of projected capacitance sensing of touch panels, with thinner glass and/or higher dielectric constant being better for performance. The ITO layer has a resistivity of 50-100Ω/sq and is typically formed into conductors, typically between 20µm and 100µm wide for glass or 100µm and 200µm for PET (Barrett & Omote 2010).

Electrode patterns influence the sensitivity of a touch interface of capacitive touch panels (Lee et al. 2014). The analysis included the simulation of four electrode patterns and construction and test of the best performing two. Lee et al. (2014)explored the effect of positioning a stylus in relation to the electrode pattern, evaluating the calculated change in capacitance as the location is moved. Lee et al. (2014) found that the largest change in capacitance was when the stylus is located at the loci of fringing of fields between sense and drive electrodes.

Performance was improved when an electrode design that increased the number of fringing fields was simulated. A fabricated model showed up to a 5.4% improvement over a traditional interlocked diamond pattern.

The dimensions of the fabricated touch sensor used in Lee et al. (2014) are shown in Figure 12 and Figure 13. The peak change in capacitance is stated as 537.056 fF for a 0.8 mm diameter stylus.

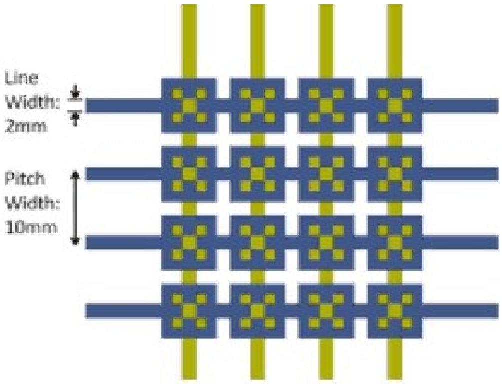

Figure 12 Top View of Fabricated Electrodes, Lee et al. (2014)

Figure 13 Cross-Section of Fabricated Electrodes, Lee et al. (2014)

Barrett and Omote (2010) also state that the change in capacitance detected by projected-capacitance touch panels are in the order of femtofarads (10^{-15} F), when used in a device with 9x16 rows and columns of electrodes.

The electronic circuits required to integrate capacitive touch panels into usable devices are available in multiple solutions. Specialised integrated controllers, packaged into a single integrated circuit (IC), or integrated as a hardware module into microcontrollers or System on Module (SoM) controllers, all for bespoke touch interfaces.

Of the controller ICs and microcontroller modules reviewed, all feature excitation drivers, charge amplifiers, multiplexers, Analogue to Digital Converters (ADC) and Digital Signal Processing (DSP) or a processor to analyse the signals (Walker 2014; Nam et al. 2021). A functional block diagram of the typical electronics required for a touch panel is shown in Figure 14.

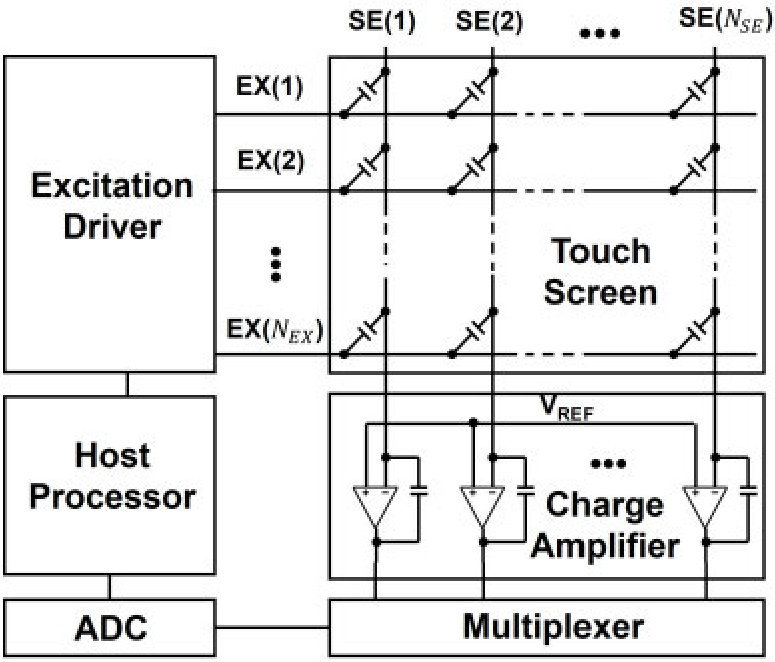

Figure 14 Touch Panel Functional Block Diagram (Nam et al. 2021)

Microcontrollers with touch interface modules are available for integration into embedded devices requiring a Human Machine Interface (HMI). The typical HMI used with microcontrollers includes buttons, sliders or rotary styles of touch interfaces (Microchip 2015).

Touch controller ICs or modules typically optimise the functionality of a touch interface through component selection, DSP filtering & noise reduction algorithms, for decoding touch inputs (Atmel 2013; Microchip 2015). Of the controllers researched, all featured contamination mitigation strategies and optimise for speed of recognition and/or multi touch. The strategies include automatic calibration of capacitance during power-up, timer rollover and automatic calibration based on press duration (Atmel 2013; Microchip 2015).

2.12. Summary

From the literature reviewed, it has been determined that the main contributor to PV performance degradation due to contamination is from reduced optical transmissibility. All studies showed that the transmissibility of contamination was correlated to a reduction in PV performance, with the level of optical transmissibility of greater significance compared to the composition of the contamination.

The reviewed literature showed that any contamination between the energy source and the PV cell reduces the performance of the cell. In a PV module, the contamination rests on the surface of the glass front, reducing the optical transmission of light from reaching the PV cells contained within the module.

Construction of PV modules typically consists of a 2-3.2mm low-iron glass front with the silicon PV cells and interconnecting electrodes adhered and encapsulated with EVA and covered with a polymer back sheet.

The literature also revealed that the established methods of determining the extent of contamination on PV modules requires the use of reference and measurement sensors, commonly PV cells or modules. The challenge is that the reference cell requires regular cleaning or maintenance, so that the level of contamination on non-cleaned cells can be determined. The localisation of contamination was also shown to be significant to the reduced performance of PV, which traditional sensing systems can fail to detect.

The properties of the real-world and controlled experiment contaminants reviewed showed a wide variety of materials and various potential properties of interest. A potential property that can be measured with no electrical (conductive) contact was determined to be the relative permittivity of the contaminant(s).

Analysis of the known contaminants showed that the biggest influence of many contaminants was due to water content. The determination of the relative permittivity of the contamination would vary with the type and amount of material, as well as moisture level.

The relative permittivity of typical PV module construction materials was also determined to be in the typical range of the dry contaminants. Relative permittivity is a property of influence in the form of capacitance in the projected-capacitive touch sensing technique.

The density and mixture of contaminants is also shown to influence the effective complex permittivity, with higher density of the contaminant material due to compaction or replacement of filling material (air, water etc.) with the material, trends the effective permittivity to that of the contaminant.

Existing technologies used in touch panel displays was analysed for their operation and similarity to the task of detecting contamination on a glass surface. The literature revealed that Projected-Capacitance touch technologies share many similarities with the construction of PV modules, having glass and polymer layers, while having embedded conductive electrodes.

Projected-Capacitance touch panels, as with all capacitive based touch technology detects a change in capacitance of an established circuit. As the electric field produced by the touch interface electrodes interacts with the introduced finger or stylus, the change in electrostatic charge can be detected with various methodologies, resulting in the control circuit interpreting, or determining the location of the input.

The sensitivity of the Projected-Capacitance touch panel is dependent on the electrode configuration, physical spacing between electrodes and the thickness of the cover glass. The change in capacitance is shown to be maximised with greater fringing flux, as the introduced object alters the generated flux lines.

An obvious deviation in the objective of a surface contamination sensor and touch panel is highlighted by the touch panel detecting coordinates of a distinct point, while a contamination sensor may only detect over its entirety (Microchip 2015).

Commercial touch controllers actively avoid the detection of contamination on the surface on the touch panel, thus the development of a contamination sensor using the researched touch controllers is contrary to the design goals of the controllers, making them unsuitable for use.

3. Methodology

3.1. Introduction to the MPA

The Measurement Process Algorithm (MPA) is the term given by Sydenham (1989) to the structured series of steps that can be applied to a measurement problem in order to find a practical solution. The MPA was developed so that when applied diligently, all measurement problems could be addressed (Sydenham 1989, pp. 36-9). The MPA will be applied to the problem of measuring the contamination on the surface of a glass plate.

The MPA progresses through the following steps:

1. Define the knowledge needed from the measurement.
2. Refer to the existing knowledge. *A literature review on the problem under investigation and supporting literature has been completed in the literature review section.*
3. Establish attributes of the measurement.
4. List all referents of the measurement.
5. Determine suitable measurands for the measurement system.
6. Establish a system extent and boundary.
7. Find and control or measure system influence variables.

The MPA will result in a specification for a measurement system which may be designed and tested. With the measurement system defined, additional steps consist of:

8. Determining signal and energy flow.
9. Establishing the signal processing required.
10. Determining the resulting system.

3.2. Measurement Requirement

For the Glass Surface Contamination Sensor System to be effective, a measurement requirement is to be established. The following list includes environmental, performance and manufacturing requirements which are considered during the further application of the MPA.

1. The Sensor System shall provide information on the extent of contamination on a glass surface.
2. The sensor element shall be able to be integrated within a PV module's construction or other glass surface.
3. The sensor element shall be able to use standard & established manufacturing processes.
4. The sensor system shall use commercially available materials and components.
5. The sensor system shall not negatively impact the performance of a PV module if integrated within the PV module.
6. The sensor system must be suitable to meet the environmental conditions typically experienced by PV modules. These conditions include temperature, humidity, moisture, and lifespan expectations.
7. Contaminants that are known to degrade PV performance are to be measured, with the output of the measurement system used to indicate the extent of contamination at the sensed area.

3.2.1. Measurement System Specification

The Glass Surface Contamination Sensor System is to have the following specifications and requirements:

- Must provide variable output correlated to surface contamination quantity.
- Shall sense multiple contamination types and combinations of contaminants.
- Shall produce an output for further integration into a control system or indicator.
- Must have the ability to operate within an environmental temperature range compatible with temperatures experienced by installed PV modules.
- Must be able to operate within a humidity range experienced by installed PV modules.
- Must produce stable or predictable output over the full temperature and humidity range.
- Shall produce repeatable indication of contamination.
- Shall have little or no maintenance requirements.
- Shall be easy to calibrate.

3.3. Existing Knowledge

Existing knowledge used in determining the measurement system is described in the Literature Review chapter. Properties of contaminants and of PV modules are explored along with existing sensor technologies that use indirect measurement techniques.

3.4. Measurement System Attributes

Using the existing knowledge from the prior studies on PV performance loss due to surface contamination attributes of interest were identified.

The properties, characteristics and features of the contamination that may be of interest in the measurement system include:

1. Physical properties
    - Optical transmissibility – How transparent is the contamination?
    - Density – How much mass per unit area?
    - Mass – What is the weight of the contamination?
    - Thickness – How thick is the contamination layer?
    - Shape and size of the material particles – How do they interlock or compact?
    - Moisture content – how much water is in the contamination?
    - Colour – what is the colour of the contamination?
    - Chemical composition – what is the contamination made from?
    - Temperature – What is the temperature of the contamination?
    - Angle of the glass plate – does the angle of the glass plate influence the contamination’s effect?
    - Altitude/air pressure – Does the atmospheric air pressure influence the contamination?

- Electrical properties
    - Conductivity/Resistance/Impedance – what is the resistivity of the contamination?
    - Relative permeability – what are the magnetic properties of the contamination?
    - Relative permittivity – what are the electrostatic properties of the contamination?

3.5. Measurement System Referents

"Referents are attributes that appear to relate to the task of measurement we wish to undertake" (Sydenham 1989, p. 38).

From the research conducted, the attributes listed above in section 3.4 Measurement System Attributes may be reduced to referents. Referents may not be the attributes or phenomena that are to be directly measured, but rather a set of characteristics that are determined to be associated to the measurement of the surface contamination.

The referents are discussed below:

Optical transmissibility: As the existing knowledge showed, the optical transmissibility of the contamination exhibited the largest influence on the performance of a PV module. However, optical sensing requires specialised sensors which are unable to be integrated into the construction of a PV module, a key measurement requirement. Thus, optical transmissibility is removed as a measurand.

Density: Sensors that typically conduct measurements of density are unable to be integrated within the construction of a PV module, which is a key measurement requirement. In addition, the density of the contamination can be inferred via the measurement of relative permittivity, as shown by Nelson (2005). Thus, the direct measurement of density is not required for this measurement system.

Contaminant composition: Sensors that conduct measurements of composition suffer from similar packaging requirements; in that they are inconsistent with the key measurement requirement of being integrated into the construction of a PV module. Contaminant composition will therefore not be considered for this measurement system.

Moisture content of the contamination: The moisture content of the contamination may be detected or measured with multiple techniques. However, techniques that require direct contact with the contaminant, such as those to measure moisture content, are not considered due to the packaging and environmental measurement requirements.

Temperature: Temperature measurement of the glass surface may be used to determine the possible presence of moisture or water. Temperature and duration of temperature may correlate to the possible water content, where evaporation or drying may be estimated. Temperature may also be used to characterise the performance of a sensing system through the properties of the construction materials and known contaminants such as water. Thus, it is desirable to include temperature as a measurand.

Relative permittivity of the contamination: The moisture content of the contamination will influence its permittivity. When moisture, with the dielectric constant of approximately $\varepsilon \cong 80$, combines with other contaminants, the overall permittivity may be described by the equation 2-9. It is therefore desirable to include relative permittivity of the contamination as a measurand.

Relative permittivity of the sensor materials: The permittivity of the PV construction is considered constant. With a stable mechanical construction, the permittivity of the materials will form the sensor system itself and not be of direct influence in the detection of contamination. Due to these factors, the construction material permittivity is removed from the measurement requirement.

Frequency of measurement: The frequency used to perform the measurement of the contamination permittivity will influence the information available, as shown in section Contaminant Properties – Relative Permittivity. Characterising the type of material through permittivity measurements is conducted for ground penetrating radar (Martinez & Byrnes 2001). The composition of the contamination is not an influencing variable, so the frequency of measurement is not considered in the measurement requirement.

Sampling period: How often the measurement is taken will determine the measurement system’s ‘understanding’ of the contamination. The measurement period is considered as a constant, which will be determined per measurement system and may be removed from the measurands.

3.6. Measurement System Measurands

“A Measurand is a Referent that is physically measurable by known equipment” (Sydenham 1989, p. 38). For each referent that has been determined as valuable, an established technique for conducting the measurement is required. The basic phenomena that are to be directly measured by established methods are listed below.

Relative permittivity: Through the measurement of capacitance, the relative permittivity of the contamination may be determined. The capacitor formed by the electrodes of the sensor is to be used to tune an oscillator. The change in oscillator frequency will relate indicate the relative permittivity change of the sensor detection area.

Temperature: The measurement of temperature is to be completed using a Resistance Temperature Device (RTD) temperature sensor. The temperature coefficient property of metals determines the resistance of a wire to change with temperature. The transducer converts the thermal energy into an electrical signal directly.

3.7. Measurement System Excluded Attributes

With consideration of the items listed in the Measurement Requirement section, attributes that may be excluded from the measurement system are determined to be:

Optical transmissibility: The optical transmissibility of the contamination is shown as the primary influence of performance reduction in PV. The attribute is excluded due to the sensors required to measure the optical transmissibility not meeting several of the measurement requirements, including durability, and packaging. Optical sensing systems will also require a reference cell to be cleaned frequently, replicating existing ‘soiling station’ operation. The measurement of the optical transmissibility is effectively completed through a surrogate measurement, which is of relative permittivity.

Density: The density of the contamination influences other properties of the contamination, for example, the relative permittivity of the contamination. Density also influences the optical transmissibility of the contamination and may be excluded as a required attribute. No direct measurement is required.

Mass: The mass of the contamination was not shown to contribute to degradation in PV performance.

Shape and Size of the particles: The physical makeup of the contamination is a contributing factor to density, as such no direct measurement is required.

Moisture content: The moisture content of the contamination is an influencing variable included in the relative permittivity measurement. The moisture content of the contamination is also likely to change over diurnal cycles, due to rain, condensation and drying from exposure to sun/wind.

Colour: The colour of the contamination was not reported in any reviewed literature as an attribute that influences the effect of the contamination on PV performance.

Chemical composition: The composition of the contamination results in the optical transmissibility of the contamination. The chemical composition offers an insight to the expected properties of the contamination however only derived properties collected through non-contact measurement will be available.

Angle of the glass plate: The angle of the glass plate may influence the way in which contamination is collected, the sensor system however is to be agnostic of direction or orientation.

Altitude/Air pressure: The atmospheric air pressure is not referenced in any literature found regarding either contamination properties or as a variable of influence on PV performance.

Conductivity/Resistance/Impedance: Direct measurement of resistivity requires contact with the contamination, compromising the packaging requirement.

Relative permeability: Magnetic properties were not evident as significant in the reported contaminants.

3.8. Measurement System Extent

The limits of the measurement system must also be defined with both imposed and physical conditions. In addition to the requirements listed in the Measurement System Specification, the sensor system may be utilised in other applications that require monitoring of glass surface contamination. The measurement system shall also be applicable to installation on other glass panels such as windows or skylights, and as such withstand the environmental and durability requirements that are typical for those conditions.

3.9. Measurement System Influence Variables

Influence variables for a glass surface contamination sensor system primarily consist of changing environmental conditions. Diurnal and seasonal changes in temperature, humidity and rainfall will all influence the properties of the contamination.

Relative permittivity of materials is influenced by temperature, pressure and frequency of measurement. Maryott (1956) established the change in dielectric constant of water from 0 to 100°C to vary from $\varepsilon = 87.74$ to $\varepsilon = 55.72$.

As the measurement system may take regular or constant measurements, the collection of temperature data is important to include as an input to the system output calculation. The measurement system processing algorithm will require information to determine the validity and accuracy of the measurement and potentially limit the influence of temperature on the system.

As the sensing system is to be mounted within a PV module, the electric fields generated by the operation of the PV module, both constant and alternating, may radiate from the PV cells generating current. The fields are a potential source of influence on the sensing system.

Time is also an influence variable, as with progressing time, the level of contamination may change. With time, increases, decreases, and changing constituents of the contamination will occur. The level of moisture present in the contamination will also change with time.

The angle that the glass surface is mounted will directly influence the collection of contamination. Other external factors such as wind and contamination consistency will change the level of contamination accumulated. The measurement of the accumulated contamination may be influenced by the angle of the surface; however the resulting contamination is the measurement being undertaken. The angle of the mounting is not included in the measurement system.

3.10. Measurand Tree

The measurand tree provides a graphical representation of the derivation of the referents listed.

A measurand tree, visually demonstrating the phenomena that are required to be directly measured is shown in Figure 15

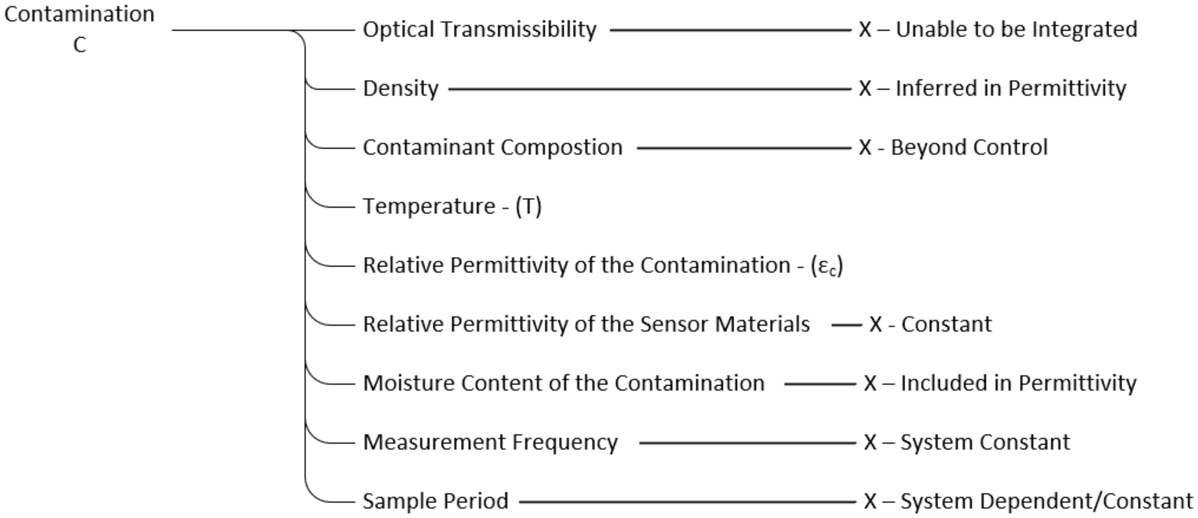

Figure 15 Measurand Tree

From the measurand tree, the Contamination level is shown to be a function of Temperature, Relative Permittivity and Measurement Frequency.

$$C = f(T\varepsilon_C)$$

Where: C is contamination level, ε_C *is the permittivity of the contaminant and* T *is temperature of the sensor (°C).*

3.11. Signal and Information Flow

A measurement system requires transducers and modifiers that change the signal and energy forms of the original measurement information into a format that is usable.

The measurement information may exist in any of the six signal domains, consisting of Chemical, Optical, Mechanical, Thermal, Magnetic, Acoustic or Nuclear. For the contamination present on the glass surface, the measurement information exists in the Mechanical and Chemical domains (USQ 2021).

The mechanical properties include the quantity or thickness and density of the contamination, which combined with the chemical properties to form the relative permittivity of the contamination.

Transducers are fundamental to a measurement system by moving the signal from one domain to another. The change of a signal domain is used to allow the measurement information to be transferred in a more convenient domain. For the glass surface contamination system, the sensor element is also a transducer which moves the measurement information into the electrical domain (USQ 2021).

Modifiers use the measurement information to modulate or modify an external energy source. This may allow the amplification, impedance change or as a direct sensing of the measurement to occur.

For the glass surface contamination sensor, the changing capacitance of the sensor element is used to modify the oscillator frequency. The oscillator output, while still in the electrical domain, is of lower impedance, allowing for further integration into the processing system.

A transducer in the form of a digital counter is used to digitise the oscillator frequency, maintaining the electrical domain of the signal, while further increasing the usability of the measurement information. The output of the counter may then be easily integrated into digital systems for processing or analysis.

The contamination information flow through the sensor system domain is shown in Figure 16.

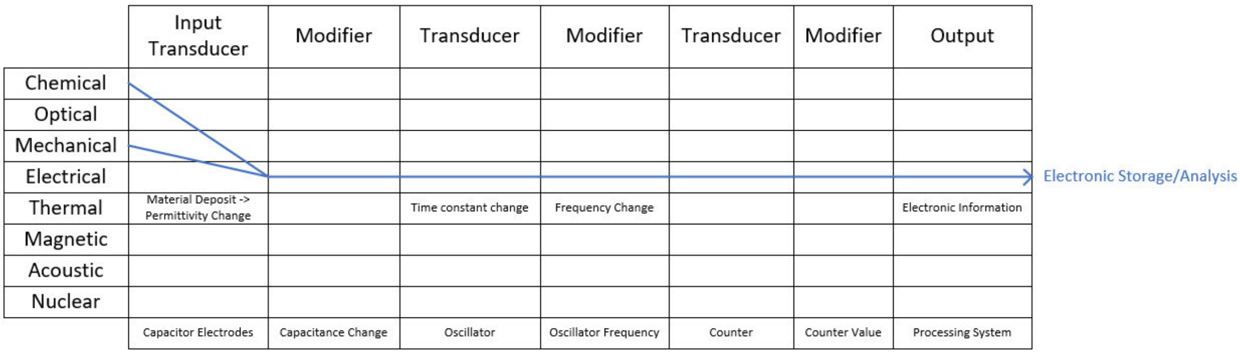

	Input Transducer	Modifier	Transducer	Modifier	Transducer	Modifier	Output
Chemical							
Optical							
Mechanical							
Electrical							
Thermal	Material Deposit -> Permittivity Change		Time constant change	Frequency Change			Electronic Information
Magnetic							
Acoustic							
Nuclear							
	Capacitor Electrodes	Capacitance Change	Oscillator	Oscillator Frequency	Counter	Counter Value	Processing System

Figure 16 Contamination Information Flow

The temperature measurement input transducer is a Resistance Temperature Device (RTD) temperature sensor. The transducer moves the signal information from the thermal domain into the electrical domain through a resistance change.

The resistance change acts as a modifier for an Analogue to Digital Converter (ADC) that maintains electrical domain while modifying the temperature information for use in the digital processing system.

The contamination information flow through the sensor system domain is shown in Figure 17.

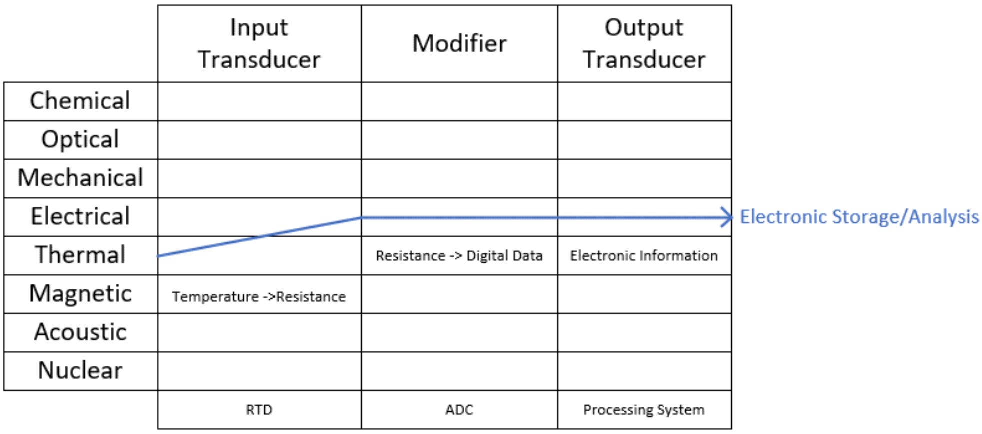

	Input Transducer	Modifier	Output Transducer
Chemical			
Optical			
Mechanical			
Electrical			
Thermal		Resistance -> Digital Data	Electronic Information
Magnetic	Temperature ->Resistance		
Acoustic			
Nuclear			
	RTD	ADC	Processing System

Figure 17 Temperature Information Flow

3.12. Signal Processing & Analysis

From the analogue world that the sensor element experiences, a digitisation of the information collected will occur in the measurement system. The digitisation allows for signal processing and analysis.

The various effects and variables that may need to be accounted for in the processing and analysis of the measurement system are primarily the diurnal weather phenomena including humidity, moisture (rain, condensation/dew, etc.) and temperature. These may all influence the properties of the contaminants on the glass surface. The time of day, as well as the interval between measurements will also allow the system to determine and evaluate change in input measurements.

Water, from humidity, rain or condensation/dew will cause both removal (cleaning) and compaction of contaminants on the glass surface. Water will also influence the properties of the contamination, modifying the relative permittivity of the contamination both while wet and due to compaction/density increase. The quantity of moisture in the contamination will also vary over the diurnal cycle, influencing the sensor system measurements.

The individual installation of a PV module, including the angle of the PV module, will also determine the type and quantity of contamination found on the module surface. Wind is considered to both deposit and remove contamination.

Temperature may influence the relative permittivity of the materials the sensor system is constructed of, while the properties of the contamination may also change. Temperature may also be an indicator of contamination moisture level, how ‘dry’ the contamination is likely to be.

All the environmental factors introduce variability to the measurement system that will need to be accounted for. Signal processing and analysis of the measurement system will be required to store and process the sensor and temperature inputs to apply the correct analysis and contamination evaluation.

The processing and analysis of the measurements performed will require the evaluation of the changes observed in the measurement of permittivity and temperature. The analysis of the permittivity versus temperature and time may predict a minima in the measurement, which can be interpreted as the current level of contamination.

The required period of contamination level evaluation may be determined by the system performance and cleaning requirements, however the rate of soiling increase in a typical application may allow for multiple-days of time between evaluations. The extended evaluation window will allow the measurement system to conduct multiple measurements, performing evaluations with many data points collected.

Pre-determined calibrations may allow the analysis of the sensor measurements to determine the moisture level, or combined with temperature data evaluate if the contamination could be considered ‘dry’.

As the primary sensor input will detect water in the contamination, the evaluation may look for a minima in contamination level, which it may determine over a multiple-reading, and possibly multiple-day period. As the relative permeability of water is much higher that that of typical contaminants (see Table 2: Permittivity of Select Materials) the evaluation may exclude ‘wet’ days and ‘wet’ measurements, performing evaluation of contamination level when ‘dry’ contamination is present on the glass surface.

3.13. Resulting system

The measurement system resulting from the investigation and analysis of the measurement problem has been found. The measurement system consists of an electrode-on-glass sensor element acting as an input transducer, moving the mechanical and chemical information of the contamination on the glass surface into the electrical domain. In addition, a RTD is used to measure the temperature of the sensor, by moving the thermal information into the electrical domain.

When a contamination or material change occurs on the glass surface, the electrodes on the underside, embedded in the backing sheet of a PV module or other material, will respond with a change in capacitance value due to the change in permittivity resulting from a change in quantity type or density of contamination.

The capacitance change of the electrodes is used as an input to an oscillator. The alteration of the capacitance input changes the oscillator output frequency, modifying the contamination information from an analogue small signal in the electrical domain into a large signal, compatible with a digital electrical and time domain.

The frequency output of the oscillator may then be measured by a digital processing system, for analysis and display.

The temperature information is used by the processing system to determine the likely moisture content of the contamination, and aid in the processing of the contamination level.

4. Simulation

4.1. Theory

The conceptual sensor included in a PV module construction of glass and EVA consists of electrodes on the rear surface of the glass plate which form a basic capacitor. The electrodes are to be encapsulated by the same materials as a typical PV cell while having controllable mechanical dimensions. The glass and encapsulating material are of known permittivity, as found in 2.7 Contaminant Properties – Relative Permittivity. The capacitance change of the sensor due to the addition of contamination on the glass surface is to be simulated.

As the sensor element is conceptualised as linear electrodes with adjustable dimensions and with simple and symmetrical electrode placement, the design lends itself to a static analysis for the calculation of capacitance per unit length.

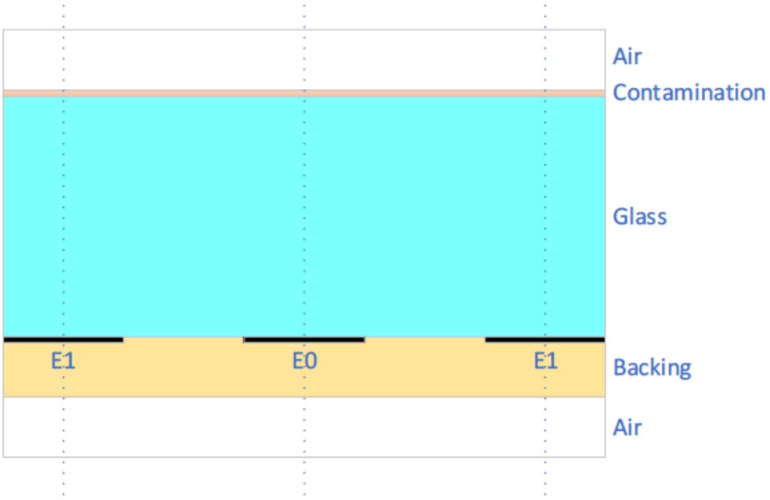

Figure 18 Contamination Sensor Cross Section

If the cross section of the sensor element is considered, a static electric field ($\boldsymbol{E}$) can be simulated between the electrodes over the cross section. The voltage gradient of the field can then be computed and an electric charge for the cross section approximated.

As a basic capacitance can be defined as:

$$C = \frac{q}{V} \qquad \text{4-1}$$

Where C capacitance, q is charge, V is voltage across parallel plates.

If the voltage of the electrodes and the permittivity of the materials of the sensor are known, the capacitance of the sensor can be calculated by finding the charge of the sensor elements.

Using Gauss's Law:

$$\nabla \cdot \boldsymbol{D} = \nabla \cdot (\varepsilon \boldsymbol{E}) = \rho \tag{4-2}$$

$$\nabla \cdot \boldsymbol{E} = -\frac{\rho}{\varepsilon} = \frac{\rho}{\varepsilon_0 \varepsilon_r} \tag{4-3}$$

Where ∇ is the Del operator, $\nabla \cdot$ is the divergence, $\boldsymbol{D}$ is displacement flux density, $\varepsilon, \varepsilon_0, \varepsilon_r$ is permittivity total, vacuum and relative, $\boldsymbol{E}$ is electric field, ρ is charge density.

Gauss's law in words can be summarised as "Electric flux out of a closed surface is equal to the charge enclosed" (USQ 2022).

The charge density for a surface area, ρ_s, can be defined as numerically equal to the perpendicular (normal) component of the displacement flux density from a surface. That is:

$$D_n dA = \rho_s dA \tag{4-4}$$

$$D_n = \rho_s \tag{4-5}$$

Where D_n is normal component of displacement flux density, ρ_s is charge density dA is a surface area.

As the sensor element consists of multiple layers of materials, each with different permittivity values, it is known that the displacement flux density ($\boldsymbol{D}$) is constant with changes in the dielectric permittivity (ε) of a capacitor, however the electric field intensity ($\boldsymbol{E}$) is not.

At the interface boundary between two dielectrics the field components can be summarised as:

Table 4 Field Components at Dielectric Boundaries

Field Component	**Boundary Relation**
Normal	$D_{n1} - D_{n2} = \rho_s$ $\varepsilon_1 E_{n1} = \varepsilon_2 E_{n2}$
Tangential	$E_{t1} = E_{t2}$

That is, displacement flux density's normal component is discontinuous by an amount equal to the surface charge, if any is present; electric field intensity is proportional to the permittivity of the two materials. Tangential electric fields are continuous over the boundary.

A simple multiple dielectric plate capacitor is shown in Figure 19 demonstrating the relationship between displacement flux density ($\boldsymbol{D}$) and the electric field intensity ($\boldsymbol{E}$).

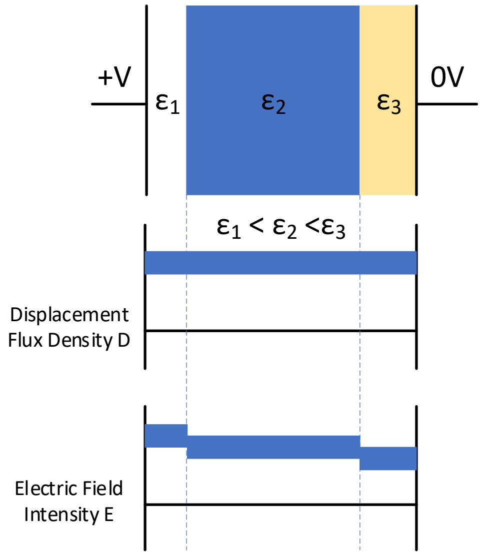

Figure 19 Displacement Flux Density Vs Electric Field Intensity

As the sensor is to be used with non-homogeneous dielectrics (the sensor consists of multiple permittivity materials), the sensor element capacitance calculation will be completed using the electric field from the simulation.

To calculate the charge contained, the cross section of the sensor element may be considered for the application of the divergence theorem (Gauss's theorem), with a closed path placed around the centre sensor element, allowing for the calculation of flux normal to the closed path.

With the application of divergence theorem to the closed path, the charge per unit length of the sensor element may be approximated by the electric field crossing the path at right-angles. Integrating over the length of the closed path around the sensor while multiplying by the permittivity allows the calculation of charge per unit length:

$$q = \varepsilon \oint_c \boldsymbol{E} \cdot \hat{\boldsymbol{n}} dl \qquad \text{4-6}$$

Where q *is charge,* $\boldsymbol{E} \cdot \hat{\boldsymbol{n}}$ *is the displacement flux normal to the path integrated over length* l*.*

If a sensor electrode voltage is chosen, the capacitance per unit length of electrode is found using equation 4-1.

As the electric field intensity ($\boldsymbol{E}$) is equal to the negative potential gradient:

$$\boldsymbol{E} = -\nabla \boldsymbol{V} \tag{4-7}$$

Substituting into Gauss's law, Poisson's equation is found:

$$\nabla \cdot \boldsymbol{E} = -\nabla\nabla \boldsymbol{V} = \frac{-\rho}{\varepsilon_0 \varepsilon_r} \tag{4-8}$$

$$\nabla^2 \boldsymbol{V} = \frac{-\rho}{\varepsilon_0 \varepsilon_r} \tag{4-9}$$

Where: ∇ is the Del Operator, $\boldsymbol{V}$ is Voltage, $\varepsilon_0, \varepsilon_r$ is permittivity vacuum and relative, ρ is charge density.

Using known voltages and permittivity of materials, the simulation allows for the calculation of equal potential curves to study the interaction of the sensor element with contaminants on the surface.

The simulation is configured to analyse sensor performance with controlled changes in physical dimensions of the electrodes (spacing and width) while also calculating performance due to different contamination properties, including thickness and permittivity values.

4.2. Finite Difference Method

A two-dimensional (2D) simulation analysis of the sensor element cross section is to be applied, allowing for the calculation of approximate unit-length capacitance of the sensor. The Finite Difference Method (FDM) allows for calculation of capacitance of the sensor cross section through the calculation of electric fields over the cross section which equation 4-6 and 4-9 may be applied. The analysis may be conducted with various physical dimensions and properties allowing for an optimisation of the sensor element design.

4.2.1. *Mesh Generation*

For the application of a 2D FDM to the sensor cross section, a mesh in the form of a grid of nodes is to be conceptualised over the surface.

Each of the nodes is to be spaced evenly from its neighbours by distance ‘h’, in a grid and assigned ‘i’ & ‘j’ for columns and rows respectively. Each node can then be referenced to other nodes by its relative position in both ‘i’ & ‘j’ grid position, as shown in Figure 20.

If the spacing between the nodes (h) is reduced greatly to where errors are negligible, the calculation of ordinary differential equations (ODE) or partial differential equations (PDE) may be achieved by converting to a system of linear equations (Nagel 2011).

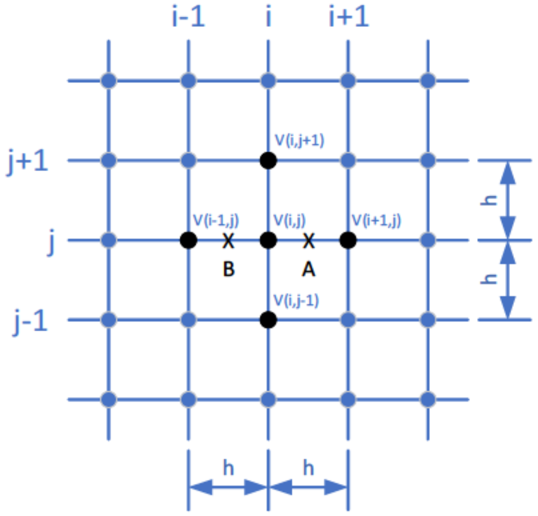

Figure 20 FDM Node 2D Grid

For the 2D grid of nodes, configured as a ‘five-point star’, shown in Figure 20, the first derivative is approximated by dividing the difference in voltage between adjacent nodes by the distance, for the x-axis:

For point ‘A’:

$$\left.\frac{\partial V}{\partial x}\right|_{(i+\frac{1}{2},j)} \cong \frac{V(i+1,j)-V(i,j)}{h} \tag{4-10}$$

For point ‘B’:

$$\left.\frac{\partial V}{\partial x}\right|_{(i-\frac{1}{2},j)} \cong \frac{V(i,j)-V(i-1,j)}{h} \tag{4-11}$$

The second derivative, as required by Poisson’s Equation (4-9) can be estimated for the x-axis using the values at point ‘A’ and ‘B’:

$$\left.\frac{\partial^2 V}{\partial x^2}\right|_{(i,j)} \cong \frac{1}{h}(A - B) \tag{4-12}$$

$$\left.\frac{\partial^2 V}{\partial x^2}\right|_{(i,j)} \cong \frac{V(i+1,j) - 2V(i,j) + V(i-1,j)}{h^2} \tag{4-13}$$

The y-axis values can also be found using the same method:

$$\left.\frac{\partial^2 V}{\partial y^2}\right|_{(i,j)} \cong \frac{V(i,j+1) - 2V(i,j) + V(i,j-1)}{h^2} \tag{4-14}$$

Combining to find:

$$\nabla^2 \boldsymbol{V_{ij}} \approx \frac{V(i,j+1) + V(i,j-1) + V(i+1,j) + V(i-1,j) - 4V(i,j)}{h^2} \tag{4-15}$$

$$\frac{V(i,j+1) + V(i,j-1) + V(i+1,j) + V(i-1,j) - 4V(i,j)}{h^2} \approx \frac{-\rho(i,j)}{\varepsilon_0 \varepsilon_r} \tag{4-16}$$

As h is a constant during the calculations, it can be removed:

$$V(i,j+1) + V(i,j-1) + V(i+1,j) + V(i-1,j) - 4V(i,j) \cong \frac{-\rho(i,j)}{\varepsilon_0 \varepsilon_r} \tag{4-17}$$

Solving for V(i,j):

$$4V(i,j) \cong V(i,j+1) + V(i,j-1) + V(i+1,j) + V(i-1,j) + \frac{-\rho(i,j)}{\varepsilon_0 \varepsilon_r} \tag{4-18}$$

If the dielectric is considered to have no charge outside of the electrode surfaces or boundaries, 4-18 simplifies to (Nagel 2011):

$$4V(i,j) \cong V(i,j+1) + V(i,j-1) + V(i+1,j) + V(i-1,j) \tag{4-19}$$

4.2.2. Electric Field Permittivity Variations

Considering Poisson’s equation (4-9) and the boundary conditions shown in Table 4 Field Components at Dielectric Boundaries, the effect of the permittivity variations to the charge density and hence capacitance is shown.

For the 2D FDM, an area around each node is designated $\Omega_{(i,j)}$, surrounding point $V_{(i,j)}$ which is bounded by the permittivity at $\varepsilon_{(i,j)}, \varepsilon_{(i-1,j)}, \varepsilon_{(i-1,j-1)}, \varepsilon_{(i,j-1)}$ as shown in Figure 21.

Rearranging the equation 4-9 to isolate the permittivity of free space and charge density:

$$\boldsymbol{\nabla} \cdot \varepsilon \boldsymbol{\nabla} \boldsymbol{V} = -\frac{1}{\varepsilon_0}\rho \qquad 4\text{-}20$$

The charge density at the point $\rho_{(i,j)}$ may be calculated by taking the surface integral of the area.

$$\iint_{\Omega(\mathrm{i,j})} \boldsymbol{\nabla} \cdot \varepsilon \boldsymbol{\nabla} \boldsymbol{V}\, d\Omega = -\frac{1}{\varepsilon_0} \iint_{\Omega(\mathrm{i,j})} \rho_s\, d\Omega \qquad 4\text{-}21$$

Simplifying the right-hand side of equation 4-21, we find that the charge density is equal to the total charge enclosed (Gauss's law) (Nagel 2011):

$$-\iint_{\Omega(\mathrm{i,j})} \rho_s\, d\Omega = -Q_{(i,j)} \qquad 4\text{-}22$$

Where $Q_{i,j}$ *is charge at point (i,j) ,* ρ_s *is charge density of the surface.*

The left-hand side of equation 4-21 may also be simplified through the divergence theorem to convert to a contour integral, with the normal component of the field:

$$\iint_{\Omega(\mathrm{i,j})} \boldsymbol{\nabla} \cdot \varepsilon \boldsymbol{\nabla} \boldsymbol{V}\, d\Omega = \oint_{\mathrm{C(i,j)}} \varepsilon \boldsymbol{\nabla} \boldsymbol{V} \cdot d\boldsymbol{n} \qquad 4\text{-}23$$

Resulting in the equation:

$$\oint_{\mathrm{C(i,j)}} \varepsilon \boldsymbol{\nabla} \boldsymbol{V} \cdot d\boldsymbol{n} = -\frac{1}{\varepsilon_0} Q_{(i,j)} \qquad 4\text{-}24$$

Due to the 2D analysis, the equation expands to:

$$\oint_{\mathrm{C(i,j)}} \left[\varepsilon\left(\frac{\boldsymbol{\delta}}{\boldsymbol{\delta}\mathbf{x}} \boldsymbol{V}\hat{\boldsymbol{\imath}} + \frac{\boldsymbol{\delta}}{\boldsymbol{\delta}\mathbf{y}} \boldsymbol{V}\hat{\boldsymbol{\jmath}}\right)\right] \cdot d\boldsymbol{n} = -\frac{1}{\varepsilon_0} Q_{(i,j)} \qquad 4\text{-}25$$

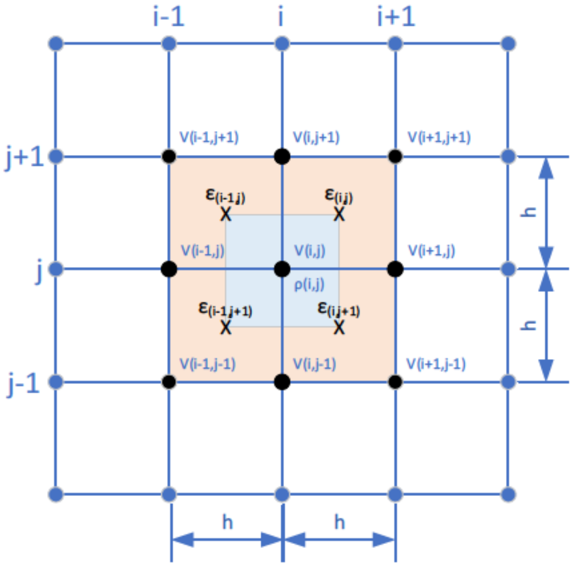

Figure 21 FDM Permittivity Surrounding a Point

Considering the gradient operator for the contour integral and the surface surrounding point is in the (i,j) mesh, the equivalent equation for the normal fields around the point $C(i,j)$ is (Nagel 2011):

$$\oint_{C(i,j)} \varepsilon \nabla \boldsymbol{V} \cdot dn = \int_{\varepsilon_{(i,j)} \to \varepsilon_{(i,j-1)}} + \int_{\varepsilon_{(i-1,j)} \to \varepsilon_{(i,j)}} + \int_{\varepsilon_{(i-1,j-1)} \to \varepsilon_{(i-1,j)}} + \int_{\varepsilon_{(i,j-1)} \to \varepsilon_{(i-1,j-1)}} \tag{4-26}$$

As the contour integral intersects the voltage nodes, the partial derivative may be substituted by the difference between the voltage components. The integral components are:

$$\int_{\varepsilon_{(i,j)} \to \varepsilon_{(i,j-1)}} \approx h \left[\frac{\varepsilon_{(i,j)} + \varepsilon_{(i,j-1)}}{2}\right] \left[\frac{V(i+1,j) - V(i,j)}{h}\right] \tag{4-27}$$

$$\int_{\varepsilon_{(i-1,j)} \to \varepsilon_{(i,j)}} \approx h \left[\frac{\varepsilon_{(i-1,j)} + \varepsilon_{(i,j)}}{2}\right] \left[\frac{V(i,j+1) - V(i,j)}{h}\right] \tag{4-28}$$

$$\int_{\varepsilon_{(i-1,j-1)} \to \varepsilon_{(i-1,j)}} \approx h \left[\frac{\varepsilon_{(i-1,j-1)} + \varepsilon_{(i-1,j)}}{2}\right] \left[\frac{V(i-1,j) - V(i,j)}{h}\right] \tag{4-29}$$

$$\int_{\varepsilon_{(i,j)} \to \varepsilon_{(i,j-1)}} \approx h \left[\frac{\varepsilon_{(i,j-1)} + \varepsilon_{(i-1,j-1)}}{2}\right] \left[\frac{V(i,j-1) - V(i,j)}{h}\right] \tag{4-30}$$

As $V(i,j)$ is common to all integrals and for compactness and *h* cancels, constants are assigned:

$$\varepsilon_{(i,j)} + \varepsilon_{(i-1,j)} + \varepsilon_{(i,j-1)} + \varepsilon_{(i-1,j-1)} = a_0 \tag{4-31}$$

$$\left[\frac{\varepsilon_{(i,j)} + \varepsilon_{(i,j-1)}}{2}\right] = a_1 \tag{4-32}$$

$$\left[\frac{\varepsilon_{(i-1,j)} + \varepsilon_{(i,j)}}{2}\right] = a_2 \tag{4-33}$$

$$\left[\frac{\varepsilon_{(i-1,j-1)} + \varepsilon_{(i-1,j)}}{2}\right] = a_3 \tag{4-34}$$

$$\left[\frac{\varepsilon_{(i,j-1)} + \varepsilon_{(i-1,j-1)}}{2}\right] = a_4 \tag{4-35}$$

Finally, the contour integral is approximated:

$$\oint_{\mathrm{C(i,j)}} \approx -a_0V(i,j) + a_1V(i+1,j) + a_2V(i,j+1) + a_3V(i-1,j) + a_4V(i,j-1) \tag{4-36}$$

Substituting back into Poisson’s equation (4-9), we find:

$$-a_0V(i,j) + a_1V(i+1,j) + a_2V(i,j+1) + a_3V(i-1,j) + a_4V(i,j-1) = -\frac{1}{\varepsilon_0}Q_{(i,j)} \tag{4-37}$$

Rearranging, the voltage at node $V(i,j)$ is found (Nagel 2011):

$$V(i,j) = \frac{1}{a_0}\left[a_1V(i+1,j) + a_2V(i,j+1) + a_3V(i-1,j) + a_4V(i,j-1) + \frac{1}{\varepsilon_0}Q_{(i,j)}\right] \tag{4-38}$$

4.2.3. Node Voltages

With the voltage at each node of $V(i,j)$ able to be calculated using the combination of the ‘five-point star’ of surrounding node voltages, as shown in Figure 20 as well as the permittivity of the materials surrounding the node, a system of simultaneous equations can be established.

If the node grid is extended to a boundary condition, either Dirichlet or Neumann, the values of the boundary are used in the equation to form the unknown nodes.

The Dirichlet condition is considered the boundary formed at the surface of a conductor, such as the electrodes of the sensor, shown at 1V in Figure 22. A Neumann condition uses symmetry or a point considerable distance from the area of interest where the gradient of the voltage is considered to reach 0, shown as the 0V border in Figure 22.

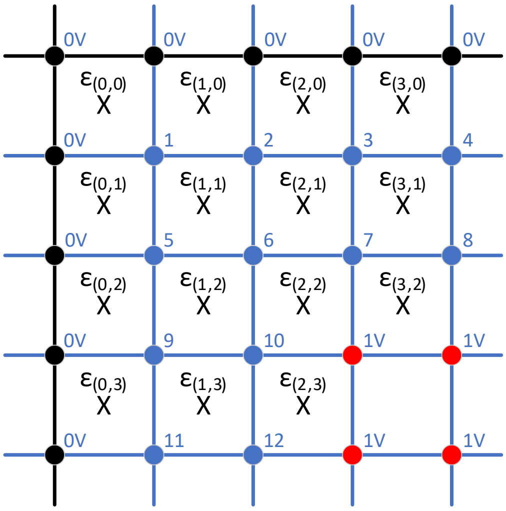

Figure 22 Example FDM Node Voltage and Boundary Conditions

If the simulation area has the nodes numbered sequentially, such as shown in Figure 22, the solution allows for the generation of a system of linear simultaneous equations, which can be represented by:

$$a_0V_1 = 0 + a_1V_2 + a_4V_5 + 0$$

$$a_0V_2 = 0 + a_1V_3 + a_4V_6 + a_3V_1$$

$$a_0V_3 = 0 + a_1V_4 + a_4V_7 + a_3V_2$$

$$|$$

$$a_0V_5 = a_2V_1 + a_1V_6 + a_4V_9 + 0$$

$$|$$

$$a_0V_7 = a_2V_3 + a_1V_8 + 1 + a_3V_6$$

$$|$$

$$a_0V_{10} = a_2V_6 + 1 + a_4V_{12} + a_3V_9$$

Where the values a_0 through a_4 are the same as demonstrated in equations 4-31 thru 4-35 above.

This sequence lends itself to representation in matrix-vector form:

$$\boldsymbol{A}x = b$$

$$\begin{bmatrix} a_0 & -a_1 & 0 & 0 & -a_4 & 0 & 0 & 0 & 0 & 0 & 0 & 0 \\ -a_3 & a_0 & -a_1 & 0 & 0 & -a_4 & 0 & 0 & 0 & 0 & 0 & 0 \\ 0 & -a_3 & a_0 & -a_1 & 0 & 0 & -a_4 & 0 & 0 & 0 & 0 & 0 \\ \vdots & \vdots & \vdots & \ddots & \vdots & \vdots & \vdots & \vdots & \vdots & \vdots & \vdots & \vdots \\ -a_2 & 0 & 0 & 0 & a_0 & -a_1 & 0 & 0 & -a_4 & 0 & 0 & 0 \\ \vdots & \vdots & \vdots & \vdots & \vdots & \ddots & \vdots & \vdots & \vdots & \vdots & \vdots & \vdots \\ 0 & 0 & -a_2 & 0 & 0 & -a_3 & a_0 & -a_1 & 0 & 0 & 0 & 0 \\ \vdots & \vdots & \vdots & \vdots & \vdots & \vdots & \vdots & \ddots & \vdots & \vdots & \vdots & \vdots \\ \vdots & \vdots & \vdots & \vdots & \vdots & \vdots & \vdots & \vdots & \ddots & \vdots & \vdots & \vdots \\ 0 & 0 & 0 & 0 & 0 & -a_2 & 0 & 0 & -a_3 & a_0 & 0 & -a_4 \end{bmatrix} \begin{bmatrix} V_1 \\ V_2 \\ V_3 \\ V_4 \\ V_5 \\ V_6 \\ V_7 \\ V_8 \\ V_9 \\ V_{10} \\ V_{11} \\ V_{12} \end{bmatrix} = \begin{bmatrix} 0 \\ 0 \\ 0 \\ 0 \\ 0 \\ 0 \\ 1 \\ 0 \\ 0 \\ 1 \\ 0 \\ 0 \end{bmatrix}$$

MATLAB allows the system of linear equations to be solved using this matrix algebra, finding node voltages V_x, which can then be substituted into the node values of the mesh.

With a very large number of nodes, the node voltages can be closely approximated to true values through minimising the error in the approximation of the differential equations used to develop the node voltages.

4.2.4. Electric Fields

The electric field generated over the sensor cross section may be calculated using the node voltages.

From the definition:

$$\boldsymbol{E} = -\nabla \mathrm{V} \qquad \text{4-39}$$

In a 2D cross section, the value of the electric field is:

$$\boldsymbol{E_{i,j}} = -\hat{\imath}\frac{\delta \mathrm{V}}{\delta \mathrm{i}} - \hat{\jmath}\frac{\delta \mathrm{V}}{\delta \mathrm{j}} \qquad \text{4-40}$$

The 2D FDM mesh allows for the calculation of the 'i' and 'j' components of the electric field vector independently as shown in Figure 23, resulting in the approximation of the electric field in the axes:

$$\boldsymbol{E_{x_{i,j}}} \approx -\frac{V(i+1,j) - V(i,j)}{h} \qquad \text{4-41}$$

$$\boldsymbol{E}_{y_{i,j}} \approx -\frac{V(i,j+1) - V(i,j)}{h} \qquad \text{4-42}$$

The electric field value at the centre of the voltage nodes, $\boldsymbol{E'}_{i,j}$, may be calculated from the four $\boldsymbol{E}_{i,j}$ components surrounding the point. At each location the electric field components consist of:

$$\boldsymbol{E}_{x}{}'_{i,j} = \frac{1}{2}\left[\boldsymbol{E}_{x_{i,j+1}} + \boldsymbol{E}_{x_{i,j}}\right] \qquad \text{4-43}$$

$$\boldsymbol{E}_{y}{}'_{i,j} = \frac{1}{2}\left[\boldsymbol{E}_{y_{i+1,j}} + \boldsymbol{E}_{y_{i,j}}\right] \qquad \text{4-44}$$

The components allow the plotting of the electric field vector for each $\boldsymbol{E'}$ location (Nagel 2011).

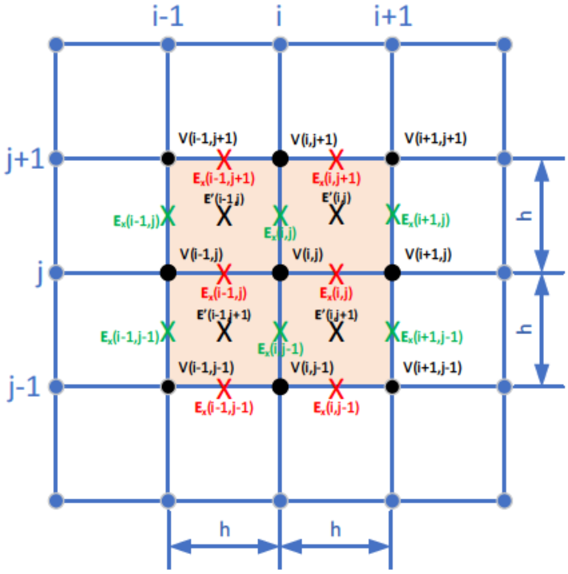

Figure 23 FDM Electric Field Calculation

4.2.5. Capacitance Calculation

With the voltage components calculated for the nodes in the mesh, the charge on the centre electrode may be calculated by forming a line integral around the conductor.

If the line integral is taken in proximity to the 0V conductors, the error in the voltage gradient due to the linear approximation of the differential equations will be minimised. Figure 24 shows the conceptual line integral path around the centre electrode, enclosing the electrode and the layers of sensor construction entirely.

Applying Gauss's law, the charge contained on the electrode by integrating the electric flux normal to the line integral path can be calculated.

Repeated for simplicity:

$$q = \varepsilon \oint_{c} \boldsymbol{E} \cdot \hat{\boldsymbol{n}} dl \tag{4-45}$$

Where q *is charge,* ε *is permittivity,* $\boldsymbol{E} \cdot \hat{\boldsymbol{n}}$ *is the electric field normal to the path integrated over length* l*.*

With the line integral shown in Figure 24 encompassing the electric fields generated in equations 4-43 and 4-44, which allows the horizontal and vertical components of the fields mesh to be easily included as normal components to the straight and perpendicular line integral.

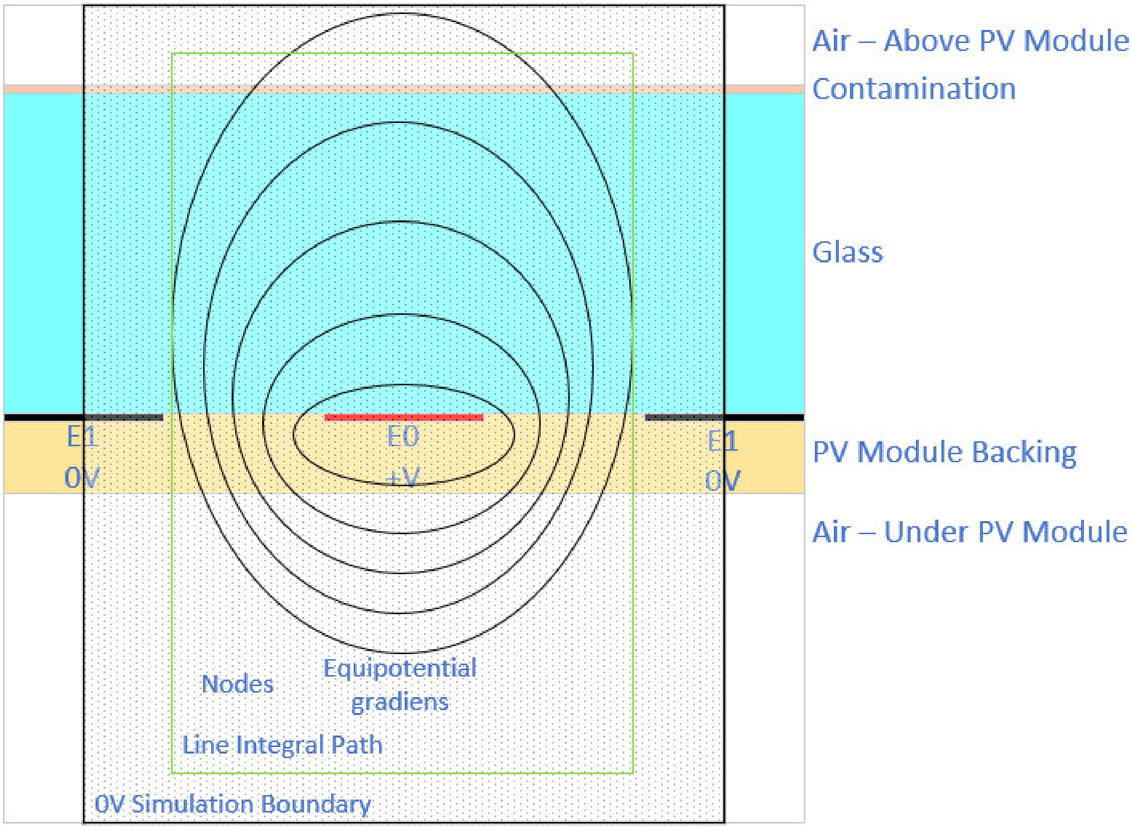

Figure 24 FDM Sensor Cross Section and Line Integral

As the electric field components are calculated using the node voltages generated by equation 4-38, the permittivity of the material on each side of the node must be included in equation 4-48. The resulting integrands are thus:

$$\int_{Vertical} \approx \varepsilon_{(i,j)}\varepsilon_{(i,j-1)}\boldsymbol{E}_{\boldsymbol{y}_{\boldsymbol{i},\boldsymbol{j}}} \tag{4-46}$$

$$\int_{Horizontal} \approx \varepsilon_{(i,j)}\varepsilon_{(i-1,j)}\boldsymbol{E}_{\boldsymbol{x}_{\boldsymbol{i},\boldsymbol{j}}} \tag{4-47}$$

The contour integral consists of two horizontal and vertical components, resulting in the integration occurring for all components:

$$q \approx \int_{Vertical} + \int_{Vertical} + \int_{Horizontal} + \int_{Horizontal} \tag{4-48}$$

Finally, to calculate the capacitance of the simulated cross section the charge must be divided by the voltage between the electrodes, as per equation 4-1.

$$C \approx \frac{\int_{Vertical} + \int_{Vertical} + \int_{Horizontal} + \int_{Horizontal}}{V} \tag{4-49}$$

The resulting capacitance is per unit length of the simulated cross section.

4.3. Simulation Code Description

4.3.1. *Introduction*

The simulation is written in MATLAB with code and functions and made available in APPENDIX C MATLAB SIMULATION CODE.

The functionality is split into two components, the first to generate and save capacitance data for the defined physical and electrical properties, while the second performs analysis and generates plots.

4.3.2. *Data Generation Code Description*

The data generation simulation is coded to perform a capacitance per unit length calculation using a FDM analysis of a sensor element cross section, as shown in Figure 24. The simulation is programmed with the physical properties and materials of the sensor element as well as the contaminants.

The sensor element width and spacing are used, as well as the thicknesses of the glass, backing sheet and surface contamination in the simulation. The permittivity of each material is also configurable, so that the effect of contamination permittivity change can be calculated.

The code was written with flexibility, so that the functionality or output of the code can be changed with simple single line modification at the top of the code.

The code begins with array definitions of the parameters to be tested. These include arrays for:

- Sensor element with, in mm.
- Sensor element spacing, in mm.
- Contamination permittivity.

Fixed physical parameters for the following are also defined in mm:

- Glass thickness.
- Backing sheet thickness.
- Contamination thickness.

Other simulation parameters are also defined at the beginning of the script including:

- Constants.
- Simulation voltage.
- Number of nodes per mm.
- Simulation height.

Once the simulation parameters are defined, the script enters a series of nested loops. The loops allow for the repeated autonomous calculation based on the testing parameters.

For each loop, the script first determines the variables to use during the iteration. The script then configures two matrices. The first represents the physical dimensions of the cross section to be tested, the second representing the permittivity layers of the cross section.

The values defined in the physical properties are used to set the size of the square matrices. The largest dimension calculated from the width and spacing of the electrodes or the maximum 'simulation height' is used to determine the matrix dimension.

The permittivity matrix is populated with the permittivity values of the materials set at the beginning of the script. The number of rows of the permittivity matrix is set by the 'nodes per mm' dimension and the thickness of the material layers, so that both the physical and electrical properties overlay correctly.

The physical dimension matrix is then populated with 'dummy values' that represent the electrodes, Dirichlet or Neumann boundaries. Dummy values are used so that the script can determine the conditions and correctly perform future calculations.

The physical matrix is populated with node numbers. The numbering begins at the first node that has not had a boundary condition applied, and increments in a row-column order, populating the full physical matrix with unique and incrementing node numbering.

A square sparse matrix 'A' of dimensions determined by the number of unique node numbers in the physical matrix is then generated. The matrix is used to hold the 'A' component in the simultaneous equations, as described in 4.2.3 Node Voltages.

A sparse single column 'b' vector of dimension that matches the number of unique nodes is also generated. The 'b' component of the simultaneous equations, as described in 4.2.3 Node Voltages.

The script then enters a conditional loop that iterates for the number of unique nodes, generating the values to fill both the 'A' and 'b' matrices.

The function 'nodefill' is passed the current node number, to which it collects the surrounding node numbers and permittivity values, performing the calculations shown in 4.2.2 Electric Field Permittivity Variations. 'nodefill' returns the a_0-a_4 values as well as the node numbering used in equation 4-38. The value for the ‘b’ vector is checked for boundary conditions and is set appropriately.

At the completion of the full set of node numbering, both the ‘A’ and ‘b’ matrix are populated as per 4.2.3 Node Voltages.

The code then performs the right-division calculation, resulting in the calculation of individual node voltages, stored sequentially in the ‘V’ vector.

A duplicate of the physical matrix is made into matrix ‘map’, allowing a second function ‘vReturn’ to be iterated through for the number of nodes. Each unique node is substituted with the corresponding values in vector ‘V’, resulting in the completed node voltage map.

With the node voltages calculated, the code proceeds to calculate the electric fields in both the ‘i’ and ‘j’ directions as per 4.2.4 Electric Fields. The resulting matrices ‘Ex’ and ‘Ey’ hold the electric fields for use in the calculation of the contour integral.

The script then performs the capacitance calculation using a contour integral as per 4.2.5 Capacitance Calculation. Using the permittivity matrix, and both the ‘Ex’ and ‘Ey’ matrices, the dimensions for the contour integral are calculated from the physical parameters set, so that the integral surrounds the centre electrode, with the integral being performed close to the outer grounded electrodes.

The horizontal and vertical components of the line integral utilise the ‘Ex’ and ‘Ey’ electric field matrices respectively, so that the normal component of the electric field is utilised in the calculation as described in section 4.2.5 Capacitance Calculation.

The line integral dimensions are saved for use in the field and equipotential plotting section to demonstrate the position of the integral relative to the electrodes.

With the line integral calculation completed, the script then performs the capacitance calculation by summing the horizontal and vertical components of the line integral, and dividing by the electrode voltage, completing the equation 4-49.

The script now enters the plotting and display section if enabled. Two plots can be generated for each unique simulation, including an equipotential plot and electric field plot. The equipotential plot demonstrates the equipotential voltages surrounding the centre electrode, while the electric field plot demonstrates the electric field vectors surrounding the centre electrode.

The code saves the value of capacitance calculated in matrix 'Results' and updated the spreadsheet file 'Results.xls' for each calculation, with each material generating a new worksheet. The spreadsheet file allows for the data to be viewed and transferred to the analysis script for use in plotting after the completion of all variable testing.

4.3.3. Analysis and Plot Generation

The Analysis and Plot Generation code was originally included in the data generation code, however due to the simulation time taken to produce data, it was separated to conduct the analysis independently.

The code uses the simulation parameters common to the data generation code, so that the physical properties of the simulated cross section and contamination are maintained correctly.

The capacitance data generated and saved into the results spreadsheet by the data generation code is loaded into a multidimensional matrix, maintaining the dimensional properties and material permittivity used in the generation.

The code calculates the change in capacitance for each electrode dimension and for all contaminant materials. The change in capacitance can be used to analyse the sensor performance at detecting contamination.

With the change in capacitance calculated, the script finds the peak efficiency of the sensor, for each of the analysed contaminants, by using the dimensions of the electrodes to calculate the change for the sensor cross sectional width. The code identifies the peak efficiency and records the dimensions of the electrode width and spacing.

The analysis script generates three plots:

1. A line chart showing capacitance per unit length, comparing the relationship between centre distance of electrodes to the calculated capacitance value for each electrode width tested. The material name and permittivity are shown on the face of the plot.
2. A 3D surface plot demonstrating the capacitance difference of the contaminated and clean sensor for each electrode dimension, showing change per sensor width and spacing. The material name and permittivity are shown on the plot face.
3. A 3D surface plot that shows the change in capacitance for each contamination sample point, normalised for sensor cross section width, demonstrating sensor sensitivity for physical space consumed. The material name and permittivity as well as the dimensions of the electrodes at peak sensor efficiency are shown on the plot face.

Each plot generated is saved as a .jpg file for inclusion in this report.

The script then normalises the capacitance change based on the permittivity of the contaminant and performs an averaging of each electrode dimension for each contaminant, resulting in a single normalised mean.

The normalised mean electrode dimension is checked for peak efficiency by comparing to the cross-section width. The resulting data is used to generate a 3D surface plot.

The script finishes by saving the calculated analysis to three spreadsheets:

1. Capacitance difference, giving the change in capacitance for each sensor dimension and simulated contamination.

2. Normalised capacitance change data, giving the capacitance change per sensor dimension normalised to the total width of the sensor, for each simulated contamination.
3. Peak sensor efficiency dimensions, as printed on the 3D surface plot, in mm.

4.4. FDM Simulation Verification and Validation

The simulation model Verification and Validation (V&V) is conducted with the comparison of ideal formulae for comparable constructions to the results calculated by the simulation. Multiple points are tested and compared.

4.4.1. Homogeneous Dielectric

The sensor element shares similar construction to traces embedded on a Printed Circuit Board (PCB), as shown in Figure 25. The calculation of trace per-unit length capacitance is shown by Paul (2008) in equation 4-50 for a single trace combination in a homogeneous dielectric. The electrode thickness is considered negligible, while the spacing and width are shown by dimensions ‘s’ and ‘w’ respectively.

As the sensor simulation consists of three conductors with the outer pair at the same 0V potential, as shown in Figure 24, the value of equation 4-50 must be doubled for the output of the simulation to be comparable to the formula result. The simulation will not account for ‘fringing fields’ that would be present in the configuration shown in Figure 25; this leads to an undercalculation of capacitance values.

As the simulation is also to be set for a homogeneous dielectric that removes the variation due to construction materials, the calculations may be iterated with multiple electrode configurations and permittivity values. This allows the testing of the simulation for consistency and offset or error to the ideal value from the equation 4-50 results.

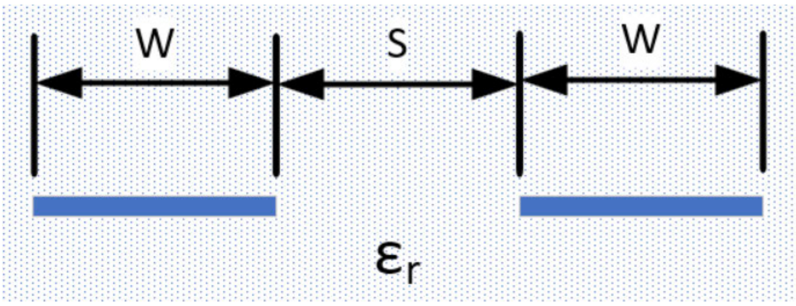

Figure 25 Embedded PCB Traces

$$C = \begin{cases} \dfrac{\varepsilon_r}{120v \ln\left(2\dfrac{1+\sqrt{k}}{1-\sqrt{k}}\right)}, for\ \dfrac{1}{\sqrt{2}} \le k \le 1 \\ \dfrac{\varepsilon_r \ln\left(2\dfrac{1+\sqrt{k'}}{1-\sqrt{k'}}\right)}{377\pi v}, for\ 0 \le k \le \dfrac{1}{\sqrt{2}} \end{cases} \qquad 4\text{-}50$$

Where: $k = \frac{s}{s+2w}$ *and* $k' = \sqrt{1-k^2}$ *(Paul 2008)*

A sample of the points tested are shown in Table 5 Calculation Vs Simulation Results. As shown, the width and spacing of the sensor element was varied, with multiple permittivity values tested for each.

The percentage difference in capacitance value between the calculation and simulation is also shown in Table 5. This demonstrates the consistency of the simulation and highlights the requirement to maintain a comparable quantity of nodes between the electrodes.

It can be seen that the simulation consistently calculates lower than the formulae value, which is explained by the lack of 'fringing fields' around the outer edges of the outermost electrodes.

The results also show that with a larger spacing between the electrodes the simulation performance improves. This is likely due to two main factors:

1. The smaller distances between the electrodes reduce the effective number of nodes when a constant nodes per mm value is applied. This lowers the resolution and accuracy of the simulation, particularly in the highest electric field area directly between the electrode ends.

2. 'Fringing Fields' will be less significant in the calculation model with larger spacing between electrodes, reducing the effect of the simulation not having them included.

The results also show that the simulation is consistent with the calculated values for changes in dielectrics. For the purpose of the sensor design, the precise capacitance value is not of significance due to the change in capacitance being of interest.

The need to maintain comparable numbers of nodes between the electrodes, the 's' distance in Figure 25, is also highlighted by the increased error in the lower spacing simulations.

This performance suggests that the simulation is valid for the calculation of changing dielectrics when used with consistent physical electrode parameters.

Table 5 Calculation Vs Simulation Results

Width	Spacing	ε_r	Calculation	Simulation	Difference
0.5	0.5	1	2.76655E-11	2.4206E-11	87.49%
0.5	0.5	2	5.5331E-11	4.8411E-11	87.49%
0.5	0.5	3	8.29965E-11	7.2617E-11	87.49%
0.5	0.5	4	1.10662E-10	9.6823E-11	87.49%
0.5	0.5	5	1.38327E-10	1.2103E-10	87.49%
3	0.5	1	4.44958E-11	3.9411E-11	88.57%
3	0.5	2	8.89915E-11	7.8821E-11	88.57%
3	0.5	3	1.33487E-10	1.1823E-10	88.57%
3	0.5	4	1.77983E-10	1.5764E-10	88.57%
3	0.5	5	2.22479E-10	1.9705E-10	88.57%
0.5	3	1	1.67096E-11	1.5431E-11	92.35%
0.5	3	2	3.34193E-11	3.0862E-11	92.35%
0.5	3	3	5.01289E-11	4.6293E-11	92.35%
0.5	3	4	6.68385E-11	6.1724E-11	92.35%
0.5	3	5	8.35482E-11	7.7155E-11	92.35%
0.5	5	1	1.46992E-11	1.3728E-11	93.39%
0.5	5	5	7.34959E-11	6.8639E-11	93.39%

4.4.2. Equipotential and Electric Field

The simulation produces multiple plots of the cross section including a plot showing equipotential and electric fields. The plots can be used to visually confirm the expected operation of the simulation code. An example of each plot is shown below in Figure 26 for a homogeneous dielectric and for the dielectric values of the materials used in PV construction, listed in Table 3 Dielectric Properties of PV Module Construction Materials, with no surface contamination layer in Figure 27.

The equipotential plot shown for homogeneous dielectrics shows a consistent and symmetrical set of curves radiating from the centre electrode. No distortion is present due to dielectric changes. The plot matches the expected shape and characteristics of an equipotential plot for the electrode configuration shown.

The equipotential plot for the multiple dielectric configuration shows distortion at the dielectric boundaries at +4mm and -1mm from the electrode centreline. The distortion demonstrates the expected change in potential due to the boundary conditions, as shown in Table 4 Field Components at Dielectric Boundaries.

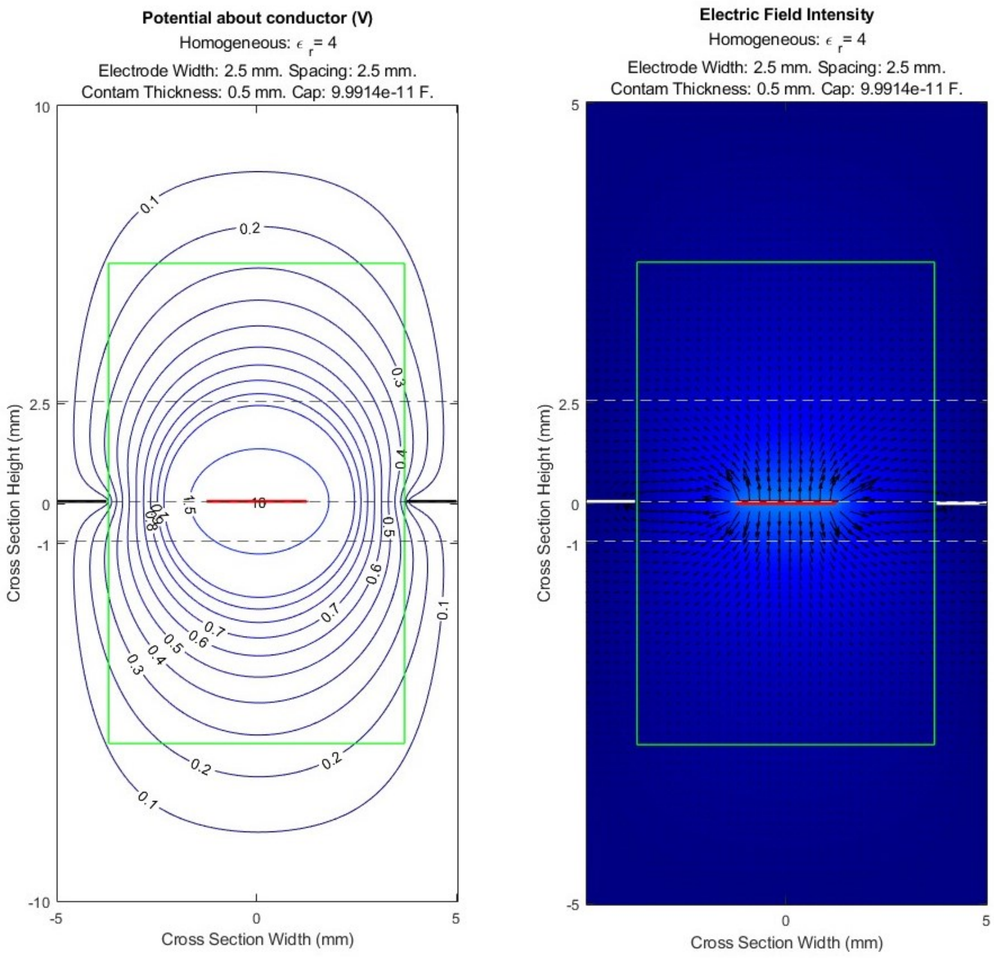

Figure 26 FDM Homogeneous Equipotential and Electric Field Plot

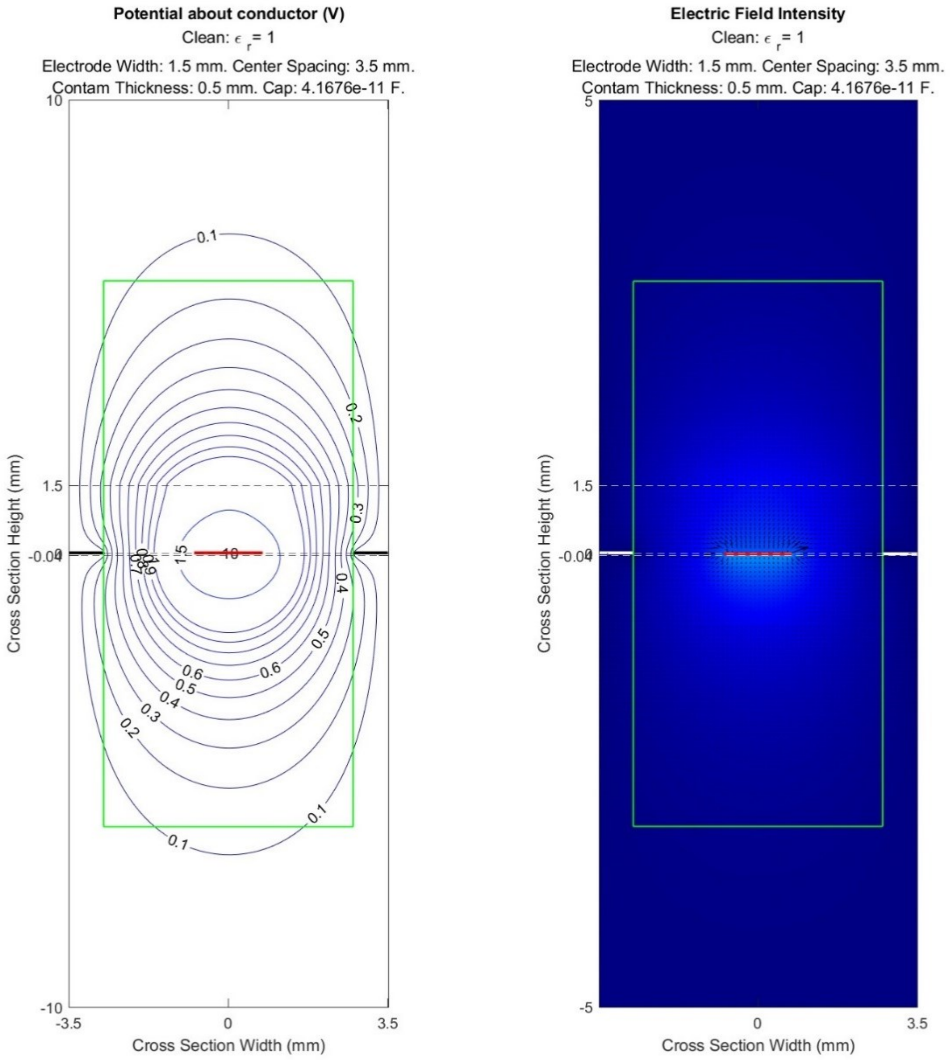

Figure 27 Clean Equipotential and Electric Field Plot

4.4.3. Node Quantity

The number of nodes included in the calculation directly relates to the accuracy of the simulation, with the number of elements requiring calculation increasing as the square of the number of nodes, as shown in section 4.2.3 Node Voltages.

The simulation output for fixed physical parameters is compared as the number of nodes per unit length is changed. The output of this comparison generates the plot as shown in Figure 28. The plot shows a near asymptotic response to a final capacitance value as the number of nodes is increased. The trade-off is simulation time and computer memory requirements. A compromise between simulation accuracy and calculation complexity is reached for the chosen number of nodes used in the simulation.

The computed value was compared to the value calculated using the equation 4-50, from section 4.4.1 Homogeneous Dielectric. The values are summarised in Table 6.

Table 6 Simulation Node Density

Nodes/mm	**Nodes in Separation**	**Simulation Capacitance (F)**	**Formulae Capacitance (F)**	**Difference**
6	12	8.018E-11	9.05E-11	-11.46%
10	20	8.122E-11	9.05E-11	-10.31%
14	28	8.168E-11	9.05E-11	-9.79%
20	40	8.203E-11	9.05E-11	-9.40%
26	52	8.222E-11	9.05E-11	-9.19%
32	64	8.235E-11	9.05E-11	-9.05%
50	100	8.254E-11	9.05E-11	-8.84%

The simulations in Table 6 were conducted with an electrode separation of 2mm, resulting in 12 to 40 nodes between the electrodes. With consideration of the simulation time shown for 20 and 40 nodes per mm in Figure 28, the minimum number of nodes per mm to be used for the FDM simulation was chosen to be 20.

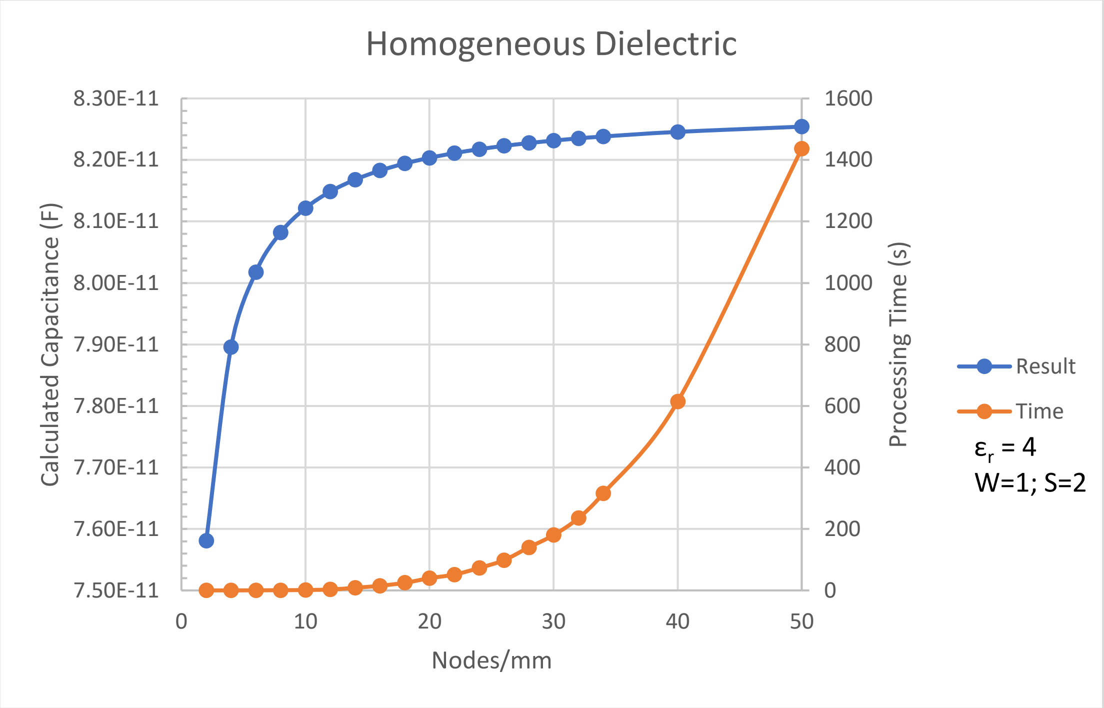

Figure 28 Calculated Capacitance and Processing Time Vs Nodes/mm

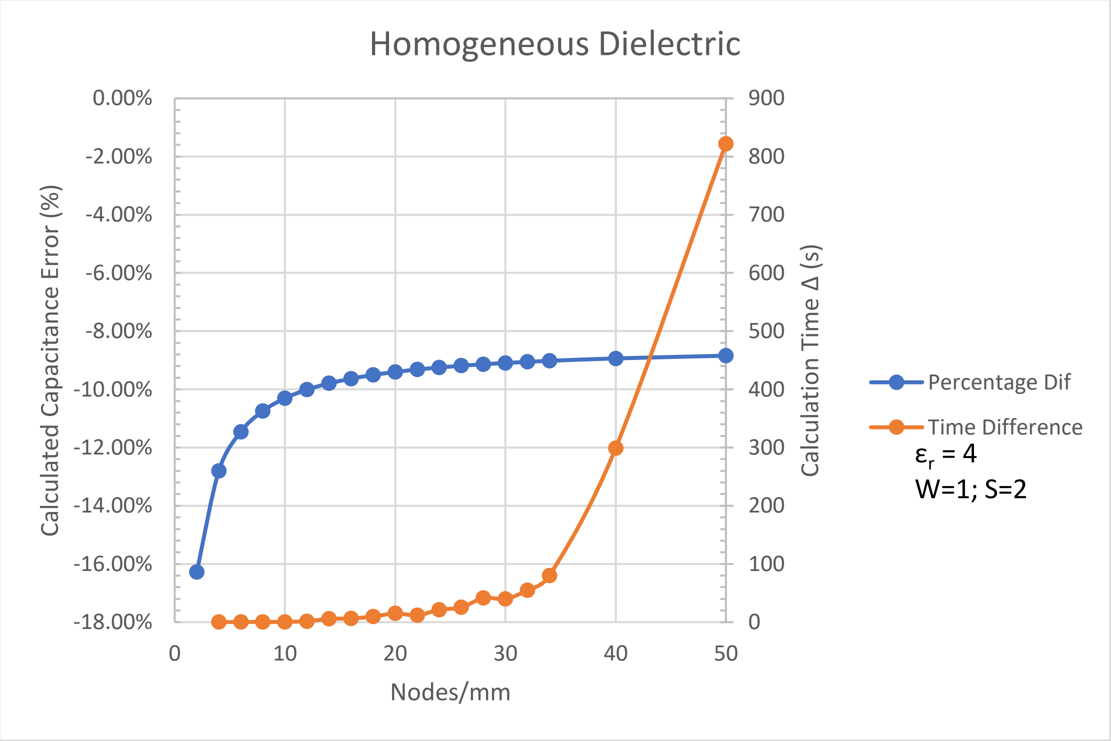

Figure 29 Calculated Error and Calculation Time Increase Vs Nodes/mm

4.5. FDM Simulation Parameters

The FDM simulation requires real-world values for the sensor materials, along with the permittivity and thickness of the contamination. The properties are discussed below.

4.5.1. Construction

The construction of a PV module was described in section 2.9 PV Module Construction, with the permittivity properties of the glass and backing material shown in Table 3 Dielectric Properties of PV Module Construction Materials.

For the FDM simulation, glass of 2.5 mm thickness with a permittivity of $\varepsilon_r = 4$ will be used.

The backing material used in the simulation is 1 mm in thickness, with a permittivity of $\varepsilon_r = 2.75$.

4.5.2. Electrode Width

The electrode width is a parameter of investigation and is shown as dimension 'w' in Figure 25. It will be tested for in increments of 0.5 mm. The lowest width to be tested is 0.5 mm through to 4.5 mm, for a total of 9 node width simulation points.

4.5.3. Electrode Spacing

The electrode spacing is a parameter of investigation and is shown in Figure 25 as dimension 's'. The spacing of the electrodes will be incremented from 1 mm to 5 mm, resulting in 9 node widths.

4.5.4. Electrode Dimension Combinations

As the electrode spacing 's' approaches zero, the FDM simulation cannot produce a result due to the physically connected electrodes. When electrode width 'w' is increased without increasing the electrode spacing 's', the simulation limits the combinations of electrode width and spacing to where electrode spacing ‘s’ is greater than 0mm. Table 7 summarises the electrode width and spacing combinations used in the simulation. The total combinations of electrode width and spacing per material is shown as 45.

Table 7 Electrode Simulation Dimensions

		Sensor Electrode Spacing (mm)									
		Electrode Centre Distance (mm)									
		0.5	**1**	**1.5**	**2**	**2.5**	**3**	**3.5**	**4**	**4.5**	**5**
Electrode Width (mm)	**0.5**		0.5	1	1.5	2	2.5	3	3.5	4	4.5
	1			0.5	1	1.5	2	2.5	3	3.5	4
	1.5				0.5	1	1.5	2	2.5	3	3.5
	2					0.5	1	1.5	2	2.5	3
	2.5						0.5	1	1.5	2	2.5
	3							0.5	1	1.5	2
	3.5								0.5	1	1.5
	4									0.5	1
	4.5										0.5

4.5.5. Nodes Per mm

As discussed in section 4.4.3, the number of nodes that are calculated in the spacing between the electrodes directly impacts the accuracy of the calculation and the time taken to complete the simulation. As the electrode spacing is simulated as per Table 7, the number of nodes per mm is selected according to Table 8, where the minimum number of nodes between sensor electrodes is 20, matching the minimum performance outlined in section 4.4.3 Node Quantity.

Table 8 Simulation Node Quantity

Spacing	Nodes/mm	Nodes Between Electrodes
4.5	20	90
4	20	80
3.5	20	70
3	20	60
2.5	20	50
2	20	40
1.5	20	30
1	32	32
0.5	60	30

4.5.6. Contamination Permittivity

Contamination permittivity is dependent on the material and how homogeneous it is. As a non-homogeneous material compacts, the density and permittivity of the material will increase due to the displaced air.

To simulate a dry and wet deposition of contamination, the permittivity listed in Table 2 will be used for a wet deposition, while equation 2-9 will be used to determine the dry permittivity with a 50% fractional density, where air is the second component.

Water, predominantly from rain or condensation, will present a significant permittivity component to the sensor element, and will be considered as a contaminant for analysis. Due to the quantity of water likely present, the typical permittivity will be used for water at room temperature. No dry deposition for water is possible.

Table 9 Simulation Permittivity Values

	Permittivity (ε_r)	
Contaminant	**Wet**	**Dry**
ASH	6000.00	1501.12
CEMENT	41791.00	10448.87
CHARCOAL	7.00	2.80
CLAY-0% Water	-	2.72
CLAY-7% Water	6.03	-
CLAY-14% Water	10.68	-
LATERITE	40.00	11.11
LOAMY - 0% Water	-	3.20
LOAMY - 5% Water	5.21	-
LOAMY - 10% Water	8.94	-
SALT	6.60	2.70
SAND - 0% Water	-	1.62
SAND - 8% Water	6.96	-
SAND - 14% Water	10.46	-
WOOD	2.00	1.40
Water	80	-

4.5.7. Contamination Thickness

The experiments conducted by Yusuf et al. (2020) utilised the weight of the samples collected, distributed over the surface of the PV module under test. The total weight or thickness of the contamination materials were not controlled.

Due to this, the contamination thickness used in the FMD simulation will be set for 0.5 mm for dry deposit contamination and 0.25 mm for wet deposit contamination. Water will be considered separately, with a thickness of 0.5 mm.

5. Simulation Results

The full simulation results including results tables and plots are available in APPENDIX G FDM SIMULATION OUTPUTS.

5.1.1. Simulation Output Numbering

The simulation outputs are in the order of pico-farads to femto-farads ($x10^{-12}$ to $x10^{-15}$) values. As a result, tolerances in floating-point calculations and total number of nodes per mm have a significant influence on the simulation output. Six significant figures are shown in the results tables.

5.1.2. Limitations & Assumptions

The time taken to perform the simulations was a significant limitation to the number of simulations and refinement that could be performed. As discussed in 4.4.3 Node Quantity, the time consumed per point was exponentially increased due to both the number of nodes and the physical simulation size.

The total number of electrode dimensions was also limited by the time taken to perform the simulations, with the 0.5 mm electrode spacing resulting in large matrices and computations as the overall sensor width increased. The number of nodes listed in 4.5.5 Nodes Per mm limited the accuracy of the results. Section 4.4.3 Node Quantity expands on the compromise reached.

Temperature and frequency effects are also not accounted for in the FDM simulation, with the assumption that the temperatures expected on the surface of PV modules do not alter the permittivity of the materials simulated, and that static analysis is suitable for the frequency used to measure the capacitance of the sensor.

5.1.3. Maximum Sensitivity Results

For each material tested, the simulation produces a calculated capacitance for each of the electrode dimensions listed in Table 7. For each dimension, the change in capacitance for each point was calculated by subtracting the calculated value from the equivalent no-contamination (clean) surface value.

The capacitance change values were normalised to the total cross section of the sensor electodes, resulting in a sensitivity value for the cross-sectional area.

The maximum sensitivity for each contaminant and the resulting electrode dimensions are summarised in Table 10 Simulation Maximum Sensitivity Results. The permittivity and contamination layer thickness used in the simulation for each of the material is also shown for comparison.

Analysis of the electrode dimensions listed in Table 10 show that dimensions for peak sensitivity occur over a range. A histogram of electrode dimensions is shown in Figure 30.

For each electrode dimension grouping, the permittivity mean was found. The average change in capacitance per metre was also calculated for comparison in Table 11.

Due to the large spread of electrode dimension combinations resulting from the peak sensitivity analysis, an additional analysis was conducted and detailed in section 5.1.4 Permittivity Normalised Sensitivity.

Table 10 Simulation Maximum Sensitivity Results

	Electrode Dimensions (mm)				
Material	**Width**	**Centre Spacing**	**Permittivity (ε_r)**	**Contaminant Thickness (mm)**	**ΔC/m**
Ash, Wet	2.5	5	6000	0.25	9.01341E-08
Ash, Dry	2.5	5	1501.124906	0.5	2.22075E-08
Cement, Wet	2.5	5	41791	0.25	6.35702E-07
Cement, Dry	2.5	5	10448.87499	0.5	1.58551E-07
Charcoal, Wet	1	2.5	7	0.25	4.46892E-12
Charcoal, Dry	2.5	4	2.8	0.5	1.10836E-12
Clay 0%	3	4	2.72	0.5	1.05958E-12
Clay 7%	1	2.5	6.03	0.25	3.09977E-12
Clay 14%	1	2.5	10.68	0.25	1.13884E-11
Laterite, Wet	1	3	40	0.25	1.39477E-10
Laterite, Dry	1	2.5	11.11	0.5	1.96663E-11
Loamy 0%	2	3.5	3.2	0.5	1.43516E-12
Loamy 5%	1	2.5	5.21	0.25	2.11122E-12
Loamy 10%	1	2.5	8.94	0.25	7.79948E-12
Salt, Dry	1	2.5	2.7	0.5	6.60575E-12
Salt, Wet	2.5	4	6.6	0.25	5.18137E-13
Sand 0%	4	5	1.62	0.5	2.0924E-13
Sand 8%	1	2.5	6.96	0.25	4.40837E-12
Sand 14%	1	2.5	10.46	0.25	1.09056E-11
Wood, Wet	0.5	1	2	0.25	1.18563E-13
Wood, Dry	4	4.5	1.4	0.5	3.09286E-13
Water	1.5	3.5	80	0.5	5.74824E-10

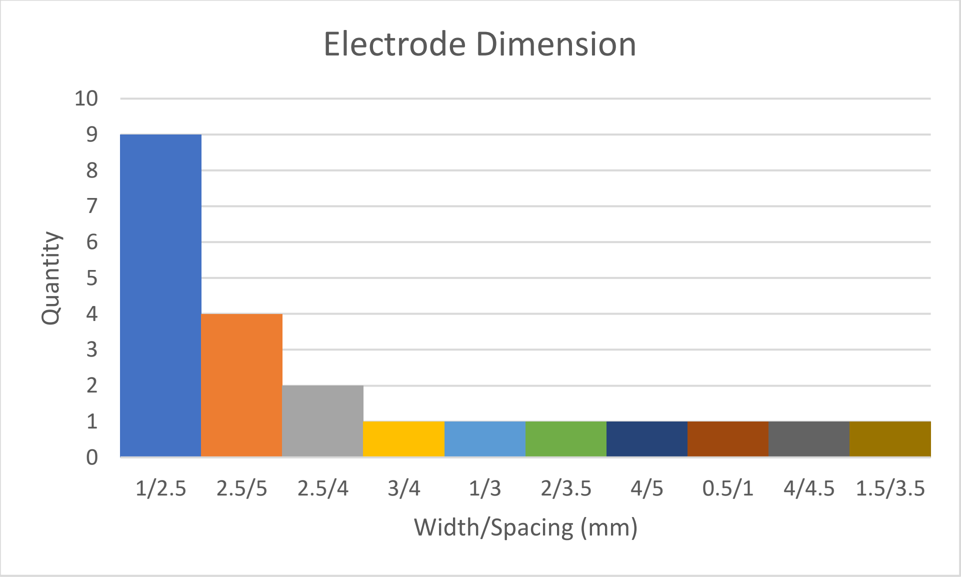

Figure 30 Electrode Dimension Histogram

Table 11 Average Electrode Dimension Results

Number of Occurence	Electrode Dimension (Width / Centre Spacing (mm))	Sensor Width (mm)	Average Permittivity	Average ΔC/m (F)
9	1/2.5	6	7.676667	7.82821E-12
4	2.5/5	12.5	14935.25	2.26649E-07
2	2.5/4	10.5	4.7	8.1325E-13
1	3/4	11	2.72	1.05958E-12
1	1/3	7	40	1.39477E-10
1	2/3.5	9	3.2	1.43516E-12
1	4/5	14	1.62	2.0924E-13
1	0.5/1	2.5	2	1.18563E-13
1	4/4.5	13	1.4	1.98819E-13
1	1.5/3.5	8.5	80	5.74824E-10

5.1.4. Permittivity Normalised Sensitivity

The results in Table 10 and Table 11 demonstrate that the capacitance calculated by the FDM simulation is primarily dependent on the permittivity of the contamination. A selection of plots is shown below demonstrating the 3D-surface plots for materials with permittivity values of or approximating those listed in Table 11.

Charcoal Wet, Laterite Wet, Water, Cement Dry and Wood Dry are shown. A line plot showing Capacitance Per Unit Length of sensor electrode dimensions, 3D-surface of the change in capacitance for each simulated dimension, as well as a 3D surface representing the sensitivity per sensor cross section width is given.

To remove permittivity as a variable from the calculations the change in capacitance for each material was normalised based on the permittivity of that material.

The normalised data points for each electrode dimension were then averaged, resulting in a mean normalised response for each electrode dimension.

The results average revealed that the optimal dimensions are 1.5 mm electrode width with 3.5 mm centre spacing, resulting in an electrode spacing of 2 mm. The 3D surface is shown in Figure 51 Permittivity Normalised Sensitivity.

The results for each contaminant for a 1.5/3.5 mm electrode are shown in Table 12 Normalised Sensor Output. The values listed in Table 12 show the expected output of the sensor and the difference from the peak sensitivity dimension for that contaminant.

Table 12 Normalised Sensor Output

	Electrode Dimensions (mm)					
Material	**Width**	**Centre Distance**	**Permittivity (ε_r)**	**ΔC/m (Original) (F)**	**Normalised ΔC/m (1.5/3.5 mm) (F)**	**ΔC/m Difference (F)**
Clean	1.5	3.5	1	5.72274E-11	5.72274E-11	0
Ash, Wet	1.5	3.5	6000	9.0134E-08	5.83902E-08	-3.17439E-08
Ash, Dry	1.5	3.5	1501.1249	2.2207E-08	1.44583E-08	-7.74916E-09
Cement, Wet	1.5	3.5	41791	6.357E-07	4.09852E-07	-2.2585E-07
Cement, Dry	1.5	3.5	10448.875	1.5855E-07	1.02273E-07	-5.62788E-08
Charcoal, Wet	1.5	3.5	7	4.4689E-12	5.69407E-12	1.22514E-12
Charcoal, Dry	1.5	3.5	2.8	1.1084E-12	8.42054E-13	-2.6631E-13
Clay 0%	1.5	3.5	2.72	1.0596E-12	7.56303E-13	-3.03276E-13
Clay 7%	1.5	3.5	6.03	3.0998E-12	4.02125E-12	9.21487E-13
Clay 14%	1.5	3.5	10.68	1.1388E-11	1.42345E-11	2.84606E-12
Laterite, Wet	1.5	3.5	40	1.3948E-10	1.60896E-10	2.14194E-11
Laterite, Dry	1.5	3.5	11.11	1.9666E-11	2.61471E-11	6.48079E-12
Loamy 0%	1.5	3.5	3.2	1.4352E-12	1.32929E-12	-1.05873E-13
Loamy 5%	1.5	3.5	5.21	2.1112E-12	2.81326E-12	7.02042E-13
Loamy 10%	1.5	3.5	8.94	7.7995E-12	9.78399E-12	1.98451E-12
Salt, Dry	1.5	3.5	2.7	6.6057E-12	8.87897E-12	2.27322E-12
Salt, Wet	1.5	3.5	6.6	5.1814E-13	3.8768E-13	-1.30457E-13
Sand 0%	1.5	3.5	1.62	2.0924E-13	7.82802E-15	-2.01412E-13
Sand 8%	1.5	3.5	6.96	4.4084E-12	5.62002E-12	1.21165E-12
Sand 14%	1.5	3.5	10.46	1.0906E-11	1.36331E-11	2.7275E-12
Wood, Wet	1.5	3.5	2	1.1856E-13	2.00748E-13	8.21853E-14
Wood, Dry	1.5	3.5	1.4	3.0929E-13	7.94222E-14	-2.29864E-13
Water	1.5	3.5	80	5.7482E-10	5.74824E-10	0
			Average:	4.1253E-08	2.66274E-08	-1.46259E-08

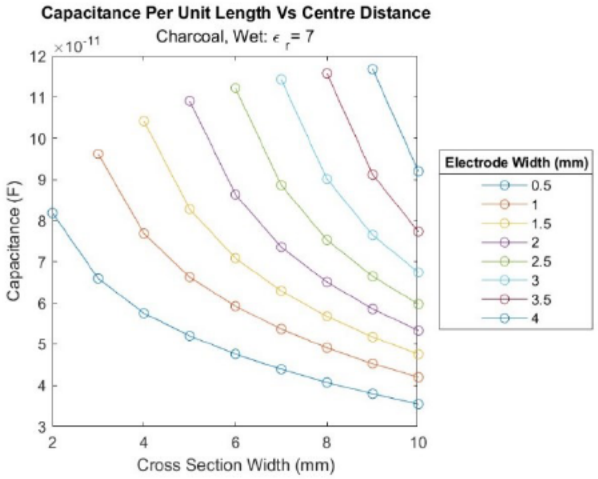

Figure 31 Unit Length Capacitance- Charcoal, Wet

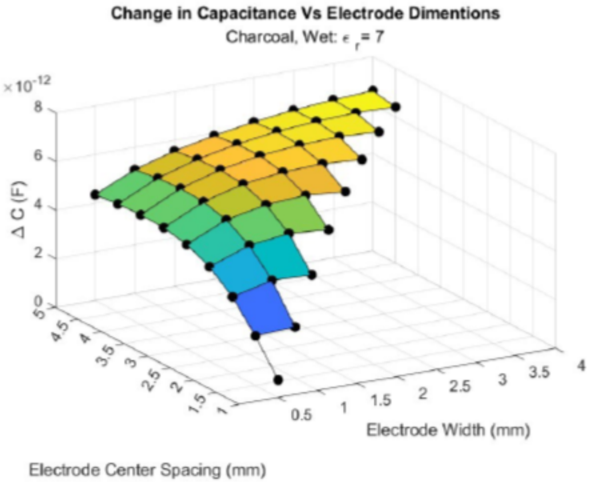

Figure 32 Change in Capacitance - Charcoal, Wet

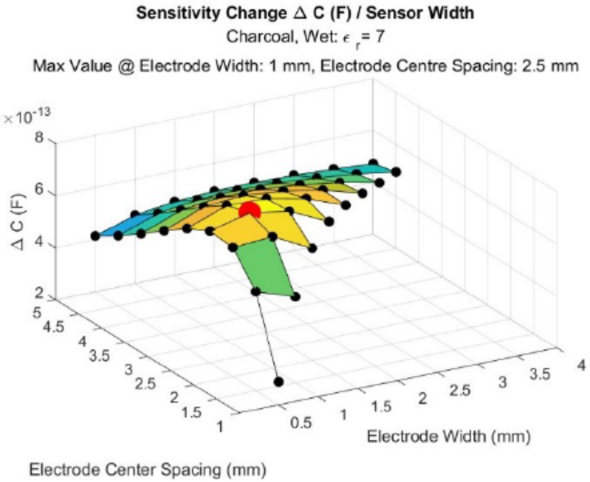

Figure 33 Sensitivity – Charcoal, Wet

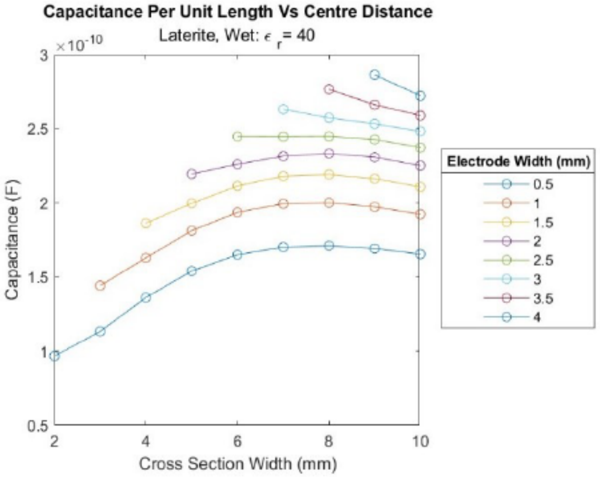

Figure 34 Unit Length Capacitance-Laterite, Wet

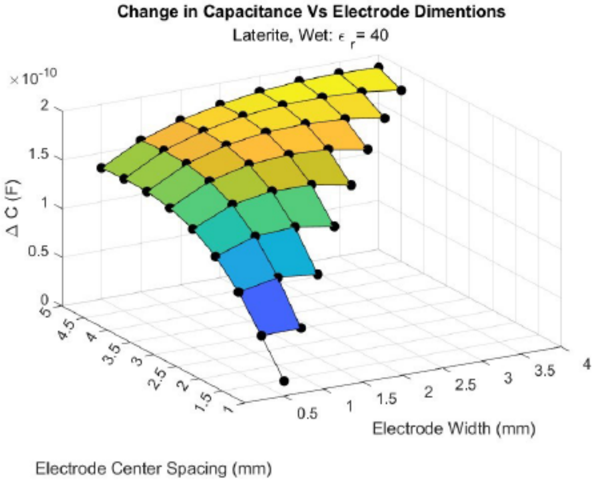

Figure 35 Change in Capacitance – Laterite, Wet

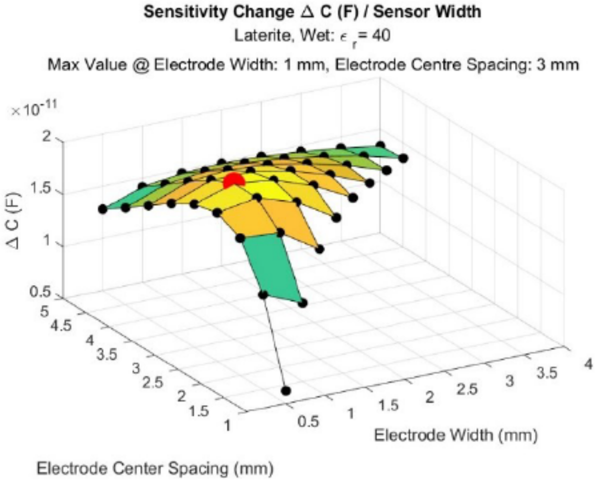

Figure 36 Sensitivity – Laterite, Wet

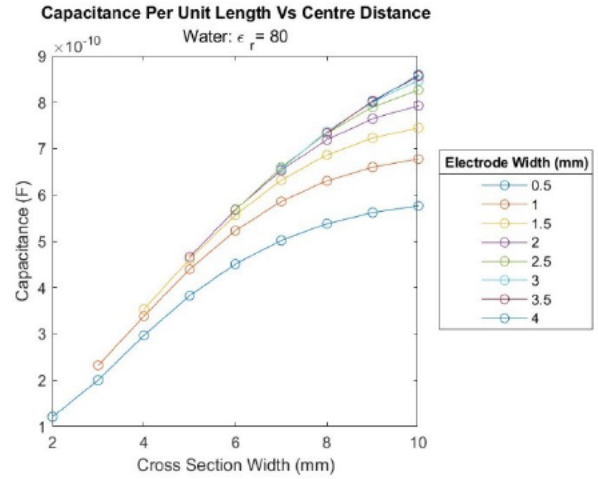

Figure 37 Unit Length Capacitance-Water

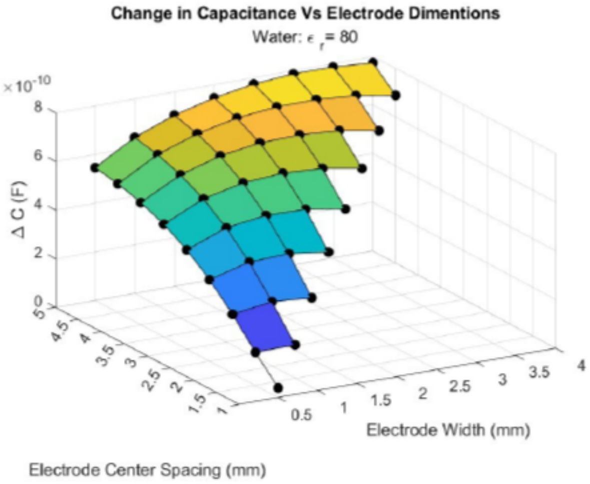

Figure 38 Change in Capacitance - Water

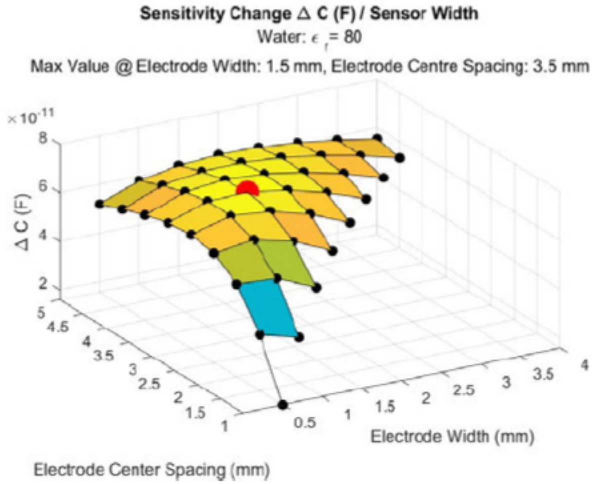

Figure 39 Sensitivity – Water

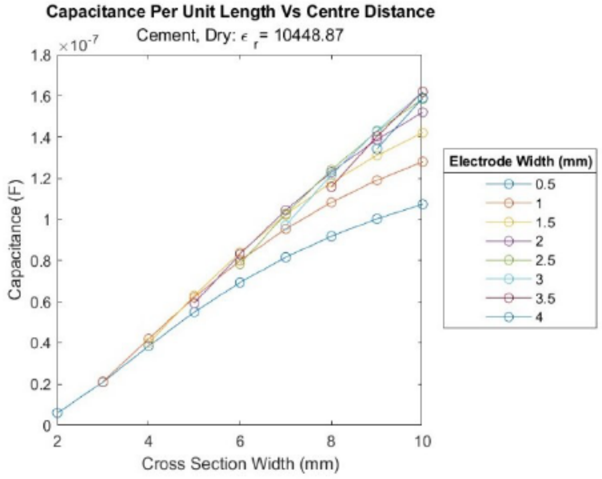

Figure 40 Unit Length Capacitance-Cement, Dry

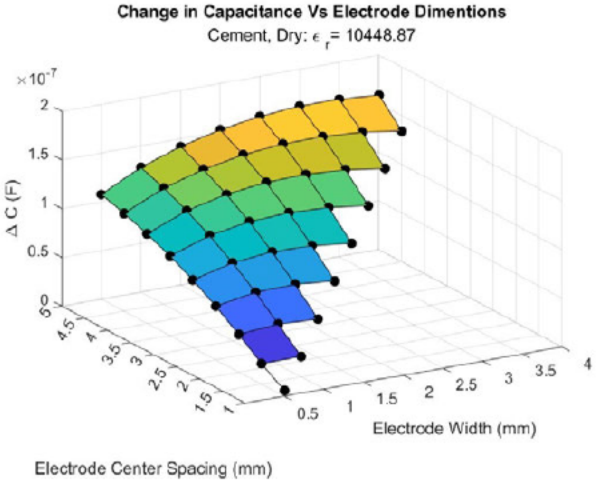

Figure 41 Change in Capacitance – Cement, Dry

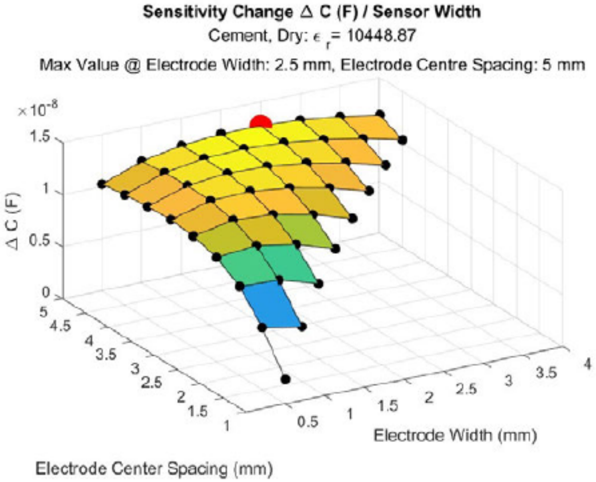

Figure 42 Sensitivity – Cement, Dry

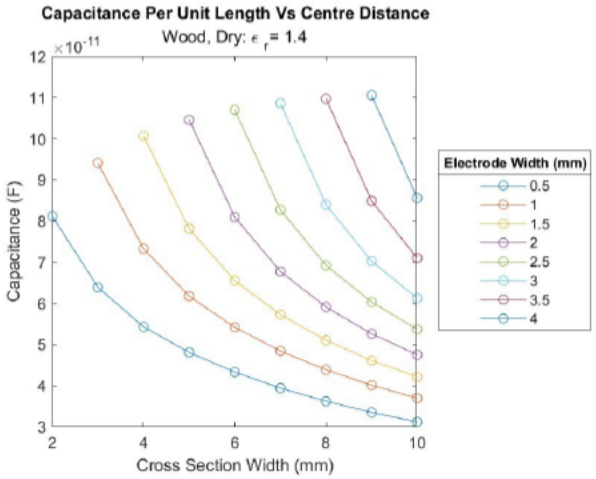

Figure 43 Unit Length Capacitance-Wood, Dry

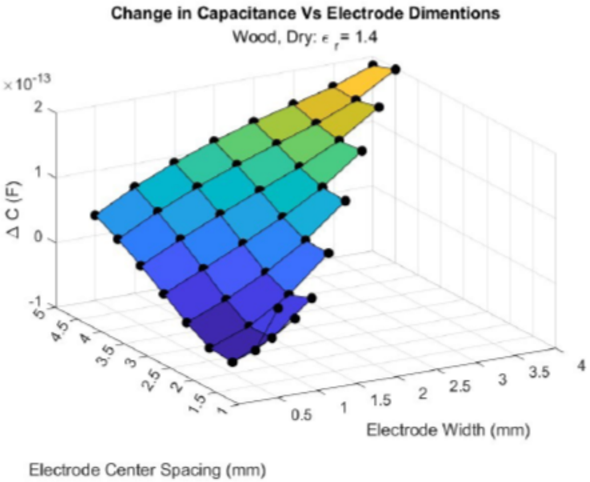

Figure 44 Change in Capacitance – Wood, Dry

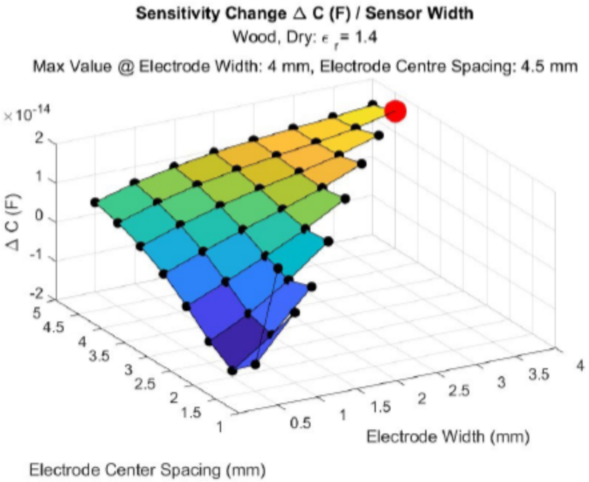

Figure 45 Sensitivity – Wood, Dry

5.2. Clean/Baseline Capacitance

For the peak sensitivity dimension shown above, 1.5/3.5 mm, the minimum capacitance per unit length for the sensor element was found by the simulation to be:

57.2274 pF/m

5.3. Equipotential and Electric Field

The simulation can produce equipotential and electric field plots for each simulation point, if enabled.

For the materials Charcoal Wet, Laterite Wet, Water, Cement Dry and Wood Dry, equipotential and electric field plots are shown below. The plots demonstrate the effect that the contamination layer has on both and demonstrate the simulation accommodating the material changes.

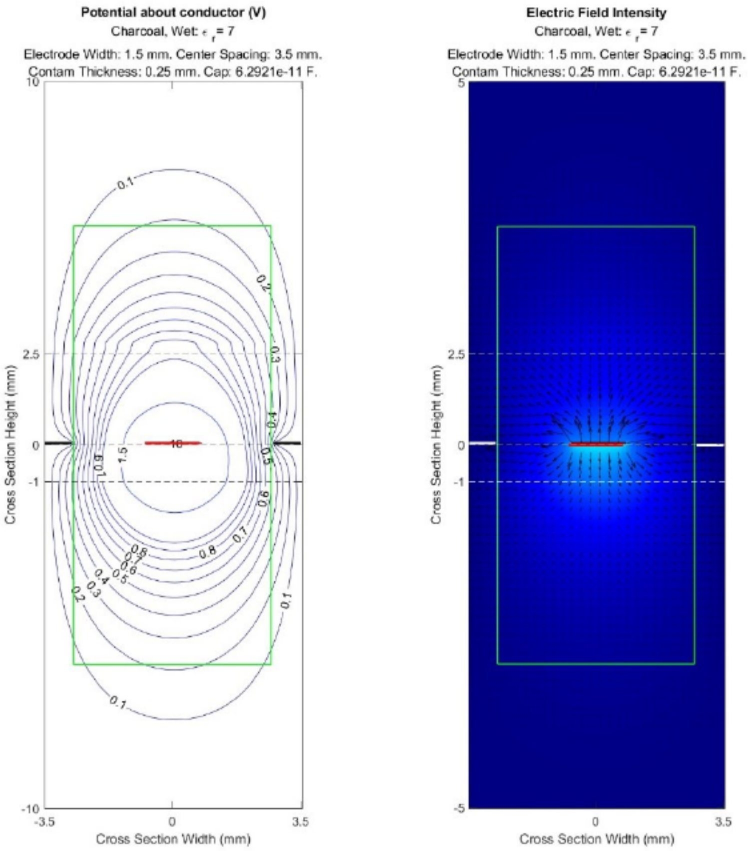

Figure 46 Potential and Field – Charcoal, Wet

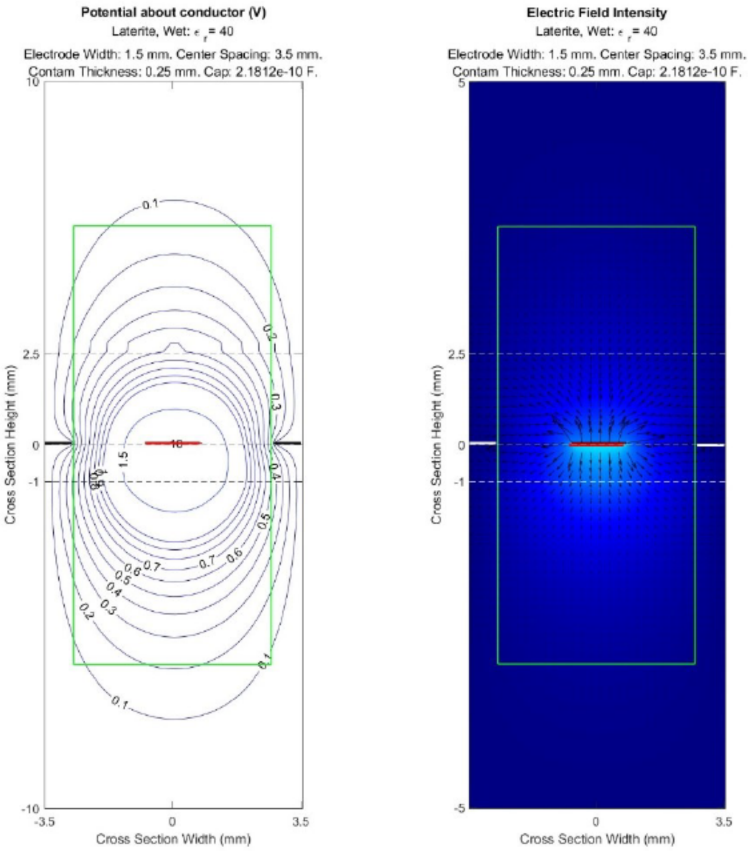

Figure 47 Potential and Field – Laterite, Wet

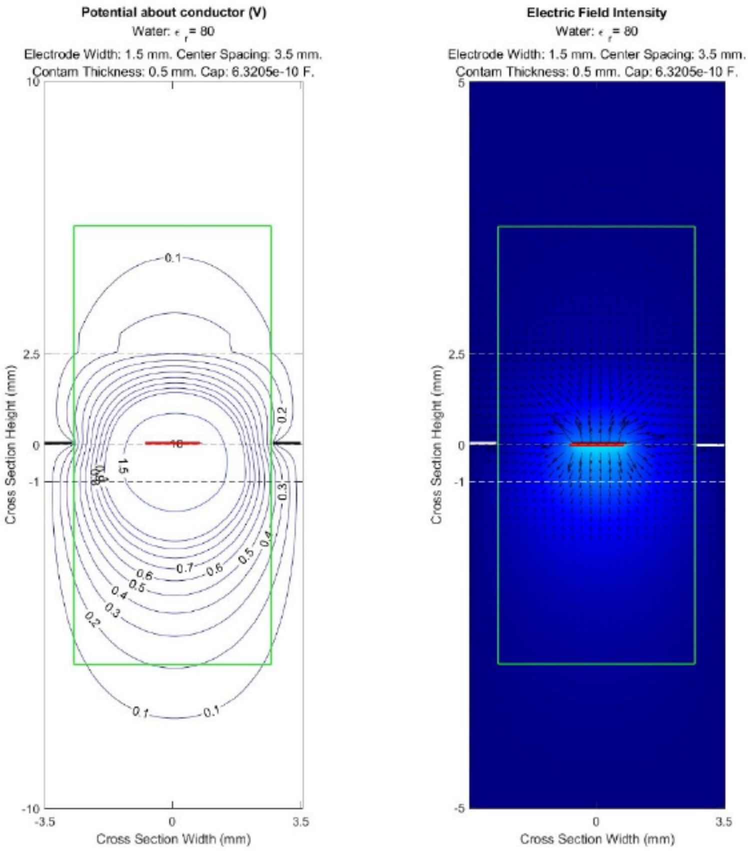

Figure 48 Potential and Field – Water

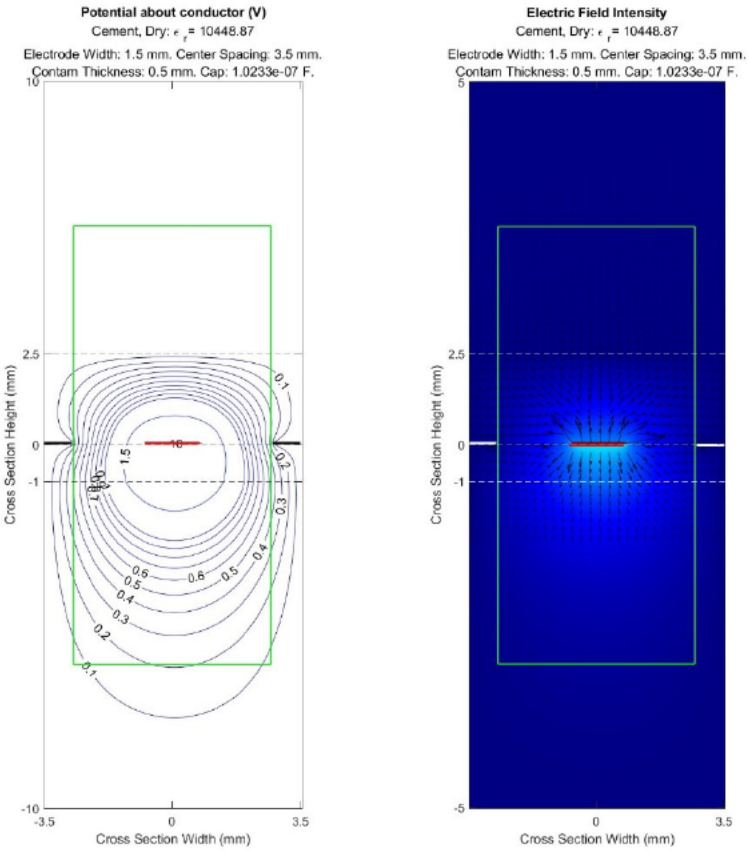

Figure 49 Potential and Field – Cement, Dry

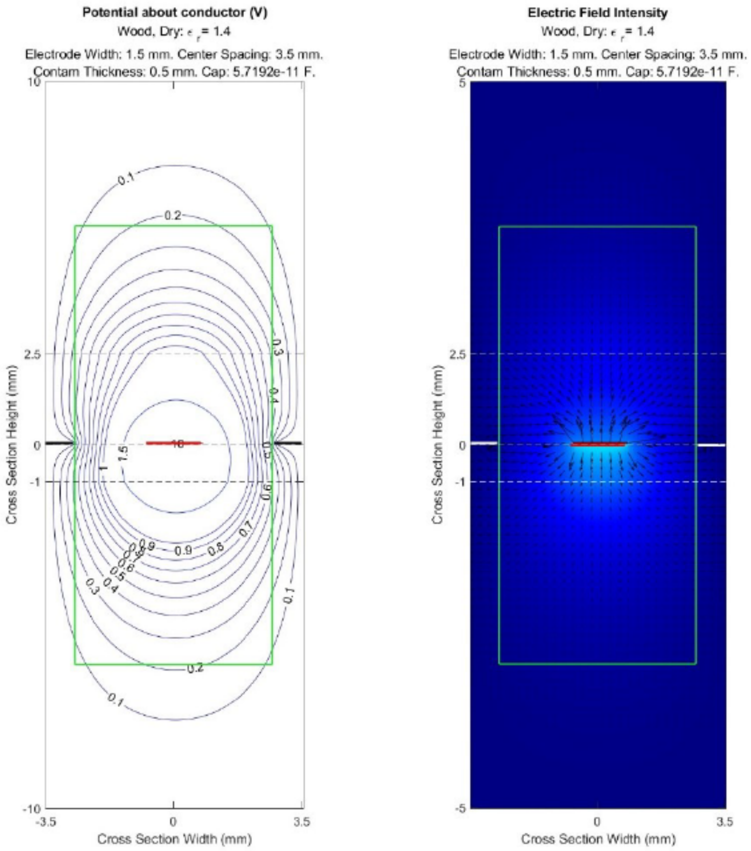

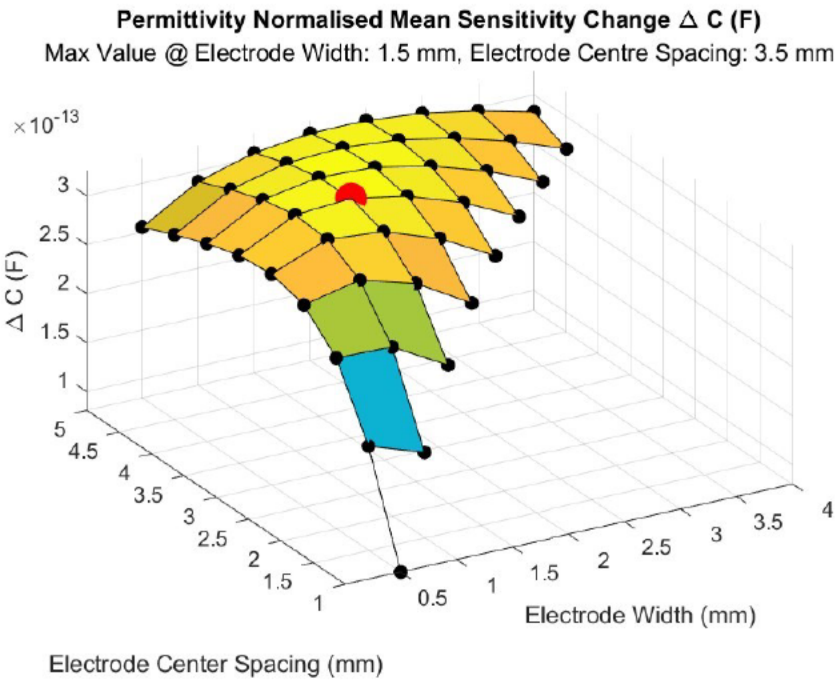

Figure 51 Permittivity Normalised Sensitivity

Figure 50 Potential and Field – Wood, Dry

6. PV Sensor Design

The FDM simulation found optimal dimensions for a glass surface contamination sensor that utilises capacitance as the output variable. This section uses the capacitance change properties of the sensor and integrates this into a design suitable for implementation into a PV module or other glass surface.

6.1. Physical Design

As the physical design of a glass surface contamination sensor may directly impact on the active PV cell area of the PV module. Any area consumed by the sensor element may reduce the area available for collecting solar energy. Due to this, the physical design of the sensor element must be limited to a suitable size.

The area available to fitting a surface contamination sensor into a PV module will depend on the manufacturer and the design of the PV module itself.

For the purposes of this design, a typical size of the sensor element was chosen so that the sensor may be integrated along the outer border of a typical PV module. This positioning has an advantage of being able to detect contamination along a bottom edge of a PV module, where contamination typically builds. A module may also have multiple sensors integrated into the construction, as shown in Figure 52 PV Module Sensor Location.

Typical PV modules are, at the time of writing, approximately 1m in width, with variations based on intended application (Solar Choice 2022). Utilising the full width of the PV module will allow for maximum contamination detection sensitivity, due to the increased detection length.

With the sensor cross section dimensions found to be 1.5 mm wide, with 3.5 mm centre separation, multiple sensor cross-sections may be used, producing interconnected fingers as shown in Figure 53 Sensor Top View. This increases the linear length of the sensor. Due to the low value of capacitance being measured, the outermost edge of the sensor is to be connected to the 0 V circuit reference, which has the added benefit of acting as a partial guard to reduce unwanted charge from impacting the sensor output.

The total height of the sensor may be described by the number of parallel sensor elements, being:

$$Height = 2S + W \tag{6-1}$$

For the design, a total of two sensor elements configured as per Figure 53 Sensor Top View is proposed.

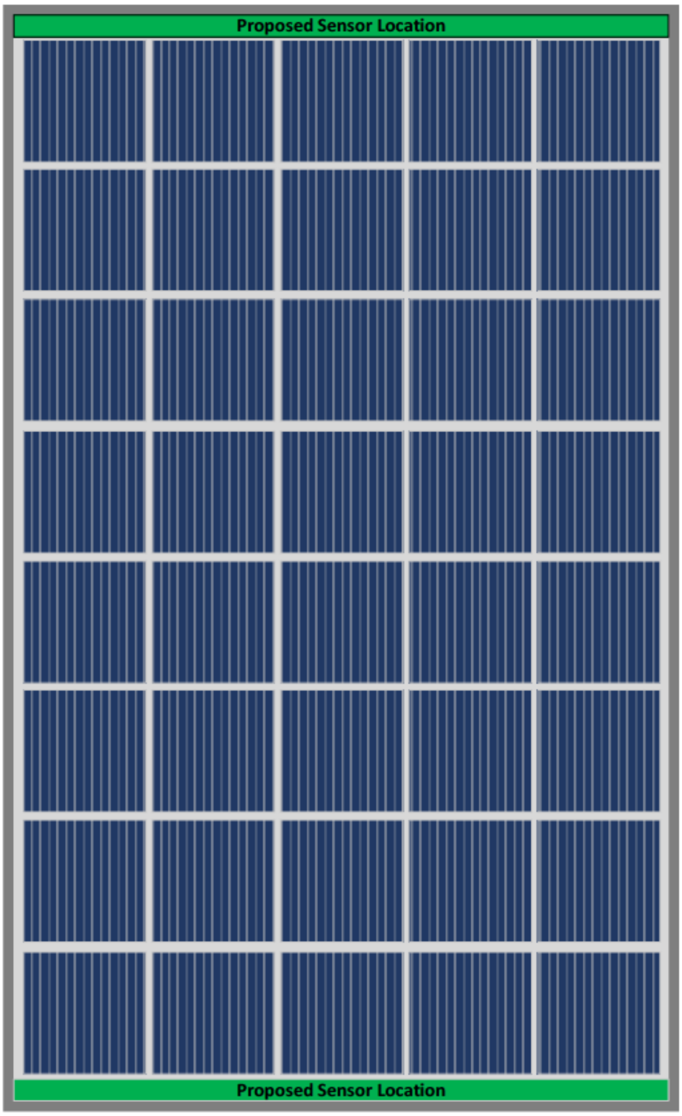

Figure 52 PV Module Sensor Location

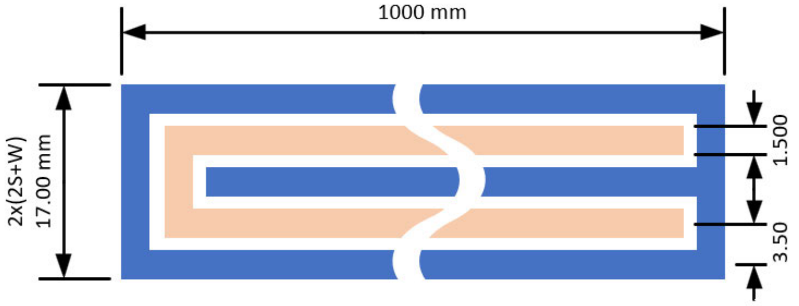

Figure 53 Sensor Top View

6.2. Sensor Output

The change in capacitance due to surface contamination for the 1.5/3.5mm sensor is shown in Table 12 Normalised Sensor Output, and is dependent on the permittivity of the contamination. For the contaminants simulated, the capacitance value of the sensor was shown to fall within a range defined by the lowest and highest permittivity materials. Table 13 demonstrates the minimum and maximum simulated capacitance for 1 m of sensor length.

Table 13 Sensor Output Range

Material	**Permittivity**	**Minimum (C/m^{-1})**	**Change (m^{-1})**
Clean	1	57.2274 pF	(Benchmark)
Cement, Wet	41791	4.09909 nF	409.852 nF
Wood, Dry	1.4	57.3068 pF	79.4222 fF
Water	80	574.824 pF	517.597 pF

For the sensor element shown in Figure 53 Sensor Top View, the sensor is to approximately 2 m in total length, giving the final design parameters of:

Table 14 Final Design Parameters

Range	**Capacitance**
Clean	114.4548 pF
Wood, Dry	114.6136 pF
Cement, Wet	8.19818 nF
Water	1.14965 nF

6.3. Temperature

The simulation results and permittivity values of the simulated contaminants shows that the influence of water impacts the detection of many surface contaminants.

As such, the design of the surface contamination sensor shall also include a temperature sensor, so that the temperature of the glass surface may be monitored. The temperature information may then be used to determine the possible water content of any contamination on the glass surface.

A RTD may be implemented to measure temperature so that the time, duration, and profile of glass temperatures is utilised and the possibility of water on the surface of the glass is approximated and accounted for.

The use of temperature data will be incorporated into the sensor control system so that appropriate timing and scaling of measurements of the contamination are made.

7. Prototype Sensor System

Due to the time and financial restrictions, full-scale integration of the glass surface contamination sensor into a PV module or other glass-surface was not viable during this dissertation period.

A prototype or demonstration sensor and interface was conceived with comparable functionality so that both the theory and simulation of the detection method could be demonstrated, tested, and verified. The sensor element was connected to a LCR meter and Vector Network Analyser for direct capacitance measurement and an interface circuit, establishing a surface contamination sensor system. The testing of each component will establish the specifications and performance of the surface contamination sensor system.

7.1. Prototype Sensor Element

To demonstrate the sensing technique and the ability of the sensor to detect material presence, a prototype sensor element was designed and constructed.

Similarities in materials and construction were identified in the normal fabrication processes used for printed circuit boards (PCBs). Typical PCB construction features thin layers of copper bonded to in inner layer of dielectric material. The outer copper layers are etched to suit the required interconnections or ‘tracks’ between components. Modern manufacturing covers the completed circuit board with an insulating layer known as solder mask, which acts to protect the copper layer from corrosion and aids in PCB soldering.

Complex shapes and fine mechanical tolerances are possible in PCB manufacturing by using Computer Aided Design (CAD) software such as Altium Designer, which was utilised in the PCB design process. The design software produces Computer Aided Manufacturing (CAM) files which were supplied to the manufacturer, “ALL PCB”, located in mainland China.

A PCB based sensor element was determined to be possible due to the properties of the PCB material and construction method, where the sensor electrodes are represented by PCB ‘tracks’ and the glass mounting material substituted by the inner dielectric material.

The glass surface to be contaminated may be fabricated free of copper, while opposite face may represent underside of the sensor, constructed with appropriate copper tracks, representing the sensor electrodes.

Due to the material and thickness change from a glass-based sensor element, FDM simulation of the PCB sensor element performance was conducted.

7.1.1. PCB Material

The laminate material of the PCB was chosen as Kingboard KB-6165F. The 1.6 mm FR4 material is stated as having a typical permittivity of 4.8 at 1 MHz and 4.7 at 1 GHz. The values listed reflect closely to the design simulation for glass, which has a permittivity of 4. The construction of FR4 is of woven fibreglass and epoxy resin, representing a close approximation to the glass-only material of which the sensor element is originally designed.

7.1.2. Prototype Sensor Simulation

The change in electrical and physical properties due to the change in material from electrode-on-glass to PCB fabrication for the prototype sensor element, the MATLAB FDM simulation for the sensor element cross section was completed. To maintain continuity from the electrode-on-glass design, the simulation was completed using the same 1.5/3.5 mm sensor dimensions as determined in section 5 Simulation Results.

Properties of the simulation were updated, with the glass surface substituted with the dielectric properties of the chosen PCB material along with the thickness.

The backing sheet included in the PV cross section sensor element was removed from the PCB simulation as it was not included in the construction of the PCB sensor element.

A summary of the property changes are shown in Table 15 PCB Sensor Element Simulation Changes.

Table 15 PCB Sensor Element Simulation Changes

	Electrode-On-Glass	**PCB**
Material Thickness	4.0 mm	1.6 mm
Permittivity	4.0	4.8
Backing Sheet Thickness	1	0
Backing Sheet Permittivity	2.75	1 (air)

7.1.3. Prototype Sensor Simulation Results

Due to the limited testing time available, restricted contaminant material testing was able to be conducted. Two data points were chosen to be simulated: Clean and Water. The simulation results are shown in Table 16 PCB Sensor Simulation Results.

Table 16 PCB Sensor Simulation Results

			PCB Sensor		**Glass Sensor**	
Material	**Permittivity (ε_r)**	**Contaminant Thickness**	**C/m**	**ΔC/m**	**Glass Sensor**	**ΔC/m**
Clean	1	0.25 mm	5.8926E-10		57.22736E-12	
Water	80	0.5 mm	1.0595E-9	4.7024E-10	574.824E-12	517.596E-12

The equipotential diagrams for the PCB sensor element simulations are shown in Figure 54 and Figure 55.

Comparison of the results to the Electrode-On-Glass sensor reveal a clean (no contamination) capacitance difference of 532 pF per meter increase for PCB construction. The simulation of a water contamination also indicates an increase in the capacitance of 541 pF per metre over the glass-based sensor. The result is a sensor element that shows a larger increase in capacitance per metre for the same contamination.

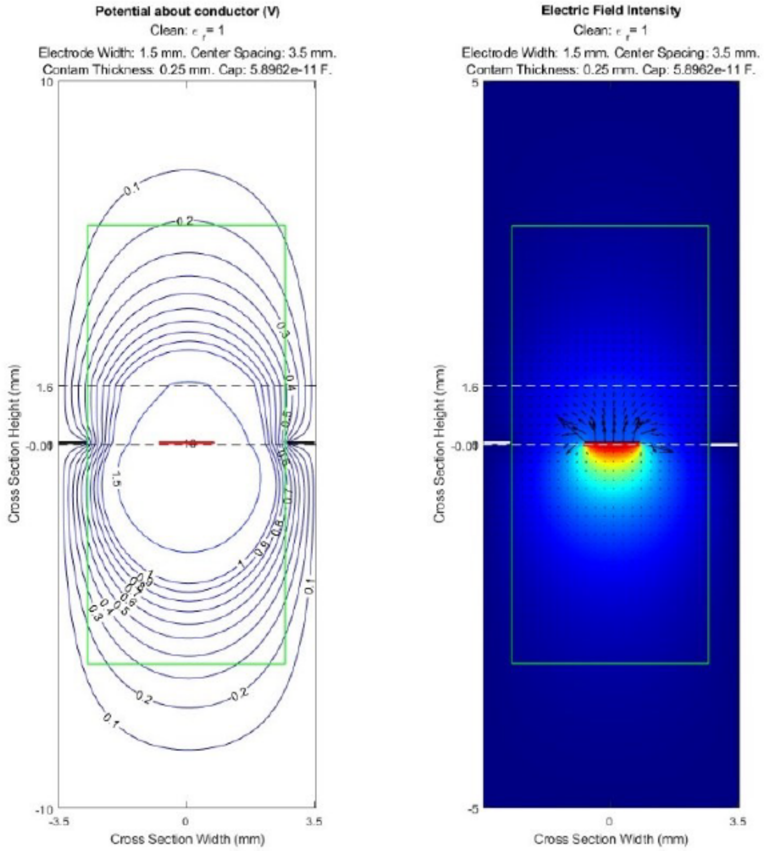

Figure 54 Potential and Field PCB Sensor Element - Clean

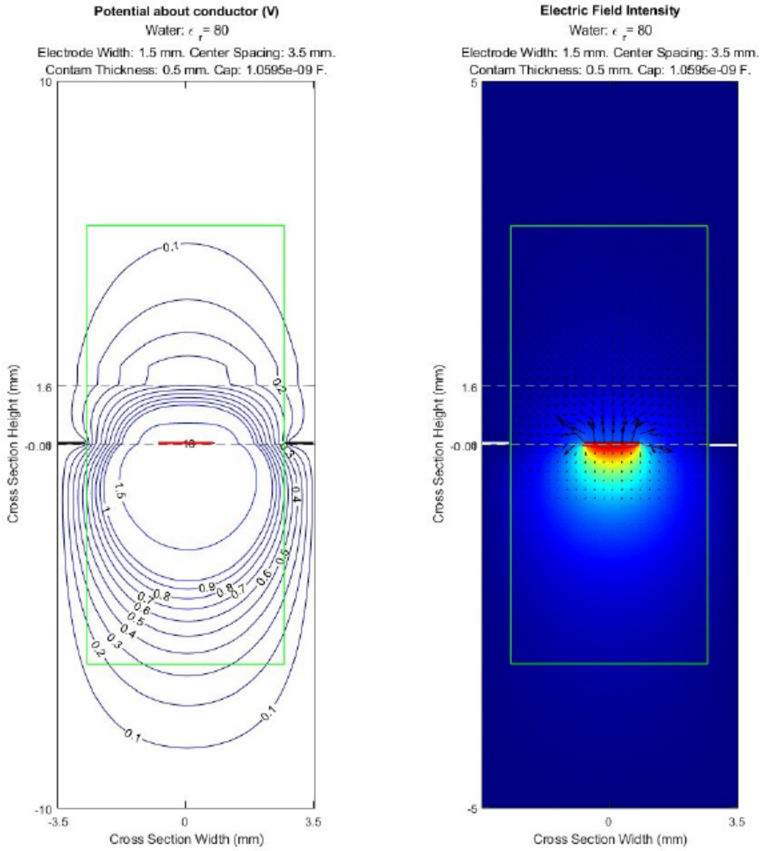

Figure 55 Potential and Field PCB Sensor Element - Water

7.1.4. Sensor Physical Design

The PCB sensor element simulation shows a higher level of sensitivity over the electrode-on-glass design. This is shown by the gradient of the equivalent contaminants in Figure 56, where the expected sensor capacitance increases as sensor length is increased.

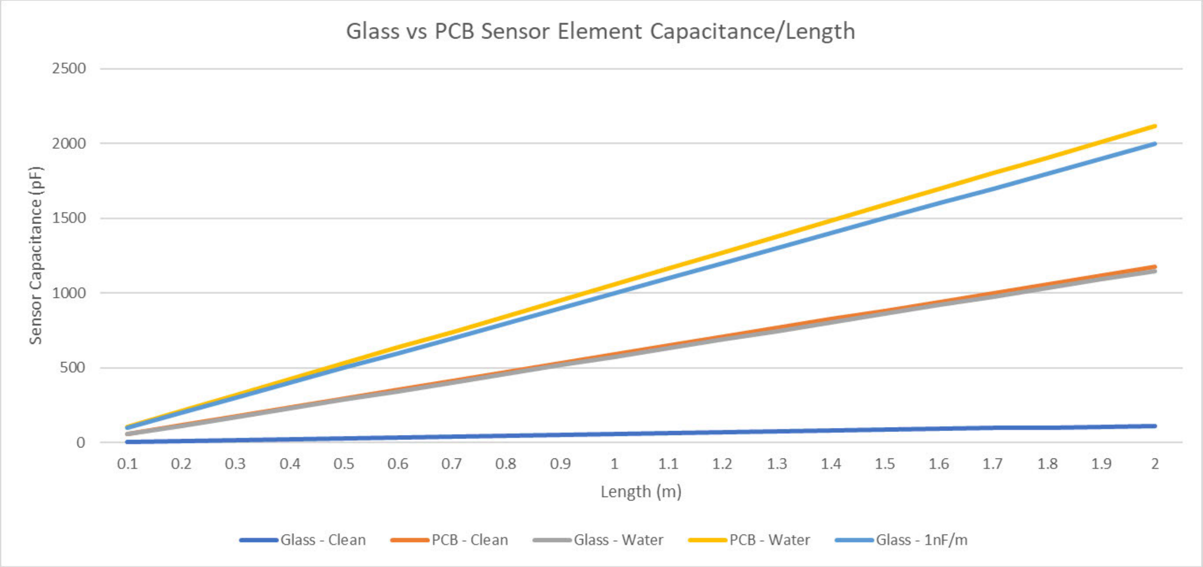

Figure 56 PCB Sensor Sensitivity Vs Glass

As the value of the electrode-on-glass water contaminated sensor and ‘Clean’ PCB sensor elements are closely overlaid the PCB sensor element was constructed with the total electrode length determined in 6.1 Physical Design.

The proposed length specified in section 6.1 Physical Design is for the equivalent of 2 linear metres of electrode-on-glass sensor cross-section. Viable PCB fabrication does not allow for dimensions approaching those of the electrode-on-glass sensor. The PCB sensor linear length was increased by increasing the number of interlaced fingers, allowing for a sensor shape approximating square. The length of the PCB sensor cross section is approximated to the number of sensor cross sections by the length of the fingers:

$$Length \approx 17 \cdot 120 \approx 2040\ mm \tag{7-1}$$

The PCB sensor copper configuration is shown in Figure 57 PCB Sensor Copper Layer, where the outer dimensions of the PCB along with mounting holes are also visible.

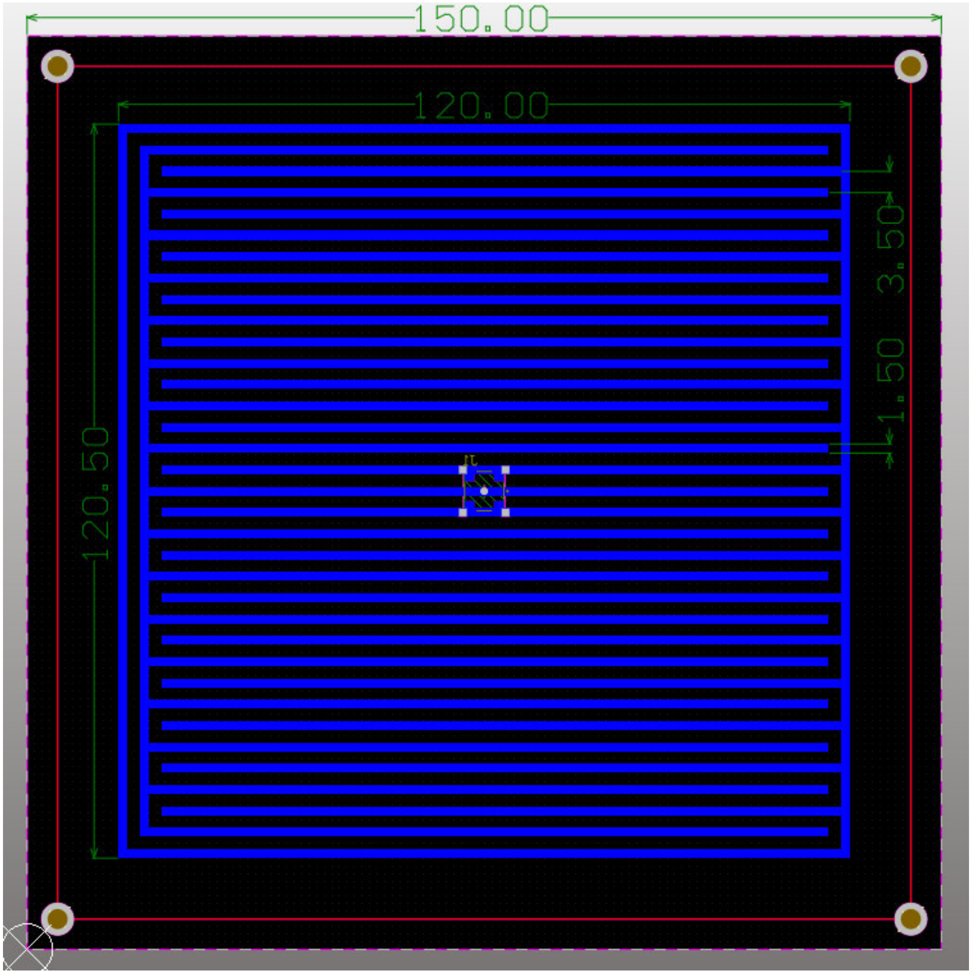

Figure 57 PCB Sensor Copper Layer

7.1.5. PCB Sensor Model

The PCB sensor model was completed in Altium designer, with the sensor copper configuration designed as a footprint representing a capacitor. For connection to the electrodes, a surface mounted SMA RF connector was determined to have physical mounting dimensions compatible with the electrode spacing of the sensor element.

The SMA connector was positioned in the centre of the PCB, with the electrodes of the sensor element aligning with the connector mounting. All copper components of the sensor element were located on the 'bottom layer' of the PCB, in the required cross section.

Mounting holes were included in the PCB sensor configuration for use in physical testing.

The 3D model of the PCB sensor element as generated by Altium Designer are shown in Figure 58 and Figure 59.

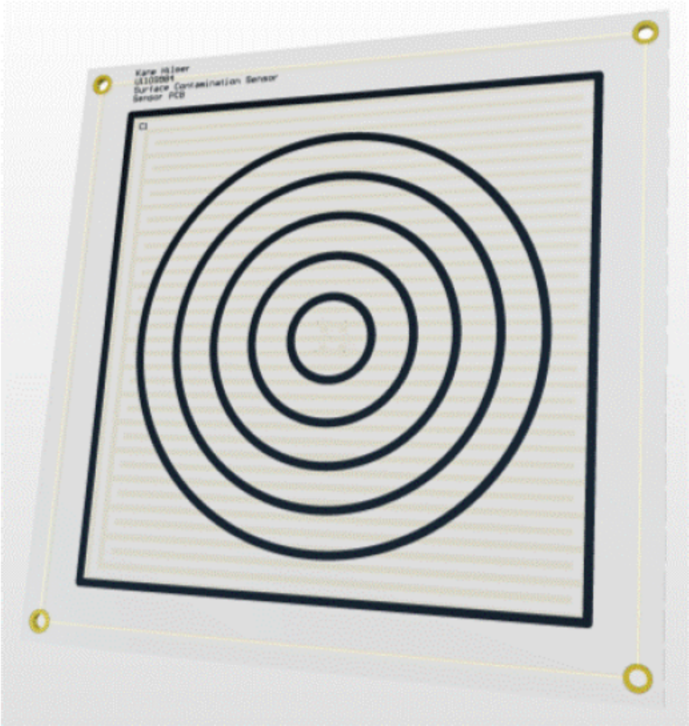

Figure 58 PCB Sensor 3D Top View

Figure 59 PCB Sensor 3D Bottom View

7.1.6. *PCB Sensor Expected Capacitance Values*

The as-built PCB sensor element includes approximately 2.04 m of sensor cross section in length. This is achieved through the multiple interlaced fingers each with the sensor cross section profile. The resulting capacitance is calculated to be:

Table 17 PCB Sensor Calculated Capacitance Values

			PCB Sensor	
Material	**Permittivity (ε_r)**	**Contaminant Thickness**	**C/m**	**Sensor Capacitance**
Clean	1	0.25 mm ($\varepsilon_r = 1$)	5.8926E-10	1.20209 nF
Water	80	0.5 mm	1.0595E-9	2.16138 nF

7.2. PCB Sensor Post-Manufacture Review

After manufacture, described in section 8 Sensor PCB Manufacture, initial electronic measurements of the PCB Sensor Element capacitance showed an unexplained difference in measured capacitance to that indicated by the simulation.

7.2.1. PCB Physical Dimensions Review

Physical measurements were completed on the received Prototype Sensor PCB, resulting in updated PCB Sensor simulation parameters. The measurements were conducted using calibrated micrometres, as shown in Figure 60. Measurements are summarised in Table 18 Micrometre Measurements of Prototype Sensor Element PCB.

Figure 60 Imperial Micrometre Measurement of PCB

Table 18 Micrometre Measurements of Prototype Sensor Element PCB

Component	Imperial	Metric
PCB + 2x Solder Mask	0.0605”	1.5367 mm
PCB + 2x Copper +2x Solder mask	0.063”	1.6002 mm
PCB only	0.059”	1.4986 mm
Copper Thickness	0.00125”	0.03175 mm
Solder Mask	0.00075”	0.01905 mm

7.2.2. PCB Solder Mask Properties

PCB solder mask properties were included in the review of the PCB Sensor Element performance. Solder mask, which was applied to the top and bottom layers of the FR4 material, is the default option for PCB fabrication and was included in the PCB Sensor Element.

He and Tang (2019) demonstrate the permittivity of solder mask and PCB properties producing large differences in the performance of high frequency signalling.

For the review of the PCB Sensor simulation, the solder mask layers will be included in the permittivity mesh, with a nominal permittivity of 3.7. The effect of the solder mask on the simulation is evident in the electric field plots shown in Figure 62 and Figure 63.

7.2.3. PCB Sensor Simulation Review

As the sensor element physical dimensions were measured, the MATLAB simulation model was reviewed and updated. The simulation parameters were updated as per Table 19. In order to accommodate the increased precision due to measurement of the PCB material, the number of nodes used in the simulation was increased to 50 nodes/mm.

Table 19 PCB Simulation Review Parameters

	Electrode-On-Glass	**PCB**	**PCB Review**
Material Thickness	4.0 mm	1.6mm	1.5mm
Permittivity	4.0	4.8	4.8
Backing Sheet Thickness	1 mm	0	0.019 mm
Backing Sheet Permittivity	2.75	1 (air)	3.8

The difference in simulated cross section is shown in Figure 61. Primary differences exist with the inclusion of the top and bottom solder mask layers.

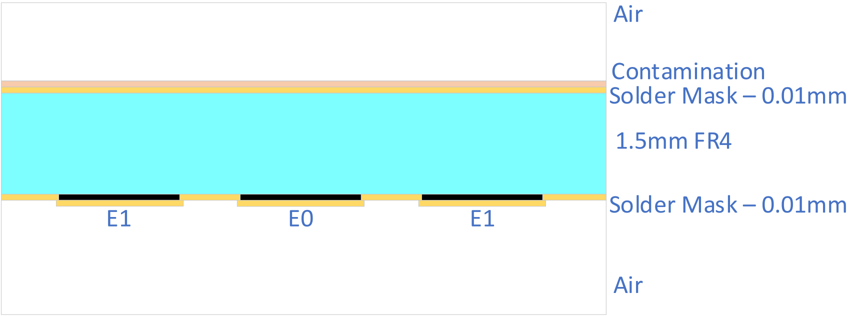

Figure 61 Reviewed PCB Simulation Cross Section

The simulation results for the PCB sensor review are shown in Table 20.

Table 20 PCB Simulation Review Results

			PCB Sensor			**PCB Sensor Review**	
Material	**Permittivity (ε_r)**	**Contaminant Thickness**	**C/m**	**ΔC/m**	**Contaminant Thickness**	**C/m**	**ΔC/m**
Clean	1	0.25 mm (ε_r=1)	5.893E-10		0.5 mm ($\varepsilon_r = 1$)	4.1676E-11	
Water	80	0.5 mm	1.0595E-9	4.702E-10	0.2 mm	5.8373E-10	5.421E-10

7.2.4. PCB Sensor Expected Capacitance Values Review

The as-built PCB sensor element contains approximately 2.04 m of sensor cross section. After the PCB review, the resulting capacitance is calculated to be:

Table 21 PCB Sensor Calculated Capacitance Values

			PCB Sensor Review	
Material	**Permittivity (ε_r)**	**Contaminant Thickness**	**C/m**	**Sensor Capacitance**
Clean	1	0.25 mm ($\varepsilon_r = 1$)	4.1676E-11	85.02 pF
Water	80	0.2 mm	5.8373E-10	1.19 nF

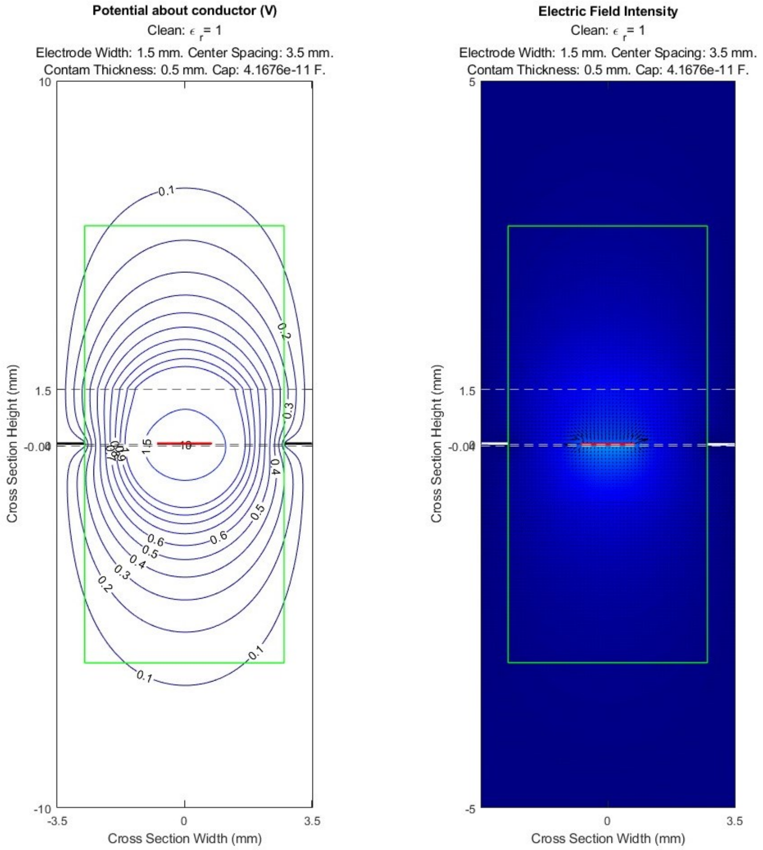

Potential about conductor (V)
Clean: $\epsilon_r = 1$
Electrode Width: 1.5 mm. Center Spacing: 3.5 mm.
Contam Thickness: 0.5 mm. Cap: 4.1676e-11 F.

Electric Field Intensity
Clean: $\epsilon_r = 1$
Electrode Width: 1.5 mm. Center Spacing: 3.5 mm.
Contam Thickness: 0.5 mm. Cap: 4.1676e-11 F.

Figure 62 Reviewed Potential and Field PCB Sensor Element - Clean

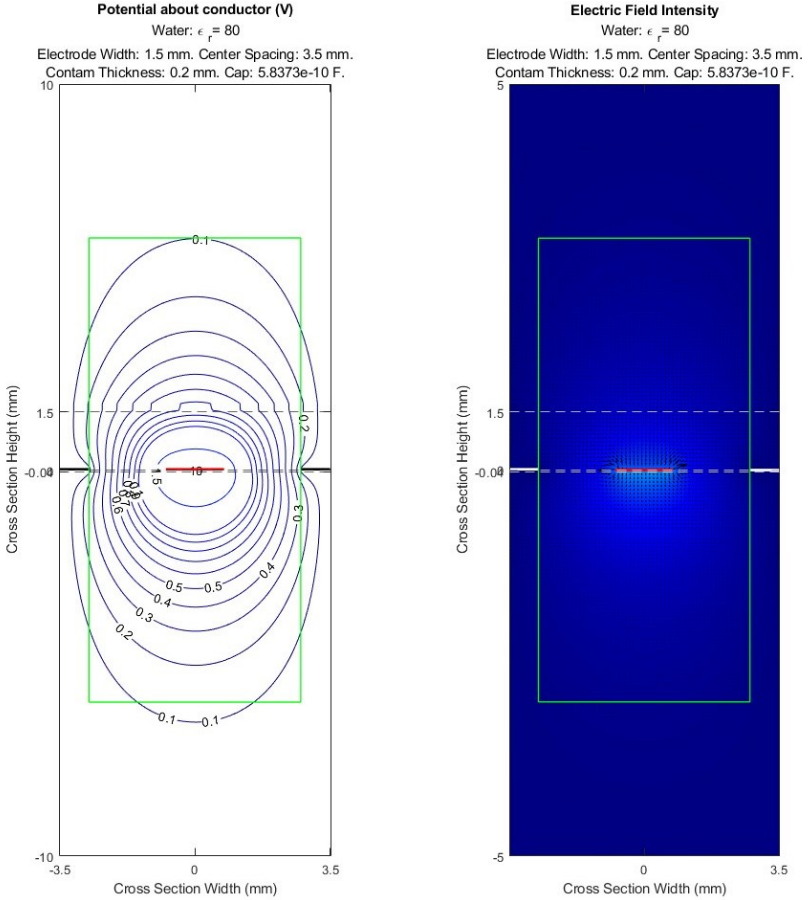

Potential about conductor (V)
Water: $\epsilon_r = 80$
Electrode Width: 1.5 mm. Center Spacing: 3.5 mm.
Contam Thickness: 0.2 mm. Cap: 5.8373e-10 F.

Electric Field Intensity
Water: $\epsilon_r = 80$
Electrode Width: 1.5 mm. Center Spacing: 3.5 mm.
Contam Thickness: 0.2 mm. Cap: 5.8373e-10 F.

Figure 63 Reviewed Potential and Field PCB Sensor Element - Water

7.3. Prototype Interface Circuit

The sensor interface circuit was designed to be capable of accepting the prototype PCB sensor described in section 7.1 Prototype Sensor Element as an input, while logic-level circuits or electronic test equipment, such as frequency counters and oscilloscopes, connected to the output. The Interface Circuit is also capable of interfacing with external fixed capacitors through adapters, to test a range of simulated sensor capacitance values.

A parallel resonance LC oscillator adapted from a publicly available design originally published by Neil Heckt for integration into an LC-meter was used with numerous modifications (Heckt 2014). The circuit modifications were performed to optimise the output for the expected sensor capacitance range, and to simplify the original circuit capabilities to capacitance-only measurements. The schematic of the circuit used is shown in figure 7.3.3 Interface Circuit Schematic.

7.3.1. Interface Circuit Description

The circuit operates from a single voltage supply and is contained on a single PCB. Measurement of the sensor capacitance change is conducted through the modification of the oscillator output frequency.

The interface circuit offers a calibration/check mode of operation which allows for the confirmation of operation with a known capacitance.

The frequency of the oscillator is set by the parallel combination of L1 (10 uH) and either the unknown capacitance connected via J1, or C2 (150 pF), using the calibration/check functionality when RF relay K1 is energised by linking the J3 (CAL/MEASURE) connector pins.

The active element of the oscillator circuit is a LM311 comparator, U1, the open-collector output is connected to the voltage rail via R2 (1 kΩ) configured to provide in-phase (0°/360°) feedback to the non-inverting input via the feedback resistor R3 (100 kΩ).

The circuit utilises a voltage divider (R1 & R4, 100 kΩ) to bias the LC section output (AC-coupled via C1, 10uF) into the U1 comparator non-inverting input to 2.5 Vdc (half voltage rail).

In-phase feedback from the output of U1 via R3 (100 kΩ) provides a modification volage to the R1 & R4 junction, providing energy in the correct phase to maintain oscillations in the LC circuit.

The RC filter formed by R5 (47 kΩ) and C3 (10 uF) sets the comparator reference voltage to the inverting input of U1. The connection of R5 to the output of U1 forms an integrator that regulates the reference voltage of the comparator to the average voltage set by the R1/R4 voltage divider. The result is a near 50% output duty cycle.

At initial turn-on, the voltage present on C3 is 0V, time constant formed by the combination of R5 and C3 provides a threshold level that increases with the output of the LC circuit during turn-on. The reference level threshold ramp provides reliable oscillator starting.

7.3.2. Component Selection

Component selection was considered during the design and simulation stages, with the commercial availability of components also a significant selection factor.

Simulation of the oscillator section, and availability of SPICE models guided the choice while simulation optimised the final values.

The use of industry standard components and industry standard connectors allowed the interfacing with electronic test equipment and assembly to rapidly occur.

Power Supply

The power supply section was included in the Prototype Interface Circuit to provide a constant 5 Vdc to the circuit. A simple linear regulator circuit, utilising a LM7805 derived surface mounted 100mA MC78L05 IC is used. The use of a linear regulator was desirable due to the lack of switching components present in switch mode power supplies. Input and output decoupling is provided as per the manufacturer datasheet requirements (available in APPENDIX D DATA SHEETS).

Comparator

The original circuit utilised an LM311 comparator as the active device in the oscillator circuit. The simulation did not indicate performance compromises in using the device, so no changes were made. The datasheet for the LM311 is available in APPENDIX D DATA SHEETS.

Resistors

Resistors were chosen from the Yaego RC series surface mount resistors. Size 1206 were chosen due to the hand assembly process to be used during construction.

Capacitors

Kemet Multilayer Ceramic capacitors were chosen for power supply decoupling, signal coupling and filtering. The 1206 size was selected in aid of hand assembly. Further analysis is included in the SPICE Simulation section with the datasheet available in APPENDIX D DATA SHEETS.

The calibration capacitor (C2), used to check the operation and frequency of the oscillator was selected as a MC series Mica dielectric capacitor from Cornell Dubilier due to the low capacitance value and very high Q, tight 1% tolerance for repeatability and RF level performance. The datasheet is available in APPENDIX D DATA SHEETS.

Relay

The relay used in the circuit is to switch between the calibration/check capacitor (C2) and the unknown capacitance on J1, typically the sensor element.

As reliable high frequency performance was required, an RF relay with high isolation between inputs was chosen. Greater than 60 dB of isolation at the expected operating frequencies will minimise errors introduced with changing sensor capacitance to the calibration frequency. The Panasonic AR series RF relays datasheet is available in APPENDIX D DATA SHEETS

Connectors

SMA input and output connectors were chosen due to their size and compatibility with existing cables and connectors. A surface mounted version chosen for J1 input due to the coupling requirements to the PCB Sensor, while edge mounted was chosen for the output due to access and interference if alternative orientations are used.

7.3.3. Interface Circuit Schematic

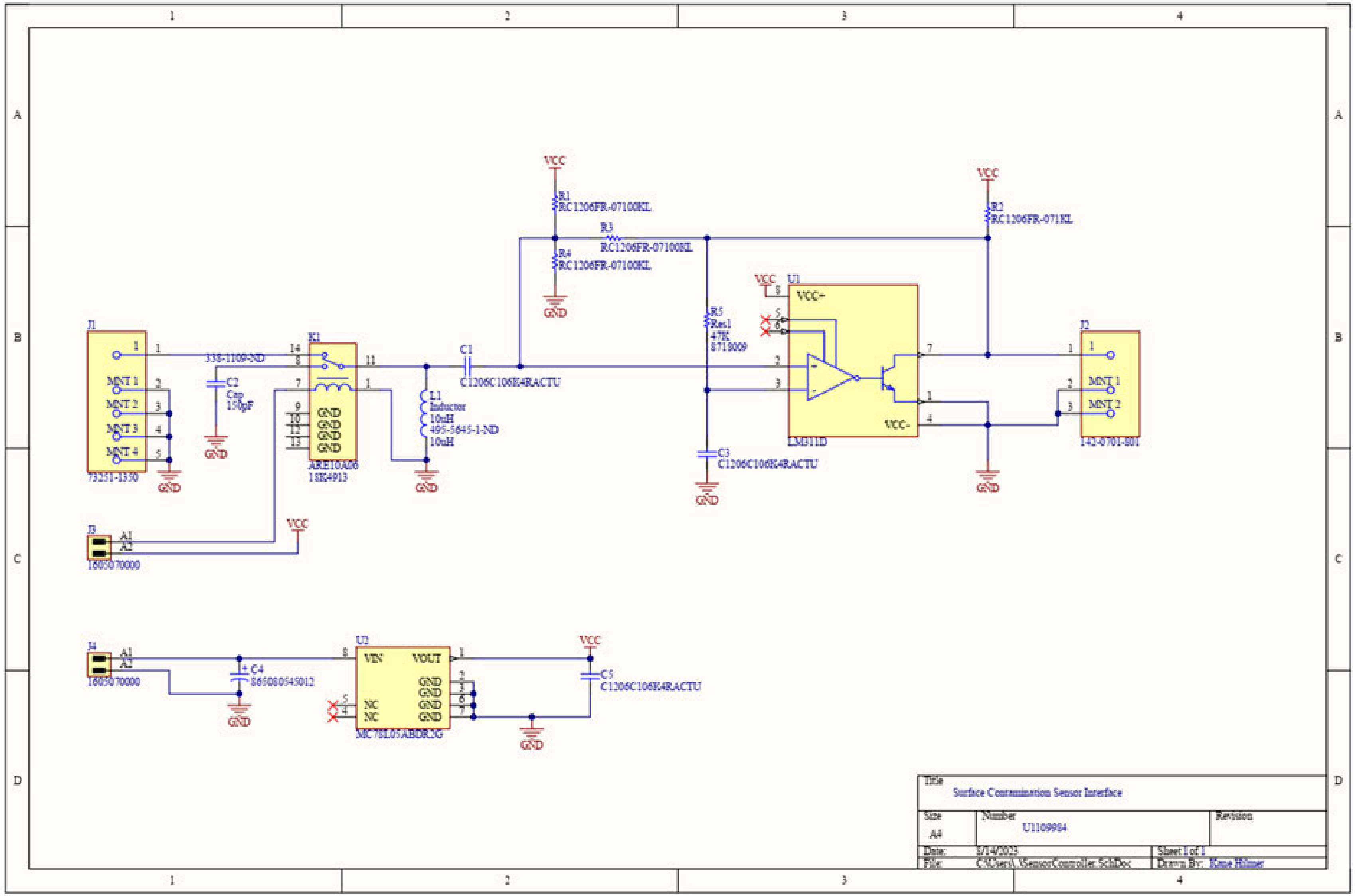

7.3.4. PCB

The PCB for the Prototype Interface Circuit was completed in Altium designer. The 60mm x 60mm dual layer PCB is shown in Figure 64 Prototype Interface PCB. The schematic shown in section 7.3.3 Interface Circuit Schematic and was used to develop the PCB and control the connections and footprints used.

Design and Layout

The component layout was configured with the interfacing input connector J1 centred on the PCB. The positions of the remaining oscillator components were chosen to minimise capacitance and inductance by minimising trace length while positioning for easy identification and assembly. No ground or shielding copper layer was implemented, so that capacitance formed between the layer and signal conductors was eliminated.

The use of a two-layer copper PCB allowed for the distribution of the ground or 0V connections to both layers of the PCB. 6 vias were used to connect the top layer mounted components to a bottom layer ground trace.

The RF Relay being the largest single component was placed so that the common output terminal was centralised between the unknown capacitor input and the calibration capacitor. Priority was given to the organisation and interconnections for the oscillator signal path, with C1, L1, R1, R3 and R4 positioned to minimise the inductance of the PCB tracks. The relay coil connections are routed clear of the signal path, routing to the connector J3 on the edge of the PCB.

The output connector is of the edge mounted type, and positioned so that the signal path is as direct as possible. Power input is via the edge mounted J4, which is set to minimise the trace length to U2, the linear voltage regulator, so that the power supply components are constrained to a compact area.

Trace width is 10 mil (0.01”), while the underside ground track 1 mm, configured to minimise inductance and offer a low impedance ground to the inductor L1, the body of J1 and grounded terminals of U1. The 3D CAD as generated by Altium Designer of the assembled PCB are shown in Figure 65 and Figure 66.

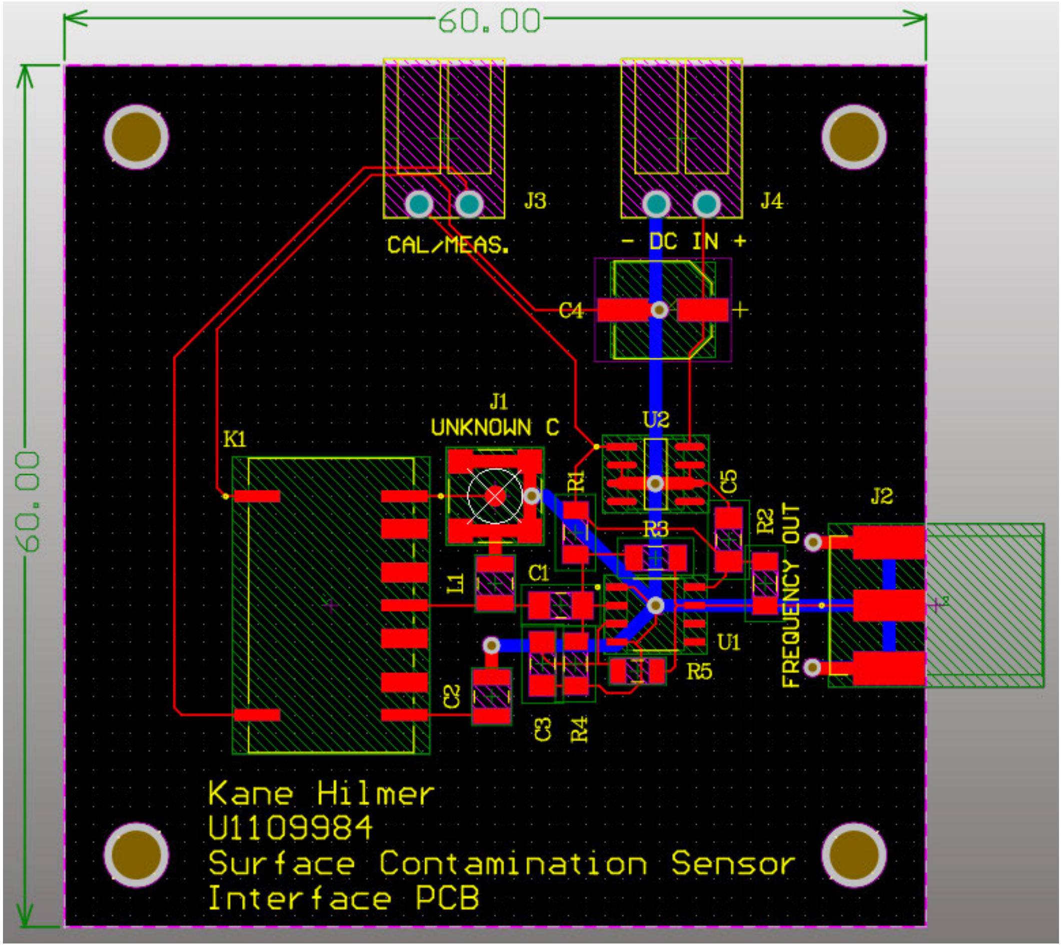

Figure 64 Prototype Interface PCB

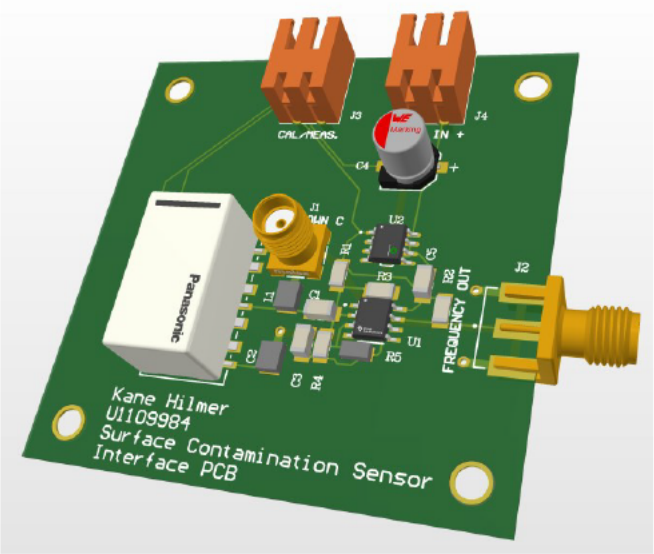

Figure 65 Prototype Interface Circuit Top Side CAD

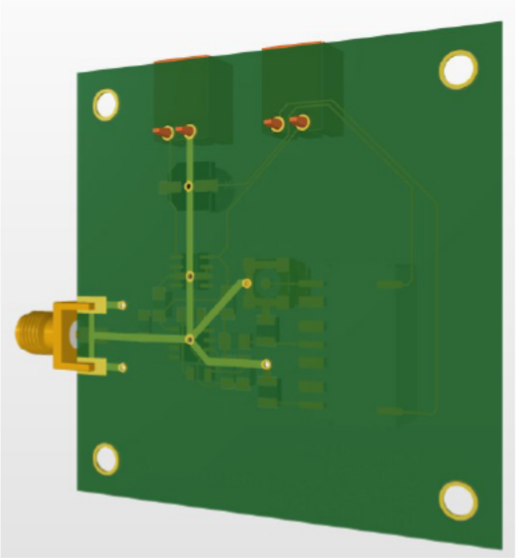

Figure 66 Prototype Interface Circuit Bottom Side CAD

7.4. SPICE Simulation

SPICE simulation of the operation and performance of the interface circuit was conducted to verify and tune the operating parameters prior to selecting the final circuit component values. The oscillator circuit was simulated using Microcap 12 with components selected from manufacture parts, cross checked as available from electronics suppliers. Commercial components were used in the simulation so that components with non-ideal values were incorporated.

Analysis of the LC circuit showed that the resonance frequency is found by equation 7-3 (Gonzalez 2006).

$$\omega_0 = \frac{1}{\sqrt{LC}} \qquad \text{7-2}$$

$$f_r = \frac{1}{2\pi\sqrt{LC}} \qquad \text{7-3}$$

Where: $L = Fixed\ Inductor$ and C= $Unknown\ Capaacitor$

The selection of the fixed inductor was chosen considering the range of capacitance expected from the sensor. For the electrode-on-glass design, a range of approximately 100 pF to 10 nF capacitance is expected. For the PCB sensor element, a range of 500pF to 10nF (for expected material tests) is predicted.

Utilising the plot shown in Figure 67 Theoretical LC Oscillator Resonance, a 10uH fixed inductor was chosen. The range of output frequencies expected with the 10uH inductor, approximately 5 MHz – 500 kHz, falling within the safe operating range of the LM311 comparator.

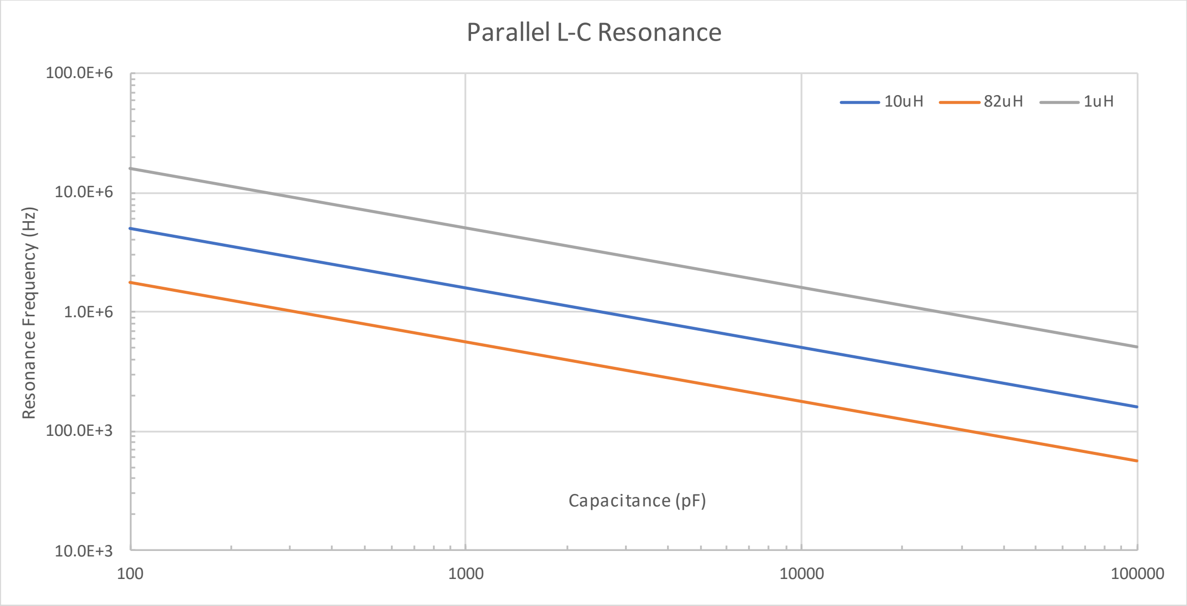

Figure 67 Theoretical LC Oscillator Resonance

The maximum usable operating frequency of the LM311 was determined by the rise and fall times listed in the data sheet available in APPENDIX D DATA SHEETS.

The inductor L1 was chosen from commercially available components that were available with a full SPICE model. A TDK SIMID series surface mount inductor was chosen as it offered high Q factor, and resonance frequency for the 10 uH value required. The datasheet is available in APPENDIX D DATA SHEETS.

The capacitors C1 and C3 share a value of 10 uF and were also chosen based on availability of components and SPICE model. Multilayer ceramic capacitors were used in these locations as non-polarised, low inductance properties are required.

Kemet X7R dielectric 10% tolerance 16V capacitors were chosen due to their decoupling and filtering characteristics, as listed in the datasheet.

The Microcap simulation circuit is shown in Figure 68.

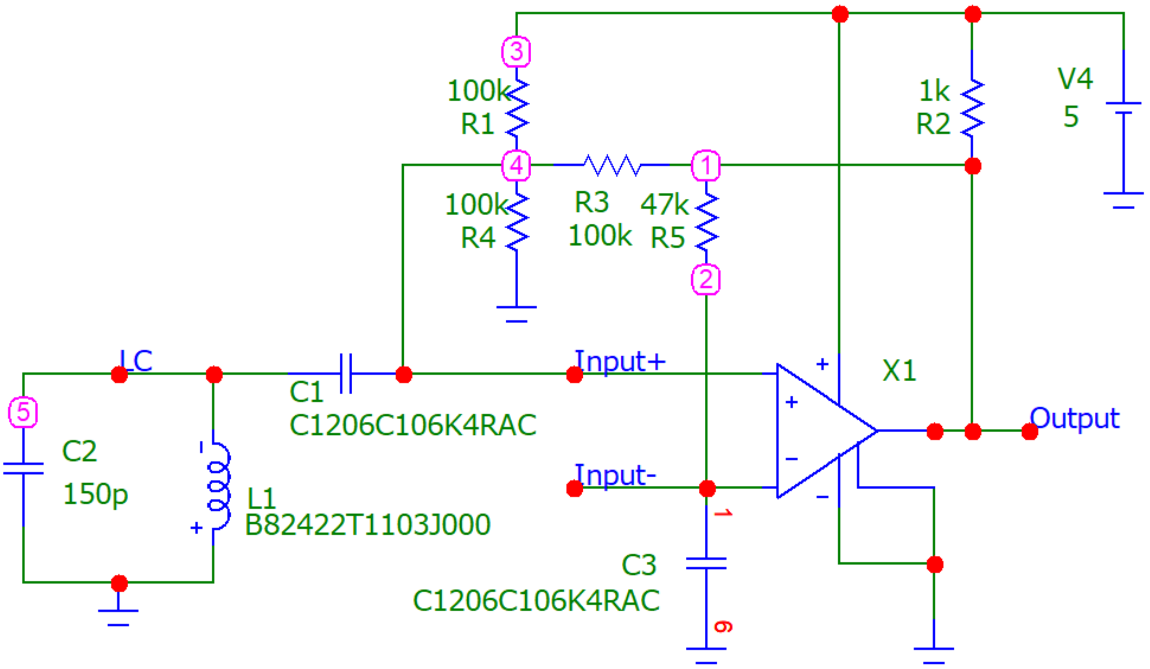

Figure 68 Microcap Simulation

7.4.1. SPICE Simulation Results

The microcap circuit shown Figure 68 Microcap Simulation had multiple simulations conducted. Simulation for both the electrode-on-glass and PCB Sensor capacitance values were conducted. Transient operating values for the multiple capacitance input values, in addition to temperature analysis was conducted as shown in Table 23.

The SPICE output waveforms for expected clean and water PCB capacitance is shown in Figure 69 and Figure 70. The red trace indicates the LM311 output, green trace for the non-inverting input of the LM311, while black shows the voltage present on the L1/C2 junction, finally the blue trace indicated the inverting input of the LM311.

Frequency output was confirmed for each capacitance value / circuit temperature test point. The simulation output frequency is compared to the theoretical resonance from equation 7-3 in Table 22.

Table 22 Interface Circuit Simulation - Frequency Vs Simulation

	Input Capacitance	**Microcap Simulation**	**Equation**	**Difference**
Calibration	150 pF	4.021 MHz	4.109 MHz	97.85%
Clean	114.46 pF	4.503 MHz	4.704 MHz	95.72%
Wood, Dry	114.62 pF	4.465 MHz	4.701 MHz	94.98%
Clean (PCB)	1202.1 pF	1.453 MHz	1.4516 MHz	100.10%
Water (PCB)	2161.4 pF	1.082 MHz	1.0826 MHz	99.95%
Cement, Wet	8198.2 pF	574.24 kHz	555.86 kHz	103.31%

Table 23 Interface Circuit - Frequency Vs Temperature

		Temperature/Frequency (MHz)			
	Input Cap.	**-10**	**20**	**50**	**80**
Calibration	150 pF	4.028	4.021	3.99	4.01
Clean	114.46 pF	4.497	4.503	4.497	4.484
Wood, Dry	114.62 pF	4.503	4.465	4.469	4.491
Clean	1202.1 pF	1.468	1.453	1.473	1.461
Water	2161.4 pF	1.096	1.082	1.100	1.073
Cement, Wet	8198.2 pF	0.575	0.574	0.575	0.574

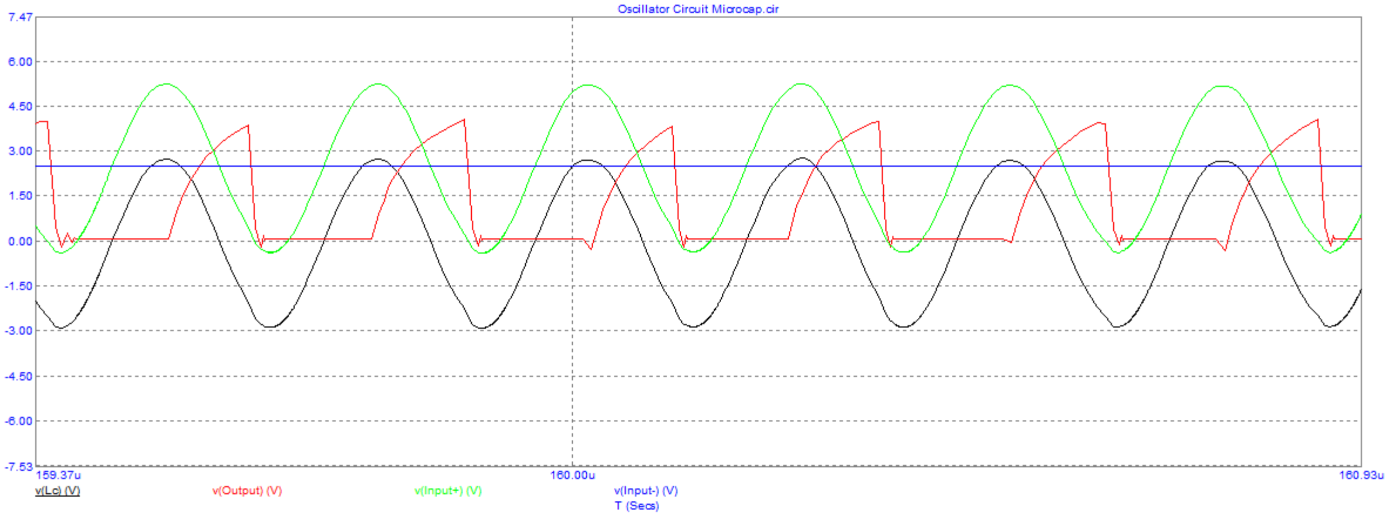

Figure 69 Calibration (150 pF) - 4.021 MHz

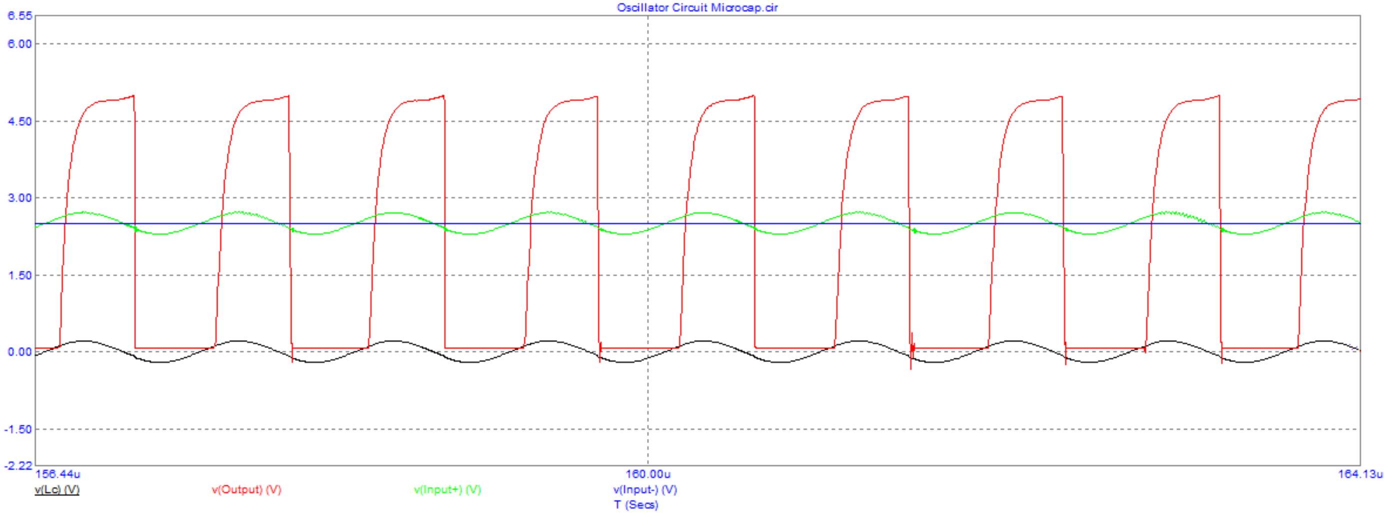

Figure 70 PCB (Water) - 1.082 MHz

7.5. Interface Circuit Post-Manufacture Review

7.5.1. Initial Testing & Troubleshooting

The Prototype Interface circuit was tested independently of the PCB Sensor, after the manufacturing described in section 8 Sensor PCB Manufacture and prior to the combination sensor system testing.

Initial testing of the Prototype Interface showed that low values of capacitance (<200pF) produced an output that would periodically stop oscillating. Introducing the calibration capacitance (150 pF) by linking the J3 pins also did not produce a reliable oscillation.

The observed output on the digital oscilloscope showed the output voltage was ‘motor boating’, with the output stalling at the Vcc voltage rail (5V). The frequency output was not stable and did not produce reliable measurements.

7.5.2. Interface Circuit Review

The circuit troubleshooting began with oscilloscope observations of the operating circuit. The observations were not conclusive, with the measure comparator reference voltage not stable. The voltage was observed decreasing to below the reference level, with the oscillator circuit cutting off. As the LC signal reduced, the DC bias of the non-inverting input to U1 exceeded the inverting input voltage.

Troubleshooting returned to MicroCap, where the simulation time was extended, resulting in the same oscillator behaviour being observed. Analysis and experimentation with parasitic capacitance added to the simulation circuit to simulate the as-built and real-world PCB. The simulation then produced repeatable stalled oscillations.

The simulation allowed for easier analysis of the stalled oscillations, as observed on the assembled circuit: the reference voltage was not increasing at the rate required to maintain oscillations.

Resistance was decreased to 500Ω for R2, to decrease the time-constant due to the connected test equipment and coaxial cable. R3 was fitted with a 22pF capacitor in parallel to increase the feedback to the LC circuit of the higher frequency components, creating a larger voltage drive to the comparator input and LC circuit.

With the additional LC circuit voltage, the simulation showed a negative voltage present on the non-inverting input of U1. The negative voltage generated spurious outputs from the LM311, which were corrected by the inclusion of a 1N4148 diode reverse-biased to circuit ground from the non-inverting input.

The final real-world observation made was that the LC circuit did not oscillate at the higher frequencies predicted by the simulation and formula. The likely cause is stray capacitance, present in the circuit construction and components and the unity gain bandwidth of the LM311.

To allow for the expected range of capacitance, the inductor L1 was increased in value to 33uH. The result is a lowering of the output frequency for a given input capacitance. The expected lower frequency also improves the performance of the LM311, allowing the increased gain required to maintain oscillation.

The circuit modifications were performed on the previously constructed Prototype Interface, using workshop-available components. R2 was modified by the application of a second 1kΩ resistor in parallel. A 22pF ceramic capacitor was installed physically on top of R3. A through-hole 1N4148 diode was lead-formed and installed between U1 pin 2 & 4. L1 was removed and replaced, resulting in the reorientation of L1 to share the ground connection to C2.

A summary of the changes made is shown in Table 24.

The modified schematic is shown in 7.5.4 Reviewed Interface Schematic, with modifications highlighted in red.

The constructed and modified circuit is shown in Figure 87.

Table 24 Interface Circuit Review Changes

Change	Previous	Reviewed	Completed By
L1 Inductance	10uH	33uH	Exchange Component
R2 Resistance	1 kΩ	500 Ω	Parallel Resistor
R3 Shunt	100 kΩ	100 kΩ || 22pF	Parallel Capacitor
D1	-	1N4148	New Component

7.5.3. Interface Circuit Simulaiton Review

Microcap Simulaitons were repeated for the reviewed capacitance values expected from Table 19 PCB Simulation Review Parameters. The revised circuit is shown in Figure 71.

Review simulation results are shown in Table 25.

Table 25 Interface Circuit Simulation Review - Frequency

	Input Capacitance	Microcap Simulation	Equation	Difference
Calibration	150 pF	2.207 MHz	2.251 MHz	98.03%
Clean	82 pF	2.435 MHz	3.049 MHz	79.85%
Water (PCB)	1190 pF	0.839 MHz	0.800 MHz	104.8%

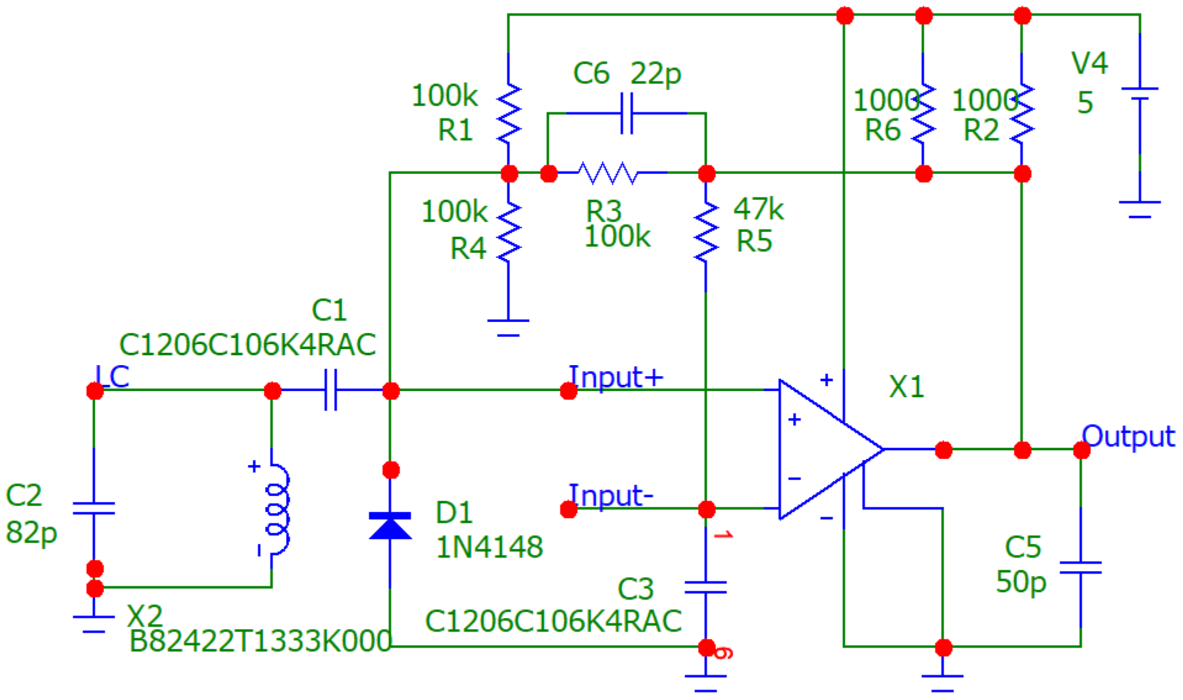

Figure 71 Reviewed Interface Circuit Simulation

7.5.4. Reviewed Interface Schematic

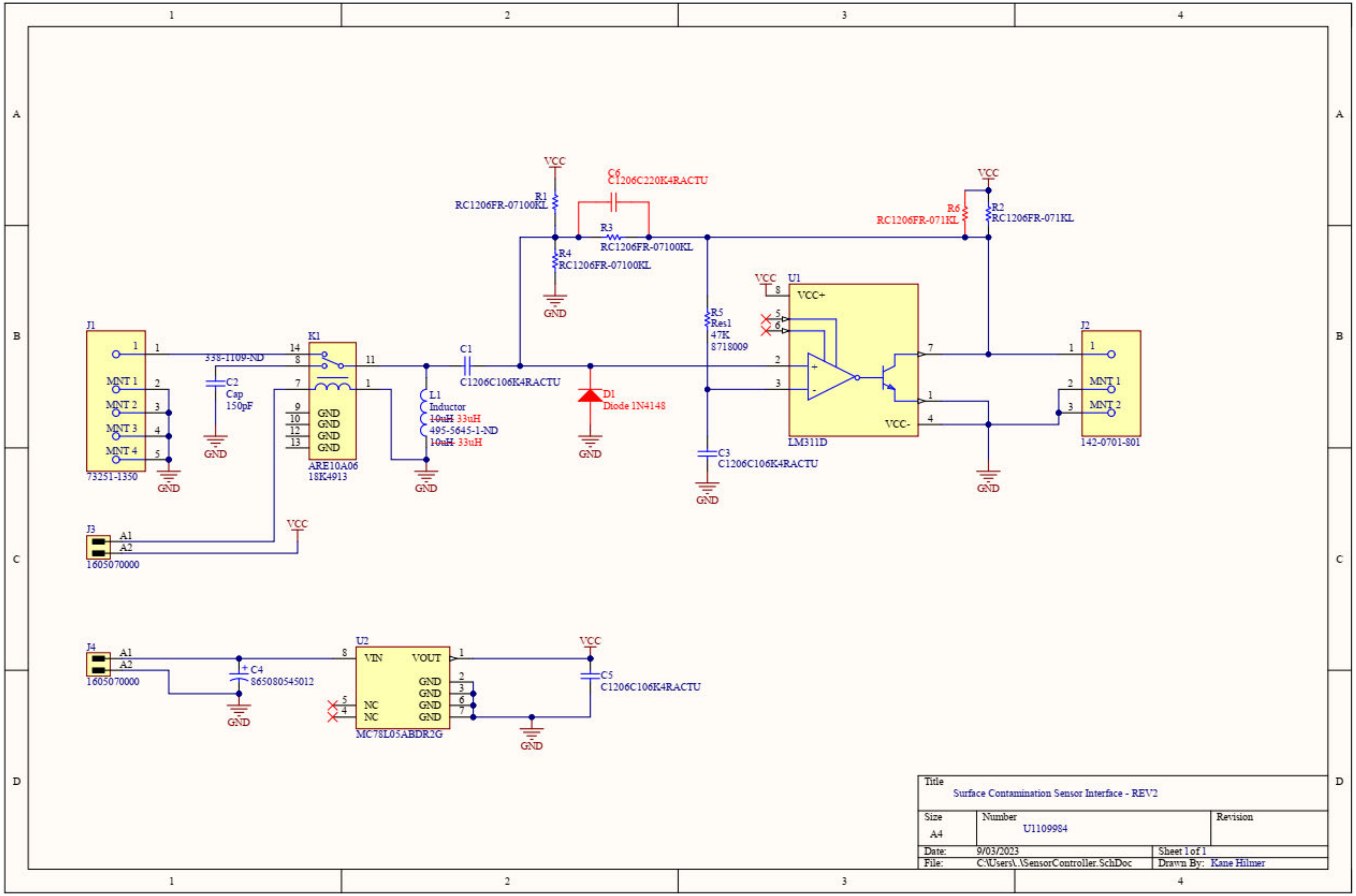

8. Sensor PCB Manufacture

The manufacture of the PCB cards was completed by “ALL PCB”, in mainland China. The manufacturing order was completed from Gerber files generated from Altium Designer PCB design software.

Components listed in the Bill of Materials (BOM) is available in APPENDIX D MANUFACTURE BOM, were ordered from DigiKey electronics, USA.

The assembly of the PCB sensor and interface circuit were completed by hand using a combination of hot-plate surface mount soldering and hand soldering. A risk assessment (available in APPENDIX B RISK ASSESMENT) was carried out prior to beginning of the assembly process, with appropriate PPE fitted and used.

A photograph of the assembled Interface circuit card is shown in Figure 87.

The complete assembled PCBs were visually inspected prior to the beginning of testing.

9. Test & Data Collection

Testing of the PCB sensor and Prototype Interface was completed using multiple pieces of electronic test equipment.

Initial testing of the PCB Sensor and Prototype Interface produced unexpected and undesirable results, resulting in the review detailed in sections 7.2 and 7.5 above.

Once the reviews were completed, testing of the revised hardware was conducted in four stages:

1. Perform capacitance measurements of the PCB Sensor with a LCR Meter.
2. Characterise the PCB Sensor using a Vector Network Analyser (VNA), to establish the frequency dependent electrical characteristics of the PCB Sensor.
3. Check operation of the Prototype Interface Circuit using fixed value capacitors.
4. Combine the PCB Sensor and Prototype Interface Circuit, check operation.

9.1. Test Equipment Used

The test equipment used during the test and data collection stages of the sensor system is listed in Table 26.

Table 26 Electronic Test Equipment

Device	Description	Calibration Due Date
Agilent E5071C Vector Network Analyser	9 kHz – 4 GHz Vector Network Analyser	Jul 2024
HP 85052B 3.5mm Calibration Kit	DC-26.5 GHz Mechanical Calibration kit	-
Rigol DS2102A Digital Oscilloscope	100 MHz, 2-Channel Digital Storage Oscilloscope	Mar 2024
Fluke 175 True RMS Multimeter	Digital Multimeter	Jul 2024
HP 5315A Universal Counter	Frequency Counter	Nov 2023
Keysight U1733C LCR Meter	100kHz Digital LCR Meter	Aug 2024
Kenwood PR36-12 DC Power Supply	0-36V, 0-1.2A Regulated DC Power supply	Jul 2024

9.1.1. E5071C VNA & 85052B 3.5mm Calibration Kit

The E5071C Vector Network Analyser (VNA) is a sensitive and sophisticated electronic instrument that can be used to characterise the parameters and performance of radio frequency (RF) devices and components, such as capacitors.

The VNA outputs a sweeping RF signal of defined frequency test points and power. Devices connected to the VNA interact with the RF signal, absorbing, transmitting or reflecting the signal, which the VNA measures and performs calculations to establish the characteristics of the device at each frequency tested.

For characterising the PCB Sensor, the VNA was configured so that a S11 measurement was conducted, where the transmission and reflection parameters from a single port were measured. The VNA was set to perform the required calculations to display the sensor capacitance value over the defined frequency range using a Smith Chart and real/imaginary frequency component plots.

Smith Charts are used to represent the complex impedance of the device connected to the VNA with a S11 measurement. The Smith Chart is a polar plot where the horizontal axis represents the real component of the impedance. The centre of the chart is normalised to the characteristic impedance of the transmission line (50 Ω) with lines of constant resistance and reactance radiating from the centre. The VNA indicates the complex impedance as a continuous line on the Smith Chart for the frequency range tested, with capacitance indicated by a plot below the horizontal axis.

Real/imaginary plots are an alternative indication of the complex impedance with the respective impedance component plotted against the frequency, on a linear frequency scale.

Due to the sensitivity of the VNA, systemic errors exist in the measurements, caused in part by the interconnecting cables' terminations, reflections, attenuation, and bandwidth. The correction of the systemic errors or 'de-embedding' is completed by performing a calibration of the instrument by including the interconnecting cables that extend to the Device Under Test (DUT).

The 85052B Calibration Kit is used to calibrate the VNA and interconnecting cable(s) over the frequency range of interest, with the number of test points programmed, correcting for the errors introduced by using the interconnecting cable. An Open, Short, Match (OSM) calibration was performed using the 85052B Calibration kit at the PCB Sensor connector.

As the PCB Sensor featured a SMA RF connector (3.5mm compatible), performing a calibration at the connector mating to the PCB Sensor ensures the VNA measurements are valid for the PCB Sensor alone and exclude cable and connector influences.

An image of the E5071C VNA & 85052B 3.5mm Calibration Kit is available in APPENDIX E TEST EQUIPMENT.

9.1.2. Rigol DS2102A Digital Oscilloscope

The DS2102A Digital Oscilloscope is used to monitor the time-domain voltage waveform of the Interface Circuit output. The DS2102A was also used to perform electrical measurements and troubleshooting of the Interface Circuit.

Frequency measurements performed by the oscilloscope are for indication only. The Universal Counter was used to perform frequency measurements.

An image of the Rigol DS2102A Digital Oscilloscope is available in APPENDIX E TEST EQUIPMENT.

9.1.3. Fluke 175 True RMS Multimeter

The Fluke 175 is a hand-held Digital Multimeter (DMM) used to measure DC voltages input to and contained within the Interface Circuit.

An image of the Fluke 175 True RMS Multimeter is available in APPENDIX E TEST EQUIPMENT.

9.1.4. HP 5315A Universal Counter

The Universal counter is used to indicate the frequency output of the Interface Circuit. The HP5315A provides a more appropriate frequency measurement than the oscilloscope with adjustable level thresholds and gate time.

An image of the HP 5315A Universal Counter is available in APPENDIX E TEST EQUIPMENT.

9.1.5. Keysight U1733C LCR Meter

The LCR Meter allows for convenient measurement of passive devices including Inductors, Capacitors and Resistors. The LCR meter was used to indicate the capacitance value of the capacitors used in verifying the Interface Circuit and for measurement of the PCB Sensor capacitance. All measurements were performed at 100 kHz, and capacitance nulled prior to measurement, to eliminate stray capacitance due to interconnections or jigs.

An image of the Keysight U1733C LCR Meter is available in APPENDIX E TEST EQUIPMENT.

9.1.6. Kenwood PR36-12 DC Power Supply

The PR36-12 is a DC Power Supply used for powering the interface circuit. Analogue control and linear regulation were chosen to reduce the possibility of switching noise coupling into the Interface Circuit or PCB Sensor.

An image of the Kenwood PR36-12 DC Power Supply is available in APPENDIX E TEST EQUIPMENT.

9.2. LCR Meter Measurement - PCB Sensor Element

The PCB Sensor was initially tested using the U1733C LCR meter. An interconnection cable was fabricated using LMR240-UF coaxial cable, SMA connector and ‘banana plugs’ to interface the PCB Sensor to the LCR meter, as shown in Figure 72. The capacitance of the interconnection was nulled prior to connection to the sensor.

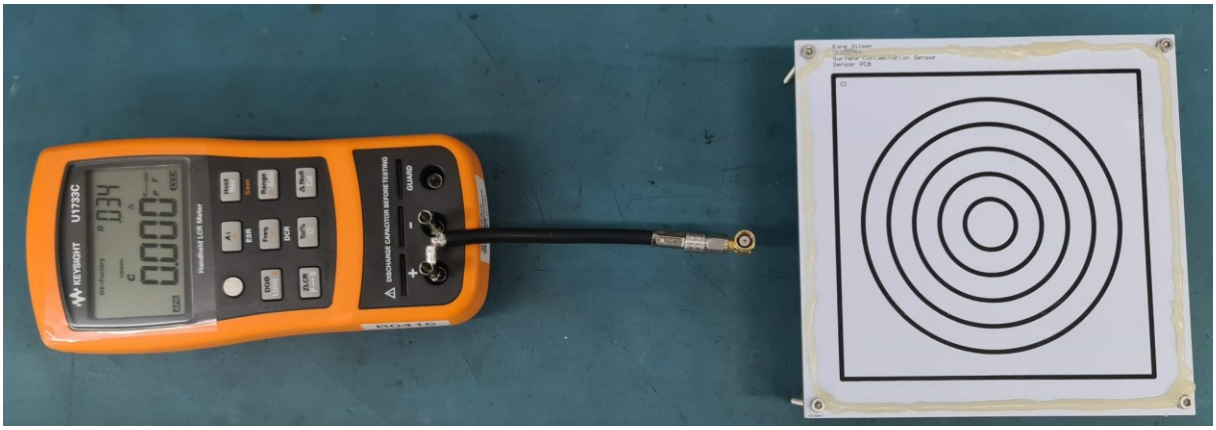

Figure 72 LCR Meter PCB Sensor Interface

The LCR Meter performed a capacitance measurement of dry PCB Sensor at 100 kHz as shown in Figure 73.

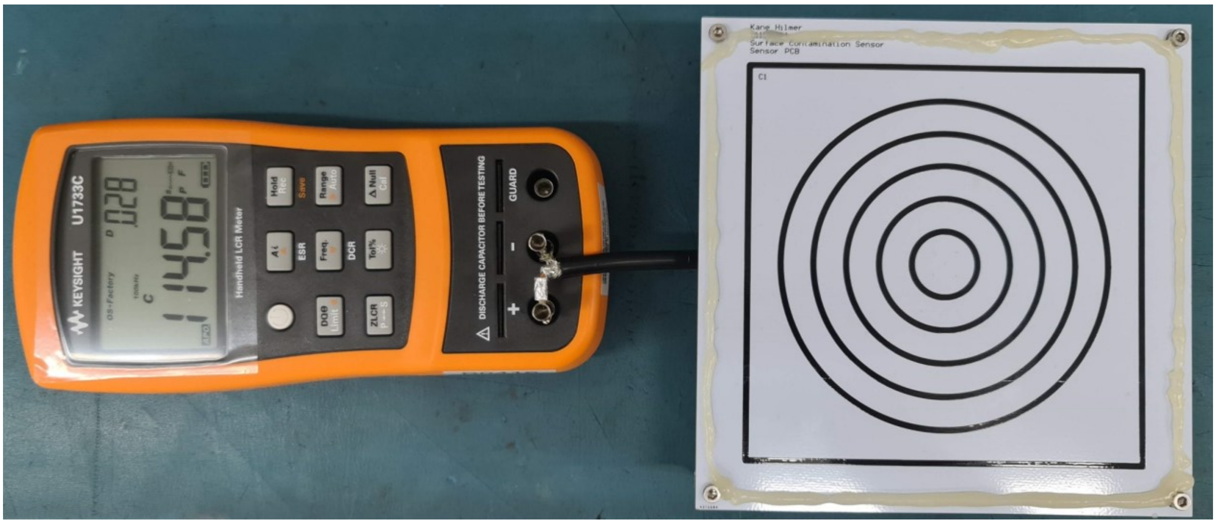

Figure 73 LCR Meter PCB Sensor Dry Capacitance Measurement

Sufficient tap water was added to the top PCB Sensor surface to ensure a complete coverage of the sensor area, shown in Figure 75. The wet capacitance of the PCB Sensor was conducted, shown in Figure 74.

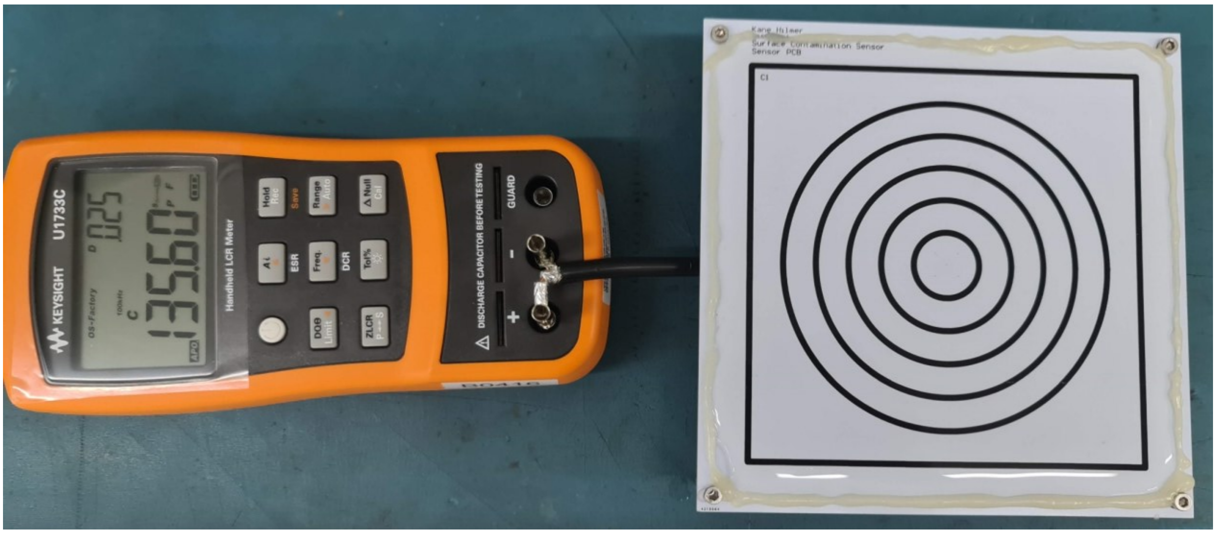

Figure 74 LCR Meter PCB Sensor Wet Capacitance Measurement

LCR Meter capacitance results are shown in Table 33 LCR Meter Results – Clean PCB Sensor and Table 34 LCR Meter Results – Wet PCB Sensor.

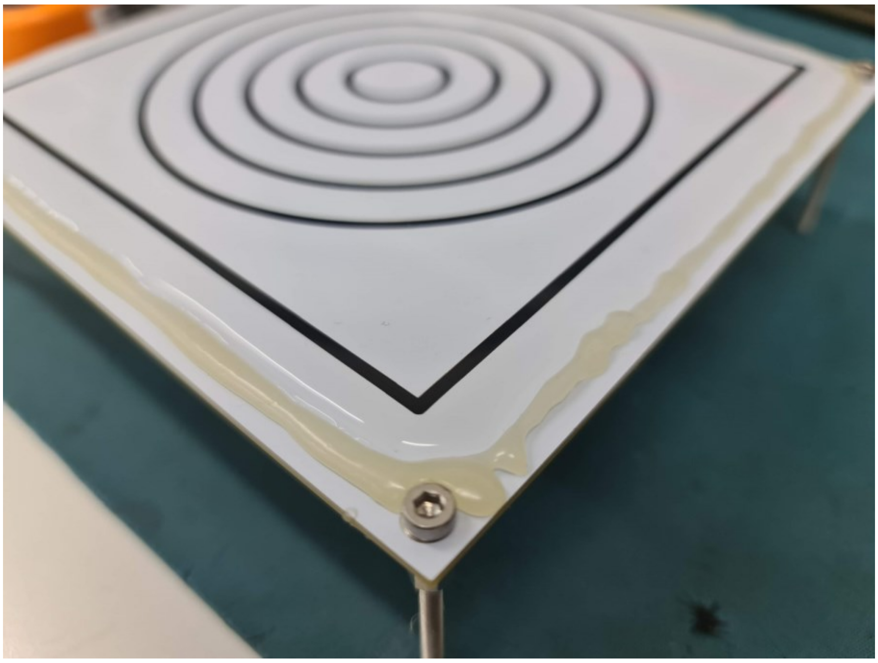

Figure 75 PCB Sensor Water Coverage

9.3. VNA Measurement - PCB Sensor Element

The PCB Sensor Element was tested and characterised using the Vector Network Analyser.

Interconnection between the VNA and PCB Sensor was completed using LMR240-UF coaxial cable fitted with a N-type Male to SMA male cable. A 90° SMA adapter was fitted to allow the PCB Sensor to present a level surface for the application of contamination.

Prior to measurements being taken, a single-port (S11) calibration for the frequency range of 10kHz – 5MHz using 1001 sample points was performed. The calibration used an Open-Short-Match (OSM) technique on the male SMA connector of the 90° adapter, using 85052B calibration kit.

With the calibration kit components removed from the 90° SMA adapter, the adapter was moved to the PCB Sensor connector.

VNA measurements were performed generating a Smith Chart, real and imaginary plots, while characterising the PCB sensor for clean, water and soil contamination. The sensor and contaminants are shown in Figure 78, with the soil collection site shown in Figure 104 Soil Contamination Collection Site (APPENDIX E TEST EQUIPMENT).

9.3.1. Clean PCB Sensor Results

The clean sensor VNA Smith Chart is shown in Figure 76. The small trace indicated between 3 o’clock and 4 o’clock is the frequency response of the PCB Sensor. The trace is completely below the horizontal axis of the chart, indicating capacitive reactance. As the line follows the outer guide of the Smith Chart, the capacitive component of the complex impedance is dominant.

Results are summarised in Table 27.

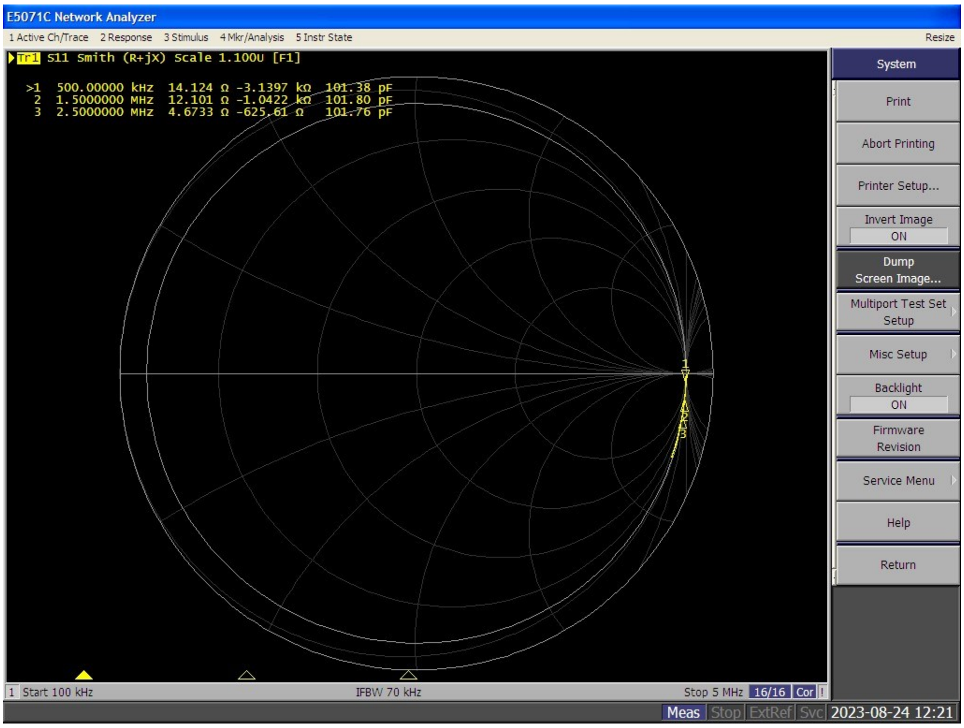

```
Tr1 S11 Smith (R+jX) Scale 1.100U [F1]

 >1  500.00000 kHz  14.124 Ω -3.1397 kΩ  101.38 pF
  2  1.5000000 MHz  12.101 Ω -1.0422 kΩ  101.80 pF
  3  2.5000000 MHz  4.6733 Ω -625.61 Ω   101.76 pF
```

Figure 76 Clean PCB Sensor Smith Chart

9.3.2. Wet PCB Sensor Results

Sufficient tap water was added to the PCB Sensor surface to ensure complete sensor area coverage. Figure 75 PCB Sensor Water Coverage demonstrates the water coverage level. The wet sensor VNA Smith Chart is shown in Figure 77. Results are summarised in Table 28. The trace location is comparable in location to the Clean PCB Sensor, indicating the capacitance is still dominant in the impedance of the Wet PCB Sensor.

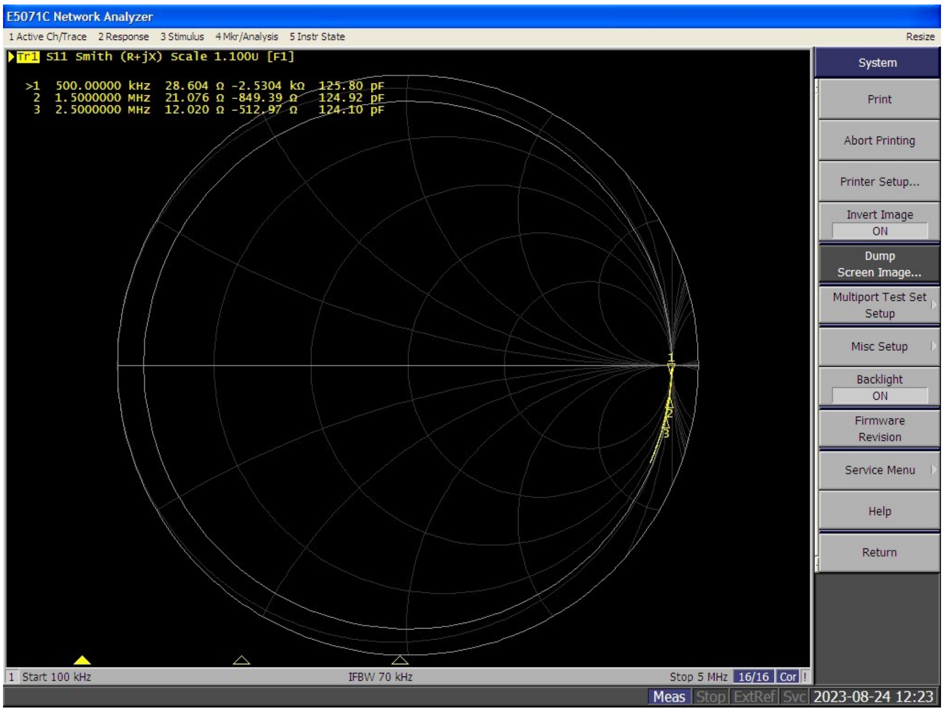

```
Tr1 S11 Smith (R+jX) Scale 1.100U [F1]

 >1  500.00000 kHz  28.604 Ω -2.5304 kΩ  125.80 pF
  2  1.5000000 MHz  21.076 Ω -849.39 Ω   124.92 pF
  3  2.5000000 MHz  12.020 Ω -512.97 Ω   124.10 pF
```

```
1  Start 100 kHz          IFBW 70 kHz          Stop 5 MHz
2023-08-24 12:23
```

Figure 77 Wet PCB Sensor Smith Chart

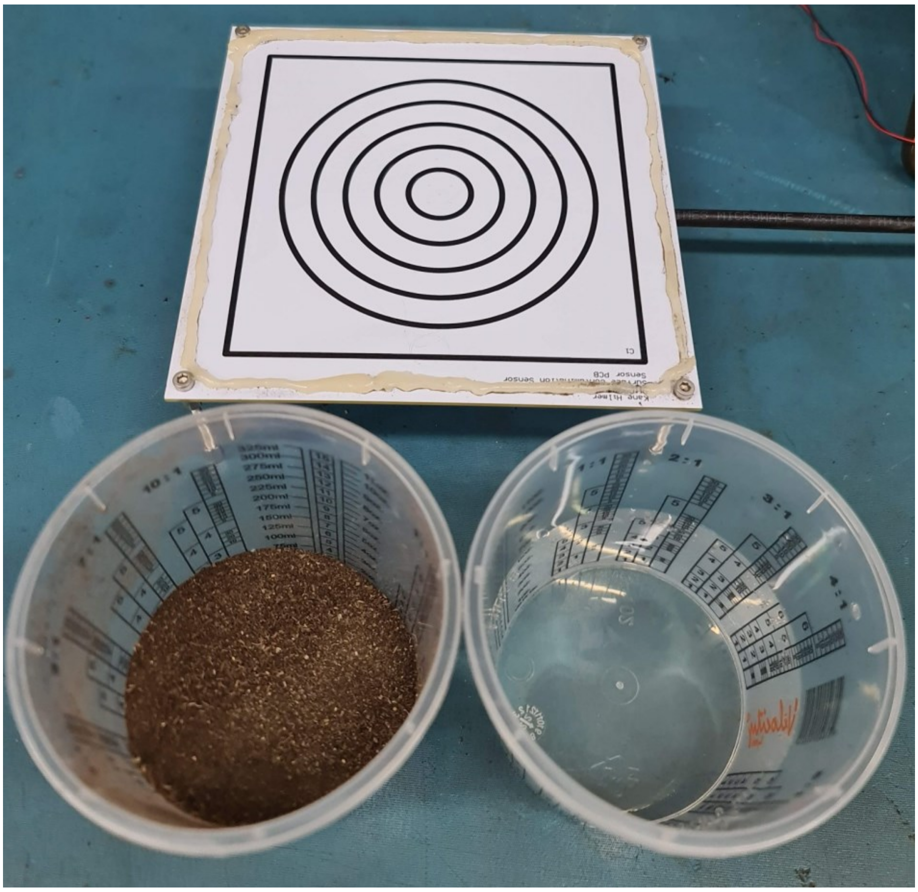

Figure 78 PCB Sensor and Surface Contaminants

9.3.3. *Dry Soil PCB Sensor Results*

The water was removed from the PCB sensor and was thoroughly dried. A soil sample was collected and passed through a sieve to remove large organic matter and pebbles. The soil sample is of unknown composition, retrieved from a garden bed. A thin layer of soil was distributed over the sensor surface, as shown in Figure 79. The resulting Smith Chart is shown in Figure 80. Results are summarised in Table 29.

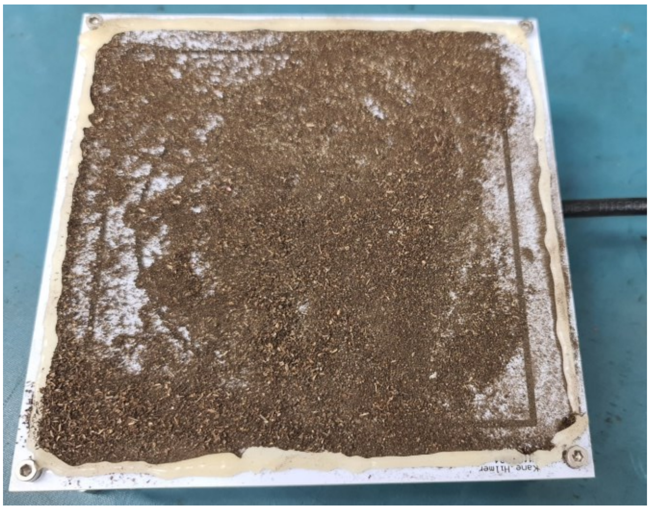

Figure 79 Dry Soil Surface Contamination

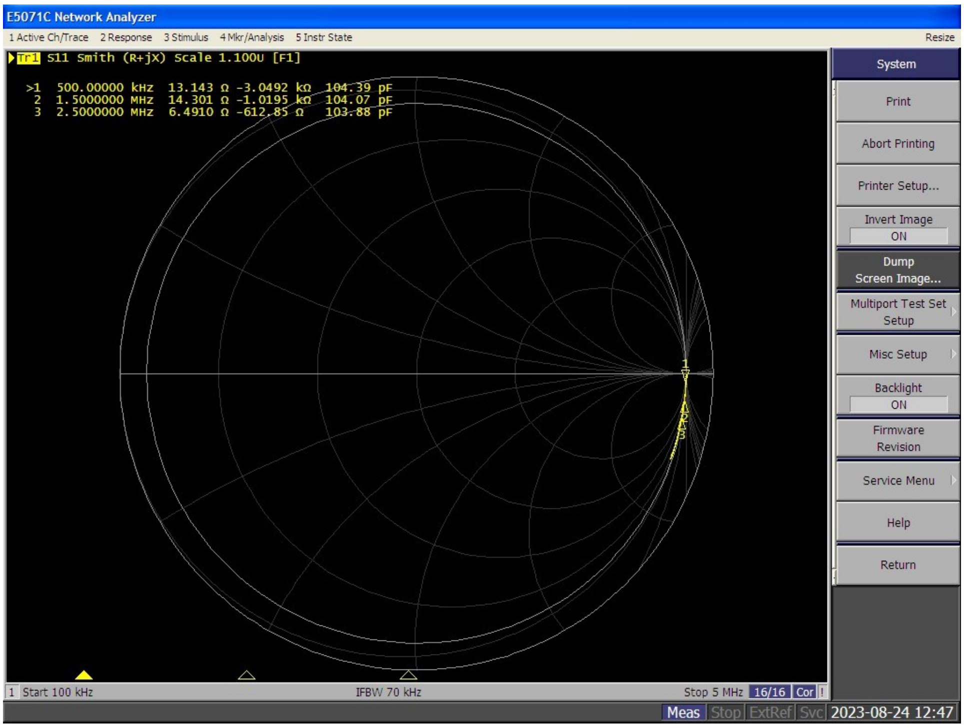

```
Tr1 S11 Smith (R+jX) Scale 1.100U [F1]

  >1  500.00000 kHz  13.143 Ω -3.0492 kΩ  104.39 pF
   2  1.5000000 MHz  14.301 Ω -1.0195 kΩ  104.07 pF
   3  2.5000000 MHz  6.4910 Ω -612.85 Ω   103.88 pF
```

Figure 80 PCB Sensor Dry Soil Smith Chart

9.3.4. *Wet Soil PCB Sensor Results*

5 ml of tap water was distributed via syringe to the soil present on the PCB sensor. The soil was mixed with the water, forming a mud/paste composition. An attempt was made to spread the composition evenly over the sensor surface, shown in Figure 81, resulting in the Smith Chart shown in Figure 82. Results are summarised in Table 30.

Figure 81 Wet Soil Surface Contamination

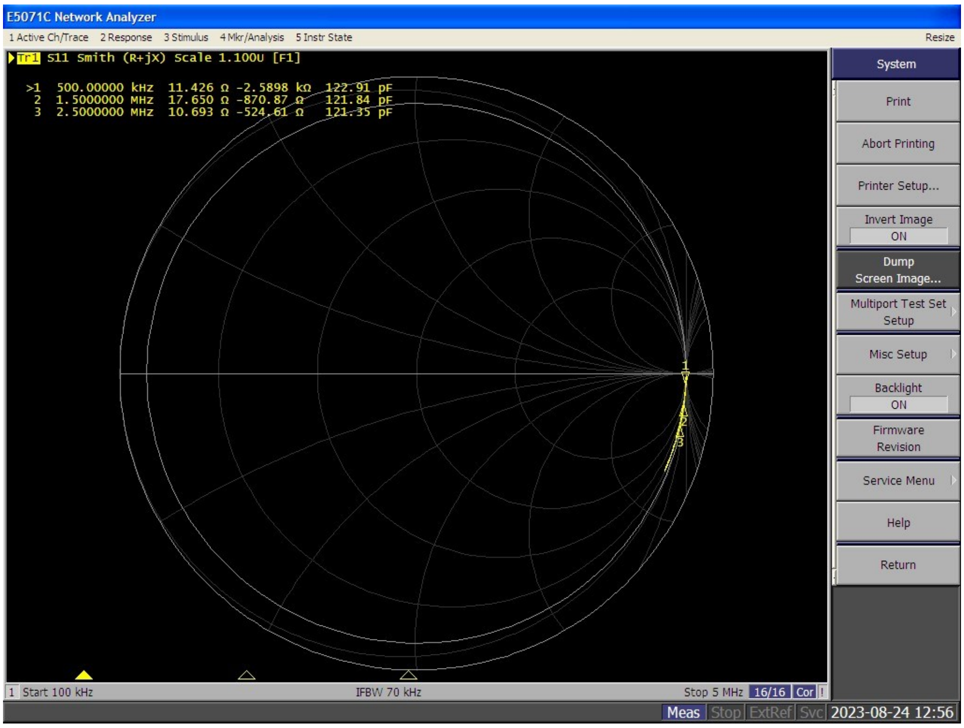

```
Tr1 S11 Smith (R+jX) Scale 1.100U [F1]

 >1  500.00000 kHz  11.426 Ω -2.5898 kΩ  122.91 pF
  2  1.5000000 MHz  17.650 Ω -870.87 Ω   121.84 pF
  3  2.5000000 MHz  10.693 Ω -524.61 Ω   121.35 pF
```

Figure 82 PCB Sensor Wet Soil Smith Chart

9.3.5. Wet Deposition Soil PCB Sensor Results

The wet soil was allowed to dry through hot air application and natural drying. The resulting deposition was notably more adhered to the PCB sensor surface. The deposition is shown in Figure 83 and Smith Chart in Figure 84. Results are summarised in Table 31.

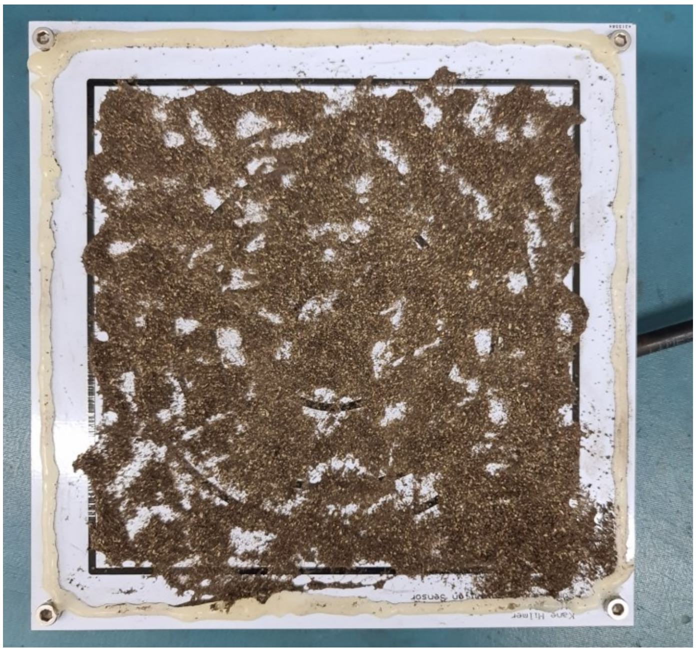

Figure 83 Wet Deposition Soil Surface Contamination

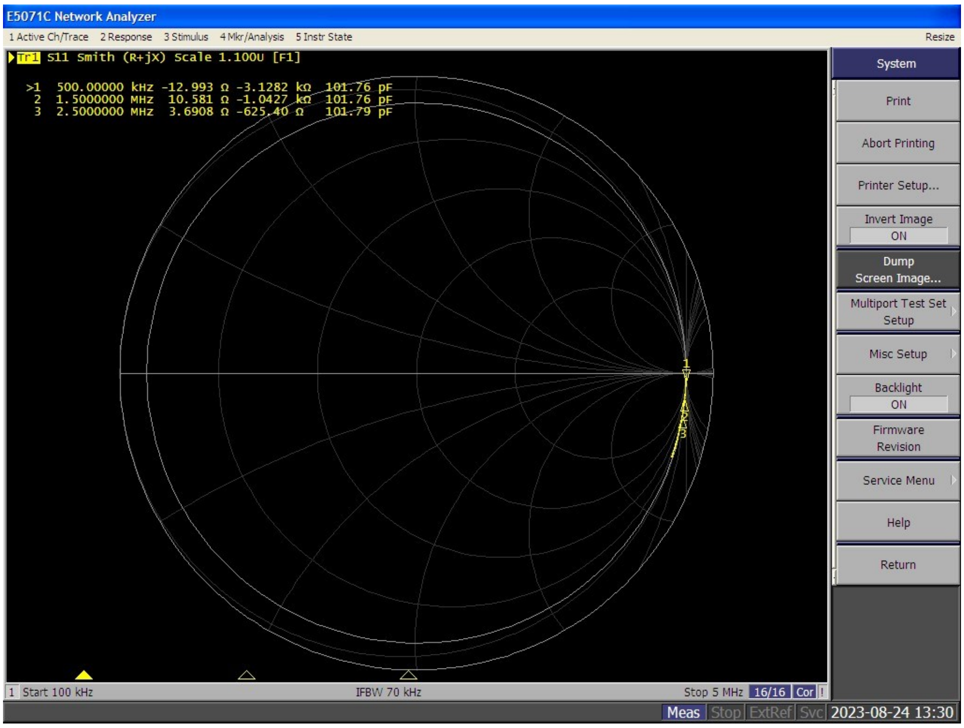

```
Tr1 S11 Smith (R+jX) Scale 1.100U [F1]

 >1  500.00000 kHz -12.993 Ω -3.1282 kΩ  101.76 pF
  2  1.5000000 MHz  10.581 Ω -1.0427 kΩ  101.76 pF
  3  2.5000000 MHz  3.6908 Ω -625.40 Ω   101.79 pF
```

```
1  Start 100 kHz          IFBW 70 kHz          Stop 5 MHz  16/16  Cor
Meas  Stop  ExtRef  Svc  2023-08-24 13:30
```

Figure 84 PCB Sensor Wet Deposition Soil Smith Chart

9.3.6. *Soil Removed PCB Sensor Results*

The soil was then removed from the PCB Sensor by physical cleaning. No liquids were used, resulting in some remaining contamination, as shown in Figure 85. A measurement was taken, with the Smith Chart shown in Figure 86. Results are summarised in Table 32.

Figure 85 Dry Cleaned PCB Sensor

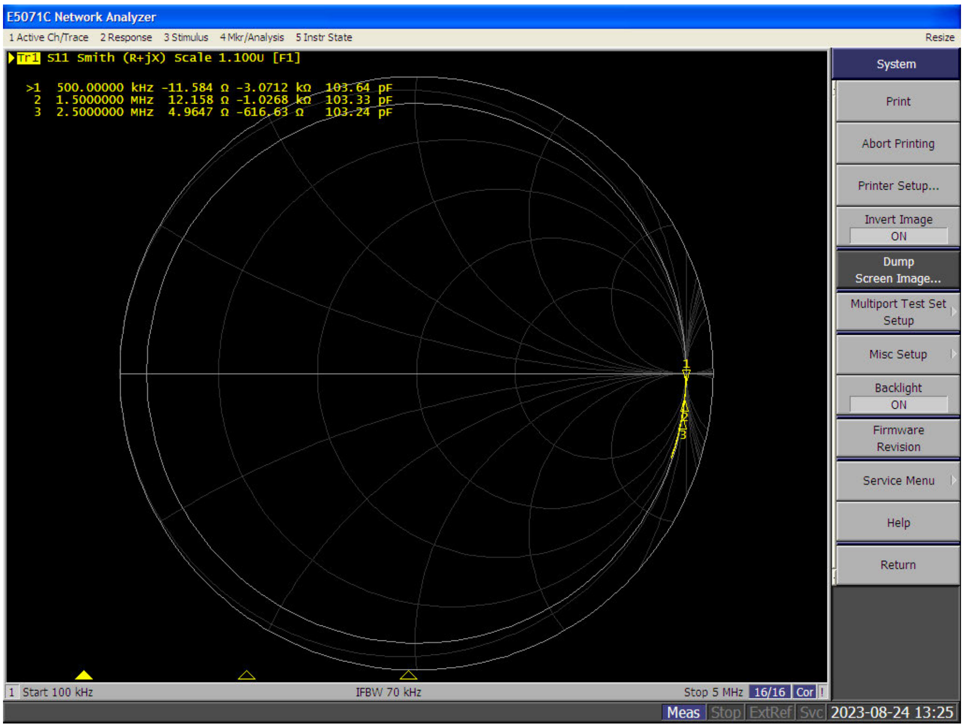

E5071C Network Analyzer

```
Tr1 S11 Smith (R+jX) Scale 1.100U [F1]

 >1  500.00000 kHz -11.584 Ω -3.0712 kΩ  103.64 pF
  2  1.5000000 MHz  12.158 Ω -1.0268 kΩ  103.33 pF
  3  2.5000000 MHz  4.9647 Ω -616.63 Ω   103.24 pF
```

1 Start 100 kHz IFBW 70 kHz Stop 5 MHz 16/16 Cor !

2023-08-24 13:25

Figure 86 PCB Sensor Soil Removed Smith Chart

9.4. Prototype Interface

9.4.1. Test Setup

The Prototype Interface was connected to the PR36-12 DC power supply via J4, set to 10 Vdc. The Digital Storage Oscilloscope (DSO) and Universal Counter were connected to the output SMA connector J2, via an SMA to BNC Coaxial cable BNC-Tee and additional BNC-BNC coaxial cable. The test configuration is shown in Figure 88.

Capacitance was added to the Prototype Interface via an SMA-BNC-Binding Post adapter, shown in Figure 89. The capacitor's capacitance values were tested and recorded using the U1733C LCR meter prior to use.

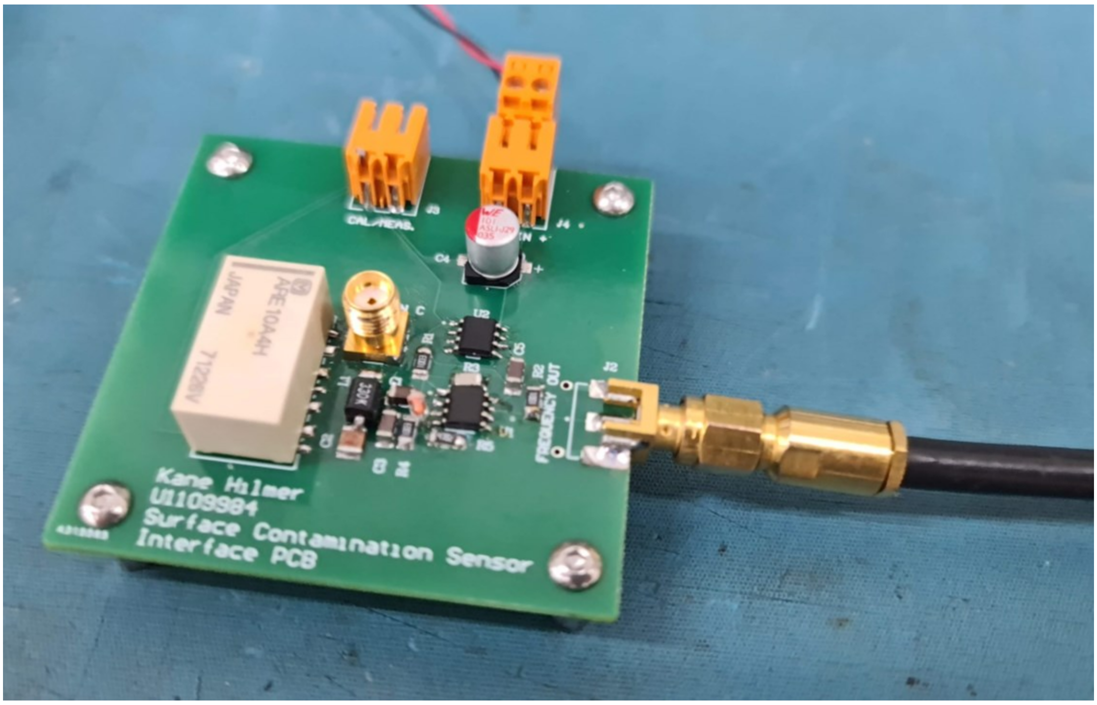

Figure 87 Modified Prototype Interface PCB

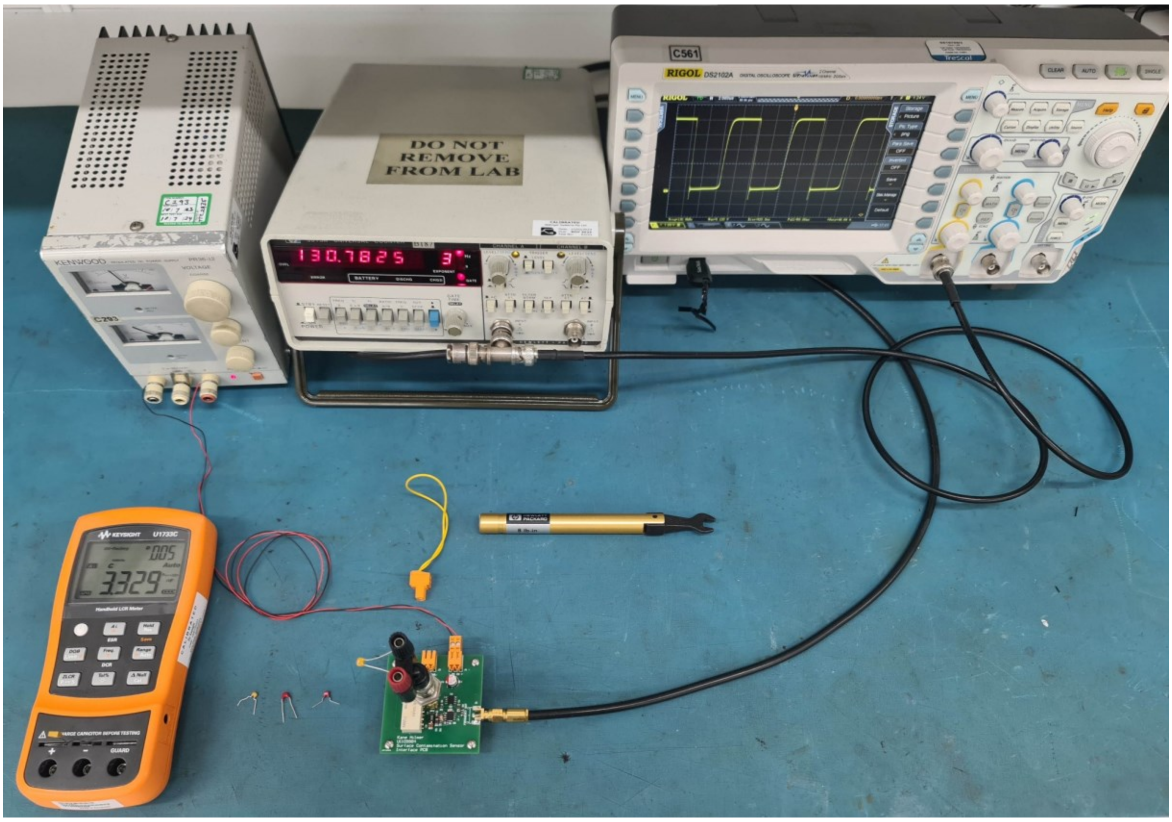

Figure 88 Prototype Interface Test Equipment

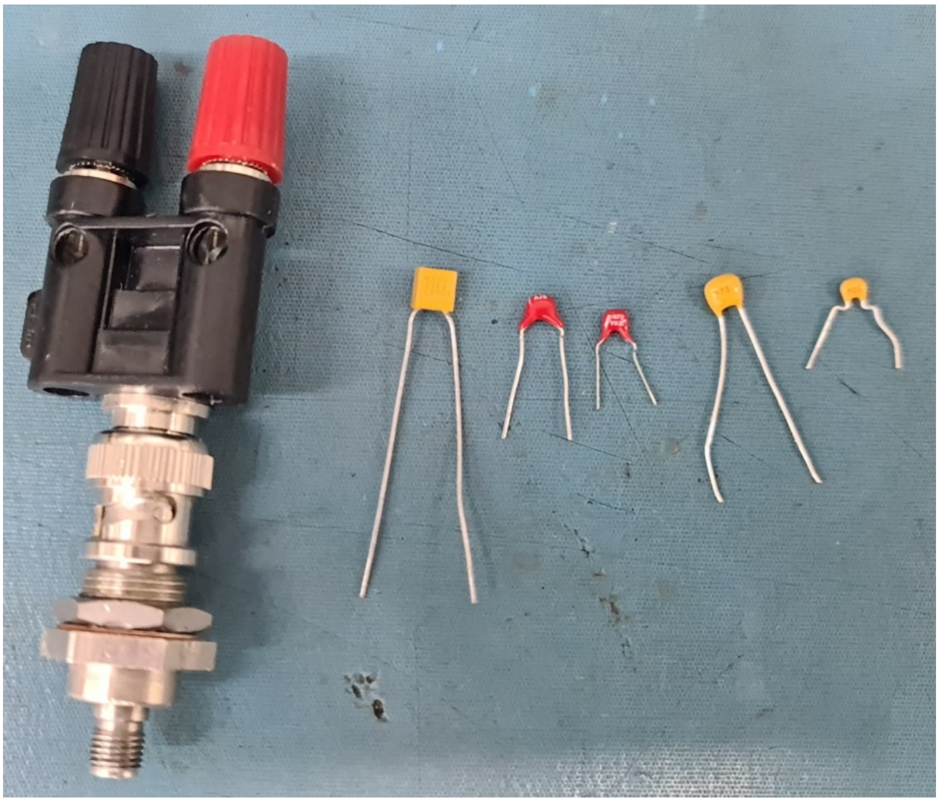

Figure 89 Test Capacitors and Adapter

9.4.2. *Testing*

With the modifications described in section 7.5 Interface Circuit Post-Manufacture Review complete, the output of the Prototype Interface PCB was tested to be stable.

With the configuration of the test equipment shown in Figure 90, testing of the Prototype Interface using the internal calibration capacitor and known external capacitors was conducted.

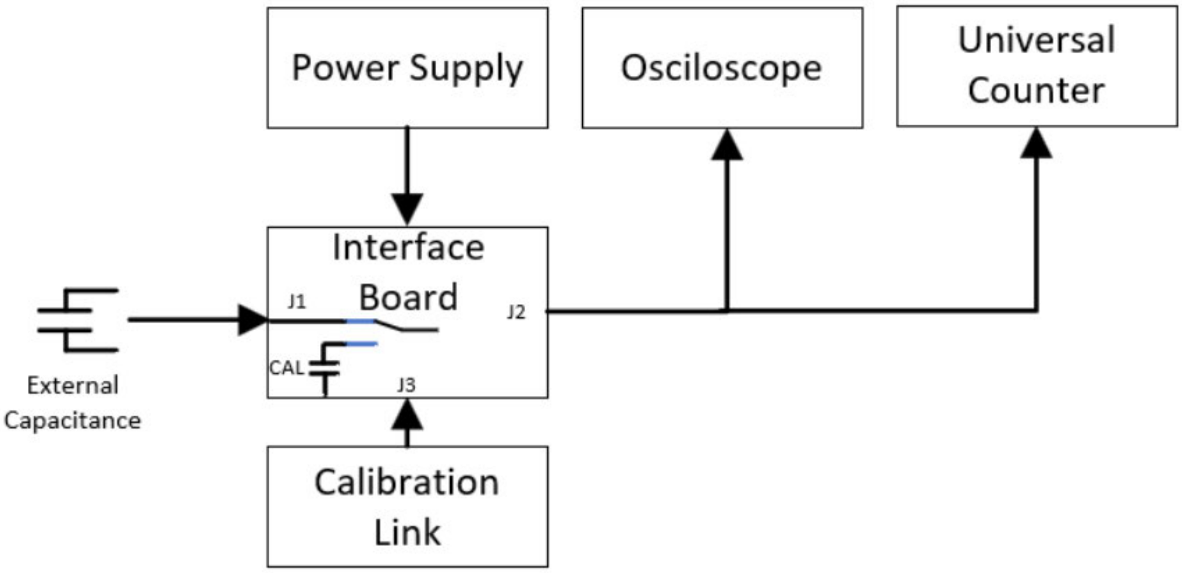

Figure 90 Interface Circuit Test Configuration Block Diagram

A link was installed in J3 to enable the 'calibration' mode of operation. No connection to J1 was completed at this time.

The power supply was powered-on, and the current monitored to ensure that no short circuits, incorrect polarity or other faults were present.

The internal voltage supply was checked using the Digital Multimeter. The connection to the Oscilloscope and Universal Counter was completed.

The output of the Prototype Interface was monitored on the DSO for expected operation or aberrations. The universal counter was adjusted for correct triggering and stable display.

9.4.3. Calibration Capacitor

With the J3 link installed, the on-board calibration capacitor C2 is placed in circuit. The waveform for the calibration capacitor is shown in Figure 91. Frequency results from the Universal Counter are available in Table 36.

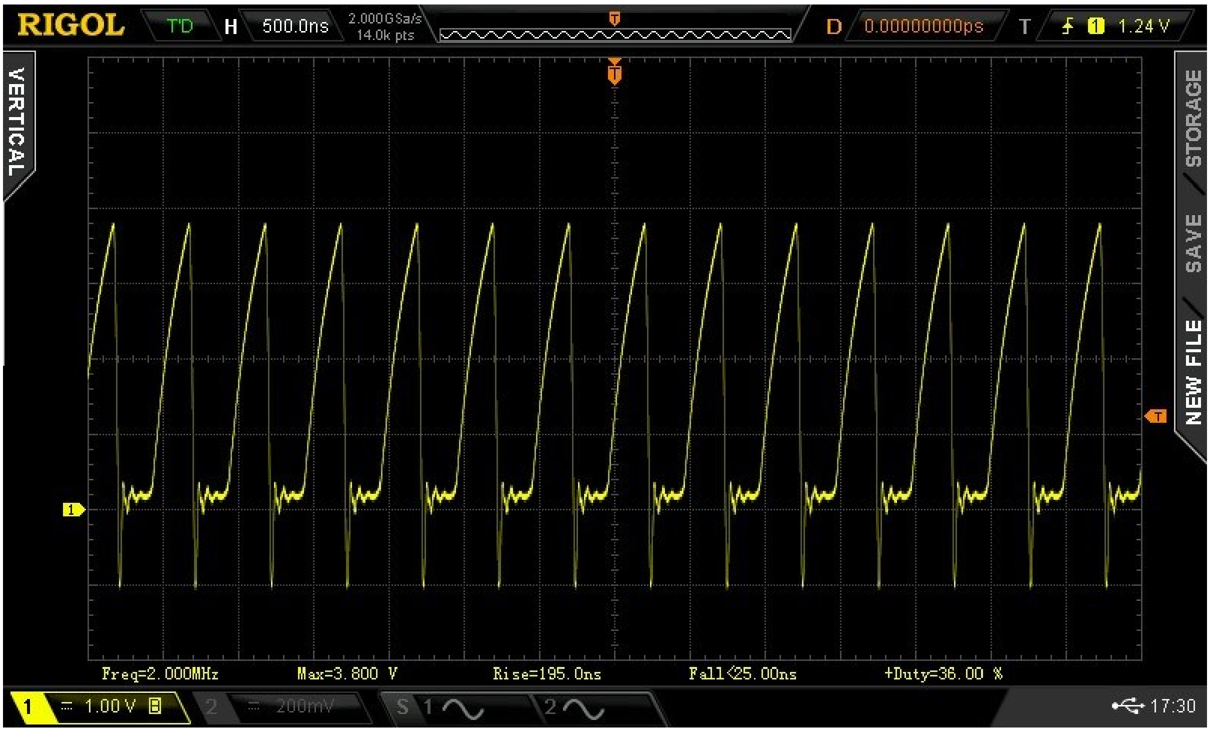

Figure 91 Interface Circuit Calibration Output

9.4.4. External Capacitors

Multiple fixed capacitors were used to establish the performance of the Prototype Interface Circuit. Before measuring the capacitance connected to J1, the link installed into J3 was first removed.

The capacitors were first measured in the LCR Meter, prior to being fitted to the binding posts, shown in Figure 89 Test Capacitors and Adapter. Each capacitor was recorded for labelled capacitance, measured capacitance, and Interface PCB output frequency. Frequency results from the Universal Counter are available in Table 35.

9.5. Sensor System

Once testing and characterisation of the PCB sensor element and Prototype Interface was complete, the individual elements of the sensor system were combined to form the completed sensor system.

The clean PCB Sensor was coupled to the Prototype Interface using an SMA male – SMA male adapter, positioned to allow the introduction of contaminants onto the PCB surface. Frequency from the Universal Counter results are available in Table 37.

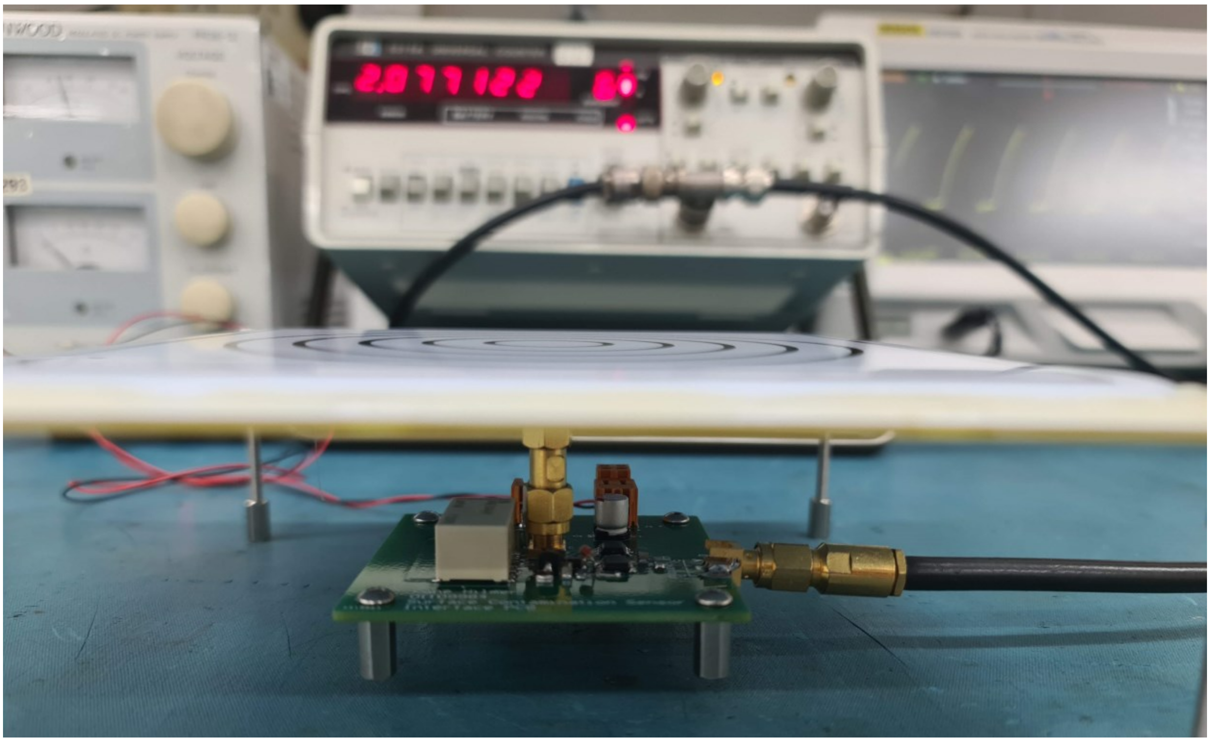

Figure 92 Sensor and Prototype Interface Board – Water on Surface

9.5.1. Calibration Capacitance

The calibration link was installed once again, with the output of the Prototype Interface monitored by the DSO and Frequency counter. This output was compared to the Prototype Interface output alone. Frequency results from the Universal Counter are available in Table 37.

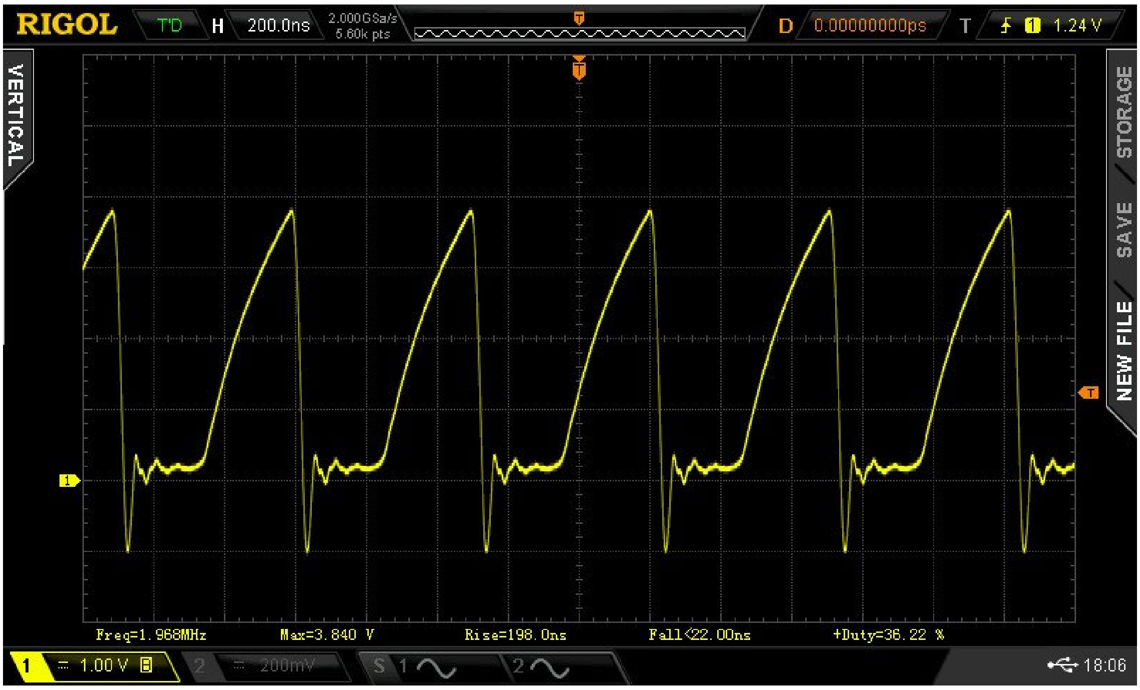

Figure 93 Interface Circuit Calibration Capacitor Output Waveform

9.5.2. Clean Sensor

The calibration link was removed, and the output of the Prototype Interface monitored and recorded. Frequency from the Universal Counter results are available in Table 37.

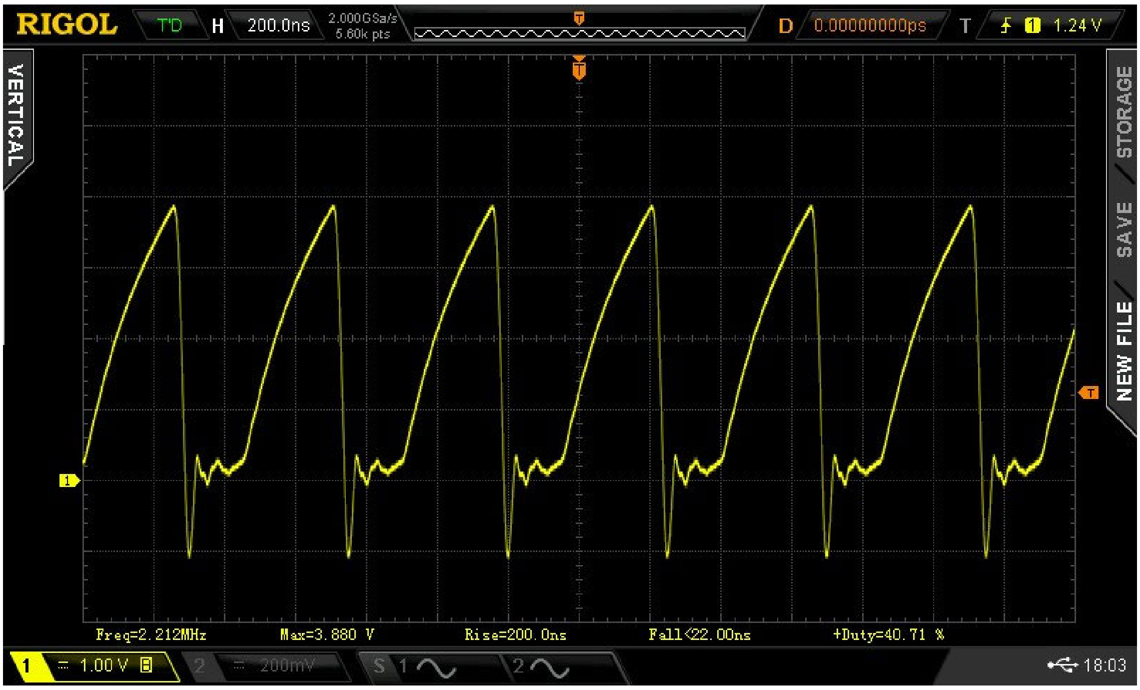

Figure 94 Interface Circuit Clean Sensor Output Waveform

9.5.3. Wet Sensor

Water was added to the surface of the PCB Sensor, sufficient to form a complete layer over the surface. The output of the Prototype Interface was monitored and recorded, and the Oscilloscope display is shown in Figure 95. Frequency results from the Universal Counter are available in Table 37.

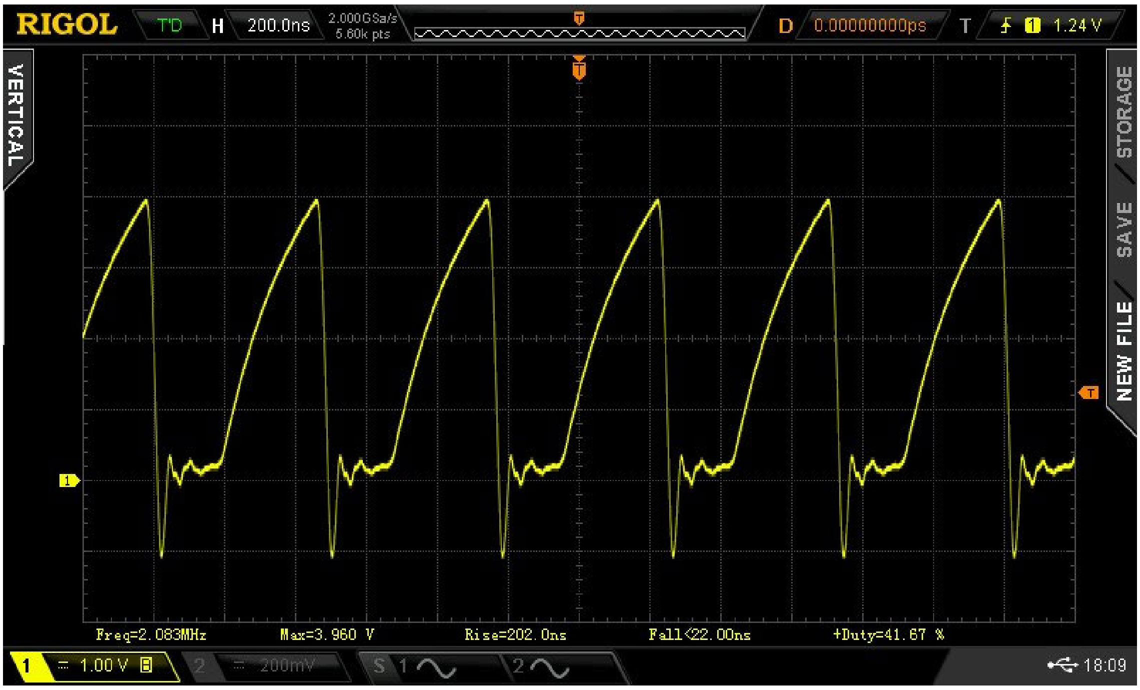

Freq=2.083MHz Max=3.960 V Rise=202.0ns Fall<22.00ns +Duty=41.67 %

Figure 95 Interface Circuit Wet Sensor Output Waveform

10. Results Summary

The data collected from testing the PCB Sensor Element and Interface Circuit are shown in Table 27 through Table 37.

For known capacitance measurements, the calculated frequency using formula 7-3 are also given.

10.1. Clean PCB Sensor Element VNA

The results collected from the VNA measurement of the clean PCB Sensor are shown in Table 27.

Table 27 VNA Results – Clean PCB Sensor

Frequency	Impedance	Real	Imaginary	Capacitance
500 kHz	3139.7 Ω	14.124 Ω	-3.1397 kΩ	101.38 pF
1.5 MHz	1042.3 Ω	12.101 Ω	-1.0422 kΩ	101.80 pF
2.5 MHz	625.63 Ω	4.673 Ω	-625.61Ω	101.76 pF

10.2. Wet PCB Sensor Element VNA

The results collected from the VNA measurement of the water covered PCB Sensor are shown in Table 28.

Table 28 VNA Results – Wet PCB Sensor

Frequency	Impedance	Real	Imaginary	Capacitance
500 kHz	2530.6 Ω	28.604 Ω	-2.5304 kΩ	125.8 pF
1.5 MHz	849.7 Ω	21.076 Ω	-849.39 Ω	124.92 pF
2.5 MHz	513.1 Ω	12.020 Ω	-512.97 Ω	124.10 pF

10.3. Dry Soil PCB Sensor Element VNA

The results collected from the VNA measurement of the PCB Sensor when covered in dry soil are shown in Table 29.

Table 29 VNA Results – Dry Soil PCB Sensor

Frequency	Impedance	Real	Imaginary	Capacitance
500 kHz	3049.2 Ω	13.143 Ω	-3.0492 kΩ	104.39 pF
1.5 MHz	1019.6 Ω	14.301 Ω	-1.0195 kΩ	104.07 pF
2.5 MHz	612.9 Ω	6.4910 Ω	-612.85Ω	103.88 pF

10.4. Wet Soil PCB Sensor Element VNA

The results collected from the VNA measurement of the PCB Sensor when covered in soil that was then made wet using tap water are shown in Table 30.

Table 30 VNA Results – Wet Soil PCB Sensor

Frequency	Impedance	Real	Imaginary	Capacitance
500 kHz	2589.8 Ω	11.426 Ω	-2.5898 kΩ	122.91 pF
1.5 MHz	871.1 Ω	17.650 Ω	-870.87 Ω	121.84 pF
2.5 MHz	524.7 Ω	10.693 Ω	-524.61 Ω	121.35 pF

10.5. Wet Deposition Soil PCB Sensor Element VNA

The results collected from the VNA measurement of the PCB Sensor when covered in soil that was deposited wet and then dried are shown in Table 31.

Table 31 VNA Results – Wet Deposition PCB Sensor

Frequency	Impedance	Real	Imaginary	Capacitance
500 kHz	3071.2 Ω	11.584 Ω	-3.0712 kΩ	103.64 pF
1.5 MHz	1026.9 Ω	12.158 Ω	-1.0268 kΩ	103.33 pF
2.5 MHz	616.7 Ω	4.9647 Ω	-616.63Ω	103.24 pF

10.6. Soil Removed PCB Sensor Element VNA

The results collected from the VNA measurement of the PCB Sensor after wet deposited soil was mechanically removed from the sensor are shown in Table 32.

Table 32 VNA Results – Soil Removed PCB Sensor

Frequency	Impedance	Real	Imaginary	Capacitance
500 kHz	3128.9 Ω	14.799 Ω	-3.1289 kΩ	101.73 pF
1.5 MHz	1041.3 Ω	10.502 Ω	-1.0412 kΩ	101.90 pF
2.5 MHz	625.4 Ω	3.9295 Ω	-625.34Ω	101.80 pF

10.7. Graphical Summary of VNA Measurements

A graphical representation of the VNA measurements is shown in Figure 96, where the difference in capacitance for the three frequencies recorded highlights the change in capacitance for the five contaminants plus clean PCB Sensor element. The higher permittivity components show a much larger capacitance change, as predicted by the FDM analysis.

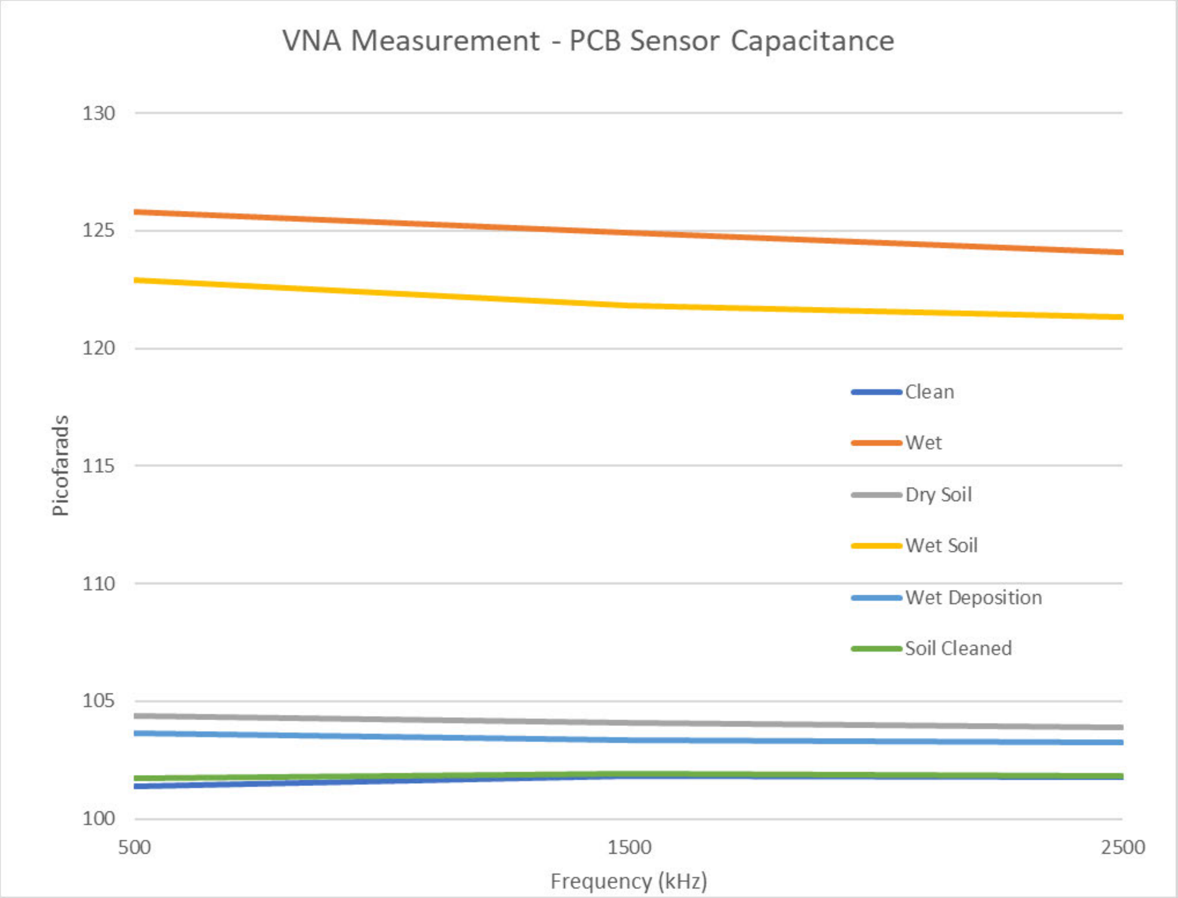

Figure 96 PCB Sensor Capacitance Line Plot

10.8. Clean PCB Sensor Element – LCR Meter

The LCR Meter results for the clean PCB Sensor are shown in Table 33. The LCR meter was nulled prior to the connection of the PCB Sensor.

Table 33 LCR Meter Results – Clean PCB Sensor

Frequency	Capacitance (pF)
100 kHz	114.58

10.9. Wet PCB Sensor Element – LCR Meter

The LCR Meter results for the PCB Senor covered in a layer of tap water are shown in Table 34.

Table 34 LCR Meter Results – Wet PCB Sensor

Frequency	Capacitance (pF)
100 kHz	135.60

10.10. Prototype Interface Fixed Capacitor

The fixed capacitor testing results of the Prototype Interface are shown in Table 35. The labelled value and LCR Meter measured values are given, as well as the measured output frequency and formula calculated frequency are shown. The results demonstrate the Prototype Interface having a changing output response to a change in input capacitance. The difference in output frequency is explained by stray capacitance that exists on the test apparatus and intrinsic to the PCB fabrication.

Table 35 Interface Circuit Results – Fixed Capacitor

Label Cap. (pF)	Measured Cap. (pF)	Output Freq. (kHz)	Formula (kHz)	Difference
150	150.44	1936.46	2251.327	86.0%
180	178.76	1818.11	2065.310	88.0%
820	785	958.12	985.5655	97.2%
3300	3.329	484.33	478.5898	101.2%
4700	4381	439.33	417.1898	105.3%
47000	47520	130.78	126.6724	103.2%

10.11. Prototype Interface Calibration Capacitor

The internal capacitor of the Prototype Interface was set via the connection of the calibration connection. The output frequency of the Prototype Interface is recorded in Table 36. Comparison the external capacitance listed in Table 35 shows consistency with the external 150pF capacitance.

Table 36 Interface Circuit Results – Calibration Capacitor

Label Cap. (pF)	Measured Cap. (pF)	Output Freq. (kHz)	Formula (kHz)	Difference
150	150	1977.11	2254.629	87.7%

The difference in output vs calculated frequency is due the stray capacitance intrinsic to the PCB fabrication. Using the formula 10-1, the capacitance correlating to the measured frequency can be found:

$$C = \frac{1}{2\pi^2 F^2 L} \tag{10-1}$$

Where: C = Capacitance F = Frequency and L = Inductance

The expected capacitance is found to be 203pF, indicating approximately 50pF of additional capacitance present in the construction of the Prototype Interface PCB.

10.12. Sensor System Test Results

The PCB Sensor and Prototype Interface PCB were coupled via a SMA male barrel as shown in Figure 92 Sensor and Prototype Interface Board – Water on Surface. The resulting output frequencies are supplied in Table 37 for the three tests conducted in the coupled state.

The change in output frequency demonstrate the ability of the sensor element to operate as a transducer in the measurement system. The change in output frequency is able to be interfaced with digital systems directly for a contamination measurement.

Table 37 Sensor System Results

Sensor	Output Freq. (kHz)
Dry	2209.2
Wet	2077.2
Dry	2220.1

11. Discussion/Improvements

11.1. Introduction Discussion

A review of the literature demonstrated that contamination of PV modules may cause a large decrease in the energy output, approaching 94% reduction for a wet ash deposition (Yusuf et al. 2020). The contamination on the surface of the PV modules can be localised, or over the entire surface, both of which can reduce the energy output (Gostein et al. 2015).

Materials and deposition methods that were previously found to contaminate PV modules were tested for their effect on the power output of PV modules by Yusuf et al. (2020). The contamination properties investigated in Yusuf et al. (2020) and Julius et al. (2015) were primarily focused on the optical transmissibility of the contamination, leaving a knowledge gap of other properties to consider.

Designing of a glass surface contamination sensor using an application of a non-contact detection method was investigated in section 2 ‘Literature Review’. The properties of the contaminants tested by Yusuf et al. (2020) were explored, focusing on non-contact measurable properties.

The permittivity of the various materials was combined in Table 2: Permittivity of Select Materials, demonstrating the range of permittivity values expected in a surface contamination of a PV module.

Techniques used to detect touch inputs on electronic displays were explored due to the comparable requirements that include the materials and physical construction. It was established that the capacitance detection method used in many touch panel technologies was a viable contamination detection method, however the challenges faced in the touch interface in seeking touch accuracy and noise reduction were actively contradictory to the requirements of a surface contamination sensor. Touch interface controllers integrate contamination-nulling circuits and algorithms developed to improve the performance of touch sensors, making them unsuitable for use in a contamination sensor system. However, it was shown that a material change on the surface of a dielectric medium (glass) will cause a capacitance change between electrodes on the opposing face of the glass due to the dielectric properties (permittivity) of the contaminating material being different to that of the air.

11.2. Simulation Discussion

The FDM sensor simulation developed and tested to calculate the capacitance of glass mounted electrodes indicates that the presence of a layer of contamination on the glass surface modifies the capacitance of electrodes placed on the opposite face of the glass pane by a calculatable and usable quantity. Dimensions and materials used in PV module construction were set in the model as the baseline simulation.

To verify the FDM analysis of the sensor cross section, a homogeneous dielectric was set in the model, so that results produced were able to be compared to ideal formula for homogeneous dielectrics in section 4.4 FDM Simulation Verification and Validation. The difference in the values, shown in Table 5 Calculation Vs Simulation Results was equated to the differences in the configuration of the electrodes, fringing fields and FDM parameters, namely the number of nodes calculated per mm.

The formula considers the ideal coplanar capacitor, with only two electrodes. As the sensor cross section consists of three, the fields developed will differ between the models. 'Fringing fields', were the electric field lines form curves at the edges of the electrodes and account for additional capacitance in a coplanar capacitor model, as described by equation 4-50, will not be accounted correctly in a three-electrode model through doubling the calculated capacitance. The value in the comparison between formula and simulation is to show that the value of simulated capacitance is consistent with permittivity change. This shows the model accounts for permittivity change and can indicate a change in permittivity in the material surrounding the electrodes.

The number of nodes used in the FDM analysis was also shown to directly impact the value of capacitance calculated. As the FDM analysis uses linear approximation of the voltage gradients present in the capacitor model, increasing the number of nodes increases the accuracy of the calculation through better approximation. Testing showed an asymptotic response of the simulation output with increasing number of nodes. This is demonstrated in Figure 28 and Figure 29.

Also shown is the processing time taken by the FDM simulation to perform the calculation, which approximates an exponential curve. A compromise between capacitance accuracy and simulation time was determined. Further testing highlighted the importance of node quantity placed between electrodes.

It was shown that the difference in capacitance values between the calculated results of a coplanar capacitance in homogeneous dielectric to those found by the FDM simulation for the same physical dimensions is dependent on node density. Table 5 Calculation Vs Simulation Results demonstrates that with constant node density, the effective number of nodes present in the space between electrodes is increased, allowing a closer approximation to the integral.

11.3. Simulation Error Discussion

During the development of the FDM simulation code, the MATLAB code output was incrementally checked and corrected, with the code verification iterated many times prior to determining its suitability. Testing was completed using smaller numbers of nodes/mm and with sensor cross sections that were able to be completed in reasonable amounts of time. Plotting and data saving was also checked and verified.

The data collection stage required the testing of 45 electrode dimensions per 23 contaminants, resulting in 1035 simulations to be completed. With each simulation taking from 2 to 100 minutes to complete, it was calculated that the simulation would require more than 21 days to complete on the available computer system.

Optimisation of the MATLAB code through vectorisation was subsequently used, which lowered the processing requirement and reduced simulation time to 15 days. The required 15 days was still determined to be too long with the possibility of re-runs and dissertation time restrictions.

The MATLAB code analyser was utilised to determine that the ‘A’ matrix generation code was performing with significant time consumed in the nested ‘for’ loops and branching to functions.

Resulting research found the parallel processing and GPU processing toolboxes for implanting efficient parallel loop iterations into the code. An attempt was made to implement both the ‘parfor’ and ‘gpuArray’/’gather’ functions for offloading of the ‘A’ matrix generation code to a more efficient process, however the dependency of multiple variables prevented the efficient implementation. A restriction to this was the time constraints in place due to the dissertation and work commitments of the author. A ‘clean’ rebuild of the MATLAB code with parallel processing integrated would likely have had greater success.

Attention was returned to the generation of the ‘A’ matrix in a traditional MATLAB environment, where testing showed incremental improvements in time with memory management, pre-initialisation of variables and reduced function calls.

Simulation time was reduced to 10 days, which was deemed acceptable. Research into the parallel processing options in MATLAB revealed that MATLAB could have multiple instances running on a single computer, with the same script operating on different data, creating a pseudo-parallel processing outcome. Testing of the code to be run in parallel, which is the same as given in the Appendix, with the restriction of material to simulated, showed the capacitance values generated were realistic and comparable to the initial code prior to optimisation. Plotting of equipotential and field lines was disabled.

Data collection was achieved in 3 days due to the use of 4 simultaneous instances on a local PC, with a single instance utilising the online MATLAB version.

Analysis of the generated data showed some unexpected results in very low permittivity materials, where negative capacitance changes were calculated. A review of the code and its output was conducted, which included the output of equipotential and field plots.

Immediately, an issue was identified which was verified by conducting several other simulations. Analysis showed that the 'A' matrix generation code was incorrect, and the data generated was not usable, producing a 'garbage' output. The result was a complete loss of the 3 days of simulation time, plus the time consumed in 'optimising' the script.

Correcting the MATLAB code was achieved by retrieving archived revisions, implementing the less efficient 'A' matrix generation, while keeping the vectorisation optimised sections. Implementation of the pseudo-parallel processing once more yielded full simulation data in an additional 4 days.

11.4. Simulation Completion

As the simulation was iterated through the electrode dimension combinations shown in Table 7 Electrode Simulation Dimensions it was determined that the number of nodes per mm used in the FDM simulation was to be set per sensor configuration. From the testing performed, the values in Table 8 Simulation Node Quantity were chosen, which maintains a minimum 30 nodes present between electrodes in the FDM mesh.

The absolute accuracy of the simulated capacitance values was determined to be not of significant consequence, due to the design goals being that of a sensor, not a capacitance meter. As such, the change in capacitance due to a material change is of interest, and having a detectable change in sensor output for a contamination change is the desired property of the sensor.

The range of capacitance the simulation showed for the sensor output was of interest, as the change in capacitance would directly determine the validity of the measurement technique.

As the FDM simulation is configured to test multiple combinations of electrode dimensions for each contaminant, finding the capacitance generated for each electrode combination. The results of the FDM simulation showed an expected result, that the contaminants with higher permittivity consistently produced larger changes in capacitance over the clean, non-contaminated sensor for all electrode dimensions tested. The results did not show a single ‘peak sensitivity’ dimension for all contaminants, however. The range of electrode dimensions found to have peak sensitivity are shown in Figure 30 Electrode Dimension Histogram.

Analysis moved to finding the result for best compromise between lower permittivity contaminants which produce lower changes in capacitance and for wider overall sensitivity. This was achieved through first normalising each of the results to the permittivity of the contamination tested before averaging the values for each electrode dimension. The result was a normalised sensitivity, shown in Figure 51 Permittivity Normalised Sensitivity, which highlighted the optimal sensor electrode dimensions at 1.5mm wide, 3.5mm centre spacing.

11.5. Design Discussion

A design for a PV module-based sensor element, utilising the width of a standard PV module was proposed, resulting in approximately 2 m of sensor length positioned along an edge of the PV module.

With the theoretical design for a PV module-based sensor simulated, a physical model was devised that utilised the concept and FDM simulation to verify the theory of the contamination detection. It was determined that due to time restrictions in producing this research, production of a glass-based senor was not fully realised. A suitable substitute to an electrode-on glass sensor construction was determined to be a PCB based sensor, due to the bonded electrodes, defined dielectric material comparable to that of glass and easy fabrication due to established software design packages and manufacturers.

11.6. Built Hardware Discussion

With the availability and properties of the PCB determined, the FDM model had the updated parameters entered. Major differences were noted in the thickness of the PCB dielectric material, FR4, and the lack of a backing material. The electrode dimensions were maintained at 1.5/3.5 mm to maintain continuity with the PV Sensor design.

The FDM model produced a meaningful capacitance value change for the PCB based sensor simulation, resulting in the design being produced in Altium Designer, as shown in Figure 57 PCB Sensor Copper Layer. The total length of electrode cross section placed on the PCB sensor was configured to that of the PV sensor, at approximately 2.04 m.

The PCB sensor was complemented with an interface circuit, devised and simulated in SPICE using MicroCap, prior to entry into Altium Designer. The design of the interface circuit is to convert the capacitance change of the sensor element into a logic-level square wave, with a frequency output representing the change in capacitance present on its input.

Construction of both the sensor PCB and interface circuit was completed prior to initial testing of the interface circuit. The interface circuit testing showed unstable operation at low capacitance values. Electronic testing of the interface circuit was conducted showing the ‘motor boating’ of the output. The observations made were in additional SPICE simulations showed that component value substitutions would produce a stable usable output. The substitutions were documented and performed.

Testing of the PCB sensor using LCR meter and VNA gave results for a clean sensor capacitance that was a close approximation the FDM simulation predicted value. Testing with water as a known permittivity contaminant modified the sensor capacitance, however the values for the application of water were different to those predicted by the simulation.

11.7. Simulated Vs Real-World Discussion

Investigation into the difference between simulated PCB Sensor capacitance and the measured when water contamination is applied began by investigating the physical dimensions of the PCB fabricated. Measurements showed that the PCB dielectric layer was approximately 1.5mm in thickness, 0.1mm less thick than that originally simulated and specified by the manufacturer.

In addition, the solder mask layer applied to the PCB was investigated for properties that may influence the capacitance of the sensor output. It was found that the dielectric properties of the solder mask are significant, with a permittivity of approximately 3.8, and is typically not included in RF circuits or those that require controlled capacitance (He & Tang 2019).

The FDM model was updated with the physical properties of the constructed PCB and set to include the permittivity of the solder mask layers, top and bottom of the dielectric FR4. The resulting calculated capacitances for ‘clean’ and ‘water’ contamination are decreased over the previous simulation. A deviation from the measured capacitance of the PCB model is still present.

The FDM simulation values of capacitance was extrapolated for 2.04 m of sensor cross section, giving a ‘clean’ sensor capacitance of 85 pF. Approximately 101 pF was measured using both the VNA and LCR meter. 16 pF of difference is within an expected range for moving from a simulated environment to the physical model.

With water contamination applied, the FDM simulation indicated an expected 1190 pF for the PCB sensor. The measured capacitance of the constructed PCB sensor is approximately 122 pF when covered with water. The deviation in capacitance for water contamination requires further investigation.

Confirmation of electrical connection using continuity measurements was conducted by confirming that both electrodes were connected to the J1 connector. Insulation was also checked by confirming no short circuits existed between electrodes.

Spot checking the sensor area with isolated contamination was used to verify a capacitance change response. While connected to the test equipment, a finger was placed on every corner of the sensor area, with the sensor confirmed to indicate the presence of the finger by an increase in capacitance.

The measurements of clean and wet contamination were repeated with the results confirmed to be reproducible. The electronic test equipment used was also checked for correct operation by substituting known capacitors and performing calibrations.

Areas of further investigation include consideration and incorporation of the inductive component of the sensor element construction, as is the conductance/resistance properties, which are not included in the FDM analysis. The shape and format of the PCB sensor may also influence the sensitivity, as Lee et al. (2014) explored, the configuration of electrodes can increase the performance of touch technologies.

11.8. Self-Reflection

Undertaking this dissertation has represented a capstone to a journey of academic and personal growth. While personal circumstances over the duration of my university career have actively obstructed the productivity and concentration typically required for successful study and learning, the completion of this work is one I am proud of.

Through the process of researching and developing the Glass Surface Contamination Sensor System, I have gained further insights into my not only the subject, but also my own strengths and weaknesses.

One aspect established is that my ability to time manage multiple aspects of work, personal and university demands has improved greatly over the duration not only university, but also the duration of this dissertation.

The demands of composing a dissertation, with research of scientific articles, journals, books, papers and websites created challenges. Determining the relevance, appropriateness and legitimacy of some sources was challenging. I also struggled to organise the mass of information I had obtained to compose a meaningful and well-presented paper.

I recognise an area of improvement for myself when it comes to this area of writing, as the temptation to skip the research and review to dive into the work of designing and testing is one that needs to be tempered. I believe my approach to the work contained in this dissertation has allowed me to develop this further, with the benefit of my literature review allowing me to progress in my project much further than if I were to start from scratch.

My skills at adapting and pivoting around challenges was also tested in this project, with the challenges of failed simulations and manufacturing ‘differences’ creating obstacles requiring overcoming.

I found that feedback from multiple sources, who read this dissertation in various stages of completion, offered consistent advice that highlighted my tendency to over-explain or repeat myself. As such a concise writing style is one I wish to pursue further.

This dissertation has not only expanded my knowledge in electrostatics and electrical engineering, but also in project management, research, time management, adaptability, and discipline. I am excited to see what opportunities the qualifications gained by the completion of this work will bring.

12. Conclusion

This dissertation has described the research, development, design, build and testing of a glass surface contamination sensor. Testing of the build model showed that it was able to detect a variety of surface contaminants.

The testing results show that the detection of surface contamination on a glass surface using bonded electrodes is possible.

The application of the design to the real-world, such as integration into PV modules, hot water systems, windowpanes, or by extension to any surface with dielectric properties is plausible due to the development methodology employed.

Future work that is beyond the scope of this dissertation is possible to further develop and test the Glass Surface Contamination Sensor. The continued review of the FDM simulation model while testing of physical models with parameters developed from the simulation will verify the model’s validity.

A full-scale implementation of a sensor into a PV module would allow the complete real-world testing of the sensor in the primary use-case. Investigation of temperature, stray capacitance, resistance and inductance to implemented designs will improve the understanding of the sensor system.

REFERENCES

Al-Qadi, IL, Hazim, O. A., Su, W., & Riad, S. M. 1995, 'Dielectric Properties of Portland Cement Concrete at Low Radio Frequencies. ', *Journal of Materials in Civil Engineering*.

Amara, CB, Hammami, H & Fakhfakh, S 2019, 'Effect of iron oxide on the electrical conductivity of soda-lime silicate glasses by dielectric spectroscopy', *Journal of Materials Science: Materials in Electronics*, vol. 30, pp. 13543-55.

Atmel 2013, *Atmel AT42QT1040 Four-key QTouch® Touch Sensor IC DATASHEET*.

Barrett, G & Omote, R 2010, 'Projected-Capacitive Touch Technology', *Information Display*, vol. 26, no. 3, pp. 16-21.

Bentley, JP 2005, *Principles of Measurement Systems*, 4th edn, Pearson Education Limited.

Bramley, A 1928, 'Dielectric constant of aqueous solutions of sodium chloride', *Journal of the Franklin Institute*, vol. 205, no. 5, pp. 649-57.

Buerhop-Lutz, C, Stroyuk, O, Pickel, T, Winkler, T, Hauch, J & Peters, IM 2021, 'PV modules and their backsheets - A case study of a Multi-MW PV power station', *Solar Energy Materials and Solar Cells*, vol. 231, p. 111295.

Ellison, C, McKeown, MS, Trabelsi, S & Boldor, D 2017, 'Dielectric Properties of Biomass/Biochar Mixtures at Microwave Frequencies', *Energies*, vol. 10, no. 4, p. 502.

Figgis, B, Bermudez, V & Lopez Garcia, J 2023, 'PV module vibration by robotic cleaning', *Solar Energy*, vol. 250, pp. 168-72.

Gonzalez, G 2006, *Foundations of Oscillator Circuit Design*, Artech House, Norwood, UNITED STATES.

Gostein, M, Düster, T & Thuman, C 2015, 'Accurately measuring PV soiling losses with soiling station employing module power measurements', *2015 IEEE 42nd Photovoltaic Specialist Conference (PVSC)*, IEEE, pp. 1-4.

He, H & Tang, R 2019, 'Effect of Permittivity and Dissipation Factor of Solder Mask upon Measured Loss'.

Heckt, N 2014, *L/C Meter IIB Instruction Manual*, http://web.archive.org/web/20140701082352/http://aade.com/manuals/lcm2b%20kit.pdf>.

Hewlett-Packard Company 1992, *Basics of Measuring the Dielectric Properties of Materials*, Hewlett-Packard Company.

IEA 2022, *World Energy Investment 2022*, IEA, Paris, https://www.iea.org/reports/world-energy-investment-2022>.

Jesch, RL 1978, *Dielectric Measurements of Five Different Soil Textural Types as Functions of Frequency and Moisture Content*, U.S Department of Commerce.

Julius, T, David, P, Jonathan, W, Tania, U & Trevor, P 2015, 'The contribution of dust to performance degradation of PV modules in a temperate climate zone', *Solar Energy*, vol. 120, pp. 147-57.

Korevaar, M, Mes, J, Nepal, P, Snijders, G & van Mechelen, X 2017, 'Novel soiling detection system for solar panels', *33rd European Photovoltaic Solar Energy Conference and Exhibition*, pp. 2349-51.

Lee, J, Cole, MT, Lai, JCS & Nathan, A 2014, 'An Analysis of Electrode Patterns in Capacitive Touch Screen Panels', *Journal of Display Technology*, vol. 10, no. 5, pp. 362-6.

Martinez, A & Byrnes, AP 2001, 'Modeling dielectric-constant values of geologic materials: An aid to ground-penetrating radar data collection and interpretation', *Current Research in Earth Sciences*, pp. 1-16.

Maryott, CGMaAA 1956, 'Dielectric Constant of Water from 0 0 to 1000 C', *Journal of Research of the National Bureau of Standards*, vol. 56.

Maxwell, I 2007, 'An overview of optical-touch technologies', *Information Display*, vol. 23, no. 12, p. 26.

Microchip 2015, *MTCH6303 Projected Capacitive Touch Controller Data Sheet*, Microchip.

Nagel, JR 2011, 'Solving the generalized Poisson equation using the finite-difference method (FDM)', *Lecture Notes, Dept. of Electrical and Computer Engineering, University of Utah*.

Nam, HA-O, Seol, KH, Lee, J, Cho, H & Jung, SW 2021, 'Review of Capacitive Touchscreen Technologies: Overview, Research Trends, and Machine Learning Approaches. LID - 10.3390/s21144776 [doi] LID - 4776', no. 1424-8220 (Electronic).

Nelson, S 2005, 'Density-Permittivity Relationships for Powdered and Granular Materials', *Instrumentation and Measurement, IEEE Transactions on*, vol. 54, pp. 2033-40.

Ozemoya, A, Swart, J, Pienaar, C & Schoeman, R 2013, 'Factors impacting on the surface temperature of a PV panel', *Sensors*, vol. 100, p. 12.

Paul, CR 2008, *Analysis of Multiconductor Transmission Lines*, John Wiley & Sons, Inc. .

Raghavendra, S, Raibagkar, R & Kulkarni, AB 2002, 'Dielectric properties of fly ash', *Bulletin of Materials Science - BULL MATER SCI*, vol. 25, pp. 37-9.

Rahaman, M, Chaki, TK & Khastgir, D 2012, 'Consideration of interface polarization in the modeling of dielectric property for ethylene vinyl acetate

(EVA)/polyaniline conductive composites prepared through in-situ polymerization of aniline in EVA matrix', *European Polymer Journal*, vol. 48, no. 7, pp. 1241-8.

Sihvola, A 2000, 'Mixing Rules with Complex Dielectric Coefficients', *Subsurface Sensing Technologies and Applications*, vol. 1, no. 4, pp. 393-415.

Smestad, GP, Germer, TA, Alrashidi, H, Fernández, EF, Dey, S, Brahma, H, Sarmah, N, Ghosh, A, Sellami, N, Hassan, IAI, Desouky, M, Kasry, A, Pesala, B, Sundaram, S, Almonacid, F, Reddy, KS, Mallick, TK & Micheli, L 2020, 'Modelling photovoltaic soiling losses through optical characterization', *Scientific Reports*, vol. 10, no. 1, p. 58.

Solar Choice 2022, *Solar Panel Sizes and Dimensions*, viewed 08/08/2023, <https://www.solarchoice.net.au/products/panels/size/#:~:text=Standard%20residential%20solar%20panels%20contain,tall%20x%201.0m%20wide.>.

Spain, E & Venkatanarayanan, A 2014, '13.02 - Review of Physical Principles of Sensing and Types of Sensing Materials', in S Hashmi, et al. (eds), *Comprehensive Materials Processing*, Elsevier, Oxford, pp. 5-46.

Supe, H, Avtar, R, Singh, D, Gupta, A, Yunus, AP, Dou, J, A Ravankar, A, Mohan, G, Chapagain, SK & Sharma, V 2020, 'Google earth engine for the detection of soiling on photovoltaic solar panels in arid environments', *Remote Sensing*, vol. 12, no. 9, p. 1466.

Sydenham, PH 1989, *Introduction to measurement science and engineering / P.H. Sydenham, N.H. Hancock, and R. Thorn*, Wiley, Chichester ; New York.

USQ 2021, 'ELE4109 Measurement Science and Instrument Engineering Study Book'.

USQ 2022, *ELE4605 Fields and Waves Study Book*, University of Southern Queensland.

Walker, G 2014, 'Part 1: Fundamentals of Projected-Capacitive Touch Technology', *Display Week '14*: *Proceedings of the Display Week '14*.

Xu, X, Wang, H, Qu, X, Cheng, L, Cai, B & Peng, G 2022, 'Study on the dielectric properties and dielectric constant model of laterite', *Frontiers in Earth Science*, vol. 10, p. 1035692.

Yusuf, NC, Aritra, G, Senthilarasu, S & Tapas, KM 2020, 'An analytical indoor experimental study on the effect of soiling on PV, focusing on dust properties and PV surface material', *Solar Energy*, vol. 203, pp. 46-68.

APPENDIX A PROJECT SPECIFICATION

ENG4111/4112 Research Project

Project Specification

For:	Kane Hilmer
Title:	Glass Surface Contamination Sensor System: Design and Verification
Major:	Electrical and Electronic Engineering
Supervisor:	Andrew Maxwell
Enrolment:	ENG4111 – EXT S1,2023 ENG4122 – EXT S2,2023
Project Aim:	To design and verify a sensor system suitable for detecting contamination of a glass plate.
Programme:	Version 2, 11 April 2023

1. Literature review of existing sensor designs and solutions.
2. Conduct a MPA for the system configuration and derive a sensor design.
3. Generate & Simulate MATLAB® model for sensor.
4. Design physical sensor based on MATLAB simulation results.
5. Simulate and verify sensor control circuit and generate schematic.
6. Prepare draft dissertation.
7. Prepare & present Professional Practice 2 presentation.
8. Complete and submit dissertation.

If time and resources permit:

9. Have sensor manufactured & control circuit fabricated.
10. Construct control circuit & testing apparatus.
11. Verify operation of sensor circuit.
12. Collect and prepare sample media, perform experiments, and collect data.
13. Analyse results.
14. Develop a user interface for the sensor control circuit.
15. Derive potential measurement and reporting algorithms for real-world use.

Project Plan

Task/ Activity	Semester 1 - Eng 4111																				Semester 2 - ENG4112														
						Recess												Recess													Recess				
	Week (Commencing 20 Feb. 2023)																																		
	1	2	3	4	5	6	7	8	9	10	11	12	13	14	15	16	17	18	19	20	21	22	23	24	25	26	27	28	29	30	31	32	33	34	35
Project Preperation																																			
Literature Review	X	X	X	X	X	X	X	X	X	X	X	X	X	X	X	X	X	X	X	X	X	X	X	X	X	X	X								
Sensor Design																																			
Conduct MPA					X	X	X																												
Simulation, Design & Manufacture																																			
Sensor Model & Simulation								X	X	X	X																								
Sensor Design											X	X																							
Control Circuit Simulation& Schematic												X	X	X																					
Sensor & Circuit Manufacture														X	X	X																			
Construct Control Circuit & Apperatus																	X	X	X																
Data																																			
Verify Operation																			X																
Collect and Prep. Media						X	X				X	X							X	X															
Collect Data																					X	X	X												
Dissertation																																			
Prep. Draft Dissertation					X	X	X	X	X	X	X	X	X	X	X	X	X	X	X	X	X	X	X	X	X	X									
Analyse Results																								X	X	X	X	X	X						
Prep and Present PP2 Pres.																												X	X	X					
Complete Dissertation																														X	X	X			

Project Resources

As the project progresses through the design, simulation, design & manufacture, and data collection stages, the resources required to complete each also evolves. The conceptualised requirements are listed below:

Sensor Design

During the sensor design stage of the project, resources required consist of a computer system and software. The computer system must be capable of operating the software packages

- Altium Designer®,
- Microcap®,
- MATLAB®
- Microsoft® Office application suite.

Licencing and access to the software is available through site licencing of the University of Southern Queensland.

Simulation, Design & Manufacture

For the Simulation, Design & Manufacture stage of the project, the same software suite will be required, however with the added need for manufacture and assembly, tooling and materials will be required. Assembling of the control circuit will require soldering facilities, including:

- Surface Mount Device (SMD) and through-hole tools.
- ‘Hot Plate’ soldering and temperature-controlled soldering pencils and consumables
- Purchased electronic components.

As the tooling and consumables are commonly accessible in an electronics laboratory, the author has ready access to all tooling required.

Data

The data collection and V&V stage of the project will require, in addition to the tooling from the manufacturing stage and computer system from the design stage, the following electronic test equipment:

- DC power supplies.
- Digital Storage Oscilloscope.
- Frequency Counter.
- Digital Multimeter.
- LCR bridge.
- Associated interfacing hardware.
- Precision digital scales.

Test media, such as demineralised water, and contamination samples will be required to verify operation. soiling material handling equipment, digital scales and the completed and verified sensor system and associated electronic equipment.

Equipment required for the collection, preparation and application of the soiling samples will be purchased prior to the commencement of the data collection phase.

APPENDIX B RISK ASSESMENT

A risk assessment was conducted on the proposed project. It was found to have few in quantity and low risk activities required to complete the project. A Safety Risk Management Plan (SRMP) was completed and available below.

Quality Assurance Plan

To limit inaccuracies in the collection of data and for confidence in the data and results, the following tasks are to be completed over the duration of the project:

- Compare measured data from the expected results from simulation prediction.
- Repeat measurements of each sample wet and dry deposition density 5 times.
- Use instruments with valid calibration.
- Supervisor review of procedure, sensor development, results collection, and dissertation completion.

Safety Risk Management Plan

UNIVERSITY OF SOUTHERN QUEENSLAND

University of Southern Queensland **Offline Version**

USQ Safety Risk Management System

Note: This is the offline version of the Safety Risk Management System (SRMS) Risk Management Plan (RMP) and is only to be used for planning and drafting sessions, and when working in remote areas or on field activities. It

Safety Risk Management Plan – Offline Version			
Assessment Title:	Glass Surface Contamination Sensor System: Design and Verification	Assessment Date:	1/08/2023
Workplace (Division/Faculty/Section):	Electrical/ Electronic Engineering	Review Date:(5 Years Max)	1/10/2023
Context			
Description:			
What is the task/event/purchase/project/procedure?	Design, Manufacture and Evaluate Sensor System		
Why is it being conducted?	Capstone research project		
Where is it being conducted?	Home/Bellinger Systems (Work)		
Course code (if applicable)	ENG4112	Chemical name (if applicable)	N/A
What other nominal conditions?			
Personnel involved	Kane Hilmer		
Equipment	Electronic Instruments, Equipment and Tools. Samples of soil		
Environment	Inside/Laboratory, outdoor for sample collection.		

Other	-
Briefly explain the procedure/process	Constructing, testing and evaluating electronic circuit, handling of soil.
Assessment Team - who is conducting the assessment?	
Assessor(s)	A/Prof Andrew Maxwell
Others consulted:	-

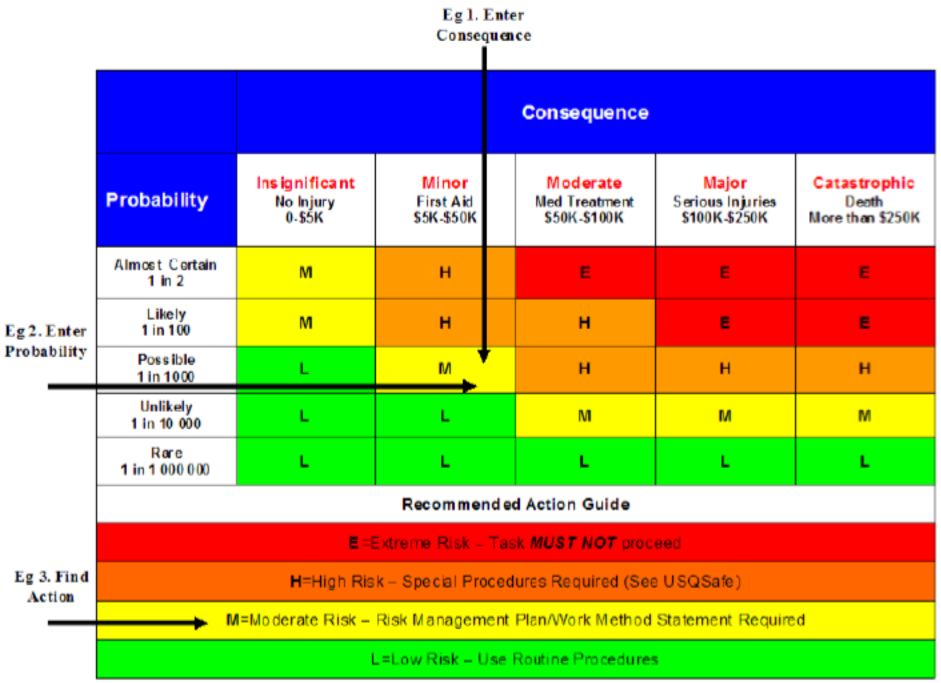

Eg 1. Enter Consequence

Eg 2. Enter Probability

Eg 3. Find Action

Probability	Consequence				
	Insignificant No Injury 0-$5K	Minor First Aid $5K-$50K	Moderate Med Treatment $50K-$100K	Major Serious Injuries $100K-$250K	Catastrophic Death More than $250K
Almost Certain 1 in 2	M	H	E	E	E
Likely 1 in 100	M	H	H	E	E
Possible 1 in 1000	L	M	H	H	H
Unlikely 1 in 10 000	L	L	M	M	M
Rare 1 in 1 000 000	L	L	L	L	L

Recommended Action Guide

E=Extreme Risk – Task ***MUST NOT*** proceed

H=High Risk – Special Procedures Required (See USQSafe)

M=Moderate Risk – Risk Management Plan/Work Method Statement Required

L=Low Risk – Use Routine Procedures

Step 1 (cont)	Step 2	Step 2a	Step 2b	Step 3			Step 4				
Hazards: From step 1 or more if identified	***The Risk:*** What can happen if exposed to the hazard without existing controls in place?	***Consequence:*** What is the harm that can be caused by the hazard without existing controls in place?	***Existing Controls:*** What are the existing controls that are already in place?	***Risk Assessment:*** Consequence x Probability = Risk Level			***Additional controls:*** Enter additional controls if required to reduce the risk level	***Risk assessment with additional controls:***			
				Probability	**Risk Level**	**ALARP? Yes/no**		**Consequence**	**Probability**	**Risk Level**	**ALARP? Yes/no**
Example											
Working in temperatures over 35º C	Heat stress/heat stroke/exhaustion leading to serious personal injury/death	catastrophic	Regular breaks, chilled water available, loose clothing, fatigue management policy.	possible	high	No	temporary shade shelters, essential tasks only, close supervision, buddy system	catastrophic	unlikely	mod	Yes
Use of Soldering equipment	Burns to skin, risk of eyeinjury, inhilation offumes, exposure to lead	Minor	Training, PPE, use of lead freesolder	Unlikely	Low	Yes	None	Minor	Unlikely	Low	Yes
Collecting Soiling media	Exposure to outdoor environment, exposure to organic materials	Minor	PPE (Hat, sunscreen, long sleeve/trousers, sunglasses, gloves) & collect samples during cooler parts of day	Possible	Moderate	Yes	Dust Mask	Insignificant	Possible	Low	Yes
Conducting Measurements	Exposure to organic materials, dust	Minor	PPE (dust mask, gloves	Possible	Low	Yes	None	Minor	Possible	Low	Yes
Conducting Measurements	Electrocution from electronic equipment	Major	In-date safety checks, training	Rare	Low	Yes	None	Major	Rare	Low	Yes
		Select a consequence		Select a probability	Select a Risk Level	Yes or No		Select a consequence	Select a probability	Select a Risk Level	Yes or No
		Select a consequence		Select a probability	Select a Risk Level	Yes or No		Select a consequence	Select a probability	Select a Risk Level	Yes or No
		Select a consequence		Select a probability	Select a Risk Level	Yes or No		Select a consequence	Select a probability	Select a Risk Level	Yes or No
				Select a probability	Select a Risk Level	Yes or No		Select a consequence	Select a probability	Select a Risk Level	Yes or No
				Select a probability	Select a Risk Level	Yes or No		Select a consequence	Select a probability	Select a Risk Level	Yes or No
				Select a probability	Select a Risk Level	Yes or No		Select a consequence	Select a probability	Select a Risk Level	Yes or No

Step 5 - Action Plan (for controls not already in place)

Additional controls:	*Resources:*	*Persons responsible:*	*Proposed implementation date:*
Soil collection	Dust Mask	Kane Hilmer	20/08/2023
Equipment Test & Tag Check	Visual Inspeciton	Kane Hilmer	17/08/2023
			Click here to enter a date.
			Click here to enter a date.
			Click here to enter a date.
			Click here to enter a date.
			Click here to enter a date.
			Click here to enter a date.
			Click here to enter a date.

Step 6 - Approval

Drafter’s name:	Kane Hilmer	Draft date:	1/08/2023
Drafter’s comments:	Low risk activity		
Approver’s name:		Approver’s title/position:	
Approver’s comments:			
I am satisfied that the risks are as low as reasonably practicable and that the resources required will be provided.			
Approver’s signature:		Approval date:	Click here to enter a date.

APPENDIX C MATLAB SIMULATION CODE

12.1. FDM Code

```
%***************************************************************************
% Kane Hilmer [redacted]
% Capacitance FDM Simulation
% Honors Thesis
% 08/2023
%***************************************************************************

clear all
close all
clc
PlotOn = 0;     %make plots

%***************************************************************************
% Define constants and initial variables
%***************************************************************************
% Strip width in mm
StripWidVec = [0.5 1 1.5 2 2.5 3 3.5 4];
% Strip Centre distance (Spacing = Distance-Width)
StripCentDisVec = [0.5 1 1.5 2 2.5 3 3.5 4 4.5 5];

%Contamination Permittivity
ContaminantErVec = [1 6000 1501.12 41791 10448.87 7.00 2.80 2.72 6.03 10.68...
    40.00 11.11 3.2 5.21 8.94 2.70 6.60  1.62 6.96 10.46 2.0 1.40 80];

% Glass Backing Contamination thickness in mm
GlassThick = 2.5;
BackingThick = 1;
ContaminationThick = 0.5;

% Glass Backing Air Vacuum Permittivity
GlassEr = 4;
BackingEr = 2.75;
AirEr = 1;
SimHeight = 10; % Simulation height bounds
e0 = 8.85418782e-12;

MatName = ["Clean";"Ash, Wet";"Ash, Dry";"Cement, Wet";"Cement, Dry";...
    "Charcoal, Wet";"Charcoal, Dry"; "Clay 0%"; "Clay 7%";"Clay 14%";...
    "Laterite, Wet"; "Laterite, Dry"; "Loamy 0%"; "Loamy 5%"; "Loamy 10%";...
    "Salt, Wet";"Salt, Dry"; "Sand 0%";"Sand 8%";"Sand 14%"; "Wood, Wet";...
    "Wood, Dry"; "Water"];

gnd = -1;   % define the gnd value
cond = -10; % define the conductor value

% Reset the Contaminant Values
ContaminantEr = 0;
StripWidth = 0;
StripCentreDistance = 0;

% Set the Results memory
Res = nan(length(StripCentDisVec),length(StripWidVec),length(ContaminantErVec));
ResDiff = nan(length(StripCentDisVec),length(StripWidVec),length(ContaminantErVec));
```

```
%**************************************************************************
% Iterate through all Materials and Dimensions
%**************************************************************************
% For each Contaminant
for erv = 1 : length(ContaminantErVec)
    % For each electrode Width
    for widthv = 1 : length(StripWidVec)
        %For each electrode Spacing
        for scdv = 1 : length(StripCentDisVec)
            % If there is a spacing between electrodes, continue.
            if StripWidVec(widthv) < StripCentDisVec(scdv)
                % determine the thickness from the material
                if erv == 1 || erv == 2 || erv == 4 || erv == 6 ||...
                   erv == 9 || erv == 10 || erv == 11 || erv == 14 ||...
                   erv == 15 || erv == 16 || erv == 19 || erv == 20 ||...
                   erv == 21;
                   ContaminationThick = 0.25
                else
                    ContaminationThick = 0.5
                end

% Set the script variables from the loop iteration number
% Contamination Permittivity
ContaminantEr = ContaminantErVec(erv);
% Strip width in mm
StripWidth = StripWidVec(widthv);
% Strip Centre distance (Spacing = Distance-Width)
StripCentreDistance = StripCentDisVec(scdv);
% Calculate the Electrode Seperation
Sep = StripCentreDistance - StripWidth

% Set the nodes/mm from the seperation calculation
if Sep == 0.5
        NodesPer_mm = 60
elseif  Sep == 1
        NodesPer_mm = 32
else
    NodesPer_mm = 20
end

% Determine the maximum matrix dimension.
maxDim = 2 * SimHeight * NodesPer_mm;
% allocate memory for the node, permittivity and Electric field matrices
nodeMat = zeros(maxDim , maxDim);
% Matrix of Permittivities
e = ones(maxDim-1,maxDim-1)*AirEr;
% Matrices for Electric feild in X & Y
Ex = zeros(maxDim-1,maxDim-1);
Ey = zeros(maxDim-1,maxDim-1);
disp('Taller')

%**************************************************************************
% Form the Node and Permittivity Matrices
%**************************************************************************

% Restrict the area of interest - keeping the matrix square
i = 1 : (maxDim-(2 * StripCentreDistance * NodesPer_mm))/2 - 1;
% Fill the nodes with ground outside of the analysis area
nodeMat(: , i) = gnd;
nodeMat(: , (maxDim-i)) = gnd;

% make the permittivity map for each layer
i =  (maxDim / 2) - (GlassThick * NodesPer_mm) - (ContaminationThick * ...
    NodesPer_mm): (maxDim / 2) - (GlassThick * NodesPer_mm)-1;
     e(i,:) = ContaminantEr;
i =  (maxDim / 2) - (GlassThick * NodesPer_mm) : maxDim / 2;
```

```
     e(i,:) = GlassEr;
i = (maxDim / 2) : (maxDim / 2) + (BackingThick * NodesPer_mm);
     e(i,:) = BackingEr;

% Draw a perimeter of grounds in the node matrix
i = 1 : maxDim;
    nodeMat(i,1) = gnd;   % Left
    nodeMat(i,maxDim)= gnd;   % Right
i = 1 : maxDim;
    nodeMat(1,i) = gnd;   % Top Row
    nodeMat(maxDim,i) = gnd;  % Bottom Row

% Insert the Electrodes
% in the middle of the matrix
i = maxDim/2;
sym = maxDim/2;
j = 1 : (StripWidth * NodesPer_mm) / 2;    % For the side electrodes, do half width
    nodeMat(i, maxDim/2+round(StripCentreDistance*NodesPer_mm-StripWidth/2*NodesPer_mm)+j)
= gnd;
    nodeMat(i, maxDim/2-round(StripCentreDistance*NodesPer_mm-StripWidth/2*NodesPer_mm)-j)
= gnd;

j = 1 : (StripWidth * NodesPer_mm);
    nodeMat(i,(maxDim/2)+j-round((StripWidth * NodesPer_mm)/2)) = cond;

%**************************************************************************
% Assign node numbering
%**************************************************************************
count = 1;  % increment the nodes
% number the nodes - Changed to include the second potential
for i = 2 : (maxDim-1)
    for j = 2 : (maxDim-1)
        if (nodeMat(i,j) ~= cond) && (nodeMat(i,j)~=gnd)
            nodeMat(i,j) = count;
            count = count + 1;
        end
    end
end
count = count - 1;   %return to the number of entries

disp(['The number of voltage nodes calculated is: ',num2str(count)])
disp('The ''Node Matrix'' matrix is complete.')

%**************************************************************************
% Voltage Matrix Generation
%**************************************************************************
% Allocate memory for 'A' and 'b' matrices for the number of nodes.
b = sparse(count,1);
A = sparse(count,count);
% Variables used in the calculaiton
U = 0;
Ab = [0 0 0 0];
% Do timing for comparison
tic
% Begin calculaitons
% Generate the 'A' Matrix

for j = 1 : count   % for the number of nodes
    % Use NodeFill to retrieve and format variables
    [U, Ab, Ac] = NodeFill(j,nodeMat,e);
    % Set for the simultaneous equations
    A(j,j) = Ac(1);
    % Put the returned nodes from NodeFill into 'A' matrix. - forming
    % the simultaneous equaitons. If Ab is not on an edge
    if all(Ab > 0)
        A(j,Ab(1)) = Ac(2)*-1+A(j,Ab(1));
```

```
        A(j,Ab(2)) = Ac(3)*-1+A(j,Ab(2));
        A(j,Ab(3)) = Ac(4)*-1+A(j,Ab(3));
        A(j,Ab(4)) = Ac(5)*-1+A(j,Ab(4));
    else
    % For each of the returnd 5-point star outer positions, allocate to the
    % correct A matrix locaiton, with scaling.
        if Ab(1) > 0
            A(j,Ab(1)) = Ac(2)*-1+A(j,Ab(1));
        end
        if Ab(2)> 0
            A(j,Ab(2)) = Ac(3)*-1+A(j,Ab(2));
        end
        if Ab(3)> 0
            A(j,Ab(3)) = Ac(4)*-1+A(j,Ab(3));
        end
        if Ab(4)> 0
            A(j,Ab(4)) = Ac(5)*-1+A(j,Ab(4));
        end
    end
    % b vector = 0, unless a conductor.
    b (j) = U;
end
%for timing
toc
disp('The ''A'' and ''b'' matrix is complete.')

%**************************************************************************
% Voltage Matrix Generation
%**************************************************************************
% Allovate the Voltage vector
V = zeros(count,1);    % define the V vector
tic
% Find the Voltage matrix
V = A\b;    % calculate the voltages
disp('The ''V'' Vector is complete.')

% Map the voltages to the node numbers.
map = nodeMat;    % define and copy into map, the value of g
toc
for i = 1 : maxDim;     % populate the map matrix
    for j = 1 : maxDim;
        k = vReturn(nodeMat,i,j,V);
        map(i,j) = k;
    end
end

%**************************************************************************
% Contour Integraiton and Capacitance Calculaiton Section
%**************************************************************************
disp(['Calculating capacitance through contour integration'])

% Find the electric fields in the  X & Y planes by averaging the voltage
% gradients
i = 1:maxDim - 1;    %Rows
    j = 1:maxDim-1;  %Cols
        Ey1(i,j) = -(map(i+1,j)-map(i,j));
        Ex1(i,j) = -(map(i,j+1)-map(i,j));

% Find the electric fields in the  X & Y planes by averaging the voltage
% gradients
i = 1:maxDim - 2;    %Rows
    j = 1:maxDim-2;  %Cols
        Ex(i,j) = (Ex1(i,j+1) + Ex1(i,j))/2;
        Ey(i,j) = (Ey1(i+1,j) + Ey1(i,j))/2;

% Dimensions for contour intergral
```

```
vertCol = round((StripCentreDistance-StripWidth/2)*NodesPer_mm-1);
horCol = 6*NodesPer_mm;
% Define and zero the electric field sums
vertSumE  = 0;
horSumE = 0;

% Sum electric fields along the verticals
for i=sym-horCol:sym+horCol
    vertSumE = vertSumE + abs((Ex(i-1,sym-vertCol-1) * e(i-1,sym-vertCol-1)^2));
    vertSumE = vertSumE + abs((Ex(i-1,sym+vertCol-1) * e(i-1,sym+vertCol-1)^2));
end
% Sum electric fields along the horizontals
for i=sym-vertCol:sym+vertCol
    horSumE = horSumE + abs((Ey(sym-horCol-1,i-1) * e(sym-horCol-1,i-1)^2));
    horSumE = horSumE + abs((Ey(sym+horCol-1,i-1) * e(sym+horCol-1,i-1)^2));
end

% Sum the horizontal and vertical electric field components, multiply by
% the permittivity of a vacuum
qE = (horSumE+vertSumE) *e0;
% Calculate the capacitance by dividing the charge by the voltage
C = qE/10;

% Save the result of the calculation into the results matrix
Res (scdv,widthv,erv) = C
% Save the result to a spreadsheet workbook
writematrix(Res(:,:,erv),'Results.xls','Sheet',MatName(erv));
disp(['The capacitance is calculated as: ', strtrim(evalc('disp(C)')) ,' F/m'])

%*************************************************************************
% Plotting Section
%*************************************************************************
disp('Plotting now.')
% Swap the direction of the voltage map to plot correctly
map = flip(map); % Swap the top to bottom
% Determine the limits of the plotting region
plotx1 = sym - StripCentreDistance * NodesPer_mm;
plotx2 = sym + StripCentreDistance * NodesPer_mm;
plotCor = plotx2-plotx1;

% If the plotting enabled
if PlotOn ==1
    % Set a new Figure with subplots
    figure
    subplot(1,2,1)

    % Make the contour plot
    y = contour (map(1:maxDim-1,plotx1:plotx2),[10 1.5 1 0.9 0.8 0.7 0.6 0.5...
        0.4 0.3 0.2 0.1], 'ShowText' , 'on','LabelSpacing',500);
    daspect([1 1 1]);   % Set the ratio of the plots
    set(gcf,'units','points','position',[10,10,800,800]) % Positioning
    % Set the text for display on the plot
    str1 = strcat (MatName(erv), ": \epsilon _r= ",...
        num2str(ContaminantErVec(erv)));
    str2 = strcat ("Electrode Width: ", num2str(StripWidth) ,...
        " mm. Spacing: ", num2str(StripCentreDistance-StripWidth)," mm." );
    str3 = strcat ("Contam Thickness: ", num2str(ContaminationThick),...
        " mm. Cap: ",num2str(C)," F.");
    str = [str1 ; str2 ; str3];
    % Add the text to the plot
    title('Potential about conductor (V)',str)
    ylabel('Cross Section Height (mm)')
    xlabel('Cross Section Width (mm)')
    % Set the ticks & axs labels on the plot
    xticks([0 plotCor/2 plotCor])
    xticklabels({-(plotCor/2)/NodesPer_mm,'0',(plotCor/2)/NodesPer_mm});
```

```
yticks([1 (SimHeight-BackingThick)*NodesPer_mm SimHeight*NodesPer_mm ...
    (SimHeight+GlassThick)*NodesPer_mm SimHeight*2*NodesPer_mm-1]);
yticklabels({-(SimHeight) , -BackingThick , 0 , GlassThick , SimHeight});

% Put the lines for indicating the material thicknesses
yline(maxDim/2+NodesPer_mm*GlassThick+1,'--')
yline(maxDim/2+1,'--')
yline(maxDim/2-NodesPer_mm*BackingThick+1,'--')
% Put the Electrodes in
line([0;StripWidth*NodesPer_mm/2],[maxDim/2+1;maxDim/2+1],'LineWidth'...
    ,2,'Color','k')
line([plotCor-StripWidth*NodesPer_mm/2,(plotCor)],[maxDim/2+1;maxDim/2+1],...
    'LineWidth',2,'Color','k')
line([plotCor/2-StripWidth*NodesPer_mm/2,(plotCor)/2+StripWidth*NodesPer_mm/2],...
    [maxDim/2+1;maxDim/2+1],'LineWidth',2,'Color','r')
% Plot the line integration path
line([(plotCor/2- vertCol),(plotCor/2 + vertCol)],[sym+horCol;sym+horCol], ...
    'LineWidth',1,'Color','g')
line([(plotCor/2 - vertCol),(plotCor/2 + vertCol)],[sym-horCol;sym-horCol], ...
    'LineWidth',1,'Color','g')
% Vertical lines
line([(plotCor/2 - vertCol),(plotCor/2- vertCol)],[sym-horCol;sym+horCol], ...
    'LineWidth',1,'Color','g')
line([(plotCor/2 + vertCol),(plotCor/2 + vertCol)],[sym-horCol;sym+horCol], ...
    'LineWidth',1,'Color','g')

% Set the Field sub plot
subplot(1,2,2)
% Make a scaled colour image with scaling and colours set
imagesc(map(1:maxDim-1,plotx1:plotx2-1));
set(gca,'YDir','normal')
colormap jet
daspect([1 1 1])
% Hold to add Quivers to plot
hold on
% Configure two matrix for Quiver plots
exx = zeros(maxDim-1,maxDim-1);
eyy = zeros(maxDim-1,maxDim-1);
i = 1 :  5: maxDim - 1;
    j = 1 : 5 : maxDim-1;
        exx(i,j) = Ex(i,j);
        eyy(i,j) = Ey(i,j);

% Make the quiver plot overlay the voltage gradient
y=quiver(exx(1:maxDim-1,plotx1:plotx2),eyy(1:maxDim-1,plotx1:plotx2),15,'k');
% Set the text for display on the plot
str1 = strcat (MatName(erv), ": \epsilon _r= ", num2str(ContaminantErVec(erv)));
str2 = strcat ("Electrode Width: ", num2str(StripWidth) ," mm. Spacing: ",...
    num2str(StripCentreDistance-StripWidth)," mm." );
str3 = strcat ("Contam Thickness: ", num2str(ContaminationThick), ...
    " mm. Cap: ",num2str(C)," F.");
str = [str1 ; str2 ; str3];
% Add the text to the plot
title('Electric Field Intensity', str)
ylabel('Cross Section Height (mm)')
xlabel('Cross Section Width (mm)')
% Set the ticks & axs labels on the plot
xticks([0 plotCor/2 plotCor])
xticklabels({-(plotCor/2)/NodesPer_mm,'0',(plotCor/2)/NodesPer_mm});
yticks([1 (SimHeight-BackingThick)*NodesPer_mm SimHeight*NodesPer_mm...
    (SimHeight+GlassThick)*NodesPer_mm SimHeight*2*NodesPer_mm-1]);
yticklabels({-(SimHeight/2) , -BackingThick , 0 , GlassThick , SimHeight/2});
% Put the lines for indicating the material thicknesses
yline(maxDim/2+NodesPer_mm*GlassThick+1,'--','Color','w')
yline(maxDim/2+1,'--','Color','w')
yline(maxDim/2-NodesPer_mm*BackingThick+1,'--','Color','w')
```

```
    % Put the Electrodes in
    line([0;StripWidth*NodesPer_mm/2],[maxDim/2+1;maxDim/2+1],...
        'LineWidth',2,'Color','w')
    line([(plotx2-plotx1)-StripWidth*NodesPer_mm/2,(plotx2-plotx1)],...
        [maxDim/2;maxDim/2],'LineWidth',2,'Color','w')
    line([(plotx2-plotx1)/2-StripWidth*NodesPer_mm/2,(plotx2-plotx1)/2 +...
        StripWidth*NodesPer_mm/2],[maxDim/2;maxDim/2],'LineWidth',2,'Color','r')
    line([(plotx2-plotx1)/2-StripWidth*NodesPer_mm/2,(plotx2-plotx1)/2 +...
        StripWidth*NodesPer_mm/2],[maxDim/2;maxDim/2],'LineWidth',2,'Color','r')
    % Plot the line integration path
    line([(plotCor/2- vertCol),(plotCor/2 + vertCol)],...
        [sym+horCol;sym+horCol],'LineWidth',1,'Color','g')
    line([(plotCor/2 - vertCol),(plotCor/2 + vertCol)],...
        [sym-horCol;sym-horCol],'LineWidth',1,'Color','g')
    % Vertical lines
    line([(plotCor/2 - vertCol),(plotCor/2- vertCol)],...
        [sym-horCol;sym+horCol],'LineWidth',1,'Color','g')
    line([(plotCor/2 + vertCol),(plotCor/2 + vertCol)],...
        [sym-horCol;sym+horCol],'LineWidth',1,'Color','g')
end

% Make the difference results by subtracting from the 'clean' values
if erv > 1
    % Save the capacitance calculaiton
    ResDiff (scdv,widthv,erv) = C - Res (scdv,widthv,1)
end
% End of the Main loops
end
end
end

%**************************************************************************
% Surface plots and data save section
%**************************************************************************

% Surface Plot the results of the Contaminant
figure
% Plot the capacitance per unit length
plot (Res(:,:,erv),'-o')
str = strcat (MatName(erv), ": \epsilon _r= ", num2str(ContaminantErVec(erv)));
title('Capacitance Per Unit Length Vs Centre Distance',str)
ylabel('Capacitance (F)')
xlabel('Cross Section Width (mm)')
lgd = legend (strcat(' ',string(num2cell(StripWidVec))),'location','eastoutside');
lgd.Title.String = 'Electrode Width (mm)';
% Save the plot
str = strcat ("Cap Per Unit Length - ",MatName(erv),".jpg");
saveas(gcf,str);

% Plot the electrode dimension surface plot
figure
surf(ResDiff(:,:,erv),'Marker','o','MarkerFaceColor',[0 0 0])
str = strcat (MatName(erv), ": \epsilon _r= ", num2str(ContaminantErVec(erv)));
title('Change in Capacitance Vs Electrode Dimensions',str)
zlabel('\Delta C (F)');
ylabel('Electrode Center Spacing (mm)');
yticks(1:length(StripCentDisVec))
yticklabels(num2str(StripCentDisVec(:)))
xlabel('Electrode Width (mm)');
xticks(1:length(StripWidVec))
xticklabels(num2str(StripWidVec(:)))
view([-30 30]);
% Save the plot
str = strcat ("Change in Cap - ",MatName(erv),".jpg");
saveas(gcf,str);
```

```
% Calculate the width of the electrode combinaitons
for i = 1 :length(StripCentDisVec)
    for j = 1 : length(StripWidVec)
        dim(i,j) = StripCentDisVec(i) + StripWidVec(j);
    end
end

% Calculate the efficiency of the sensor c/m
eff(:,:,:) = ResDiff(:,:,:)./dim

% Plot the efficiency surface plot
figure
h=surf(eff(:,:,erv),'Marker','o','MarkerFaceColor',[0 0 0]);
% Collect the maximum efficincy width and strip
[row,col]=find(eff(:,:,erv)==max(eff(:,:,erv),[],"all"));
str2 = strcat("Max Value @ Electrode Width: ",num2str(StripWidVec(col)),...
    " mm, Electrode Centre Spacing: ",num2str(StripCentDisVec(row))," mm");
str = strcat (MatName(erv), ": \epsilon _r= ", num2str(ContaminantErVec(erv)));
str3 = [str;str2];
title('Sensitivity Change \Delta C (F) / Sensor Width',str3)
zlabel('\Delta C (F)');
ylabel('Electrode Center Spacing (mm)');
yticks(1:length(StripCentDisVec))
yticklabels(num2str(StripCentDisVec(:)))
xlabel('Electrode Width (mm)');
xticks(1:length(StripWidVec))
xticklabels(num2str(StripWidVec(:)))
% Rotate the view
view([-30 40]);
% Save the plot
str = strcat ("Sensitivity - ",MatName(erv),".jpg");
saveas(gcf,str);

% Save results to spreadsheets
% Save the Results Matrix
writematrix(ResDiff(:,:,erv),'ResultsDR.xls','Sheet',MatName(erv));
% Save the Sensitivity Matrix
writematrix(eff(:,:,erv),'EffResults.xls','Sheet',MatName(erv));
if erv > 1
    % Save the strip width, Distance and difference results to workbooks
    effrec = [StripWidVec(col), StripCentDisVec(row), ResDiff(row,col,i)];
    writematrix(effrec,'MaxEffResults.xls','Sheet',MatName(erv));
end
% End of contaminant loop
end

%***************************************************************************
% END
%***************************************************************************

%---------------------------------
% Function vReturn
% Returns the voltage for a node number from the V vector
% completes a lookup of node number in the V vector and checks for ground
% or conductor
% Requires: matrix of node numbers, x&y coordinates for lookup value, V
% vector
% Returns: double value from V vector
%---------------------------------
function retV = vReturn(g,i,j,v)
gnd = -1;   % define gnd
cond = -10; % define conductor voltage
a = g(i,j); % get the value to find in the vector
    if a == gnd;
        retV = 0;
    elseif a == cond;
```

```
        retV = 10;
    else
    retV =  v(g(i,j)); % return the voltage in the vector
    end
end

%---------------------------------
% Function NodeFill
% generates the A matrix Values by generating a matric of the 4 adjacent
% nodes of the location passed to it. The generated matrix is then checked
% for the value of Vx component passed to it. The count of the number of
% times the Vx is in the generated matrix is added to the A matrix
% location. The V vector component is also generated and saved.
% Requires: nodes matrix, x & y coordinates of node matrix, A matrix for
% summing the values into.
% Returns: number of Vx components at that node, Voltage of node equation
%---------------------------------
function [b, Aa, Ac] = NodeFill(y,g,e)
gnd = -1;
cond = -10;
b=0;
cnt = 0;    % zero the count of nodes

[row col] = find(g == y,1);   % find the location in G for the Vnode

a0 =  e(row,col) + e(row-1,col) + e(row,col-1) +e(row-1,col-1);
a1 = (e(row,col) + e(row,col-1))/2;
a2 = (e(row-1,col) + e(row,col))/2;
a3 = (e(row-1,col-1) + e(row-1,col))/2;
a4 = (e(row,col-1) + e(row-1,col-1))/2;

Ac = [a0 a1 a2 a3 a4];
% Form a matrix of the surrounding nodes
Aa =[g(row+1,col) g(row,col+1) g(row-1,col) g(row,col-1)];
% If any of the values in the matrix are the conductor
if (numel(Aa(Aa == cond)));
    b = 10;         % Set to 10 volts
end
end
```

12.2. Analysis Code

```
%***************************************************************************
% Kane Hilmer [redacted]
% FDM Simulation Results Analysis
% Honors Thesis
% 08/2023
%***************************************************************************

clear all
close all
clc

%***************************************************************************
% Define constants and initial variables
%***************************************************************************
% Strip width in mm
StripWidthVec = [0.5 1 1.5 2 2.5 3 3.5 4];
% Strip Centre distance (Spacing = Distance-Width)
StripCentreDistanceVec = [0.5 1 1.5 2 2.5 3 3.5 4 4.5 5];

%Contamination Permittivity
ContaminantErVec = [1 6000 1501.12 41791 10448.87 7.00 2.80 2.72 6.03 10.68...
    40.00 11.11 3.2 5.21 8.94 2.70 6.60  1.62 6.96 10.46 2.0 1.40 80];

%***************************************************************************
% Load FDM results from Spreadsheet
%***************************************************************************
MatName=sheetnames('Results.xls')
for i = 1: length(MatName)
Results(:,:,i) = readmatrix('Results.xls','Sheet',MatName(i),'Range','A1:H10')
end

%***************************************************************************
% Calculate and Plot
%***************************************************************************
% For the number of materials do the plotting
for i = 2 : length(MatName)
    % Record the change due to the contamination
    ResultsD (:,:,i) = Results (:,:,i)-Results (:,:,1)
    % Plot the results of the Cap Per Unit Length per material
    figure
    plot (Results(:,:,i),'-o')
    str = strcat (MatName(i), ": \epsilon _r= ", num2str(ContaminantErVec(i)));
    title('Capacitance Per Unit Length Vs Centre Distance',str)
    ylabel('Capacitance (F)')
    xlabel('Cross Section Width (mm)')
    lgd = legend (strcat(' ',string(num2cell(StripWidthVec))),'location','eastoutside');
    lgd.Title.String = 'Electrode Width (mm)';
    str = strcat ("Cap Per Unit Length - ",MatName(i),".jpg");
    saveas(gcf,str);

    % Plot the difference results
    figure
    surf(ResultsD(:,:,i),'Marker','o','MarkerFaceColor',[0 0 0])
    str = strcat (MatName(i), ": \epsilon _r= ", num2str(ContaminantErVec(i)));
    title('Change in Capacitance Vs Electrode Dimentions',str)
    zlabel('\Delta C (F)');
    ylabel('Electrode Center Spacing (mm)');
    yticks(1:length(StripCentreDistanceVec))
    yticklabels(num2str(StripCentreDistanceVec(:)))
    xlabel('Electrode Width (mm)');
    xticks(1:length(StripWidthVec))
    xticklabels(num2str(StripWidthVec(:)))
    view([-30 30]);
```

```
    str = strcat ("Change in Cap - ",MatName(i),".jpg");
    saveas(gcf,str);
end

% Calculate the overall width of the spacing
for i = 1 : length(StripWidthVec)
    for j = i : length(StripCentreDistanceVec)
        dim(j,i) = StripWidthVec(i)+StripCentreDistanceVec(j)*2;
    end
end

% Calculate the space efficiency
for k = 1:length(ContaminantErVec)
    for i = 1 :length(StripCentreDistanceVec)
        for j = 1 : length(StripWidthVec)
            eff(i,j,k) = ResultsD(i,j,k)./dim(i,j)
        end
    end
end

for i = 2 : length(MatName)
    figure
    h=surf(eff(:,:,i),'Marker','o','MarkerFaceColor',[0 0 0]);
    hold on
    % Collect the maximum efficincy width and strip
    [row,col]=find(eff(:,:,i)==max(eff(:,:,i),[],"all"));
    plot3(col,row,eff(row,col,i),'.r','markersize',50)
    str2 = strcat("Max Value @ Electrode Width: ",num2str(StripWidthVec(col))," " + ...
    "mm, Electrode Centre Spacing: ",num2str(StripCentreDistanceVec(row))," mm");
    str = strcat (MatName(i), ": \epsilon _r= ", num2str(ContaminantErVec(i)));
    str3 = [str;str2];
    title('Sensitivity Change \Delta C (F) / Sensor Width',str3)
    zlabel('\Delta C (F)');
    ylabel('Electrode Center Spacing (mm)');
    yticks(1:length(StripCentreDistanceVec))
    yticklabels(num2str(StripCentreDistanceVec(:)))
    xlabel('Electrode Width (mm)');
    xticks(1:length(StripWidthVec))
    xticklabels(num2str(StripWidthVec(:)))
    view([-30 40]);
    str = strcat ("Sensitivity - ",MatName(i),".jpg");
    saveas(gcf,str);

    for k = 2 : length(MatName)
    % Record the change due to the contamination
    % Save the capacitance calculaiton
    ResultsDP (:,:,k) = (Results (:,:,k)-Results (:,:,1))./ContaminantErVec(k);
    end

%***************************************************************************
% Save Data to Spreadsheets
%***************************************************************************
 % Save the Results Matrix
    writematrix(ResultsD(:,:,i),'ResultsD.xls','Sheet',MatName(i));
    % Save the Sensitivity Matrix
    writematrix(eff(:,:,i),'EffResults.xls','Sheet',MatName(i));
    % Save the Normalised Difference Matrix
    writematrix(ResultsDP(:,:,i),'PermNormalisedResultsDiff.xls','Sheet',MatName(i));
    if i > 1
        % Save the strip width and Distance
        effrec = [StripWidthVec(col), StripCentreDistanceVec(row),ResultsD(row,col,i)];
        writematrix(effrec,'MaxEffResults.xls','Sheet',MatName(i));
    end
end
```

```
%**************************************************************************
% Calculate the mean and permittivity normalised values
%**************************************************************************
% Find the mean of the tested points
meanDeltaP = mean(ResultsDP,3);
% Calculate the sensitivity for used width
PkDimPm = meanDeltaP./dim;
%Locate the peak value
[rowm,colm]=find(PkDimPm()==max(PkDimPm,[],"all")) ;
%Print out the Parameters
str=("Averaging the Normalised permittivity response shows a sensativity peak at:");
strcat(str + newline+ "Electrode Width: ",num2str(StripWidthVec(colm))," mm," + ...
" Electrode Centre Spacing: ",num2str(StripCentreDistanceVec(rowm))," mm," + ...
" Total Width: ",num2str(dim(rowm,colm))," mm")

% Plot the Normalised values response
figure
h=surf(PkDimPm(:,:),'Marker','o','MarkerFaceColor',[0 0 0]);
hold on
plot3(colm,rowm,PkDimPm(rowm,colm),'.r','markersize',50)
str2 = strcat("Max Value @ Electrode Width: ",num2str(StripWidthVec(colm))," " + ...
   "mm, Electrode Centre Spacing: ",num2str(StripCentreDistanceVec(rowm))," mm");
title('Permittivity Normalised Mean Sensitivity Change \Delta C (F)',str2)
zlabel('\Delta C (F)');
ylabel('Electrode Center Spacing (mm)');
yticks(1:length(StripCentreDistanceVec))
yticklabels(num2str(StripCentreDistanceVec(:)))
xlabel('Electrode Width (mm)');
xticks(1:length(StripWidthVec))
xticklabels(num2str(StripWidthVec(:)))
view([-30 40]);
str = strcat ("NormSensitivity.jpg");
saveas(gcf,str);
% Save the data to spreadsheets
writematrix(meanDeltaP,'MeanNormalisedResults.xls','Sheet','MeanNormalised');
writematrix(PkDimPm,'MeanNormalisedResults.xls','Sheet','NormalSensSpace');
```

APPENDIX D MANUFACTURE BOM

12.2.1. PCB Sensor

Description	Designator	Quantity	PartNumber	Value
CONN SMA JACK STR 50 OHM SMD	J1	1	73251-1350	-

12.2.2. Prototype Interface

Description	Designator	Quantity	Part Number	Value
CAP, Ceramic, 10 uF, +/- 10%, 16 V, -55 to 125 degC, 1206 (3216 Metric), RoHS, Tape and Reel	C1, C3, C5	3	C1206C106K4RACTU	10uF
Cap Mica 150pF 100V 1% (3.2 X 2.5 X 2mm) SMD 125C Automotive	C2	1	MC12FA151F-F	150pF
Cap Aluminum electrolytic 100uF 35V 20% (6.3 X 7.7mm) SMD 300mA 2000h 105C T/R	C4	1	865080545012	100uF
CAP, Ceramic, 22 pF, +/- 10%, 16 V, -55 to 125 degC, 1206 (3216 Metric), RoHS, Tape and Reel	C6	1	C1206C220K4RACTU	22pF
Diode, Small Signal, 1N4148	D1	1	1N4184	-
CONN SMA JACK STR 50 OHM SMD	J1	1	73251-1350	-
CONN SMA JACK STR 50OHM EDGE MNT	J2	1	142-0701-801	-
OMNIMATE Connector	J3, J4	2	1605070000	-
RELAY RF SPDT 500MA 6V	K1	1	ARE10A06	-
Ind General Purpose Chip Molded 10uH 5% 2.52MHz 27Q-Factor Ferrite 150mA 1210	L1	1	B82422T1103J000	10uH
Chip Resistor, 100 KOhm, +/- 1%, 0.25 W, -55 to 155 degC, 1206 (3216 Metric), RoHS	R1, R3, R4	3	RC1206FR-07100KL	100k
Chip Resistor, 1 KOhm, +/- 1%, 0.25 W, -55 to 155 degC, 1206 (3216 Metric), RoHS	R2, R6	2	RC1206FR-071KL	1k
SMD Chip Resistor, 47 kOhm, ± 1%, 250 mW, 1206 [3216 Metric], Thick Film	R5	1	RC1206FR-0747KL	47K
IC DIFF COMP W/STROBE 8-SOIC	U1	1	LM311D	-
IC REG LINEAR 5V 100MA 8SOIC	U2	1	MC78L05ABDR2G	-

APPENDIX D DATA SHEETS

12.3. FR4

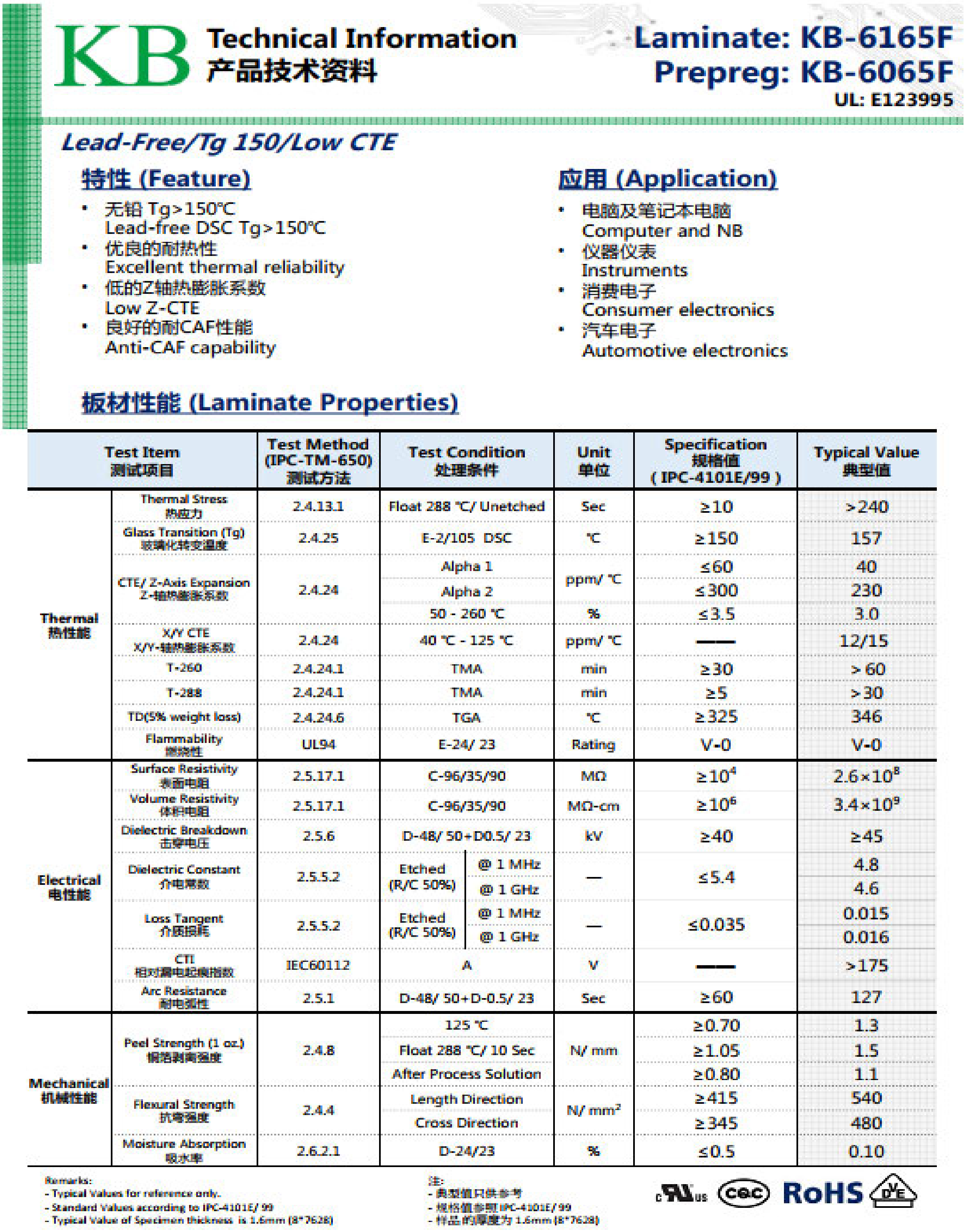

KB Technical Information
产品技术资料

Laminate: KB-6165F
Prepreg: KB-6065F
UL: E123995

Lead-Free/Tg 150/Low CTE

特性 (Feature)

- 无铅 Tg>150℃
  Lead-free DSC Tg>150℃
- 优良的耐热性
  Excellent thermal reliability
- 低的Z轴热膨胀系数
  Low Z-CTE
- 良好的耐CAF性能
  Anti-CAF capability

应用 (Application)

- 电脑及笔记本电脑
  Computer and NB
- 仪器仪表
  Instruments
- 消费电子
  Consumer electronics
- 汽车电子
  Automotive electronics

板材性能 (Laminate Properties)

Test Item 测试项目		Test Method (IPC-TM-650) 测试方法	Test Condition 处理条件	Unit 单位	Specification 规格值 (IPC-4101E/99)	Typical Value 典型值
Thermal 热性能	Thermal Stress 热应力	2.4.13.1	Float 288 ℃/ Unetched	Sec	≥10	>240
	Glass Transition (Tg) 玻璃化转变温度	2.4.25	E-2/105 DSC	℃	≥150	157
	CTE/ Z-Axis Expansion Z-轴热膨胀系数	2.4.24	Alpha 1	ppm/ ℃	≤60	40
			Alpha 2		≤300	230
			50 - 260 ℃	%	≤3.5	3.0
	X/Y CTE X/Y-轴热膨胀系数	2.4.24	40 ℃ - 125 ℃	ppm/ ℃	——	12/15
	T-260	2.4.24.1	TMA	min	≥30	> 60
	T-288	2.4.24.1	TMA	min	≥5	> 30
	TD(5% weight loss)	2.4.24.6	TGA	℃	≥325	346
	Flammability 燃烧性	UL94	E-24/ 23	Rating	V-0	V-0
Electrical 电性能	Surface Resistivity 表面电阻	2.5.17.1	C-96/35/90	MΩ	$\geq 10^4$	2.6×10^8
	Volume Resistivity 体积电阻	2.5.17.1	C-96/35/90	MΩ-cm	$\geq 10^6$	3.4×10^9
	Dielectric Breakdown 击穿电压	2.5.6	D-48/ 50+D0.5/ 23	kV	≥40	≥45
	Dielectric Constant 介电常数	2.5.5.2	Etched (R/C 50%) @ 1 MHz	—	≤5.4	4.8
			@ 1 GHz			4.6
	Loss Tangent 介质损耗	2.5.5.2	Etched (R/C 50%) @ 1 MHz	—	≤0.035	0.015
			@ 1 GHz			0.016
	CTI 相对漏电起痕指数	IEC60112	A	V	——	>175
	Arc Resistance 耐电弧性	2.5.1	D-48/ 50+D-0.5/ 23	Sec	≥60	127
Mechanical 机械性能	Peel Strength (1 oz.) 铜箔剥离强度	2.4.8	125 ℃	N/ mm	≥0.70	1.3
			Float 288 ℃/ 10 Sec		≥1.05	1.5
			After Process Solution		≥0.80	1.1
	Flexural Strength 抗弯强度	2.4.4	Length Direction	N/ mm²	≥415	540
			Cross Direction		≥345	480
	Moisture Absorption 吸水率	2.6.2.1	D-24/23	%	≤0.5	0.10

Remarks:
- Typical Values for reference only.
- Standard Values according to IPC-4101E/ 99
- Typical Value of Specimen thickness is 1.6mm (8*7628)

注:
- 典型值只供参考
- 规格值参照IPC-4101E/ 99
- 样品的厚度为1.6mm (8*7628)

RoHS

12.4. LM311

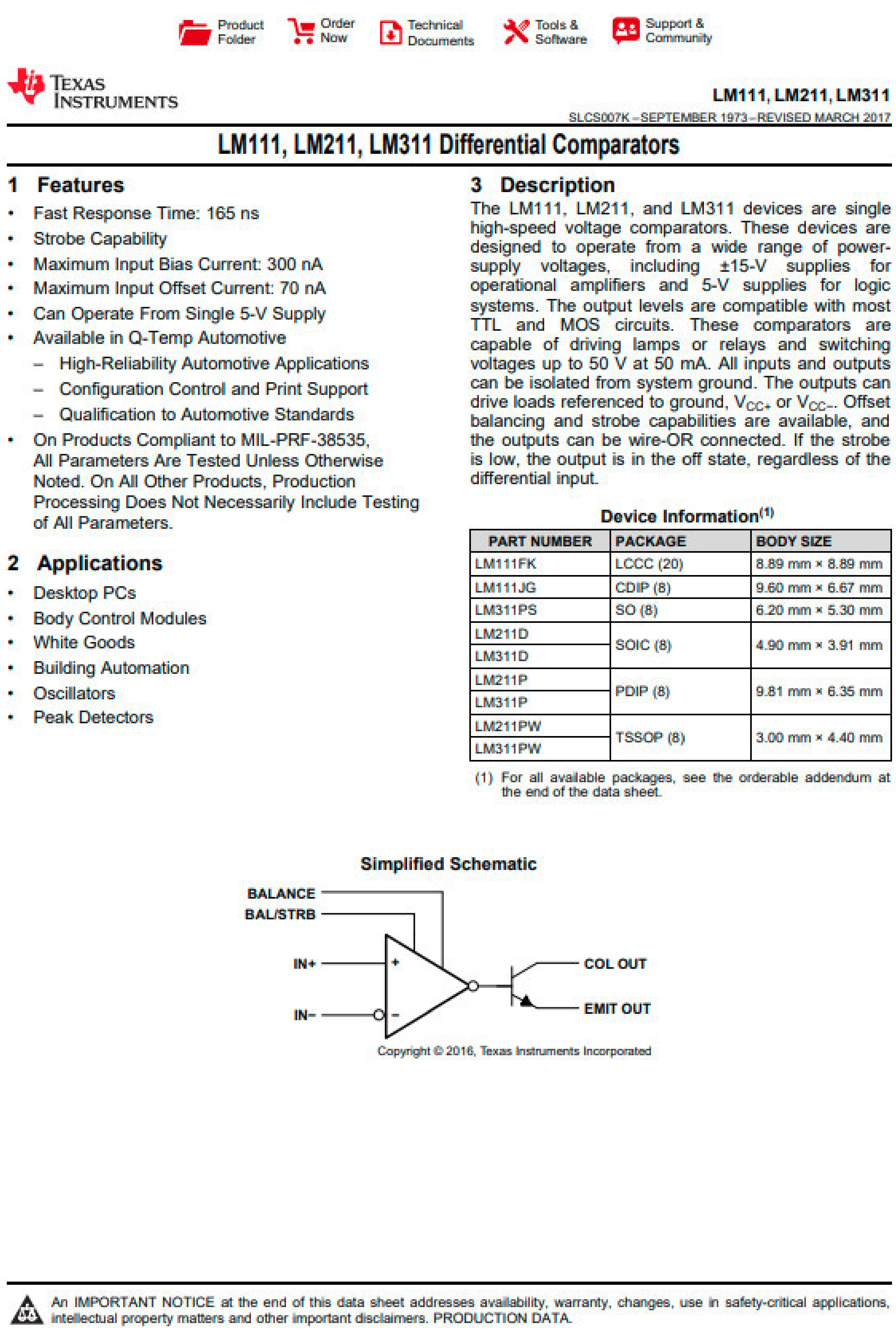

Product Folder | Order Now | Technical Documents | Tools & Software | Support & Community

TEXAS INSTRUMENTS

LM111, LM211, LM311

SLCS007K – SEPTEMBER 1973 – REVISED MARCH 2017

LM111, LM211, LM311 Differential Comparators

1 Features

- Fast Response Time: 165 ns
- Strobe Capability
- Maximum Input Bias Current: 300 nA
- Maximum Input Offset Current: 70 nA
- Can Operate From Single 5-V Supply
- Available in Q-Temp Automotive
  - High-Reliability Automotive Applications
  - Configuration Control and Print Support
  - Qualification to Automotive Standards
- On Products Compliant to MIL-PRF-38535, All Parameters Are Tested Unless Otherwise Noted. On All Other Products, Production Processing Does Not Necessarily Include Testing of All Parameters.

2 Applications

- Desktop PCs
- Body Control Modules
- White Goods
- Building Automation
- Oscillators
- Peak Detectors

3 Description

The LM111, LM211, and LM311 devices are single high-speed voltage comparators. These devices are designed to operate from a wide range of power-supply voltages, including ±15-V supplies for operational amplifiers and 5-V supplies for logic systems. The output levels are compatible with most TTL and MOS circuits. These comparators are capable of driving lamps or relays and switching voltages up to 50 V at 50 mA. All inputs and outputs can be isolated from system ground. The outputs can drive loads referenced to ground, V_{CC+} or V_{CC-}. Offset balancing and strobe capabilities are available, and the outputs can be wire-OR connected. If the strobe is low, the output is in the off state, regardless of the differential input.

Device Information(1)

PART NUMBER	PACKAGE	BODY SIZE
LM111FK	LCCC (20)	8.89 mm × 8.89 mm
LM111JG	CDIP (8)	9.60 mm × 6.67 mm
LM311PS	SO (8)	6.20 mm × 5.30 mm
LM211D	SOIC (8)	4.90 mm × 3.91 mm
LM311D		
LM211P	PDIP (8)	9.81 mm × 6.35 mm
LM311P		
LM211PW	TSSOP (8)	3.00 mm × 4.40 mm
LM311PW		

(1) For all available packages, see the orderable addendum at the end of the data sheet.

Simplified Schematic

12.5. MC78L05

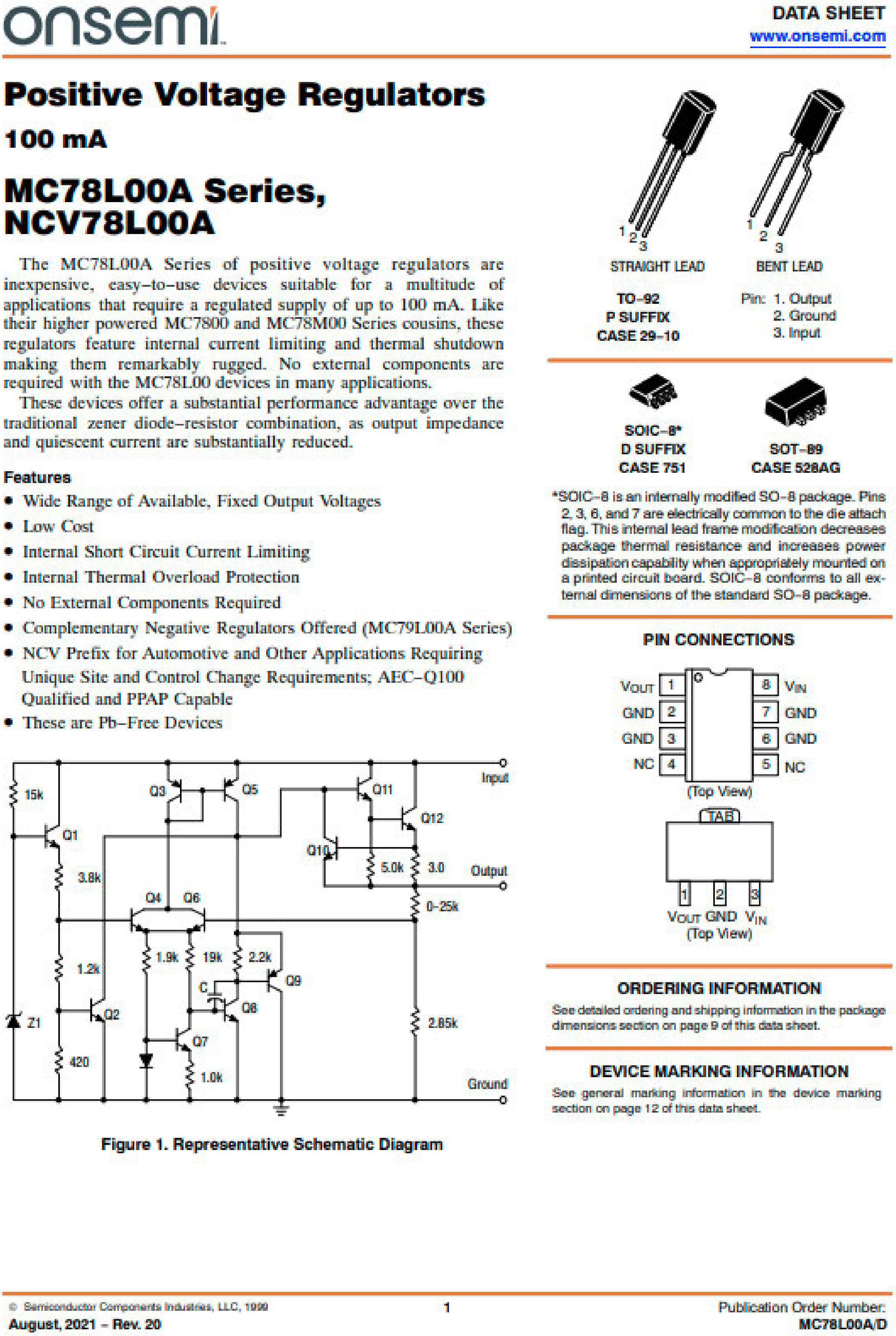

onsemi

DATA SHEET
www.onsemi.com

Positive Voltage Regulators

100 mA

MC78L00A Series, NCV78L00A

The MC78L00A Series of positive voltage regulators are inexpensive, easy−to−use devices suitable for a multitude of applications that require a regulated supply of up to 100 mA. Like their higher powered MC7800 and MC78M00 Series cousins, these regulators feature internal current limiting and thermal shutdown making them remarkably rugged. No external components are required with the MC78L00 devices in many applications.

These devices offer a substantial performance advantage over the traditional zener diode−resistor combination, as output impedance and quiescent current are substantially reduced.

Features

- Wide Range of Available, Fixed Output Voltages
- Low Cost
- Internal Short Circuit Current Limiting
- Internal Thermal Overload Protection
- No External Components Required
- Complementary Negative Regulators Offered (MC79L00A Series)
- NCV Prefix for Automotive and Other Applications Requiring Unique Site and Control Change Requirements; AEC−Q100 Qualified and PPAP Capable
- These are Pb−Free Devices

Figure 1. Representative Schematic Diagram

TO−92
P SUFFIX
CASE 29−10

Pin: 1. Output
2. Ground
3. Input

SOIC−8*
D SUFFIX
CASE 751

SOT−89
CASE 528AG

*SOIC−8 is an internally modified SO−8 package. Pins 2, 3, 6, and 7 are electrically common to the die attach flag. This internal lead frame modification decreases package thermal resistance and increases power dissipation capability when appropriately mounted on a printed circuit board. SOIC−8 conforms to all external dimensions of the standard SO−8 package.

PIN CONNECTIONS

ORDERING INFORMATION

See detailed ordering and shipping information in the package dimensions section on page 9 of this data sheet.

DEVICE MARKING INFORMATION

See general marking information in the device marking section on page 12 of this data sheet.

August, 2021 − Rev. 20

Publication Order Number:
MC78L00A/D

12.6. MC12FA151F-F

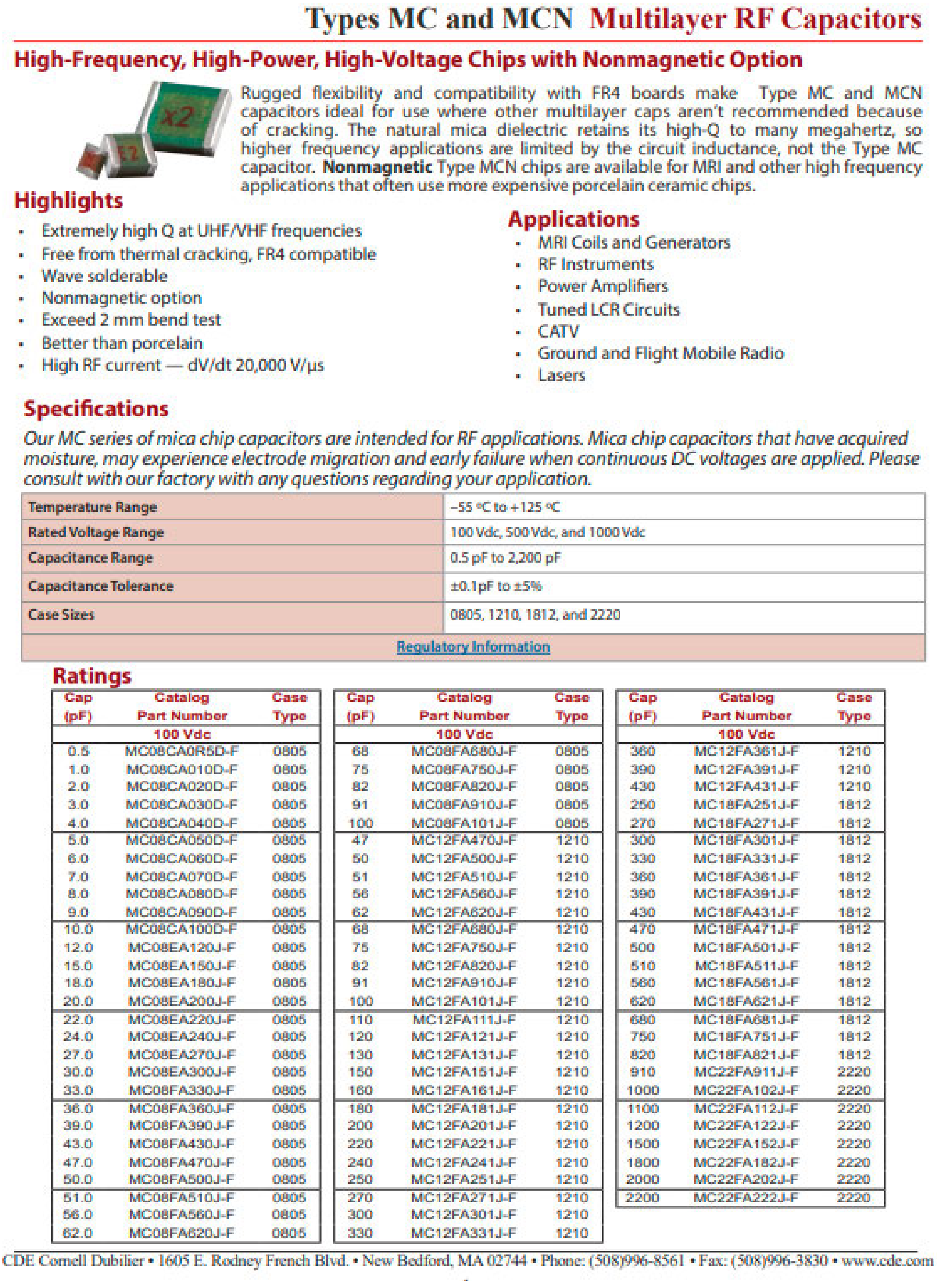

Types MC and MCN Multilayer RF Capacitors

High-Frequency, High-Power, High-Voltage Chips with Nonmagnetic Option

Rugged flexibility and compatibility with FR4 boards make Type MC and MCN capacitors ideal for use where other multilayer caps aren't recommended because of cracking. The natural mica dielectric retains its high-Q to many megahertz, so higher frequency applications are limited by the circuit inductance, not the Type MC capacitor. **Nonmagnetic** Type MCN chips are available for MRI and other high frequency applications that often use more expensive porcelain ceramic chips.

Highlights

- Extremely high Q at UHF/VHF frequencies
- Free from thermal cracking, FR4 compatible
- Wave solderable
- Nonmagnetic option
- Exceed 2 mm bend test
- Better than porcelain
- High RF current — dV/dt 20,000 V/µs

Applications

- MRI Coils and Generators
- RF Instruments
- Power Amplifiers
- Tuned LCR Circuits
- CATV
- Ground and Flight Mobile Radio
- Lasers

Specifications

Our MC series of mica chip capacitors are intended for RF applications. Mica chip capacitors that have acquired moisture, may experience electrode migration and early failure when continuous DC voltages are applied. Please consult with our factory with any questions regarding your application.

Temperature Range	–55 °C to +125 °C
Rated Voltage Range	100 Vdc, 500 Vdc, and 1000 Vdc
Capacitance Range	0.5 pF to 2,200 pF
Capacitance Tolerance	±0.1pF to ±5%
Case Sizes	0805, 1210, 1812, and 2220
Regulatory Information	

Ratings

Cap (pF)	Catalog Part Number	Case Type
	100 Vdc	
0.5	MC08CA0R5D-F	0805
1.0	MC08CA010D-F	0805
2.0	MC08CA020D-F	0805
3.0	MC08CA030D-F	0805
4.0	MC08CA040D-F	0805
5.0	MC08CA050D-F	0805
6.0	MC08CA060D-F	0805
7.0	MC08CA070D-F	0805
8.0	MC08CA080D-F	0805
9.0	MC08CA090D-F	0805
10.0	MC08CA100D-F	0805
12.0	MC08EA120J-F	0805
15.0	MC08EA150J-F	0805
18.0	MC08EA180J-F	0805
20.0	MC08EA200J-F	0805
22.0	MC08EA220J-F	0805
24.0	MC08EA240J-F	0805
27.0	MC08EA270J-F	0805
30.0	MC08EA300J-F	0805
33.0	MC08FA330J-F	0805
36.0	MC08FA360J-F	0805
39.0	MC08FA390J-F	0805
43.0	MC08FA430J-F	0805
47.0	MC08FA470J-F	0805
50.0	MC08FA500J-F	0805
51.0	MC08FA510J-F	0805
56.0	MC08FA560J-F	0805
62.0	MC08FA620J-F	0805

Cap (pF)	Catalog Part Number	Case Type
	100 Vdc	
68	MC08FA680J-F	0805
75	MC08FA750J-F	0805
82	MC08FA820J-F	0805
91	MC08FA910J-F	0805
100	MC08FA101J-F	0805
47	MC12FA470J-F	1210
50	MC12FA500J-F	1210
51	MC12FA510J-F	1210
56	MC12FA560J-F	1210
62	MC12FA620J-F	1210
68	MC12FA680J-F	1210
75	MC12FA750J-F	1210
82	MC12FA820J-F	1210
91	MC12FA910J-F	1210
100	MC12FA101J-F	1210
110	MC12FA111J-F	1210
120	MC12FA121J-F	1210
130	MC12FA131J-F	1210
150	MC12FA151J-F	1210
160	MC12FA161J-F	1210
180	MC12FA181J-F	1210
200	MC12FA201J-F	1210
220	MC12FA221J-F	1210
240	MC12FA241J-F	1210
250	MC12FA251J-F	1210
270	MC12FA271J-F	1210
300	MC12FA301J-F	1210
330	MC12FA331J-F	1210

Cap (pF)	Catalog Part Number	Case Type
	100 Vdc	
360	MC12FA361J-F	1210
390	MC12FA391J-F	1210
430	MC12FA431J-F	1210
250	MC18FA251J-F	1812
270	MC18FA271J-F	1812
300	MC18FA301J-F	1812
330	MC18FA331J-F	1812
360	MC18FA361J-F	1812
390	MC18FA391J-F	1812
430	MC18FA431J-F	1812
470	MC18FA471J-F	1812
500	MC18FA501J-F	1812
510	MC18FA511J-F	1812
560	MC18FA561J-F	1812
620	MC18FA621J-F	1812
680	MC18FA681J-F	1812
750	MC18FA751J-F	1812
820	MC18FA821J-F	1812
910	MC22FA911J-F	2220
1000	MC22FA102J-F	2220
1100	MC22FA112J-F	2220
1200	MC22FA122J-F	2220
1500	MC22FA152J-F	2220
1800	MC22FA182J-F	2220
2000	MC22FA202J-F	2220
2200	MC22FA222J-F	2220

CDE Cornell Dubilier • 1605 E. Rodney French Blvd. • New Bedford, MA 02744 • Phone: (508)996-8561 • Fax: (508)996-3830 • www.cde.com

12.7. C1206C106K4RACTU

Surface Mount Multilayer Ceramic Chip Capacitors (SMD MLCCs)

X7R Dielectric, 6.3 – 250 VDC (Commercial Grade)

KEMET
a YAGEO company

Overview

KEMET's X7R dielectric features a 125°C maximum operating temperature and is considered temperature stable. The Electronics Components, Assemblies and Materials Association (EIA) characterizes X7R dielectric as a Class II material. Components of this classification are fixed, ceramic dielectric capacitors suited for bypass and decoupling applications or for frequency discriminating circuits where Q and stability of capacitance characteristics are not critical. X7R exhibits a predictable change in capacitance with respect to time and voltage, boasting a minimal change in capacitance with reference to ambient temperature. Capacitance change is limited to ±15% from −55°C to +125°C.

Benefits

- −55°C to +125°C operating temperature range
- Lead (Pb)-free, RoHS, and REACH Compliant
- Temperature stable dielectric
- EIA 0402, 0603, 0805, 1206, 1210, 1808, 1812, 1825, 2220, and 2225 case sizes
- DC voltage ratings of 6.3 V, 10 V, 16 V, 25 V, 35 V, 50 V, 100 V, 200 V, and 250 V
- Capacitance offerings ranging from 10 pF to 47 µF
- Available capacitance tolerances of ±5%, ±10%, and ±20%
- Non-polar device, minimizing installation concerns
- 100% pure matte tin-plated termination finish allowing for excellent solderability
- SnPb termination finish option available upon request (5% Pb minimum)

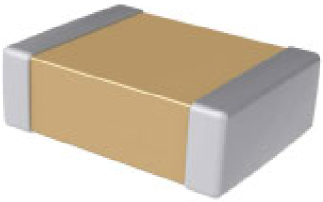

Applications

Typical applications include decoupling, bypass, filtering and transient voltage suppression.

12.8. ARE10A06

Panasonic
ideas for life

3 GHz MICROWAVE RELAYS
Miniature size
Lineup includes
50/75Ω type

RS RELAYS (ARS)

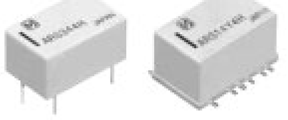

RoHS compliant

FEATURES

1. Super miniature design
14 × 8.6 × 7.2 mm .551 × .339 × .283 inch
(standard PC board terminal)

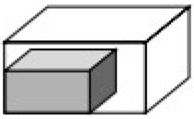
60% OFF in volume (Compared to RK relay)

2. Lineup includes silent type.
(75Ω type only)
Operation noise (Unit: dB)

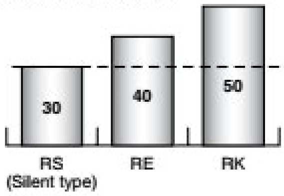

3. Excellent high frequency characteristics

- Impedance: 50Ω
(Standard PC board terminal)

Frequency	to 900 MHz	to 3 GHz
V. S. W. R. (Max.)	1.20	1.40
Insertion loss (dB, Max.)	0.10	0.35
Isolation (dB, Min.)	60	35

- Impedance: 75Ω
(Standard PC board terminal)

Frequency	to 900 MHz	to 3 GHz
V. S. W. R. (Max.)	1.15	1.40
Insertion loss (dB, Max.)	0.10	0.30
Isolation (dB, Min.)	60	30

- Impedance: 50Ω
(Surface-mount terminal)

Frequency	to 900 MHz	to 3 GHz
V. S. W. R. (Max.)	1.20	1.40
Insertion loss (dB, Max.)	0.20	0.40
Isolation (dB, Min.)	55	30

- Impedance: 75Ω
(Surface-mount terminal)

Frequency	to 900 MHz	to 3 GHz
V. S. W. R. (Max.)	1.20	1.50
Insertion loss (dB, Max.)	0.20	0.50
Isolation (dB, Min.)	55	30

4. Lineup includes surface-mount terminal type
E and Y layouts available.

5. Lineup includes reversed contact type
Great design freedom is possible using reversed contact type in which the positions of the N.O. and N.C. contacts are switched.

TYPICAL APPLICATIONS

1. Broadcasting and video equipment markets

- Digital broadcasting equipment
- STB/tuner, etc.

2. Mobile phone base stations

3. Communications market

- Antenna switching
- All types of wireless devices

4. Measurement equipment market

- Spectrum analyzer and oscilloscope, etc.

If you wish to use in applications with low level loads or with high frequency switching, please consult us.

ORDERING INFORMATION

ARS ☐ ☐ ☐ ☐☐ ☐

RS relays

Contact arrangement
1: Standard contact type (1 Form C)
3: Reversed contact type (1 Form C)

Operating function
0: Single side stable standard type (Impedance: 75Ω)
1: 1 coil latching type (Impedance: 75Ω)
2: 2 coil latching type (Impedance: 75Ω)
3: Single side stable silent type (Impedance: 75Ω)
4: Single side stable type (Impedance: 50Ω)
5: 1 coil latching type (Impedance: 50Ω)
6: 2 coil latching type (Impedance: 50Ω)

Nil: Standard PC board terminal
A: Surface-mount terminal, E layout
Y: Surface-mount terminal, Y layout

Coil voltage, DC
03: 3 V, 4H: 4.5 V, 09: 9 V, 12: 12 V, 24: 24 V (H=0.5)

Packing style
Nil: Carton packing (Standard PC board terminal only)
Tube packing (Surface-mount terminal only)
X: Tape and reel packing (picked from 2-pin side) (Surface-mount terminal only)
Z: Tape and reel packing (picked from 18-pin side) (Surface-mount terminal only)

APPENDIX E TEST EQUIPMENT

Electronic test equipment used for the measuring of the PCB Sensor and prototype interface circuit are shown below. The soil collection site is shown in Figure 104.

Figure 97 E5071C VNA

Figure 98 85052B 3.5mm Calibration Kit

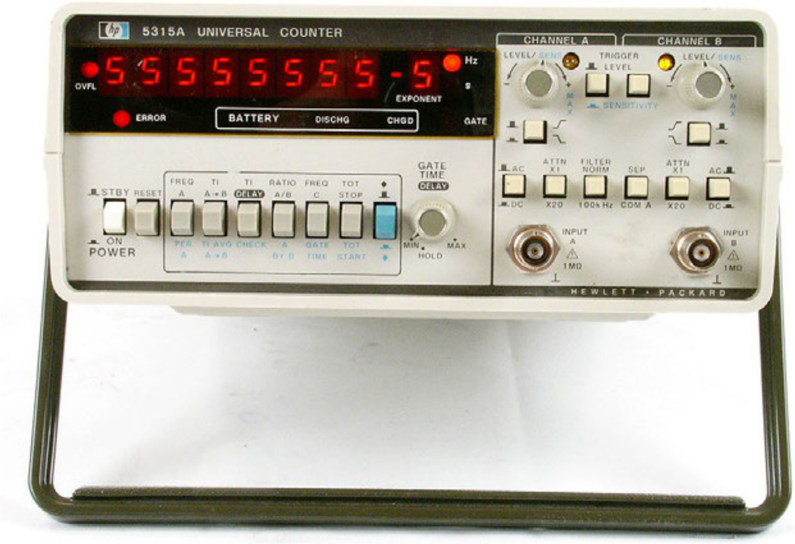

Figure 99 5315A Universal Counter

Figure 100 U1733C LCR Meter

Figure 101 175 RMS DMM

Figure 102 DC Power Supply

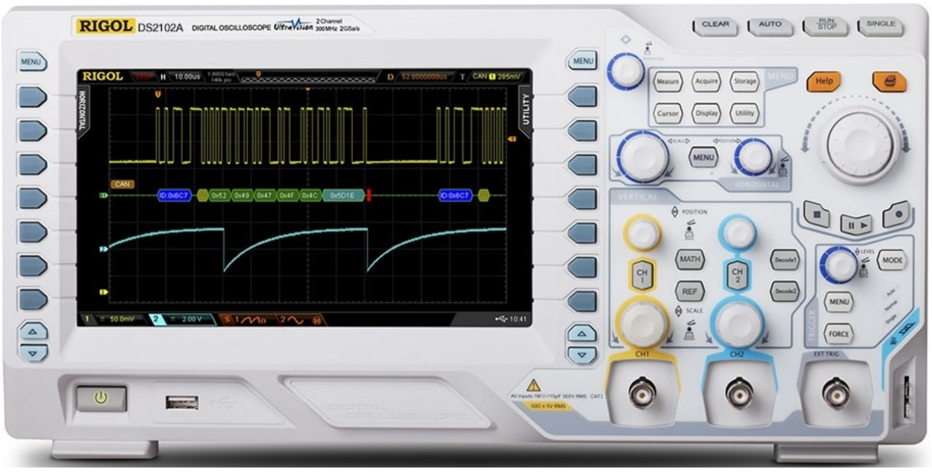

Figure 103 DS102A Digital Oscilloscope

Figure 104 Soil Contamination Collection Site

APPENDIX F VNA TEST RESULTS

Additional plots collected from the VNA during PCB Sensor testing are shown below. Real and Imaginary components for each test are shown.

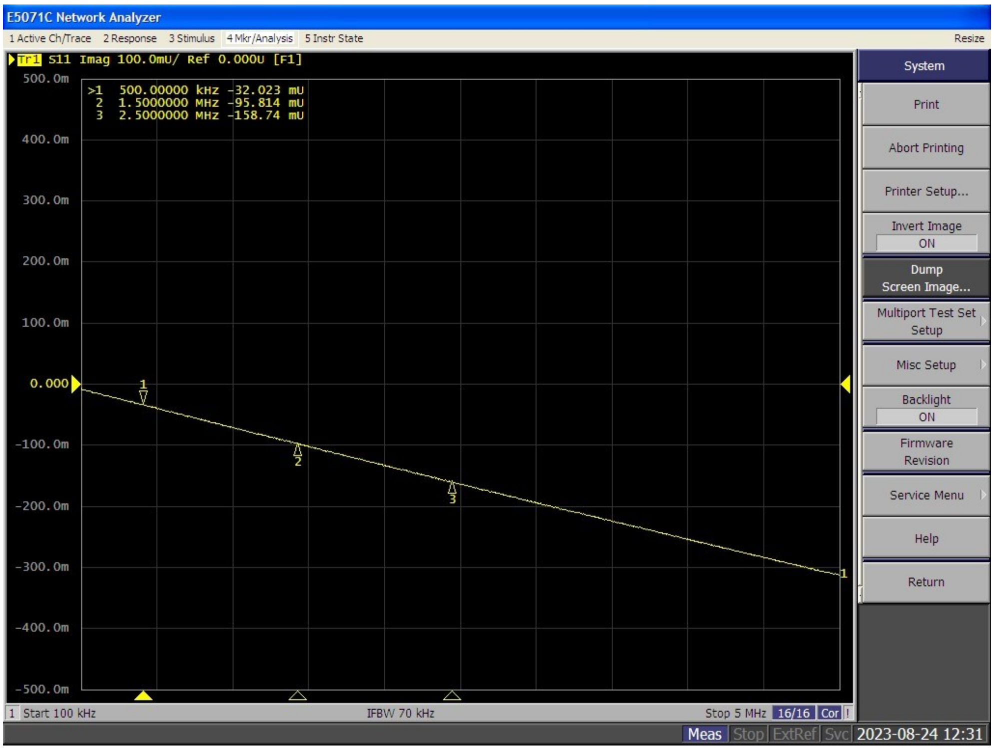

```
Tr1 S11 Imag 100.0mU/ Ref 0.000U [F1]
>1  500.00000 kHz -32.023 mU
 2  1.5000000 MHz -95.814 mU
 3  2.5000000 MHz -158.74 mU
```

```
1 Start 100 kHz    IFBW 70 kHz    Stop 5 MHz 16/16 Cor
Meas Stop ExtRef Svc 2023-08-24 12:31
```

Figure 105 Clean PCB Sensor Imaginary Component Plot

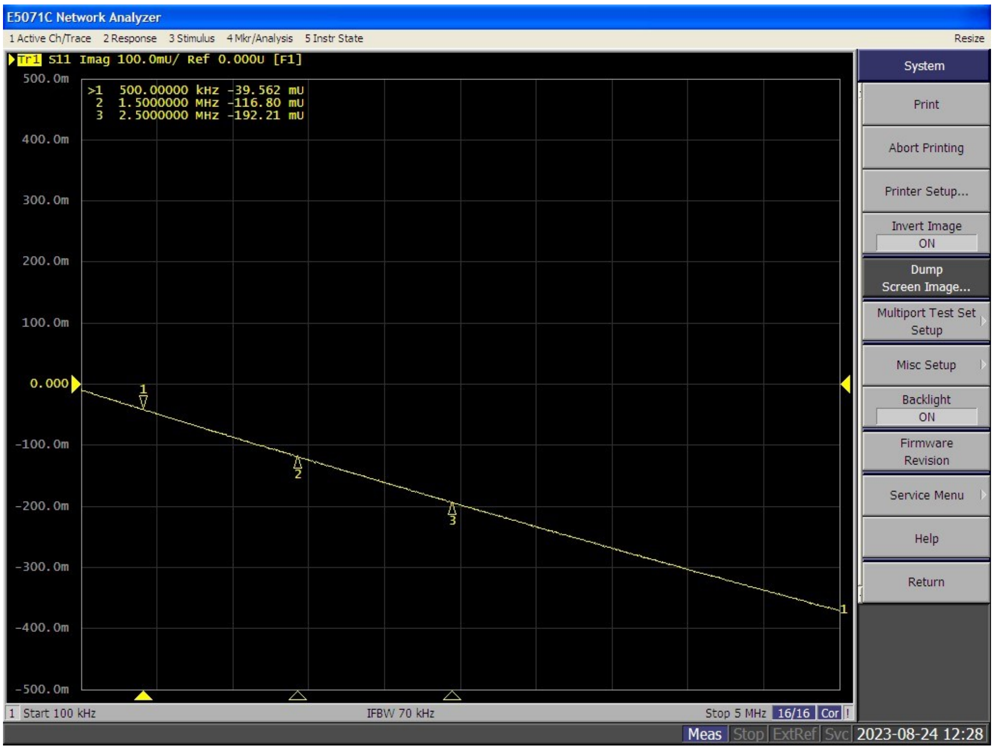

```
Tr1 S11 Imag 100.0mU/ Ref 0.000U [F1]
>1  500.00000 kHz -39.562 mU
 2  1.5000000 MHz -116.80 mU
 3  2.5000000 MHz -192.21 mU
```

Figure 106 Wet PCB Sensor Imaginary Component Plot

```
Tr1 S11 Imag 100.0mU/ Ref 0.000U [F1]
>1  500.00000 kHz -32.905 mU
 2  1.5000000 MHz -97.616 mU
 3  2.5000000 MHz -161.57 mU
```

Figure 107 Dry Soil PCB Sensor Imaginary Component Plot

Tr1 S11 Imag 100.0mU/ Ref 0.000U [F1]

```
>1  500.00000 kHz -38.553 mU
 2  1.5000000 MHz -114.10 mU
 3  2.5000000 MHz -188.31 mU
```

1 Start 100 kHz IFBW 70 kHz Stop 5 MHz

2023-08-24 12:55

Figure 108 Wet Soil PCB Sensor Imaginary Component Plot

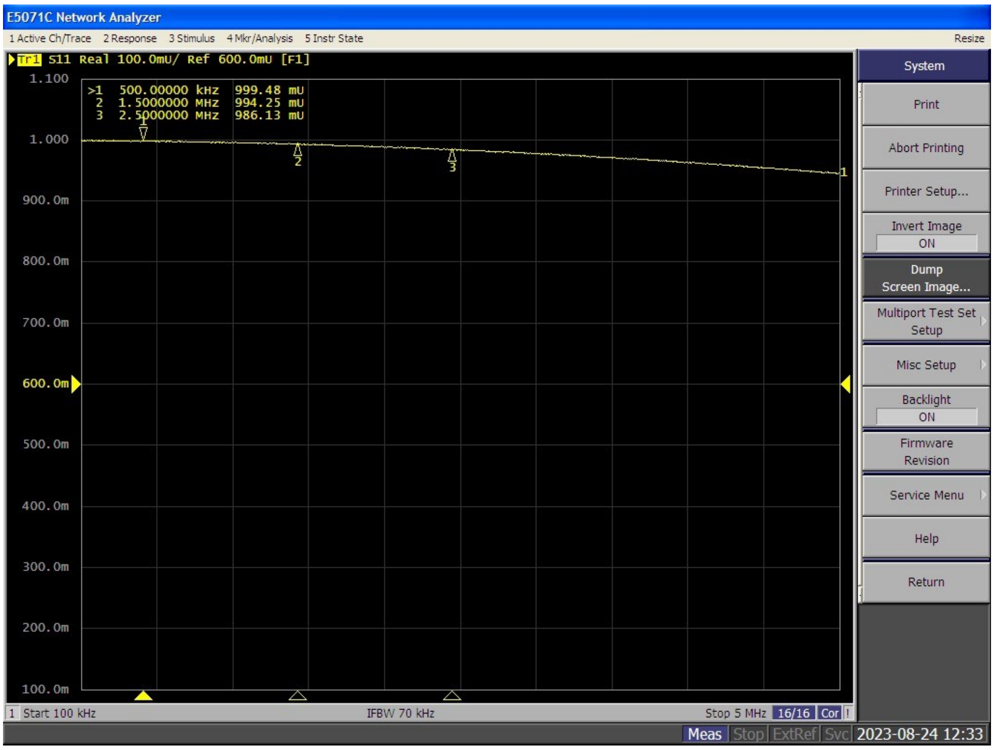

Tr1 S11 Real 100.0mU/ Ref 600.0mU [F1]

```
>1  500.00000 kHz  999.48 mU
 2  1.5000000 MHz  994.25 mU
 3  2.5000000 MHz  986.13 mU
```

1 Start 100 kHz IFBW 70 kHz Stop 5 MHz

2023-08-24 12:33

Figure 109 Clean PCB Sensor Real Component Plot

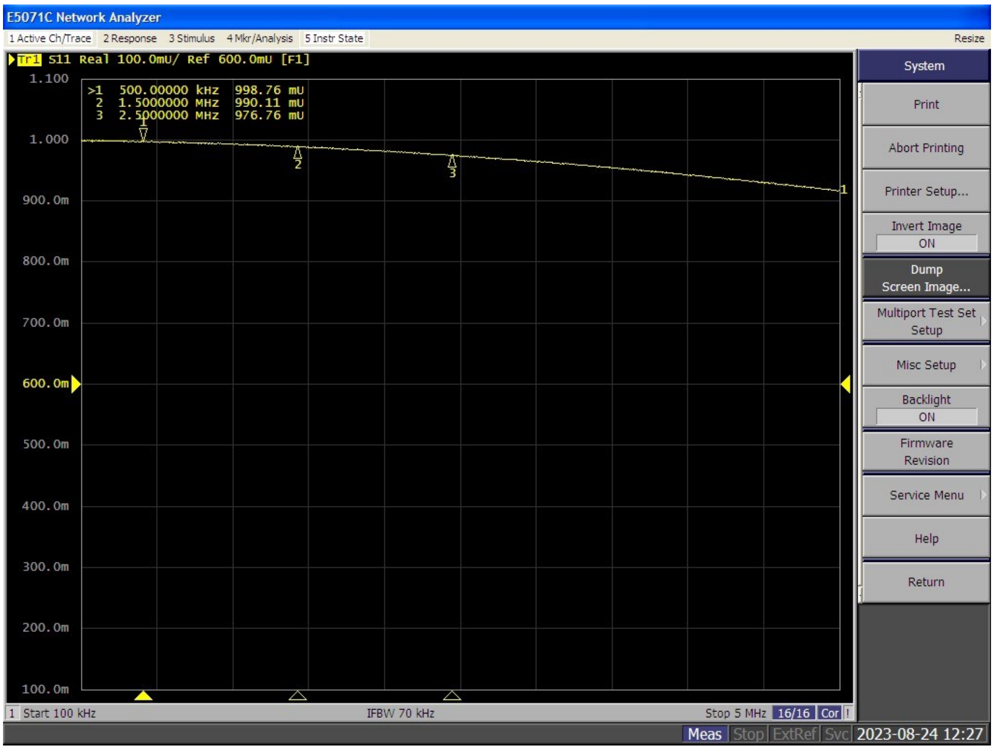

```
Tr1 S11 Real 100.0mU/ Ref 600.0mU [F1]
>1   500.00000 kHz   998.76 mU
 2   1.5000000 MHz   990.11 mU
 3   2.5000000 MHz   976.76 mU
```

Figure 110 Wet PCB Sensor Real Component Plot

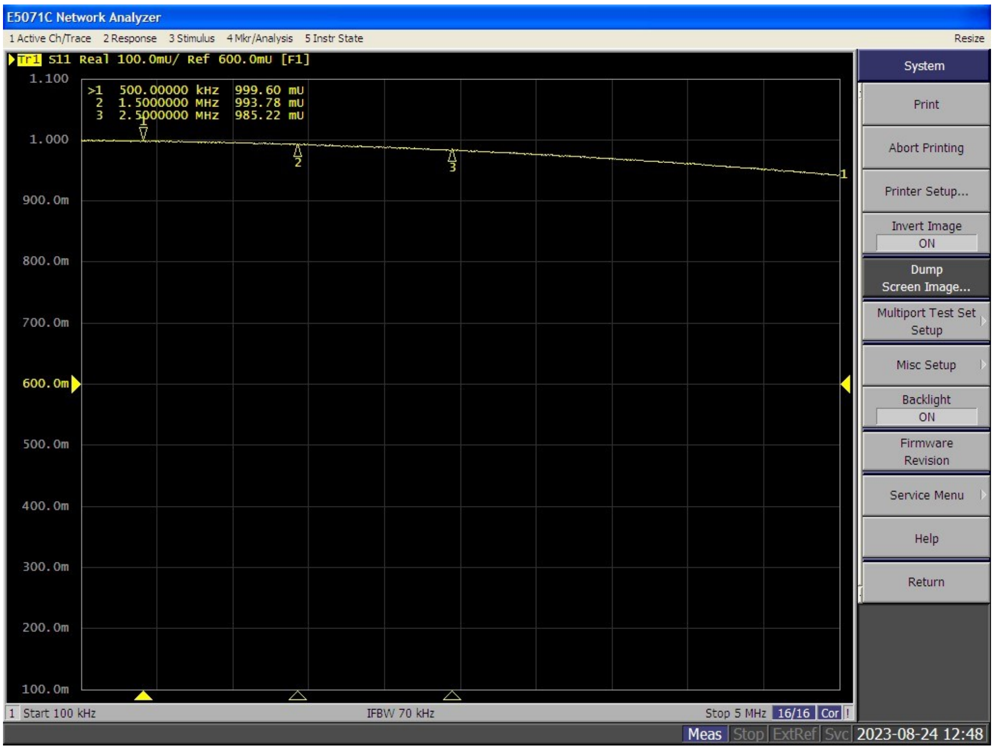

```
Tr1 S11 Real 100.0mU/ Ref 600.0mU [F1]
>1   500.00000 kHz   999.60 mU
 2   1.5000000 MHz   993.78 mU
 3   2.5000000 MHz   985.22 mU
```

Figure 111 Dry Soil PCB Sensor Real Component Plot

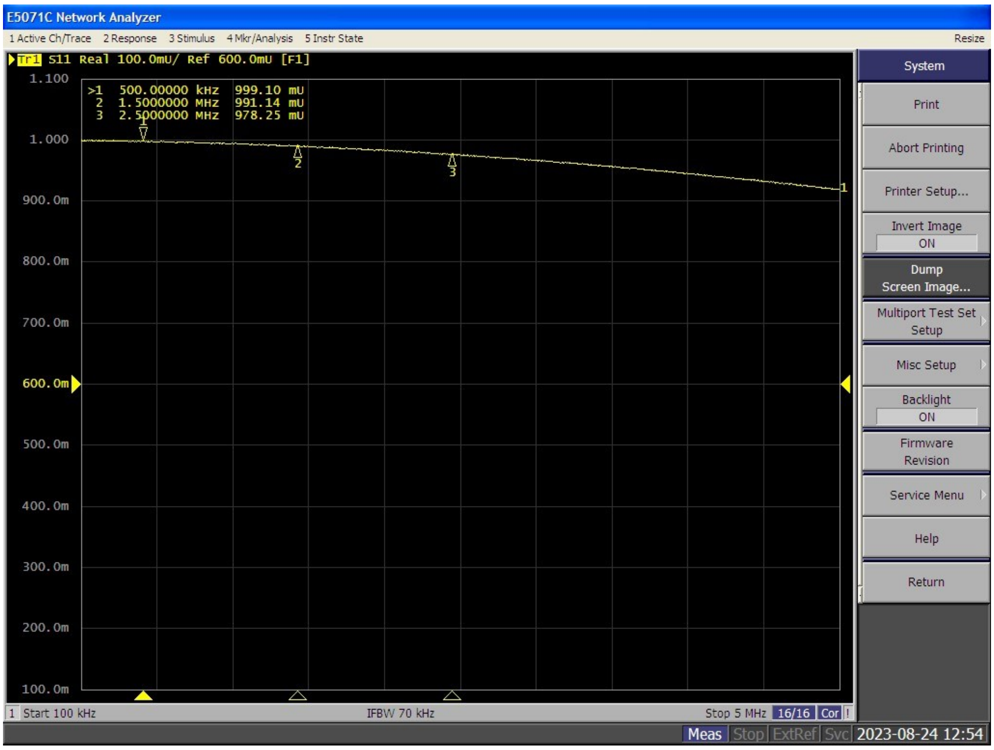

E5071C Network Analyzer

Tr1 S11 Real 100.0mU/ Ref 600.0mU [F1]

```
>1  500.00000 kHz  999.10 mU
 2  1.5000000 MHz  991.14 mU
 3  2.5000000 MHz  978.25 mU
```

Start 100 kHz IFBW 70 kHz Stop 5 MHz

2023-08-24 12:54

Figure 112 Wet Soil PCB Sensor Real Component Plot

APPENDIX G FDM SIMULATION OUTPUTS

Peak Sensitivity Potential and Electric Field Plots

For all contaminants simulated.

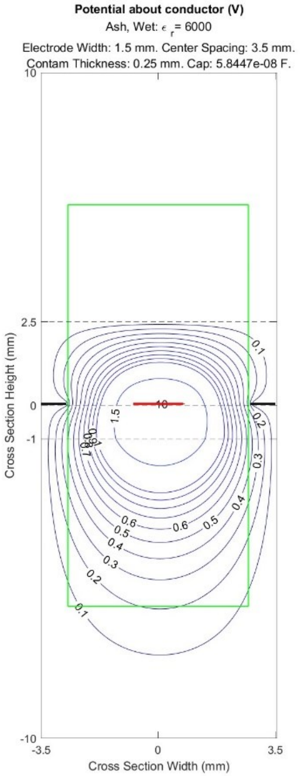

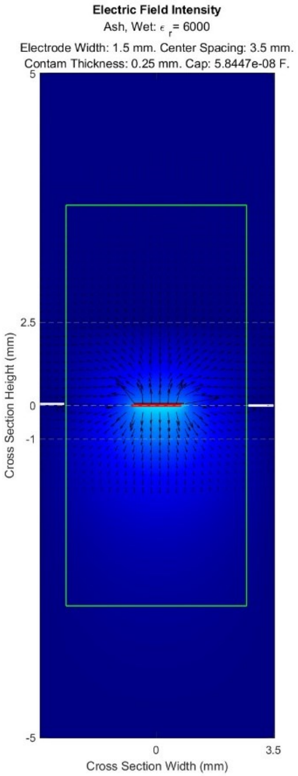

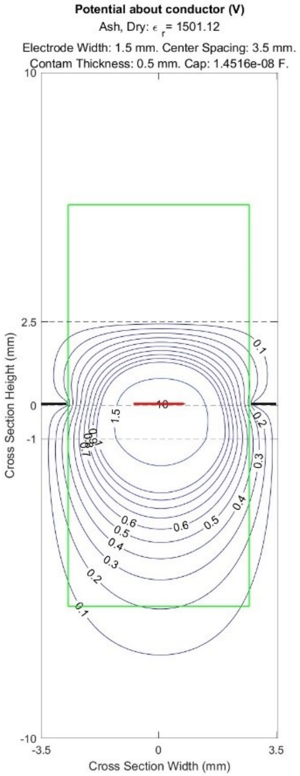

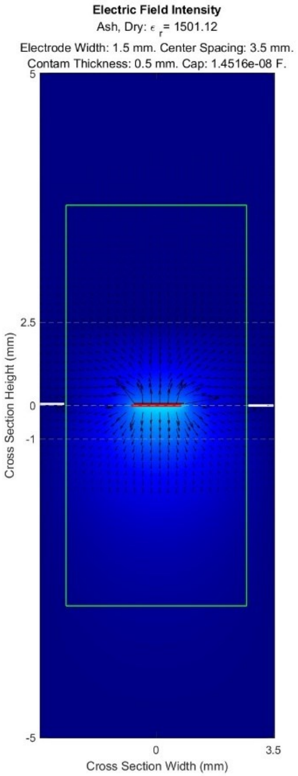

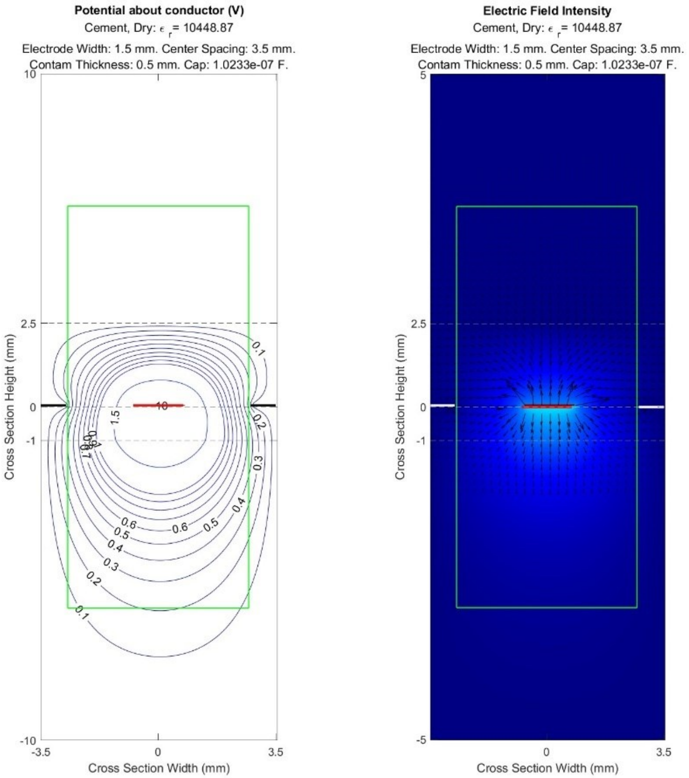
Potential about conductor (V)
Cement, Dry: ϵ_r = 10448.87
Electrode Width: 1.5 mm. Center Spacing: 3.5 mm.
Contam Thickness: 0.5 mm. Cap: 1.0233e-07 F.
Electric Field Intensity
Cement, Dry: ϵ_r = 10448.87
Electrode Width: 1.5 mm. Center Spacing: 3.5 mm.
Contam Thickness: 0.5 mm. Cap: 1.0233e-07 F.
Cross Section Height (mm)
Cross Section Width (mm)
10
2.5
0
-1
-10
5
-5
-3.5
3.5
10
1.5
0.6
0.5
0.4
0.3
0.2
0.1

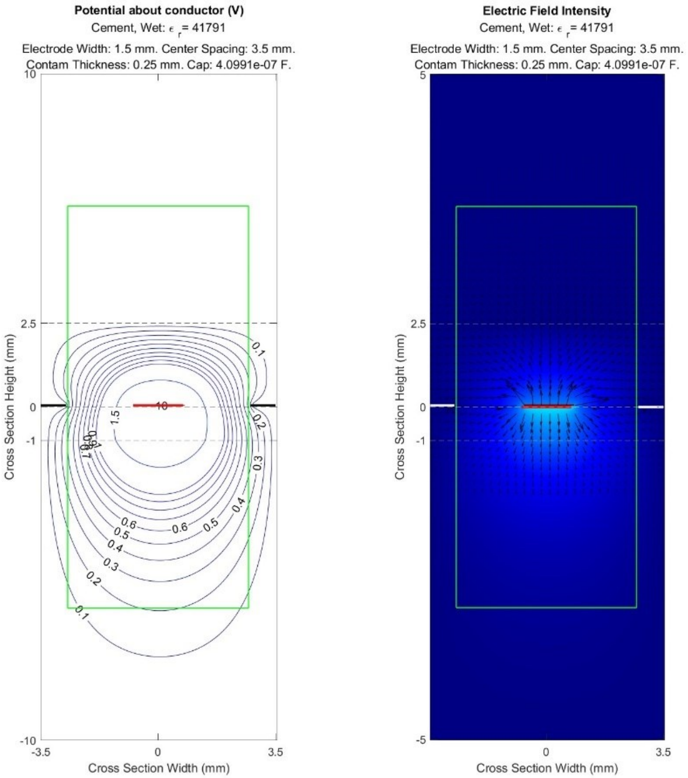
Potential about conductor (V)
Cement, Wet: ϵ_r = 41791
Electrode Width: 1.5 mm. Center Spacing: 3.5 mm.
Contam Thickness: 0.25 mm. Cap: 4.0991e-07 F.
Electric Field Intensity
Cement, Wet: ϵ_r = 41791
Electrode Width: 1.5 mm. Center Spacing: 3.5 mm.
Contam Thickness: 0.25 mm. Cap: 4.0991e-07 F.
Cross Section Height (mm)
Cross Section Width (mm)
10
2.5
0
-1
-10
5
-5
-3.5
3.5
10
1.5
0.6
0.5
0.4
0.3
0.2
0.1

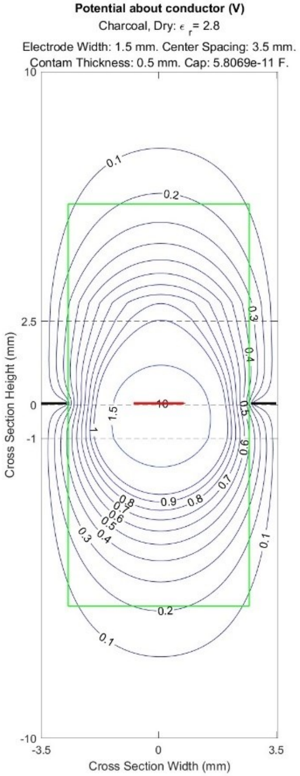

Potential about conductor (V)
Charcoal, Dry: $\epsilon_r = 2.8$
Electrode Width: 1.5 mm. Center Spacing: 3.5 mm.
Contam Thickness: 0.5 mm. Cap: 5.8069e-11 F.

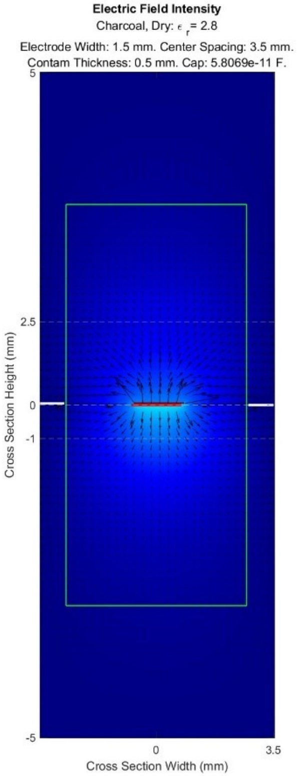

Electric Field Intensity
Charcoal, Dry: $\epsilon_r = 2.8$
Electrode Width: 1.5 mm. Center Spacing: 3.5 mm.
Contam Thickness: 0.5 mm. Cap: 5.8069e-11 F.

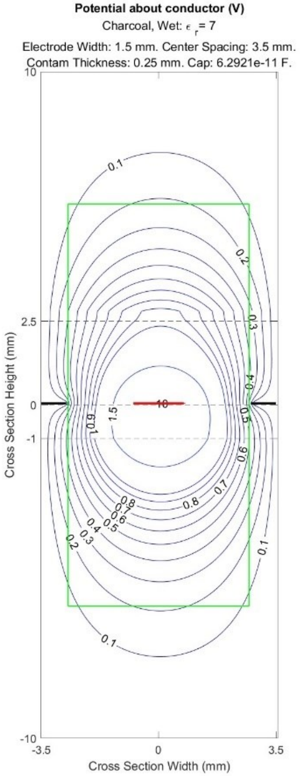

Potential about conductor (V)
Charcoal, Wet: $\epsilon_r = 7$
Electrode Width: 1.5 mm. Center Spacing: 3.5 mm.
Contam Thickness: 0.25 mm. Cap: 6.2921e-11 F.

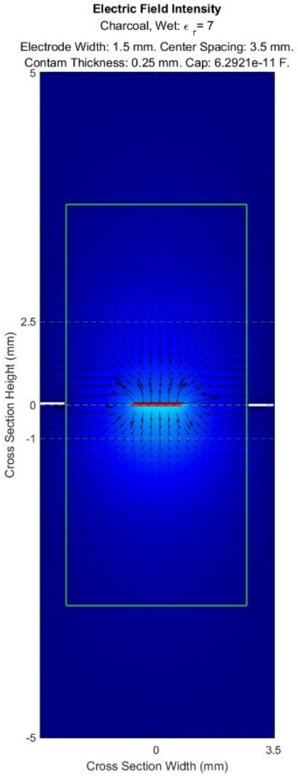

Electric Field Intensity
Charcoal, Wet: $\epsilon_r = 7$
Electrode Width: 1.5 mm. Center Spacing: 3.5 mm.
Contam Thickness: 0.25 mm. Cap: 6.2921e-11 F.

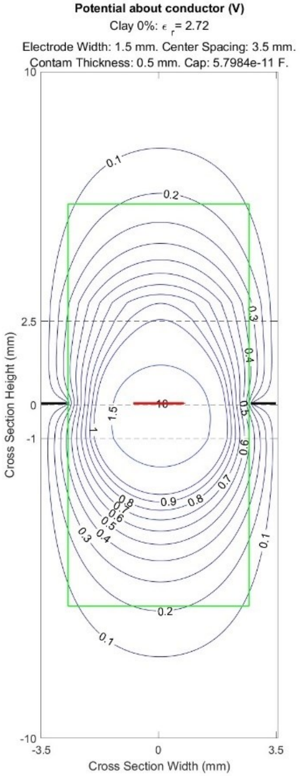
Potential about conductor (V)
Clay 0%: ϵ_r= 2.72
Electrode Width: 1.5 mm. Center Spacing: 3.5 mm.
Contam Thickness: 0.5 mm. Cap: 5.7984e-11 F.

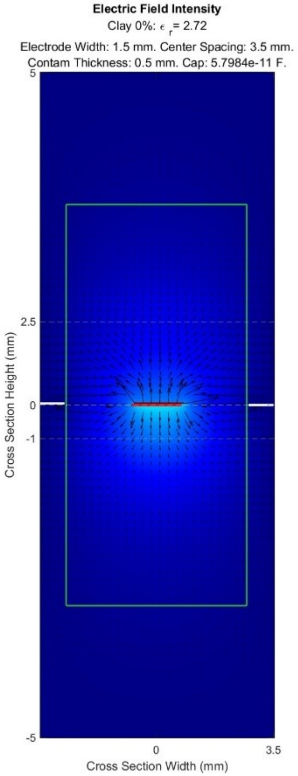
Electric Field Intensity
Clay 0%: ϵ_r= 2.72
Electrode Width: 1.5 mm. Center Spacing: 3.5 mm.
Contam Thickness: 0.5 mm. Cap: 5.7984e-11 F.

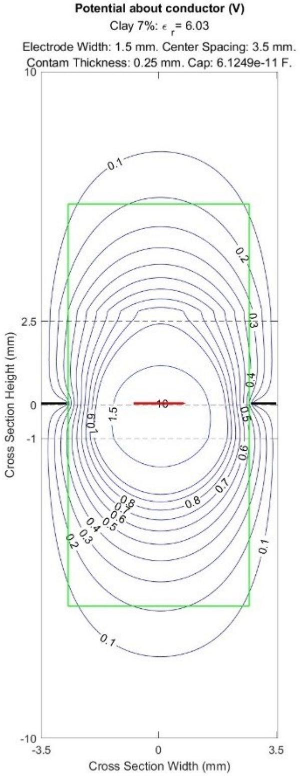
Potential about conductor (V)
Clay 7%: ϵ_r= 6.03
Electrode Width: 1.5 mm. Center Spacing: 3.5 mm.
Contam Thickness: 0.25 mm. Cap: 6.1249e-11 F.

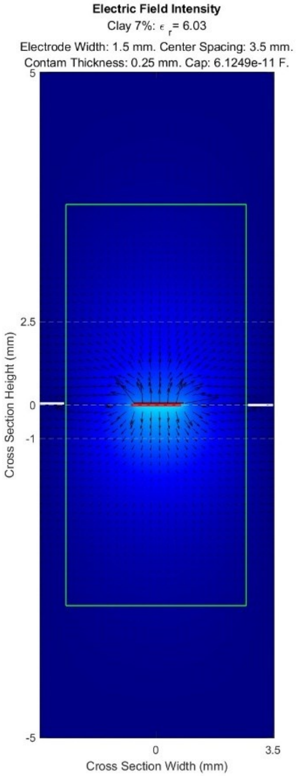
Electric Field Intensity
Clay 7%: ϵ_r= 6.03
Electrode Width: 1.5 mm. Center Spacing: 3.5 mm.
Contam Thickness: 0.25 mm. Cap: 6.1249e-11 F.

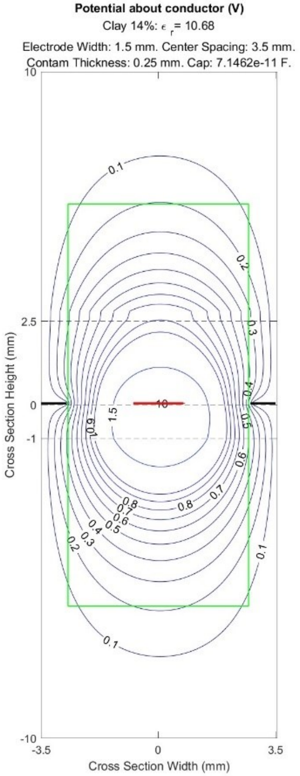
Potential about conductor (V)
Clay 14%: ϵ_r = 10.68
Electrode Width: 1.5 mm. Center Spacing: 3.5 mm.
Contam Thickness: 0.25 mm. Cap: 7.1462e-11 F.
Cross Section Height (mm)
Cross Section Width (mm)
10
2.5
0
-1
-10
-3.5
0
3.5
0.1
0.2
0.3
0.4
0.5
0.6
0.7
0.8
0.9
1.5
10

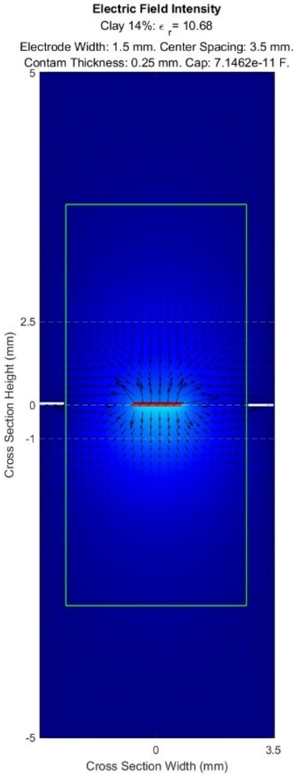
Electric Field Intensity
Clay 14%: ϵ_r = 10.68
Electrode Width: 1.5 mm. Center Spacing: 3.5 mm.
Contam Thickness: 0.25 mm. Cap: 7.1462e-11 F.
Cross Section Height (mm)
Cross Section Width (mm)
5
2.5
0
-1
-5
0
3.5

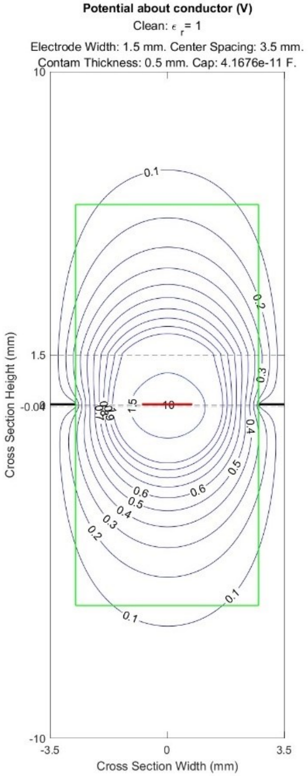
Potential about conductor (V)
Clean: ϵ_r = 1
Electrode Width: 1.5 mm. Center Spacing: 3.5 mm.
Contam Thickness: 0.5 mm. Cap: 4.1676e-11 F.
Cross Section Height (mm)
Cross Section Width (mm)
10
1.5
-0.04
-10
-3.5
0
3.5
0.1
0.2
0.3
0.4
0.5
0.6
1.5
10

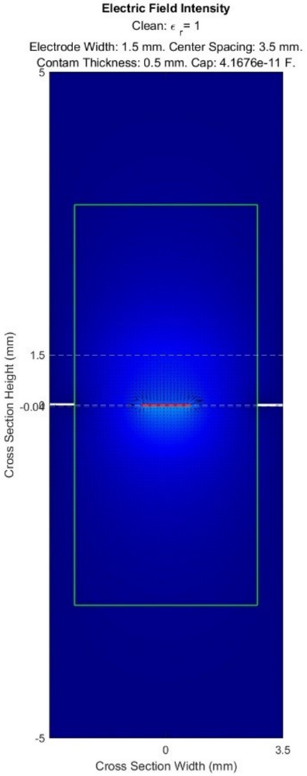
Electric Field Intensity
Clean: ϵ_r = 1
Electrode Width: 1.5 mm. Center Spacing: 3.5 mm.
Contam Thickness: 0.5 mm. Cap: 4.1676e-11 F.
Cross Section Height (mm)
Cross Section Width (mm)
5
1.5
-0.04
-5
0
3.5

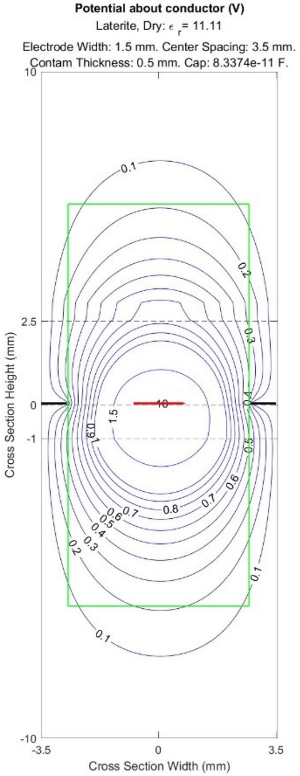
Potential about conductor (V)
Laterite, Dry: ϵ_r= 11.11
Electrode Width: 1.5 mm. Center Spacing: 3.5 mm.
Contam Thickness: 0.5 mm. Cap: 8.3374e-11 F.
Cross Section Height (mm)
Cross Section Width (mm)
10
2.5
0
-1
-10
-3.5
0
3.5
0.1
0.2
0.3
0.4
0.5
0.6
0.7
0.8
0.9
1.5
10

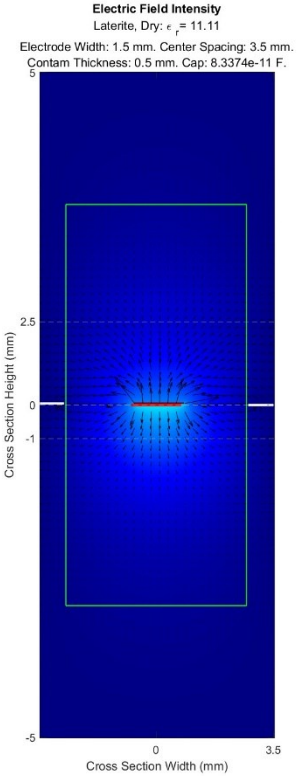
Electric Field Intensity
Laterite, Dry: ϵ_r= 11.11
Electrode Width: 1.5 mm. Center Spacing: 3.5 mm.
Contam Thickness: 0.5 mm. Cap: 8.3374e-11 F.
Cross Section Height (mm)
Cross Section Width (mm)
5
2.5
0
-1
-5
0
3.5

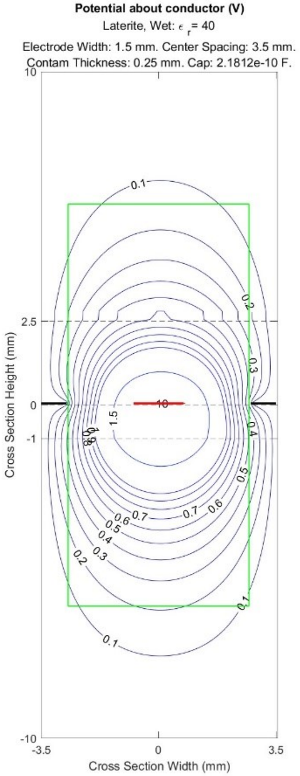
Potential about conductor (V)
Laterite, Wet: ϵ_r= 40
Electrode Width: 1.5 mm. Center Spacing: 3.5 mm.
Contam Thickness: 0.25 mm. Cap: 2.1812e-10 F.
Cross Section Height (mm)
Cross Section Width (mm)
10
2.5
0
-1
-10
-3.5
0
3.5
0.1
0.2
0.3
0.4
0.5
0.6
0.7
0.8
0.9
1.5
10

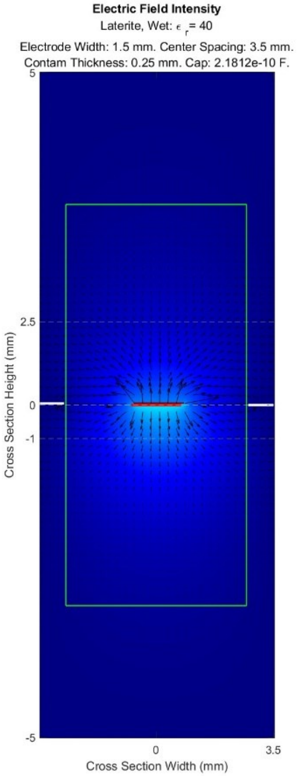
Electric Field Intensity
Laterite, Wet: ϵ_r= 40
Electrode Width: 1.5 mm. Center Spacing: 3.5 mm.
Contam Thickness: 0.25 mm. Cap: 2.1812e-10 F.
Cross Section Height (mm)
Cross Section Width (mm)
5
2.5
0
-1
-5
0
3.5

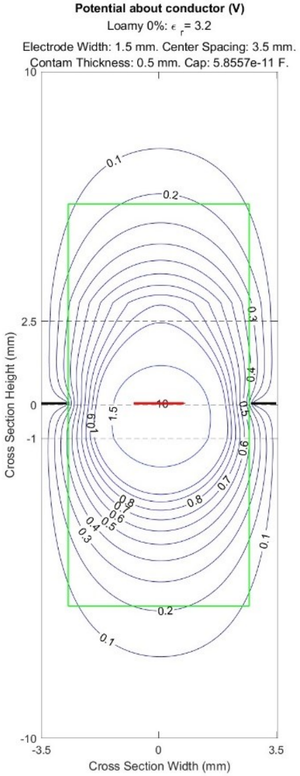
Potential about conductor (V)
Loamy 0%: ϵ r = 3.2
Electrode Width: 1.5 mm. Center Spacing: 3.5 mm.
Contam Thickness: 0.5 mm. Cap: 5.8557e-11 F.
Cross Section Height (mm)
Cross Section Width (mm)
10
2.5
0
-1
-10
-3.5
0
3.5
0.1
0.2
0.3
0.4
0.5
0.6
0.7
0.8
0.9
1
1.5
10

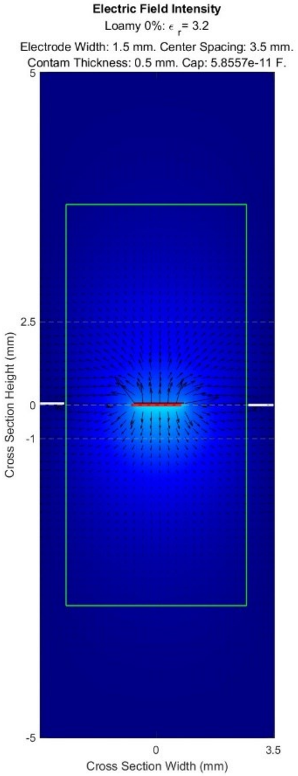
Electric Field Intensity
Loamy 0%: ϵ r = 3.2
Electrode Width: 1.5 mm. Center Spacing: 3.5 mm.
Contam Thickness: 0.5 mm. Cap: 5.8557e-11 F.
Cross Section Height (mm)
Cross Section Width (mm)
5
2.5
0
-1
-5
0
3.5

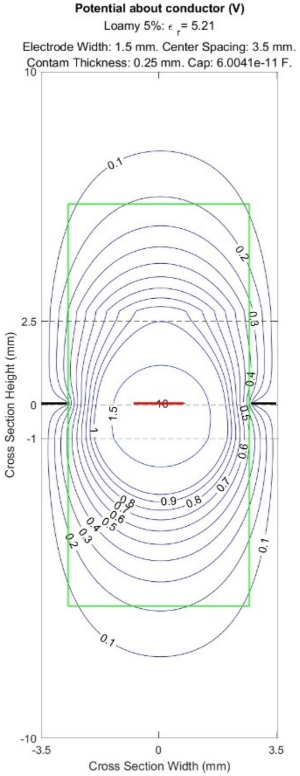
Potential about conductor (V)
Loamy 5%: ϵ r = 5.21
Electrode Width: 1.5 mm. Center Spacing: 3.5 mm.
Contam Thickness: 0.25 mm. Cap: 6.0041e-11 F.
Cross Section Height (mm)
Cross Section Width (mm)
10
2.5
0
-1
-10
-3.5
0
3.5
0.1
0.2
0.3
0.4
0.5
0.6
0.7
0.8
0.9
1
1.5
10

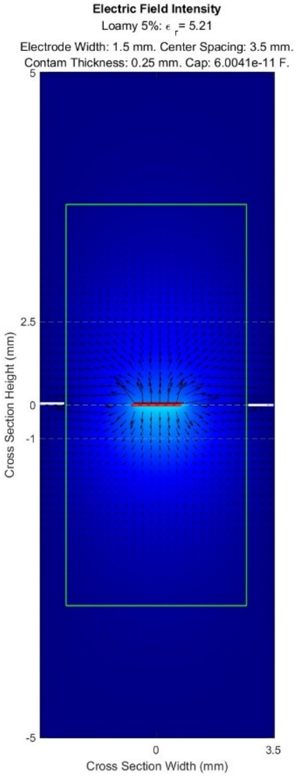
Electric Field Intensity
Loamy 5%: ϵ r = 5.21
Electrode Width: 1.5 mm. Center Spacing: 3.5 mm.
Contam Thickness: 0.25 mm. Cap: 6.0041e-11 F.
Cross Section Height (mm)
Cross Section Width (mm)
5
2.5
0
-1
-5
0
3.5

Potential about conductor (V)
Loamy 5%: $\epsilon_r = 5.21$
Electrode Width: 1.5 mm. Center Spacing: 3.5 mm.
Contam Thickness: 0.25 mm. Cap: 6.0041e-11 F.

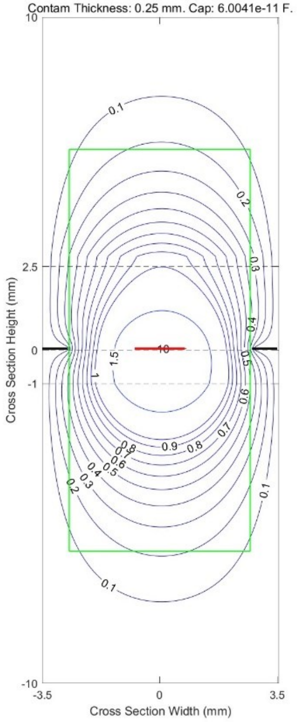

Electric Field Intensity
Loamy 5%: $\epsilon_r = 5.21$
Electrode Width: 1.5 mm. Center Spacing: 3.5 mm.
Contam Thickness: 0.25 mm. Cap: 6.0041e-11 F.

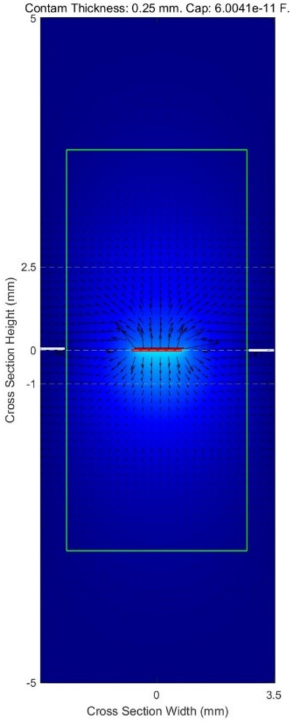

Potential about conductor (V)
Loamy 10%: $\epsilon_r = 8.94$
Electrode Width: 1.5 mm. Center Spacing: 3.5 mm.
Contam Thickness: 0.25 mm. Cap: 6.7011e-11 F.

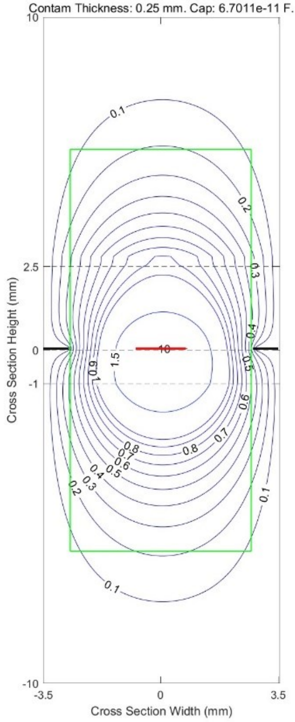

Electric Field Intensity
Loamy 10%: $\epsilon_r = 8.94$
Electrode Width: 1.5 mm. Center Spacing: 3.5 mm.
Contam Thickness: 0.25 mm. Cap: 6.7011e-11 F.

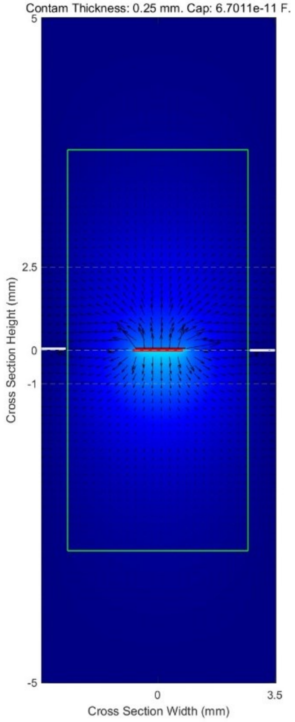

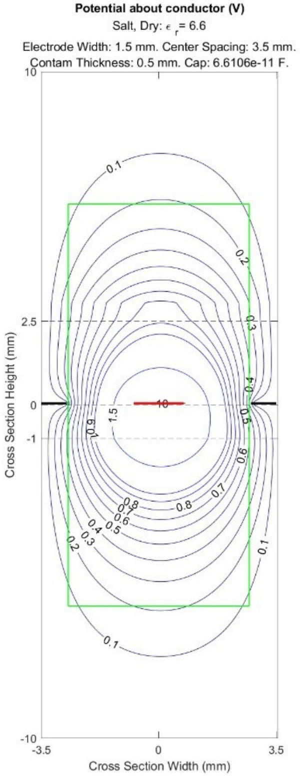
Potential about conductor (V)
Salt, Dry: ϵ_r= 6.6
Electrode Width: 1.5 mm. Center Spacing: 3.5 mm.
Contam Thickness: 0.5 mm. Cap: 6.6106e-11 F.
Cross Section Height (mm)
Cross Section Width (mm)
10
2.5
0
-1
-10
-3.5
0
3.5
0.1
0.2
0.3
0.4
0.5
0.6
0.7
0.8
0.9
1.5
10

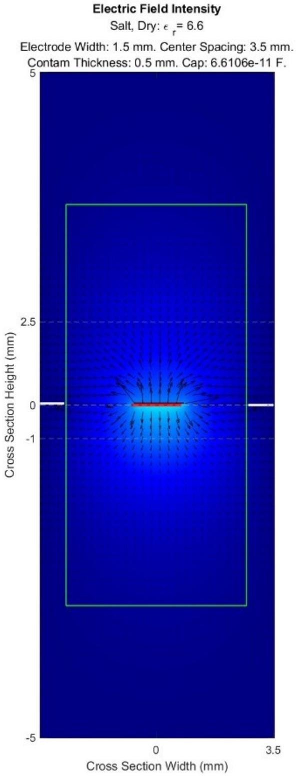
Electric Field Intensity
Salt, Dry: ϵ_r= 6.6
Electrode Width: 1.5 mm. Center Spacing: 3.5 mm.
Contam Thickness: 0.5 mm. Cap: 6.6106e-11 F.
Cross Section Height (mm)
Cross Section Width (mm)
5
2.5
0
-1
-5
0
3.5

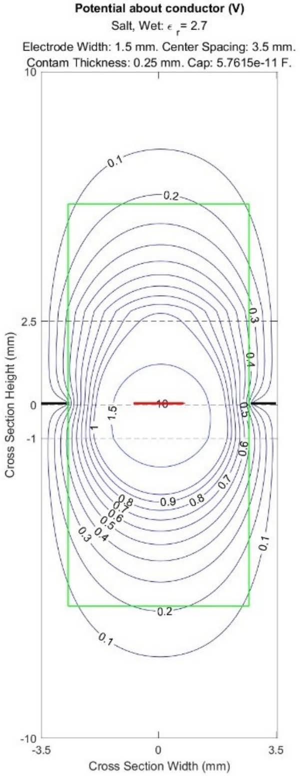
Potential about conductor (V)
Salt, Wet: ϵ_r= 2.7
Electrode Width: 1.5 mm. Center Spacing: 3.5 mm.
Contam Thickness: 0.25 mm. Cap: 5.7615e-11 F.
Cross Section Height (mm)
Cross Section Width (mm)
10
2.5
0
-1
-10
-3.5
0
3.5
0.1
0.2
0.3
0.4
0.5
0.6
0.7
0.8
0.9
1
1.5
10

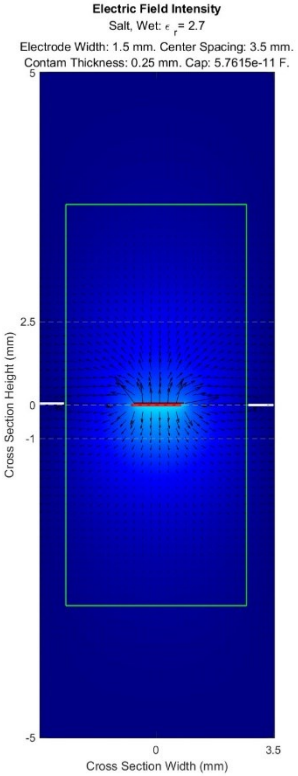
Electric Field Intensity
Salt, Wet: ϵ_r= 2.7
Electrode Width: 1.5 mm. Center Spacing: 3.5 mm.
Contam Thickness: 0.25 mm. Cap: 5.7615e-11 F.
Cross Section Height (mm)
Cross Section Width (mm)
5
2.5
0
-1
-5
0
3.5

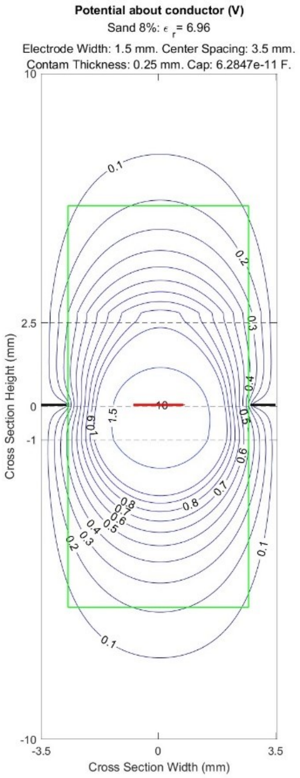
Potential about conductor (V)
Sand 8%: ϵ_r= 6.96
Electrode Width: 1.5 mm. Center Spacing: 3.5 mm.
Contam Thickness: 0.25 mm. Cap: 6.2847e-11 F.
0.1
0.2
0.3
0.4
0.5
0.6
0.7
0.8
0.9
1.5
10
Cross Section Height (mm)
Cross Section Width (mm)
10
2.5
0
-1
-10
-3.5
0
3.5

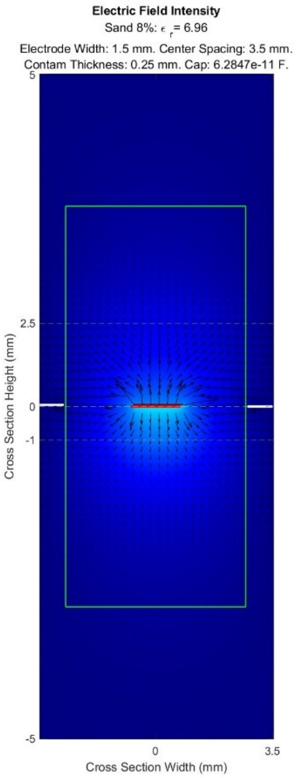
Electric Field Intensity
Sand 8%: ϵ_r= 6.96
Electrode Width: 1.5 mm. Center Spacing: 3.5 mm.
Contam Thickness: 0.25 mm. Cap: 6.2847e-11 F.
Cross Section Height (mm)
Cross Section Width (mm)
5
2.5
0
-1
-5
0
3.5

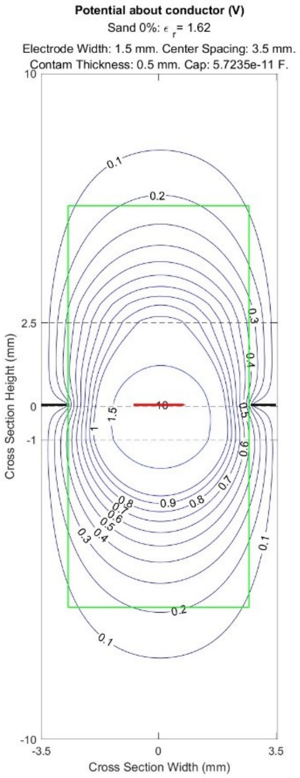
Potential about conductor (V)
Sand 0%: ϵ_r= 1.62
Electrode Width: 1.5 mm. Center Spacing: 3.5 mm.
Contam Thickness: 0.5 mm. Cap: 5.7235e-11 F.
0.1
0.2
0.3
0.4
0.5
0.6
0.7
0.8
0.9
1
1.5
10
Cross Section Height (mm)
Cross Section Width (mm)
10
2.5
0
-1
-10
-3.5
0
3.5

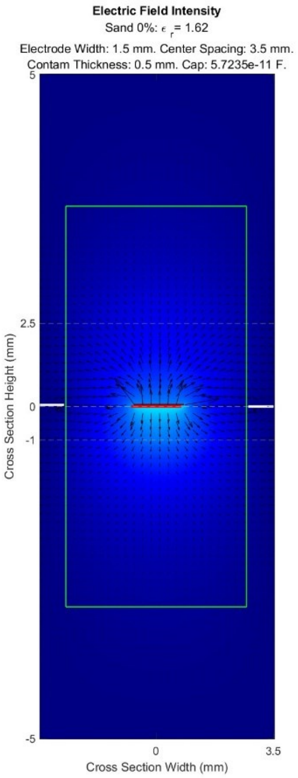
Electric Field Intensity
Sand 0%: ϵ_r= 1.62
Electrode Width: 1.5 mm. Center Spacing: 3.5 mm.
Contam Thickness: 0.5 mm. Cap: 5.7235e-11 F.
Cross Section Height (mm)
Cross Section Width (mm)
5
2.5
0
-1
-5
0
3.5

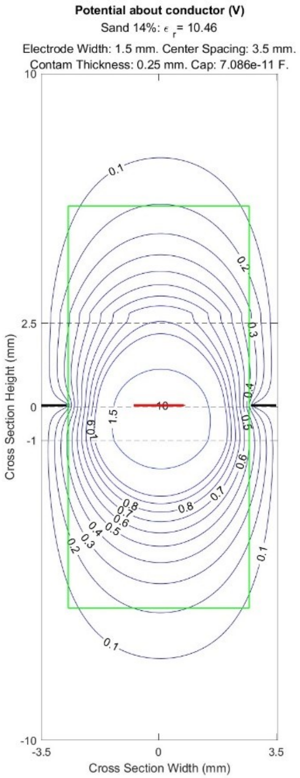
Potential about conductor (V)
Sand 14%: ϵ_r= 10.46
Electrode Width: 1.5 mm. Center Spacing: 3.5 mm.
Contam Thickness: 0.25 mm. Cap: 7.086e-11 F.
Cross Section Height (mm)
Cross Section Width (mm)
10
2.5
0
-1
-10
-3.5
0
3.5
0.1
0.2
0.3
0.4
0.5
0.6
0.7
0.8
0.9
1.5
10

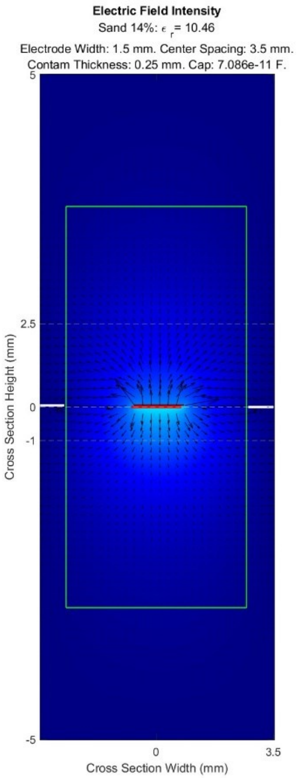
Electric Field Intensity
Sand 14%: ϵ_r= 10.46
Electrode Width: 1.5 mm. Center Spacing: 3.5 mm.
Contam Thickness: 0.25 mm. Cap: 7.086e-11 F.
Cross Section Height (mm)
Cross Section Width (mm)
5
2.5
0
-1
-5
0
3.5

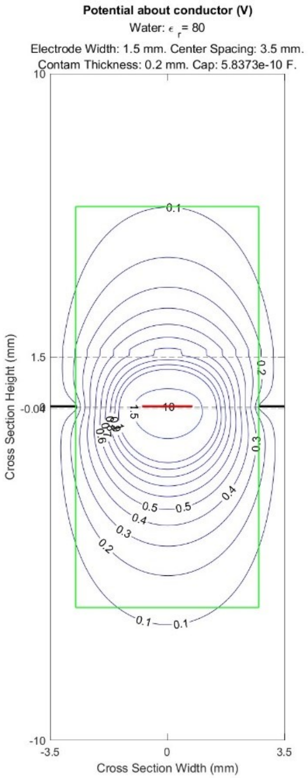
Potential about conductor (V)
Water: ϵ_r= 80
Electrode Width: 1.5 mm. Center Spacing: 3.5 mm.
Contam Thickness: 0.2 mm. Cap: 5.8373e-10 F.
Cross Section Height (mm)
Cross Section Width (mm)
10
1.5
-0.0
-10
-3.5
0
3.5
0.1
0.2
0.3
0.4
0.5
0.6
1.5
10

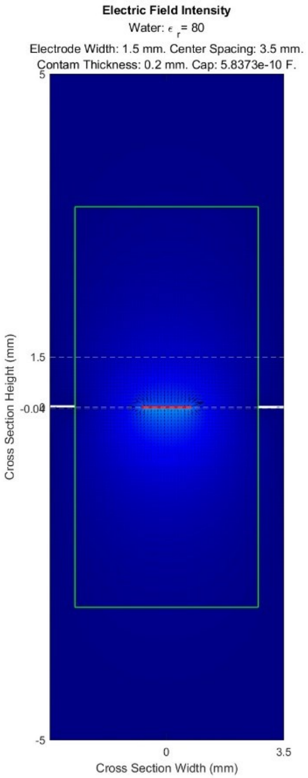
Electric Field Intensity
Water: ϵ_r= 80
Electrode Width: 1.5 mm. Center Spacing: 3.5 mm.
Contam Thickness: 0.2 mm. Cap: 5.8373e-10 F.
Cross Section Height (mm)
Cross Section Width (mm)
5
1.5
-0.0
-5
0
3.5

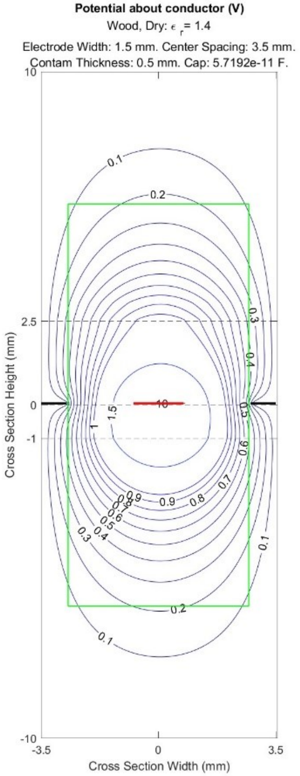
Potential about conductor (V)
Wood, Dry: ϵ_r= 1.4
Electrode Width: 1.5 mm. Center Spacing: 3.5 mm.
Contam Thickness: 0.5 mm. Cap: 5.7192e-11 F.
10
2.5
0
-1
-10
-3.5
0
3.5
Cross Section Height (mm)
Cross Section Width (mm)
0.1
0.2
0.3
0.4
0.5
0.6
0.7
0.8
0.9
1
1.5
10

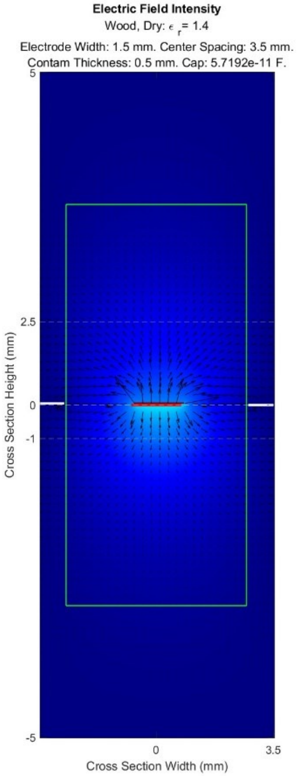
Electric Field Intensity
Wood, Dry: ϵ_r= 1.4
Electrode Width: 1.5 mm. Center Spacing: 3.5 mm.
Contam Thickness: 0.5 mm. Cap: 5.7192e-11 F.
5
2.5
0
-1
-5
0
3.5
Cross Section Height (mm)
Cross Section Width (mm)

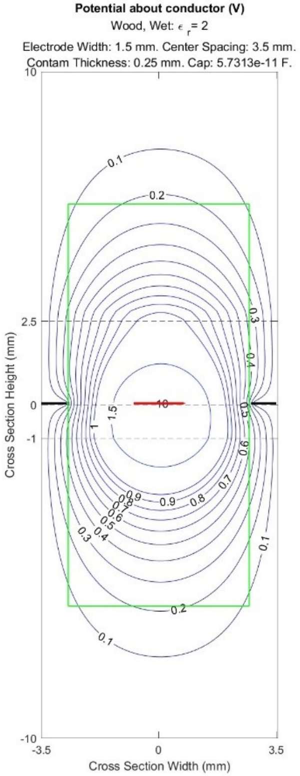
Potential about conductor (V)
Wood, Wet: ϵ_r= 2
Electrode Width: 1.5 mm. Center Spacing: 3.5 mm.
Contam Thickness: 0.25 mm. Cap: 5.7313e-11 F.
10
2.5
0
-1
-10
-3.5
0
3.5
Cross Section Height (mm)
Cross Section Width (mm)
0.1
0.2
0.3
0.4
0.5
0.6
0.7
0.8
0.9
1
1.5
10

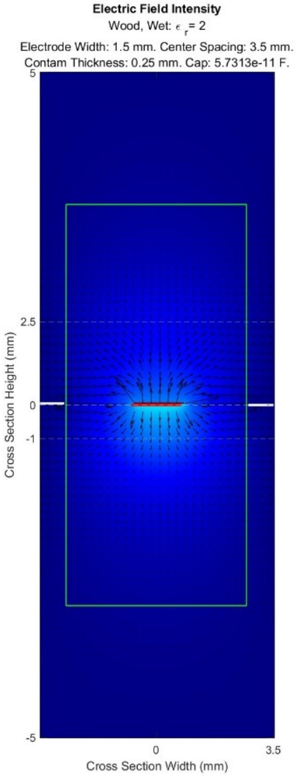
Electric Field Intensity
Wood, Wet: ϵ_r= 2
Electrode Width: 1.5 mm. Center Spacing: 3.5 mm.
Contam Thickness: 0.25 mm. Cap: 5.7313e-11 F.
5
2.5
0
-1
-5
0
3.5
Cross Section Height (mm)
Cross Section Width (mm)

Simulation Capacitance Results

For all contaminants simulated.

Electrode Spacing (mm)	Clean Sensor (Capacitance, F)								
	1	8.1137E-11							
	1.5	6.39146E-11	9.40943E-11						
	2	5.43736E-11	7.33384E-11	1.00722E-10					
	2.5	4.858272E-11	6.17885E-11	7.81271E-11	1.04554E-10				
	3	4.33329E-11	5.41951E-11	6.55178E-11	8.09048E-11	1.06926E-10			
	3.5	3.94412E-11	4.84204E-11	5.72E-11	6.7694E-11	8.26582E-11	1.08484E-10		
	4	3.62091E-11	4.38208E-11	5.09775E-11	5.90182E-11	6.90972E-11	8.38507E-11	1.09572E-10	
	4.5	3.34752E-11	4.0049E-11	4.60374E-11	5.25113E-11	6.0201E-11	7.00829E-11	8.47211E-11	1.10379E-10
		0.5	**1**	**1.5**	**2**	**2.5**	**3**	**3.5**	**4**
	Electrode Width (mm)								

Electrode Spacing (mm)	Ash, Wet (Capacitance, F)								
	1	3.48244E-09							
	1.5	1.2077E-08	1.22173E-08						
	2	2.21234E-08	2.41143E-08	2.29416E-08					
	2.5	3.14862E-08	3.55961E-08	3.60931E-08	3.39493E-08				
	3	3.96796E-08	4.57712E-08	4.80187E-08	4.75771E-08	4.48206E-08			
	3.5	4.66193E-08	5.44694E-08	5.84474E-08	5.96466E-08	5.86346E-08	5.55164E-08		
	4	5.2402E-08	6.17672E-08	6.72876E-08	7.01645E-08	7.07474E-08	6.93963E-08	6.61E-08	
	4.5	5.71774E-08	6.78255E-08	7.46788E-08	7.9049E-08	8.1294E-08	8.15111E-08	8E-08	7.65E-08
		0.5	**1**	**1.5**	**2**	**2.5**	**3**	**3.5**	**4**
	Electrode Width (mm)								

Electrode Spacing (mm)		Ash, Dry (Capacitance, F)							
	1	9.26475E-10							
	1.5	3.04803E-09	3.10847E-09						
	2	5.53236E-09	6.04493E-09	5.77755E-09					
	2.5	7.84887E-09	8.87852E-09	9.01808E-09	8.50925E-09				
	3	9.87093E-09	1.13882E-08	1.19529E-08	1.18587E-08	1.11983E-08			
	3.5	1.15774E-08	1.35260E-08	1.45156E-08	1.48187E-08	1.45828E-08	1.38339E-08		
	4	1.29930E-08	1.53112E-08	1.66780E-08	1.73921E-08	1.75416E-08	1.72222E-08	1.64236E-08	
	4.5	1.41555E-08	1.67846E-08	1.84755E-08	1.95539E-08	2.01097E-08	2.01680E-08	1.97997E-08	1.89742E-08
		0.5	**1**	**1.5**	**2**	**2.5**	**3**	**3.5**	**4**
		Electrode Width (mm)							

Electrode Spacing (mm)		Cement, Wet (Capacitance, F)							
	1	2.382847E-08							
	1.5	8.401307E-08	8.480926E-08						
	2	1.544240E-07	1.682306E-07	1.598576E-07					
	2.5	2.201707E-07	2.488767E-07	2.522523E-07	2.370734E-07				
	3	2.778615E-07	3.205269E-07	3.362348E-07	3.330408E-07	3.135449E-07			
	3.5	3.268880E-07	3.819891E-07	4.099094E-07	4.182970E-07	4.110948E-07	3.890261E-07		
	4	3.679070E-07	4.337766E-07	4.726281E-07	4.928764E-07	4.969575E-07	4.873566E-07	4.637855E-07	
	4.5	4.019445E-07	4.769892E-07	5.253400E-07	5.561961E-07	5.720519E-07	5.735723E-07	5.625314E-07	5.380812E-07
		0.5	**1**	**1.5**	**2**	**2.5**	**3**	**3.5**	**4**
		Electrode Width (mm)							

Cement, Dry (Capacitance, F)

Electrode Spacing (mm)	**1**	6.001322E-09							
	1.5	2.099647E-08	2.123680E-08						
	2	3.854936E-08	4.203283E-08	3.998472E-08					
	2.5	5.496802E-08	6.213796E-08	6.301696E-08	5.926813E-08				
	3	6.937244E-08	8.002439E-08	8.394822E-08	8.318466E-08	7.835691E-08			
	3.5	8.160802E-08	9.536128E-08	1.023298E-07	1.044242E-07	1.026581E-07	9.718801E-08		
	4	9.183853E-08	1.082757E-07	1.179689E-07	1.230194E-07	1.240370E-07	1.216713E-07	1.158272E-07	
	4.5	1.003208E-07	1.190426E-07	1.311020E-07	1.387956E-07	1.427470E-07	1.431243E-07	1.403992E-07	1.343375E-07
		0.5	**1**	**1.5**	**2**	**2.5**	**3**	**3.5**	**4**
		Electrode Width (mm)							

Charcoal, Dry (Capacitance, F)

Electrode Spacing (mm)	**1**	8.113324E-11							
	1.5	6.394392E-11	9.416003E-11						
	2	5.451164E-11	7.356089E-11	1.009968E-10					
	2.5	4.843387E-11	6.219720E-11	7.862513E-11	1.051032E-10				
	3	4.376006E-11	5.477829E-11	6.620757E-11	8.167264E-11	1.077363E-10			
	3.5	3.998094E-11	4.913868E-11	5.806942E-11	6.862134E-11	8.364874E-11	1.095078E-10		
	4	3.683319E-11	4.463527E-11	5.192504E-11	6.006114E-11	7.020554E-11	8.500923E-11	1.107559E-10	
	4.5	3.415870E-11	4.092714E-11	4.705232E-11	5.362686E-11	6.138954E-11	7.132129E-11	8.599998E-11	1.116784E-10
		0.5	**1**	**1.5**	**2**	**2.5**	**3**	**3.5**	**4**
		Electrode Width (mm)							

Charcoal, Wet (Capacitance, F)

Electrode Spacing (mm)								
1	8.186106E-11							
1.5	6.594956E-11	9.621359E-11						
2	5.750786E-11	7.687074E-11	1.041890E-10					
2.5	5.202053E-11	6.625741E-11	8.279362E-11	1.090878E-10				
3	4.762455E-11	5.921400E-11	7.086683E-11	8.635306E-11	1.122321E-10			
3.5	4.391909E-11	5.368298E-11	6.292143E-11	7.359180E-11	8.861712E-11	1.143220E-10		
4	4.072268E-11	4.912741E-11	5.676113E-11	6.509332E-11	7.532139E-11	9.013097E-11	1.157643E-10	
4.5	3.793087E-11	4.527744E-11	5.175308E-11	5.856051E-11	6.647721E-11	7.649191E-11	9.119708E-11	1.168030E-10
	0.5	**1**	**1.5**	**2**	**2.5**	**3**	**3.5**	**4**
	Electrode Width (mm)							

Clay 0% (Capacitance, F)

Electrode Spacing (mm)								
1	8.112481E-11							
1.5	6.391887E-11	9.413335E-11						
2	5.447096E-11	7.351391E-11	1.009497E-10					
2.5	4.838110E-11	6.213506E-11	7.855902E-11	1.050378E-10				
3	4.369935E-11	5.470586E-11	6.612923E-11	8.159171E-11	1.076564E-10			
3.5	3.991563E-11	4.906046E-11	5.798367E-11	6.853160E-11	8.355714E-11	1.094171E-10		
4	3.676568E-11	4.455446E-11	5.183592E-11	5.996673E-11	7.010815E-11	8.491029E-11	1.106576E-10	
4.5	3.409064E-11	4.084591E-11	4.696254E-11	5.353112E-11	6.128971E-11	7.121898E-11	8.589614E-11	1.115749E-10
	0.5	**1**	**1.5**	**2**	**2.5**	**3**	**3.5**	**4**
	Electrode Width (mm)							

Electrode Spacing (mm)	Clay 7% (Capacitance, F)							
1	8.162590E-11							
1.5	6.529151E-11	9.553950E-11						
2	5.651166E-11	7.576862E-11	1.031249E-10					
2.5	5.081374E-11	6.488825E-11	8.138569E-11	1.077403E-10				
3	4.631086E-11	5.770190E-11	6.927547E-11	8.475232E-11	1.106929E-10			
3.5	4.256858E-11	5.211957E-11	6.124862E-11	7.187581E-11	8.690039E-11	1.126576E-10		
4	3.937888E-11	4.756990E-11	5.508053E-11	6.334218E-11	7.353999E-11	8.834705E-11	1.140196E-10	
4.5	3.661929E-11	4.375913E-11	5.010845E-11	5.683194E-11	6.469370E-11	7.467951E-11	8.937594E-11	1.150078E-10
	0.5	**1**	**1.5**	**2**	**2.5**	**3**	**3.5**	**4**
	Electrode Width (mm)							

Electrode Spacing (mm)	Clay 14% (Capacitance, F)							
1	8.298764E-11							
1.5	6.919680E-11	9.952657E-11						
2	6.250899E-11	8.237847E-11	1.094833E-10					
2.5	5.814100E-11	7.317688E-11	8.987861E-11	1.158368E-10				
3	5.433564E-11	6.691298E-11	7.894265E-11	9.444235E-11	1.199728E-10			
3.5	5.085436E-11	6.168745E-11	7.146182E-11	8.232343E-11	9.731609E-11	1.227162E-10		
4	4.764933E-11	5.713438E-11	6.538045E-11	7.404945E-11	8.440122E-11	9.918637E-11	1.245801E-10	
4.5	4.470923E-11	5.310607E-11	6.021650E-11	6.743561E-11	7.560817E-11	8.573869E-11	1.004516E-10	1.258866E-10
	0.5	**1**	**1.5**	**2**	**2.5**	**3**	**3.5**	**4**
	Electrode Width (mm)							

		Laterite, Dry (Capacitance, F)							
Electrode Spacing (mm)	**1**	8.379613E-11							
	1.5	7.216577E-11	1.025658E-10						
	2	6.783847E-11	8.827538E-11	1.151666E-10					
	2.5	6.540867E-11	8.145480E-11	9.837868E-11	1.239383E-10				
	3	6.298198E-11	7.692281E-11	8.948790E-11	1.050064E-10	1.300595E-10			
	3.5	6.037561E-11	7.279406E-11	8.337448E-11	9.450977E-11	1.094203E-10	1.343387E-10		
	4	5.765165E-11	6.883586E-11	7.805700E-11	8.723711E-11	9.772528E-11	1.123952E-10	1.373463E-10	
	4.5	5.490578E-11	6.503731E-11	7.321141E-11	8.109181E-11	8.961617E-11	9.982347E-11	1.144288E-10	1.394816E-10
		0.5	**1**	**1.5**	**2**	**2.5**	**3**	**3.5**	**4**
		Electrode Width (mm)							

		Laterite, Wet (Capacitance, F)							
Electrode Spacing (mm)	**1**	9.673334E-11							
	1.5	1.133150E-10	1.442240E-10						
	2	1.362060E-10	1.629488E-10	1.863477E-10					
	2.5	1.540645E-10	1.812855E-10	1.997842E-10	2.196206E-10				
	3	1.650122E-10	1.936716E-10	2.114295E-10	2.261035E-10	2.446866E-10			
	3.5	1.701895E-10	1.994267E-10	2.181232E-10	2.315063E-10	2.445774E-10	2.631834E-10		
	4	1.711466E-10	2.001390E-10	2.192568E-10	2.333615E-10	2.447610E-10	2.574190E-10	2.766803E-10	
	4.5	1.692215E-10	1.973763E-10	2.163587E-10	2.308296E-10	2.427362E-10	2.534173E-10	2.662736E-10	2.864556E-10
		0.5	**1**	**1.5**	**2**	**2.5**	**3**	**3.5**	**4**
		Electrode Width (mm)							

Electrode Spacing (mm)	Loamy 0% (Capacitance, F)								
	1	8.118433E-11							
	1.5	6.409469E-11	9.431902E-11						
	2	5.475331E-11	7.383709E-11	1.012710E-10					
	2.5	4.874319E-11	6.255833E-11	7.900636E-11	1.054772E-10				
	3	4.411222E-11	5.519512E-11	6.665574E-11	8.213291E-11	1.081881E-10			
	3.5	4.035664E-11	4.958542E-11	5.855665E-11	6.912913E-11	8.416483E-11	1.100164E-10		
	4	3.721887E-11	4.509389E-11	5.242861E-11	6.059284E-11	7.075236E-11	8.556313E-11	1.113043E-10	
	4.5	3.454532E-11	4.138584E-11	4.755729E-11	5.416377E-11	6.194818E-11	7.189276E-11	8.657871E-11	1.122541E-10
		0.5	**1**	**1.5**	**2**	**2.5**	**3**	**3.5**	**4**
	Electrode Width (mm)								

Electrode Spacing (mm)	Loamy 5% (Capacitance, F)								
	1	8.145335E-11							
	1.5	6.481414E-11	9.504918E-11						
	2	5.579275E-11	7.497082E-11	1.023524E-10					
	2.5	4.994470E-11	6.389970E-11	8.036629E-11	1.067618E-10				
	3	4.536587E-11	5.661144E-11	6.812525E-11	8.359231E-11	1.095744E-10			
	3.5	4.159757E-11	5.099283E-11	6.004062E-11	7.063409E-11	8.565519E-11	1.114471E-10		
	4	3.841275E-11	4.644767E-11	5.386751E-11	6.207607E-11	7.224959E-11	8.705205E-11	1.127501E-10	
	4.5	3.567612E-11	4.266508E-11	4.892158E-11	5.558268E-11	6.340277E-11	7.336547E-11	8.805303E-11	1.137010E-10
		0.5	**1**	**1.5**	**2**	**2.5**	**3**	**3.5**	**4**
	Electrode Width (mm)								

Loamy 10% (Capacitance, F)

Electrode Spacing (mm)								
1	8.241488E-11							
1.5	6.752860E-11	9.782650E-11						
2	5.992326E-11	7.953432E-11	1.067527E-10					
2.5	5.496367E-11	6.958796E-11	8.620816E-11	1.123450E-10				
3	5.084128E-11	6.290749E-11	7.474474E-11	9.024246E-11	1.159595E-10			
3.5	4.723518E-11	5.751322E-11	6.701135E-11	7.777753E-11	9.279276E-11	1.183576E-10		
4	4.402855E-11	5.295131E-11	6.088010E-11	6.937684E-11	7.966887E-11	9.447267E-11	1.199976E-10	
4.5	4.116146E-11	4.901055E-11	5.579088E-11	6.279758E-11	7.084051E-11	8.091579E-11	9.563076E-11	1.211612E-10
	0.5	**1**	**1.5**	**2**	**2.5**	**3**	**3.5**	**4**
	Electrode Width (mm)							

Salt, Wet (Capacitance, F)

Electrode Spacing (mm)								
1	8.111829E-11							
1.5	6.389723E-11	9.409708E-11						
2	5.440762E-11	7.341459E-11	1.008288E-10					
2.5	4.825638E-11	6.195822E-11	7.834314E-11	1.047996E-10				
3	4.351521E-11	5.445332E-11	6.582926E-11	8.125632E-11	1.073013E-10			
3.5	3.968170E-11	4.874746E-11	5.761504E-11	6.812365E-11	8.311944E-11	1.089632E-10		
4	3.649331E-11	4.419710E-11	5.141839E-11	5.950512E-11	6.961531E-11	8.439307E-11	1.101271E-10	
4.5	3.379029E-11	4.045808E-11	4.651264E-11	5.303474E-11	6.075872E-11	7.066342E-11	8.532044E-11	1.109881E-10
	0.5	**1**	**1.5**	**2**	**2.5**	**3**	**3.5**	**4**
	Electrode Width (mm)							

		Salt, Dry (Capacitance, F)							
Electrode Spacing (mm)	**1**	8.203990E-11							
	1.5	6.665710E-11	9.695529E-11						
	2	5.882320E-11	7.836300E-11	1.056587E-10					
	2.5	5.385933E-11	6.839424E-11	8.503153E-11	1.112621E-10				
	3	4.984574E-11	6.183386E-11	7.366835E-11	8.920479E-11	1.150006E-10			
	3.5	4.638991E-11	5.661469E-11	6.610634E-11	7.688814E-11	9.193455E-11	1.175535E-10		
	4	4.333739E-11	5.223399E-11	6.016384E-11	6.866698E-11	7.896586E-11	9.378372E-11	1.193385E-10	
	4.5	4.061168E-11	4.845890E-11	5.525163E-11	6.226616E-11	7.030622E-11	8.037114E-11	9.508248E-11	1.206229E-10
		0.5	**1**	**1.5**	**2**	**2.5**	**3**	**3.5**	**4**
		Electrode Width (mm)							

		Sand 0% (Capacitance, F)							
Electrode Spacing (mm)	**1**	8.108223E-11							
	1.5	6.377827E-11	9.397078E-11						
	2	5.421022E-11	7.318943E-11	1.006055E-10					
	2.5	4.800365E-11	6.166500E-11	7.803560E-11	1.044995E-10				
	3	4.323063E-11	5.411976E-11	6.547366E-11	8.089408E-11	1.069483E-10			
	3.5	3.938251E-11	4.839584E-11	5.723519E-11	6.773134E-11	8.272400E-11	1.085764E-10		
	4	3.619082E-11	4.384196E-11	5.103227E-11	5.910105E-11	6.920325E-11	8.397878E-11	1.097197E-10	
	4.5	3.349150E-11	4.010828E-11	4.613131E-11	5.263271E-11	6.034365E-11	7.024189E-11	8.489617E-11	1.105685E-10
		0.5	**1**	**1.5**	**2**	**2.5**	**3**	**3.5**	**4**
		Electrode Width (mm)							

Electrode Spacing (mm)	Sand 8% (Capacitance, F)								
	1	8.185075E-11							
	1.5	6.592056E-11	9.618392E-11						
	2	5.746382E-11	7.682208E-11	1.041421E-10					
	2.5	5.196710E-11	6.619686E-11	8.273143E-11	1.090283E-10				
	3	4.756634E-11	5.914706E-11	7.079644E-11	8.628234E-11	1.121641E-10			
	3.5	4.385921E-11	5.361372E-11	6.284738E-11	7.351590E-11	8.854127E-11	1.142486E-10		
	4	4.066308E-11	4.905838E-11	5.668669E-11	6.501581E-11	7.524261E-11	9.005215E-11	1.156873E-10	
	4.5	3.787268E-11	4.521013E-11	5.168021E-11	5.848397E-11	6.639829E-11	7.641177E-11	9.111663E-11	1.167238E-10
		0.5	**1**	**1.5**	**2**	**2.5**	**3**	**3.5**	**4**
	Electrode Width (mm)								

Electrode Spacing (mm)	Sand 14% (Capacitance, F)								
	1	8.291184E-11							
	1.5	6.897424E-11	9.929992E-11						
	2	6.216221E-11	8.199733E-11	1.091177E-10					
	2.5	5.771339E-11	7.269412E-11	8.938526E-11	1.153679E-10				
	3	5.386410E-11	6.637271E-11	7.837673E-11	9.387661E-11	1.194327E-10			
	3.5	5.036497E-11	6.112321E-11	7.086050E-11	8.170959E-11	9.670581E-11	1.221287E-10		
	4	4.715894E-11	5.656799E-11	6.477130E-11	7.341730E-11	8.376143E-11	9.854967E-11	1.239618E-10	
	4.5	4.422813E-11	5.255080E-11	5.961661E-11	6.680717E-11	7.496255E-11	8.508611E-11	9.979994E-11	1.252484E-10
		0.5	**1**	**1.5**	**2**	**2.5**	**3**	**3.5**	**4**
	Electrode Width (mm)								

Electrode Spacing (mm)	Wood, Dry (Capacitance, F)							
1	8.125584E-11							
1.5	6.393223E-11	9.418071E-11						
2	5.434506E-11	7.335514E-11	1.008169E-10					
2.5	4.855392E-11	6.179326E-11	7.818574E-11	1.046926E-10				
3	4.331673E-11	5.421456E-11	6.557969E-11	8.102037E-11	1.071180E-10			
3.5	3.944651E-11	4.846228E-11	5.730679E-11	6.781384E-11	8.282767E-11	1.087249E-10		
4	3.623612E-11	4.388535E-11	5.107682E-11	5.915148E-11	6.926608E-11	8.406430E-11	1.098514E-10	
4.5	3.352150E-11	4.013337E-11	4.615487E-11	5.265888E-11	6.037748E-11	7.028988E-11	8.496828E-11	1.106880E-10
	0.5	**1**	**1.5**	**2**	**2.5**	**3**	**3.5**	**4**
	Electrode Width (mm)							

Electrode Spacing (mm)	Wood, Wet (Capacitance, F)							
1	8.125556E-11							
1.5	6.395030E-11	9.420212E-11						
2	5.438996E-11	7.340920E-11	1.008728E-10					
2.5	4.818234E-11	6.187476E-11	7.827323E-11	1.047798E-10				
3	4.340055E-11	5.431504E-11	6.568819E-11	8.113194E-11	1.072277E-10			
3.5	3.953963E-11	4.857364E-11	5.742811E-11	6.793947E-11	8.295447E-11	1.088491E-10		
4	3.633379E-11	4.400169E-11	5.120415E-11	5.928479E-11	6.940148E-11	8.419993E-11	1.099844E-10	
4.5	3.362050E-11	4.025076E-11	4.628359E-11	5.279459E-11	6.051689E-11	7.043027E-11	8.510864E-11	1.108261E-10
	0.5	**1**	**1.5**	**2**	**2.5**	**3**	**3.5**	**4**
	Electrode Width (mm)							

Electrode Spacing (mm)	Water (Capacitance, F)							
1	1.209425E-10							
1.5	2.002858E-10	2.321375E-10						
2	2.968703E-10	3.382341E-10	3.530963E-10					
2.5	3.825821E-10	4.395816E-10	4.618566E-10	4.661707E-10				
3	4.508423E-10	5.230518E-10	5.566843E-10	5.683121E-10	5.671771E-10			
3.5	5.018253E-10	5.859542E-10	6.320511E-10	6.532860E-10	6.592787E-10	6.560467E-10		
4	5.379066E-10	6.305282E-10	6.864142E-10	7.190889E-10	7.335375E-10	7.369343E-10	7.336143E-10	
4.5	5.618750E-10	6.599848E-10	7.228578E-10	7.644893E-10	7.896186E-10	8.005137E-10	8.031099E-10	8.008502E-10
	0.5	**1**	**1.5**	**2**	**2.5**	**3**	**3.5**	**4**
	Electrode Width (mm)							

Capacitance Per Unit Length Plots

For all contaminants simulated.

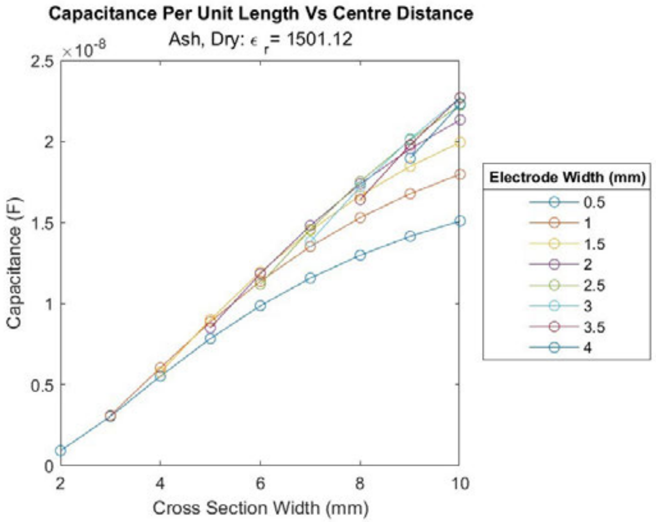

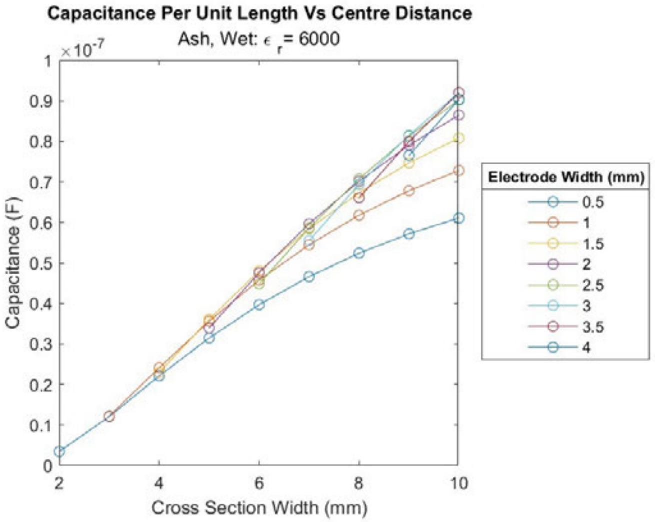

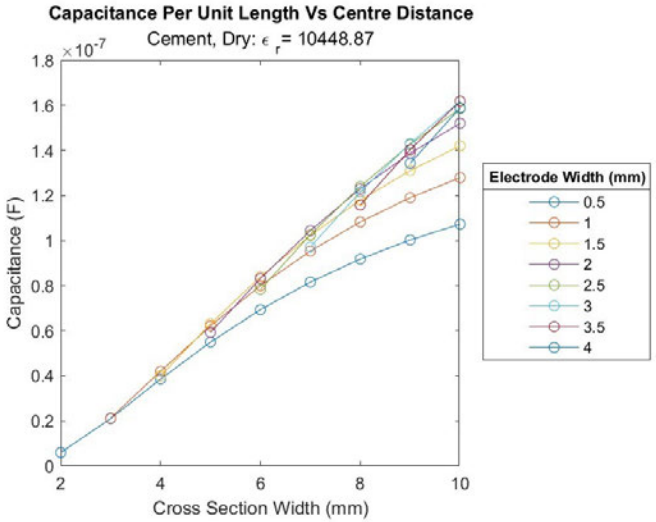

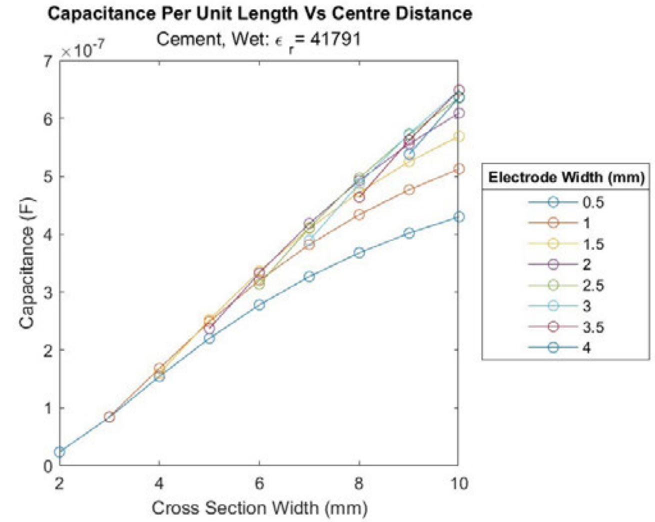

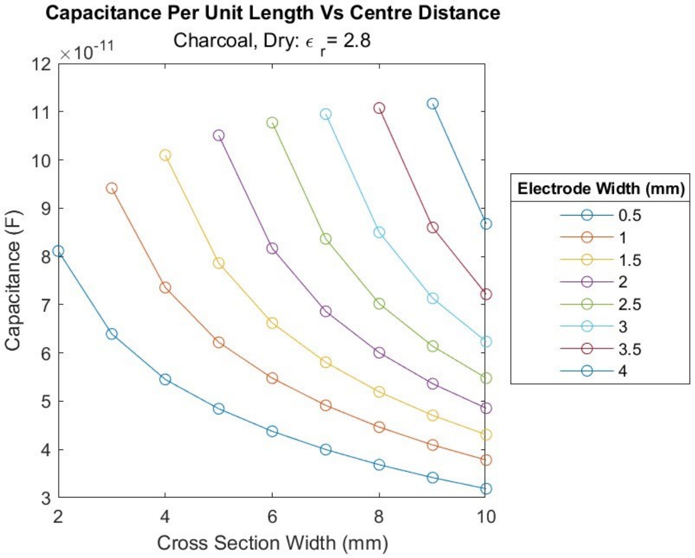
Capacitance Per Unit Length Vs Centre Distance
Charcoal, Dry: ϵ r= 2.8
×10-11
12
11
10
9
8
7
6
5
4
3
Capacitance (F)
2
4
6
8
10
Cross Section Width (mm)
Electrode Width (mm)
0.5
1
1.5
2
2.5
3
3.5
4

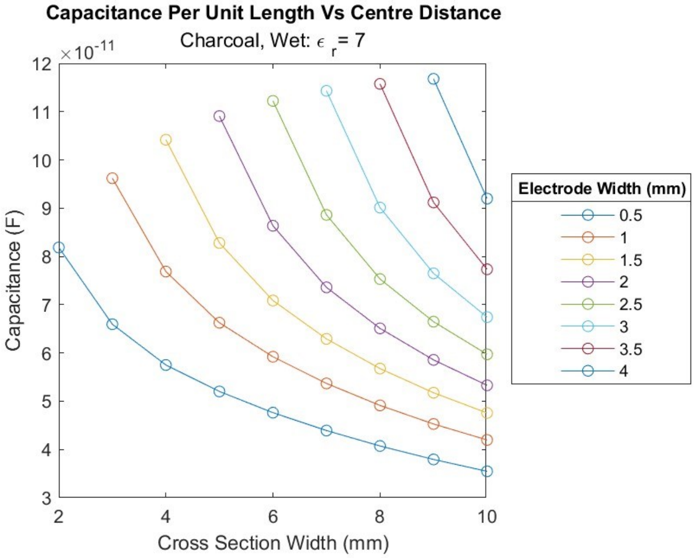
Capacitance Per Unit Length Vs Centre Distance
Charcoal, Wet: ϵ r= 7
×10-11
12
11
10
9
8
7
6
5
4
3
Capacitance (F)
2
4
6
8
10
Cross Section Width (mm)
Electrode Width (mm)
0.5
1
1.5
2
2.5
3
3.5
4

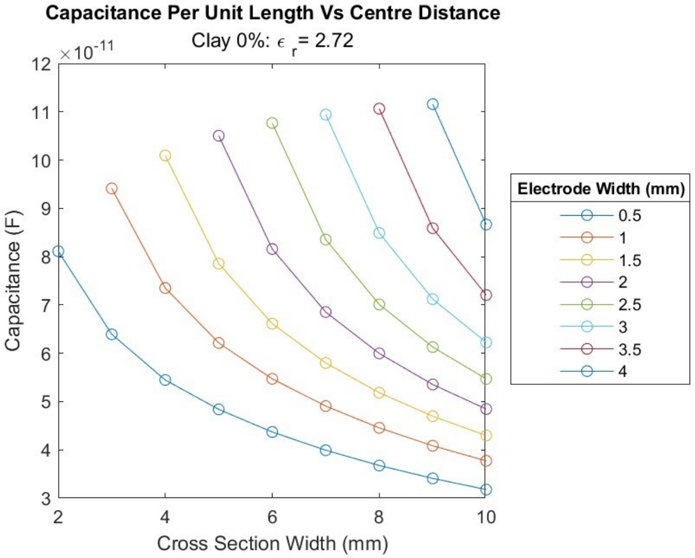
Capacitance Per Unit Length Vs Centre Distance
Clay 0%: ϵ r= 2.72
×10-11
12
11
10
9
8
7
6
5
4
3
Capacitance (F)
2
4
6
8
10
Cross Section Width (mm)
Electrode Width (mm)
0.5
1
1.5
2
2.5
3
3.5
4

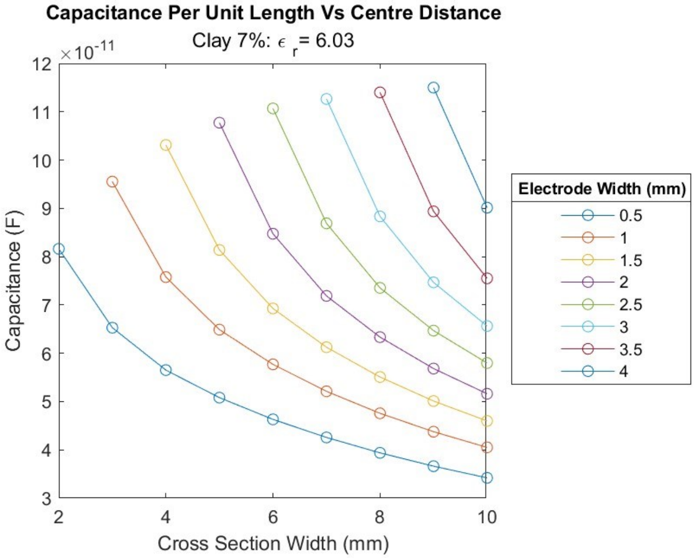
Capacitance Per Unit Length Vs Centre Distance
Clay 7%: ϵ r= 6.03
×10-11
12
11
10
9
8
7
6
5
4
3
Capacitance (F)
2
4
6
8
10
Cross Section Width (mm)
Electrode Width (mm)
0.5
1
1.5
2
2.5
3
3.5
4

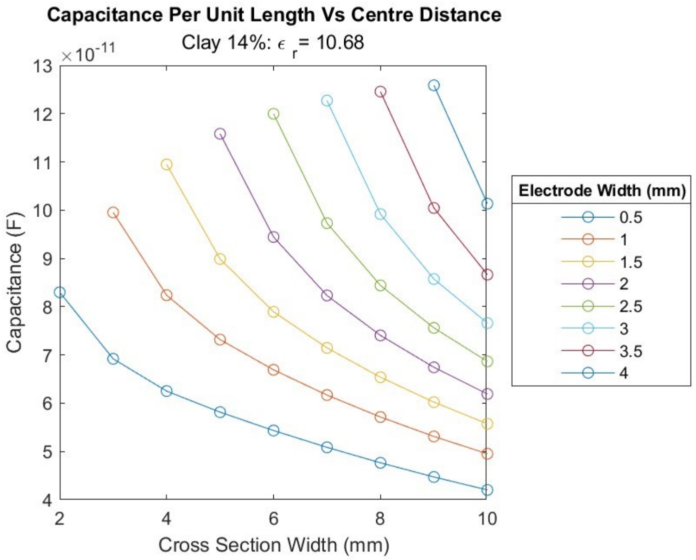
Capacitance Per Unit Length Vs Centre Distance

Clay 14%: ϵ_r= 10.68

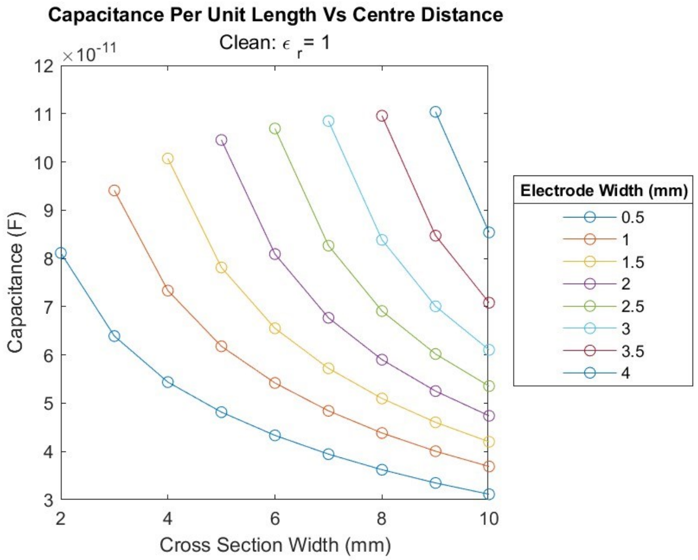
Capacitance Per Unit Length Vs Centre Distance

Clean: ϵ_r= 1

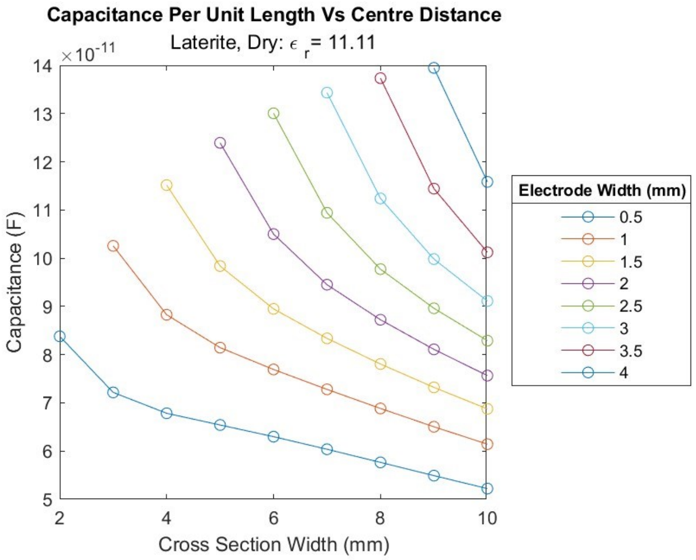
Capacitance Per Unit Length Vs Centre Distance

Laterite, Dry: ϵ_r= 11.11

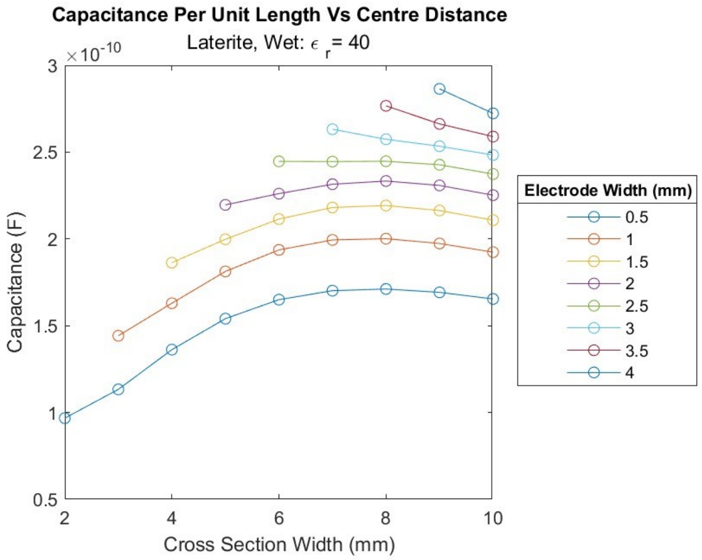
Capacitance Per Unit Length Vs Centre Distance

Laterite, Wet: ϵ_r= 40

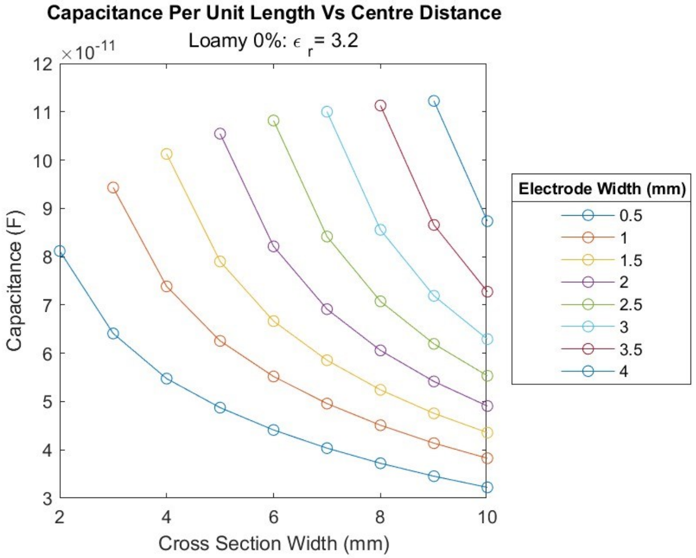
Capacitance Per Unit Length Vs Centre Distance
Loamy 0%: ϵ_r= 3.2
$\times 10^{-11}$
Capacitance (F)
12
11
10
9
8
7
6
5
4
3
Cross Section Width (mm)
2
4
6
8
10
Electrode Width (mm)
0.5
1
1.5
2
2.5
3
3.5
4

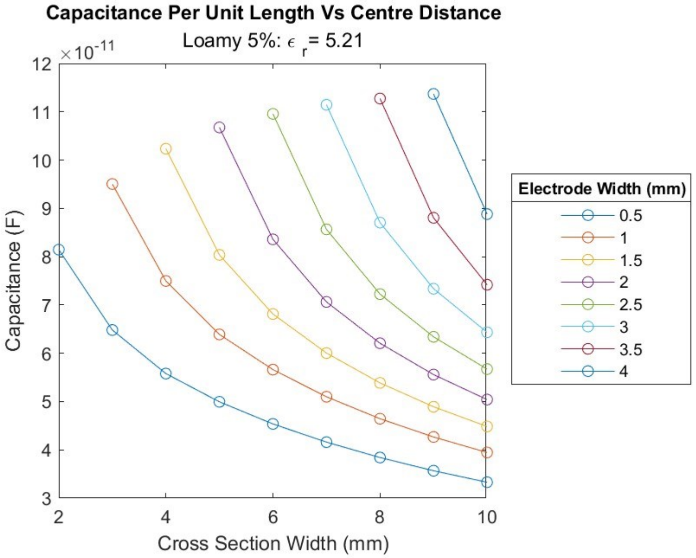
Capacitance Per Unit Length Vs Centre Distance
Loamy 5%: ϵ_r= 5.21
$\times 10^{-11}$
Capacitance (F)
12
11
10
9
8
7
6
5
4
3
Cross Section Width (mm)
2
4
6
8
10
Electrode Width (mm)
0.5
1
1.5
2
2.5
3
3.5
4

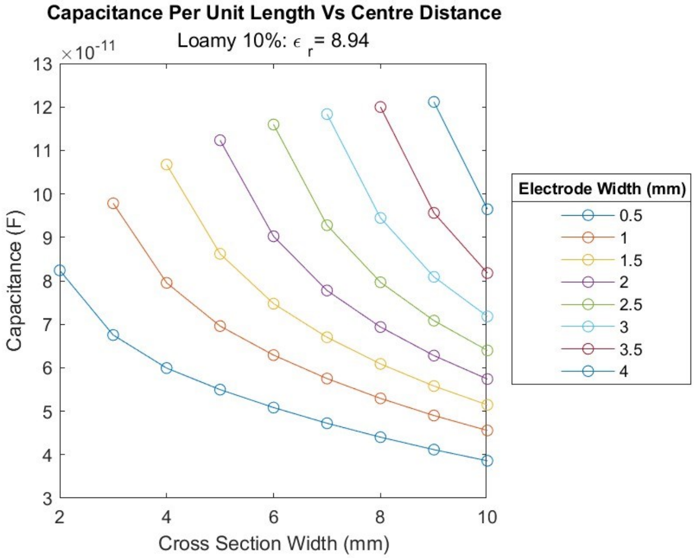
Capacitance Per Unit Length Vs Centre Distance
Loamy 10%: ϵ_r= 8.94
$\times 10^{-11}$
Capacitance (F)
13
12
11
10
9
8
7
6
5
4
3
Cross Section Width (mm)
2
4
6
8
10
Electrode Width (mm)
0.5
1
1.5
2
2.5
3
3.5
4

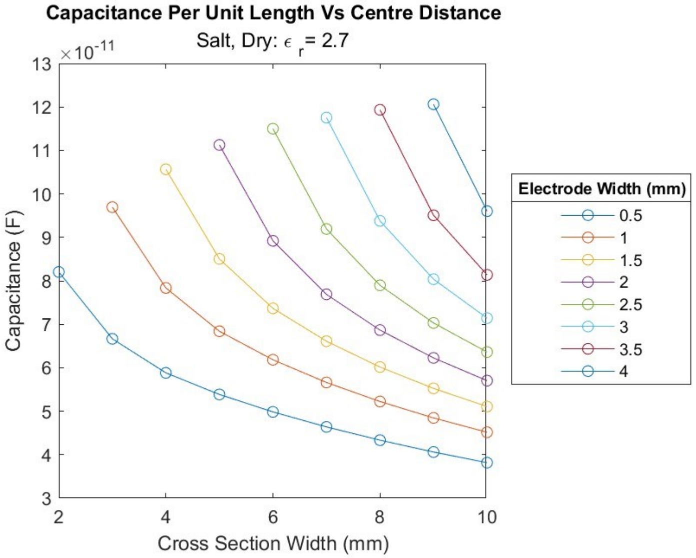
Capacitance Per Unit Length Vs Centre Distance
Salt, Dry: ϵ_r= 2.7
$\times 10^{-11}$
Capacitance (F)
13
12
11
10
9
8
7
6
5
4
3
Cross Section Width (mm)
2
4
6
8
10
Electrode Width (mm)
0.5
1
1.5
2
2.5
3
3.5
4

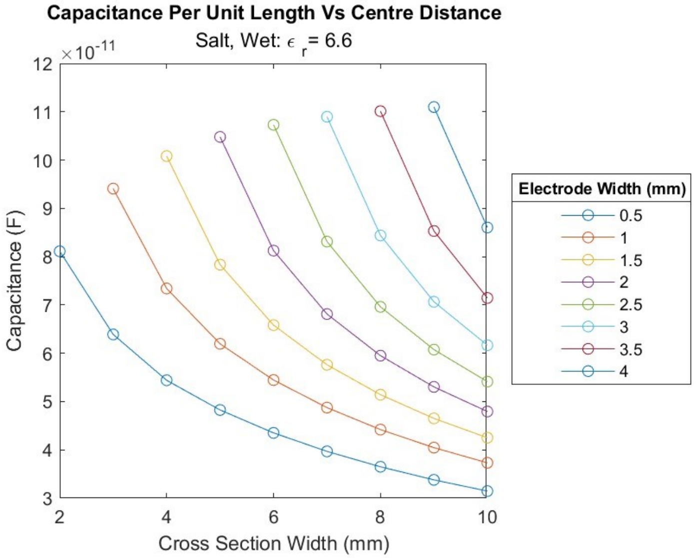
Capacitance Per Unit Length Vs Centre Distance

Salt, Wet: ϵ_r = 6.6

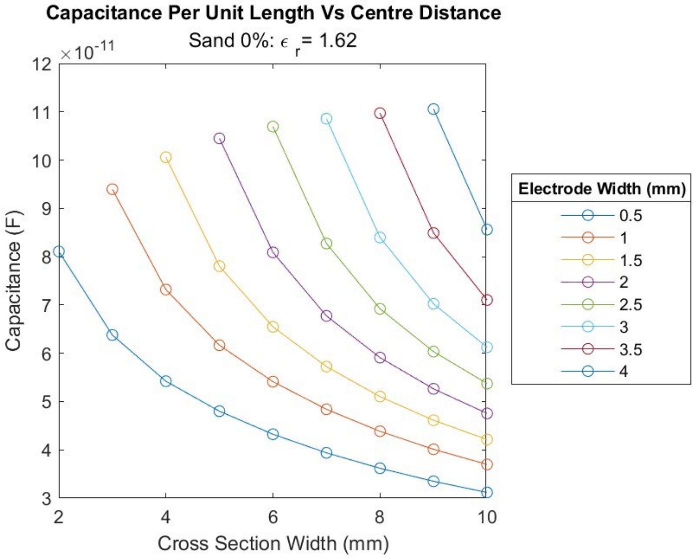
Capacitance Per Unit Length Vs Centre Distance

Sand 0%: ϵ_r = 1.62

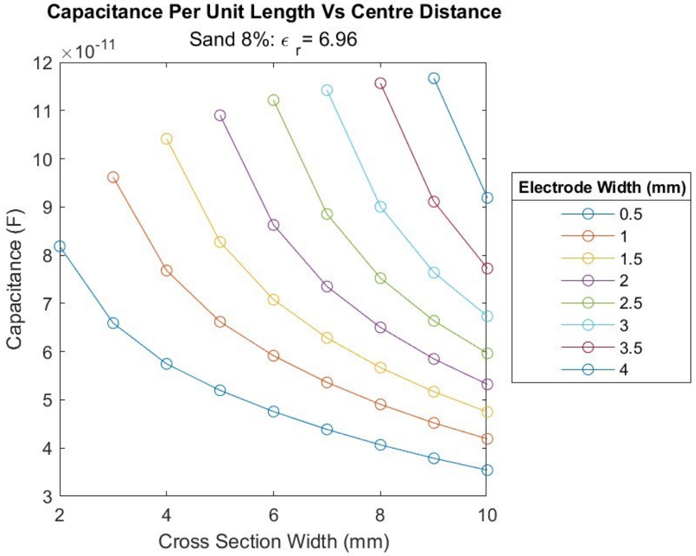
Capacitance Per Unit Length Vs Centre Distance

Sand 8%: ϵ_r = 6.96

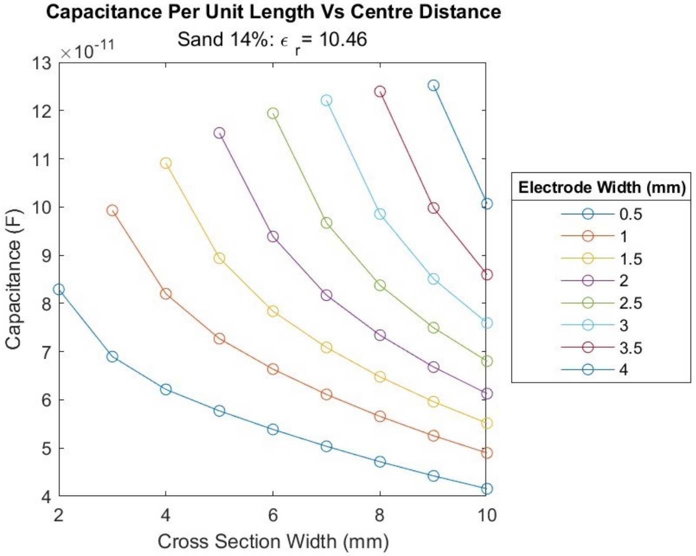
Capacitance Per Unit Length Vs Centre Distance

Sand 14%: ϵ_r = 10.46

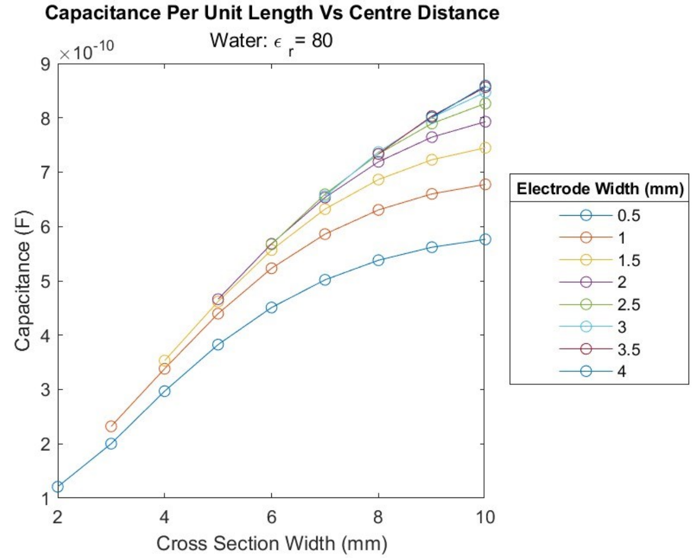
Capacitance Per Unit Length Vs Centre Distance
Water: ϵ r= 80
×10-10
9
8
7
6
5
4
3
2
1
Capacitance (F)
2
4
6
8
10
Cross Section Width (mm)
Electrode Width (mm)
0.5
1
1.5
2
2.5
3
3.5
4

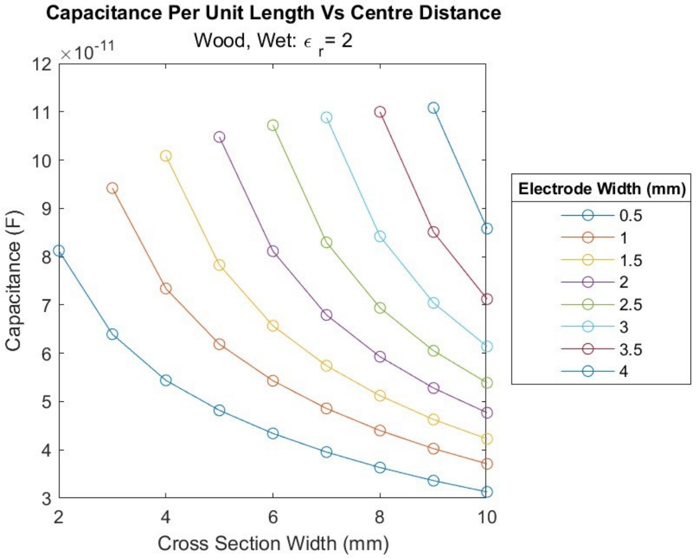
Capacitance Per Unit Length Vs Centre Distance
Wood, Wet: ϵ r= 2
×10-11
12
11
10
9
8
7
6
5
4
3
Capacitance (F)
2
4
6
8
10
Cross Section Width (mm)
Electrode Width (mm)
0.5
1
1.5
2
2.5
3
3.5
4

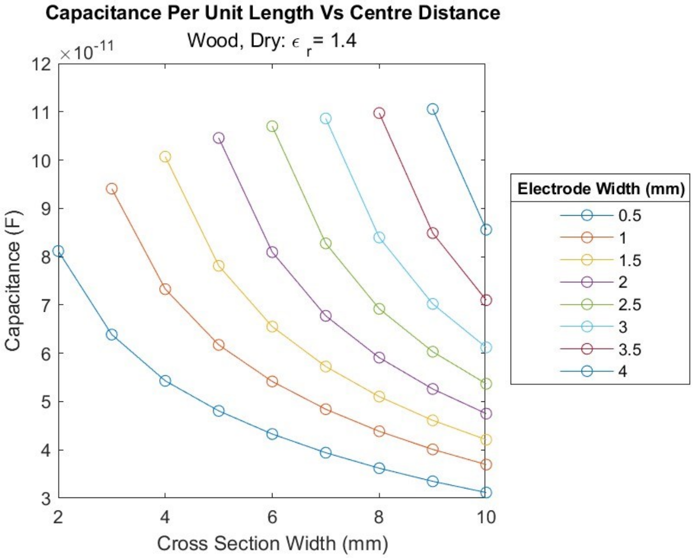
Capacitance Per Unit Length Vs Centre Distance
Wood, Dry: ϵ r= 1.4
×10-11
12
11
10
9
8
7
6
5
4
3
Capacitance (F)
2
4
6
8
10
Cross Section Width (mm)
Electrode Width (mm)
0.5
1
1.5
2
2.5
3
3.5
4

Change in Capacitance Vs Electrode Dimensions Plots

For all contaminants simulated.

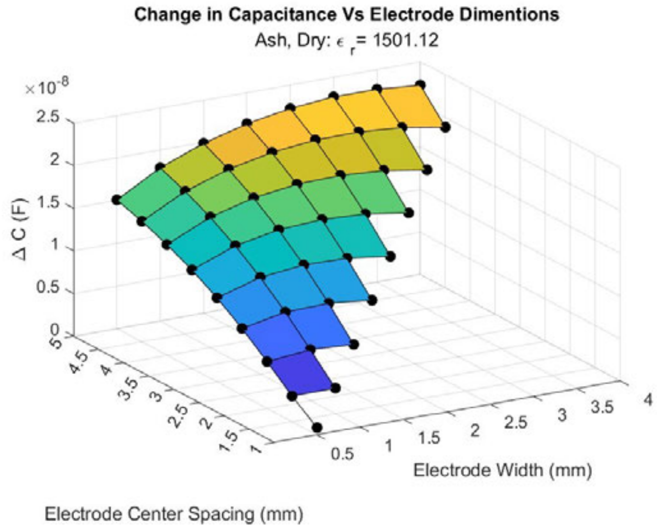

Change in Capacitance Vs Electrode Dimentions

Ash, Dry: ϵ_r= 1501.12

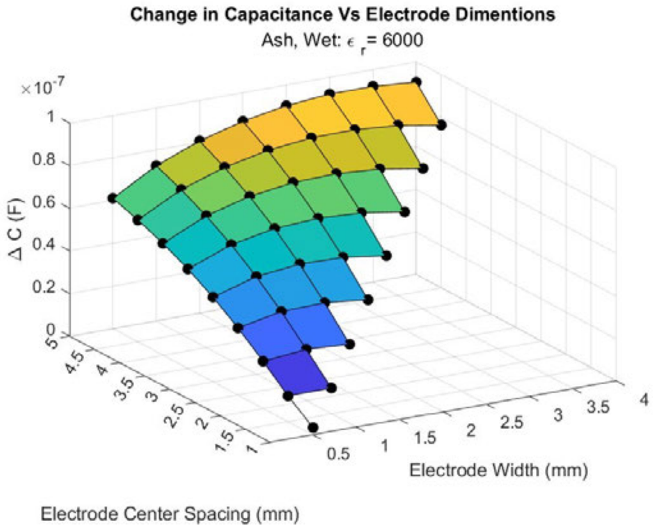

Change in Capacitance Vs Electrode Dimentions

Ash, Wet: ϵ_r= 6000

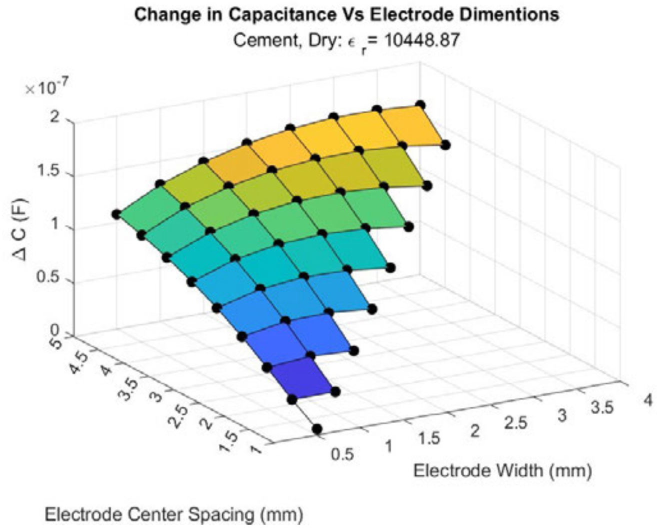

Change in Capacitance Vs Electrode Dimentions

Cement, Dry: ϵ_r= 10448.87

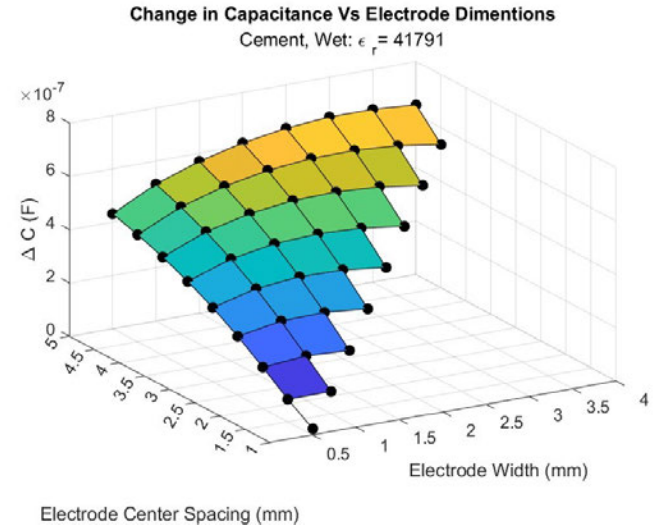

Change in Capacitance Vs Electrode Dimentions

Cement, Wet: ϵ_r= 41791

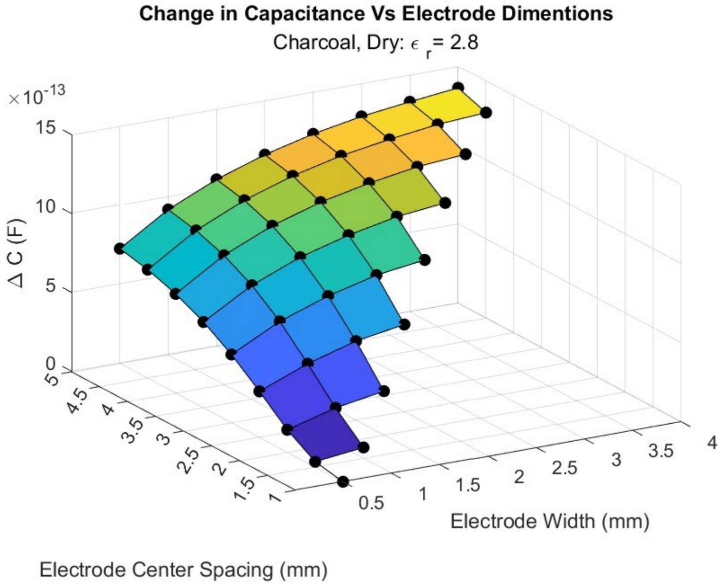
Change in Capacitance Vs Electrode Dimentions
Charcoal, Dry: ϵ_r= 2.8
$\times 10^{-13}$
15
10
5
0
Δ C (F)
5
4.5
4
3.5
3
2.5
2
1.5
1
Electrode Center Spacing (mm)
0.5
1
1.5
2
2.5
3
3.5
4
Electrode Width (mm)

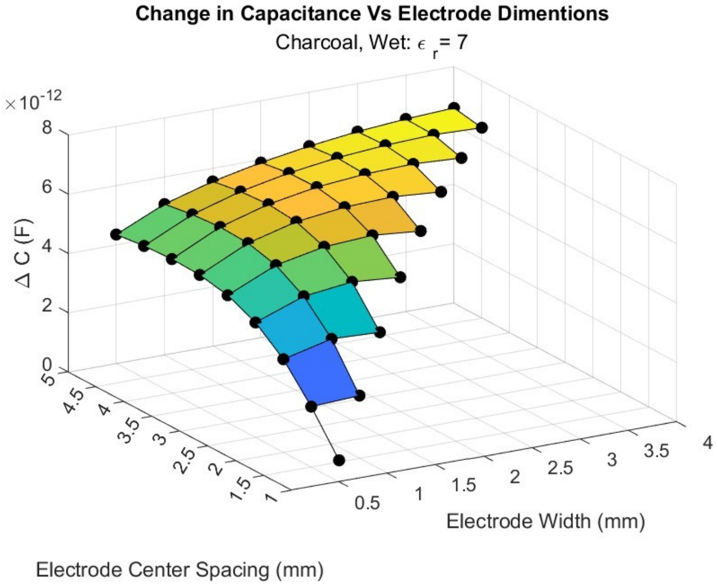
Change in Capacitance Vs Electrode Dimentions
Charcoal, Wet: ϵ_r= 7
$\times 10^{-12}$
8
6
4
2
0
Δ C (F)
5
4.5
4
3.5
3
2.5
2
1.5
1
Electrode Center Spacing (mm)
0.5
1
1.5
2
2.5
3
3.5
4
Electrode Width (mm)

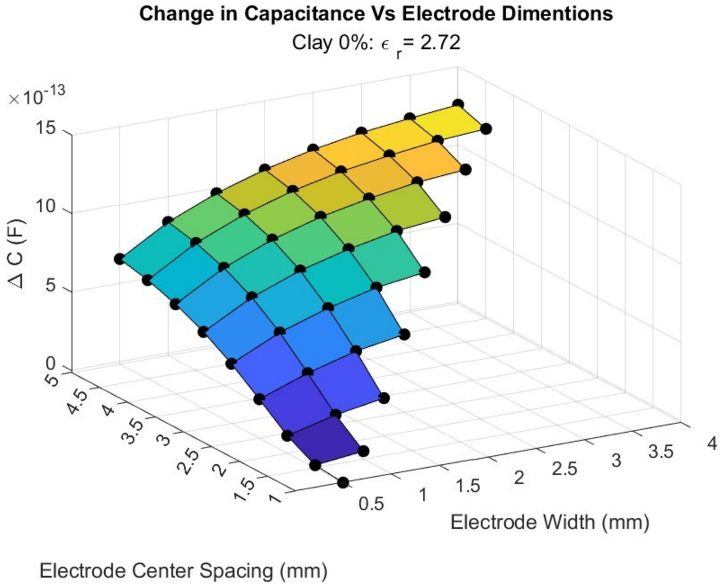
Change in Capacitance Vs Electrode Dimentions
Clay 0%: ϵ_r= 2.72
$\times 10^{-13}$
15
10
5
0
Δ C (F)
5
4.5
4
3.5
3
2.5
2
1.5
1
Electrode Center Spacing (mm)
0.5
1
1.5
2
2.5
3
3.5
4
Electrode Width (mm)

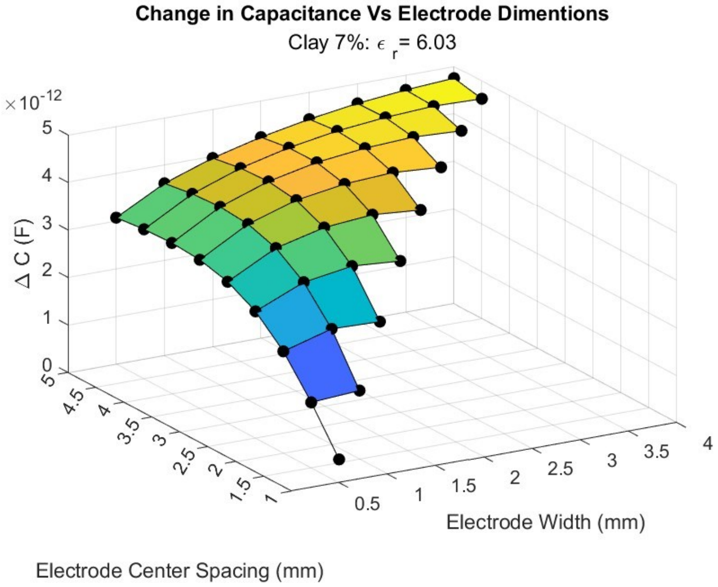
Change in Capacitance Vs Electrode Dimentions
Clay 7%: ϵ_r= 6.03
$\times 10^{-12}$
5
4
3
2
1
0
Δ C (F)
5
4.5
4
3.5
3
2.5
2
1.5
1
Electrode Center Spacing (mm)
0.5
1
1.5
2
2.5
3
3.5
4
Electrode Width (mm)

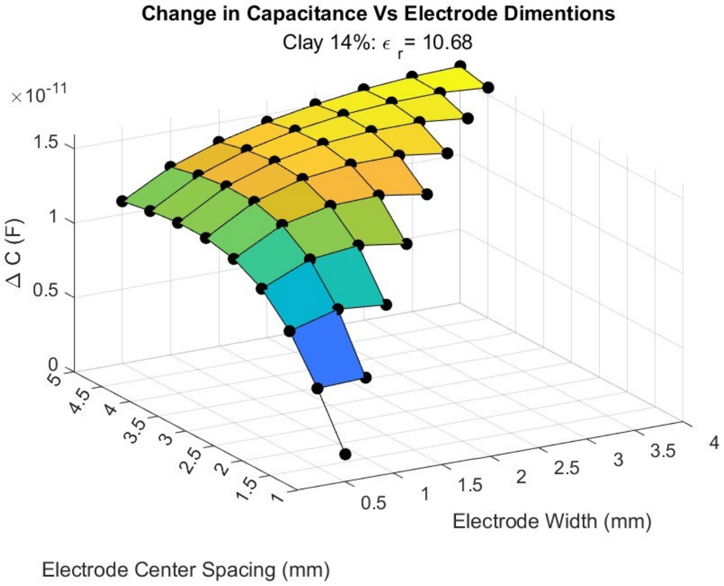
Change in Capacitance Vs Electrode Dimentions

Clay 14%: ϵ_r = 10.68

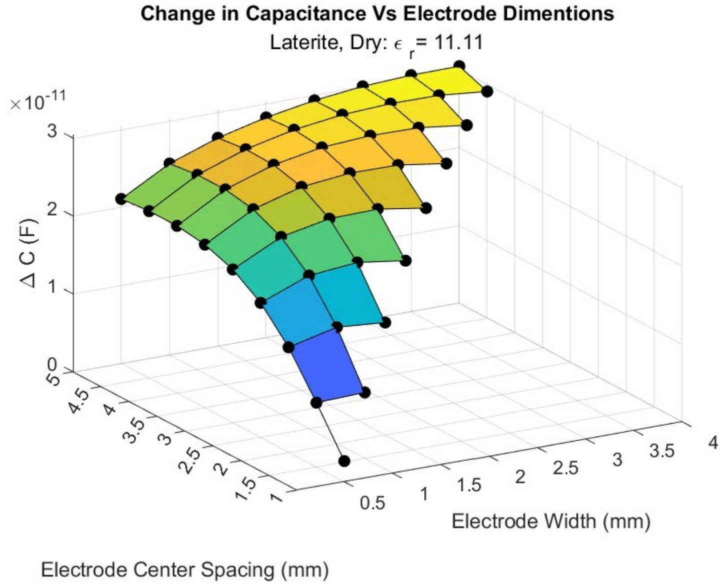
Change in Capacitance Vs Electrode Dimentions

Laterite, Dry: ϵ_r = 11.11

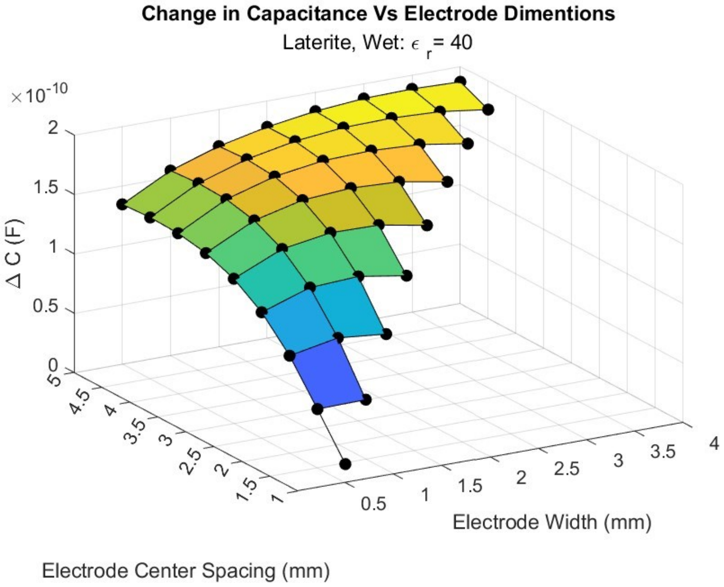
Change in Capacitance Vs Electrode Dimentions

Laterite, Wet: ϵ_r = 40

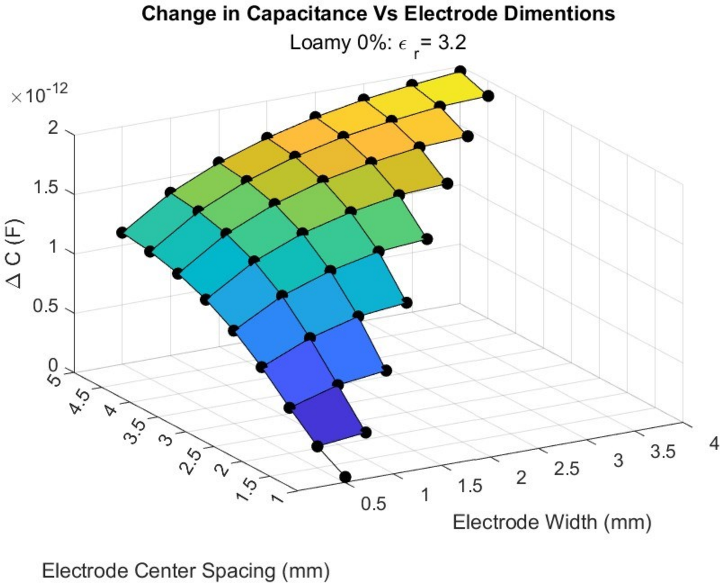
Change in Capacitance Vs Electrode Dimentions

Loamy 0%: ϵ_r = 3.2

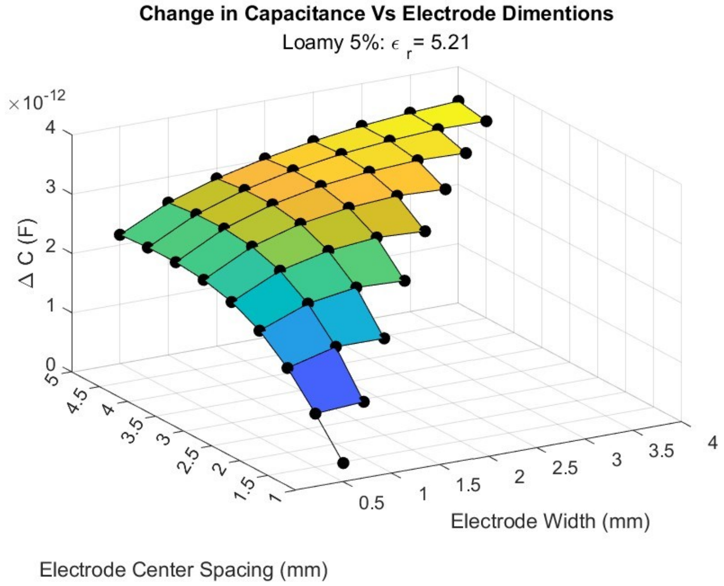

Change in Capacitance Vs Electrode Dimentions

Loamy 5%: $\epsilon_r = 5.21$

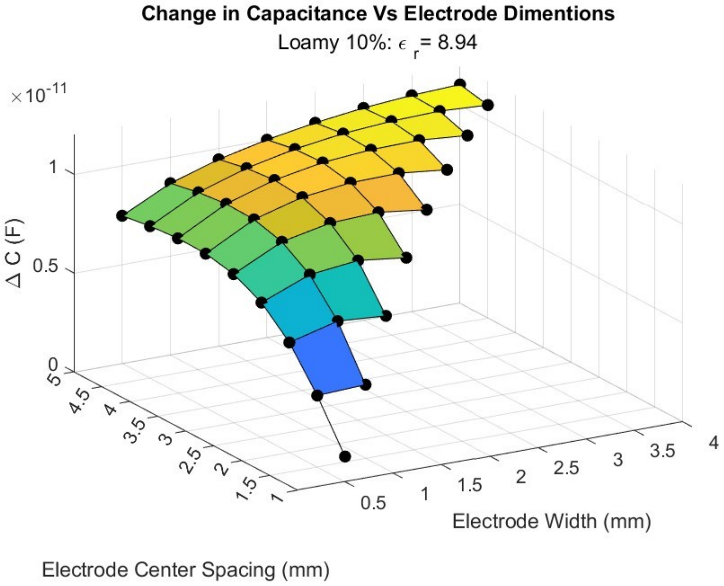

Change in Capacitance Vs Electrode Dimentions

Loamy 10%: $\epsilon_r = 8.94$

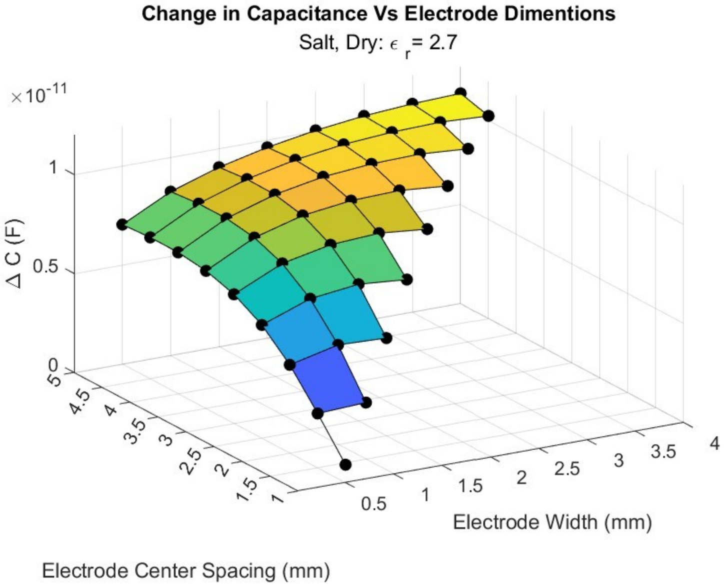

Change in Capacitance Vs Electrode Dimentions

Salt, Dry: $\epsilon_r = 2.7$

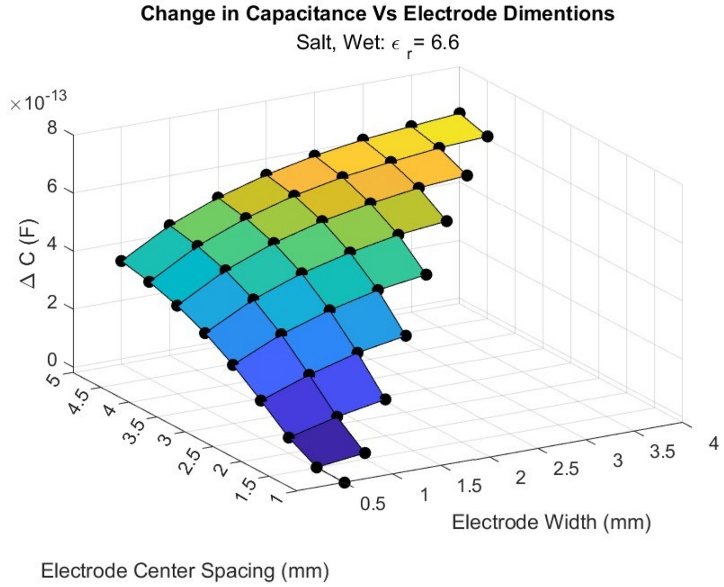

Change in Capacitance Vs Electrode Dimentions

Salt, Wet: $\epsilon_r = 6.6$

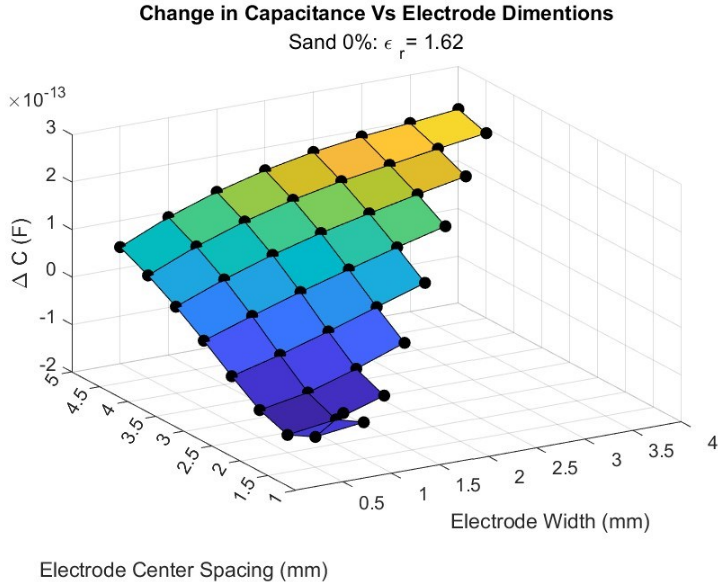

Change in Capacitance Vs Electrode Dimentions

Sand 0%: $\epsilon_r = 1.62$

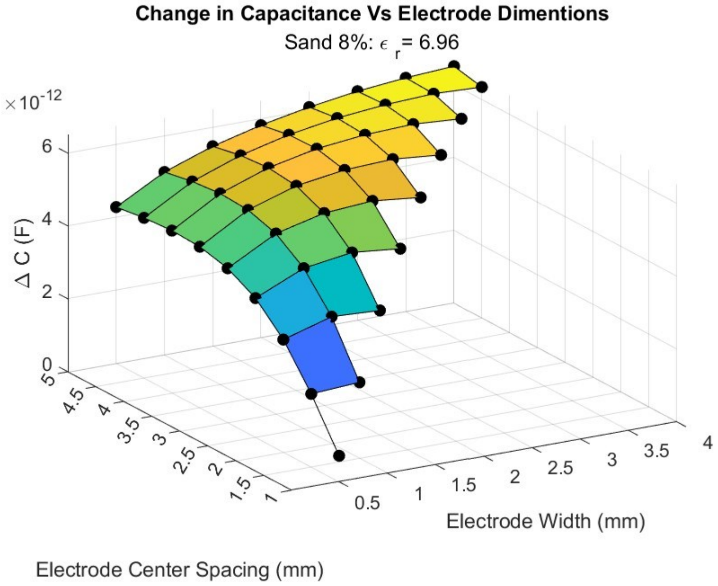

Change in Capacitance Vs Electrode Dimentions

Sand 8%: $\epsilon_r = 6.96$

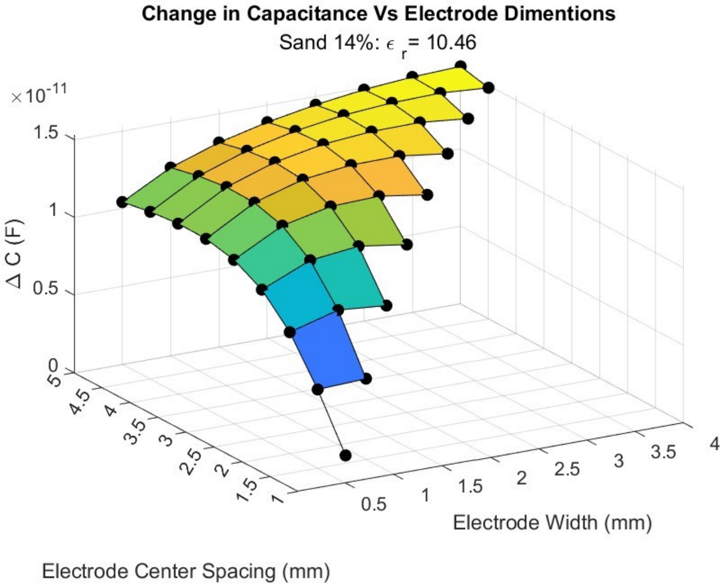

Change in Capacitance Vs Electrode Dimentions

Sand 14%: $\epsilon_r = 10.46$

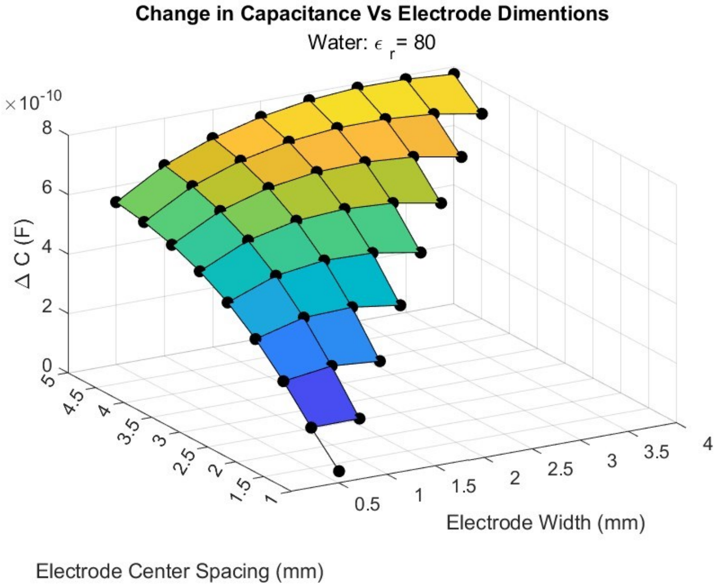

Change in Capacitance Vs Electrode Dimentions

Water: $\epsilon_r = 80$

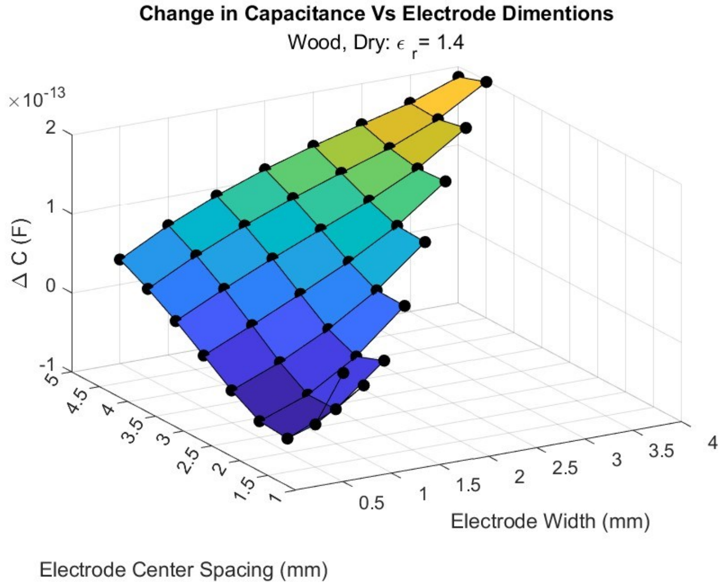
Change in Capacitance Vs Electrode Dimentions
Wood, Dry: ϵ_r= 1.4
×10^-13
2
1
0
-1
Δ C (F)
5
4.5
4
3.5
3
2.5
2
1.5
1
0.5
1
1.5
2
2.5
3
3.5
4
Electrode Width (mm)
Electrode Center Spacing (mm)

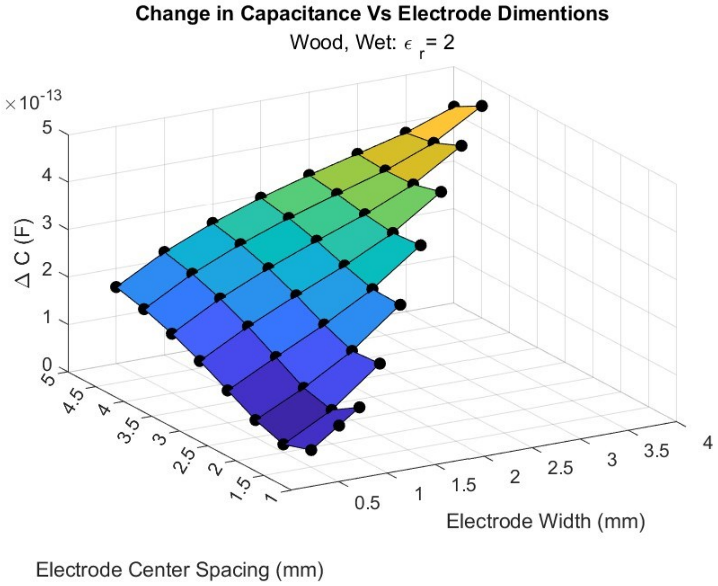
Change in Capacitance Vs Electrode Dimentions
Wood, Wet: ϵ_r= 2
×10^-13
5
4
3
2
1
0
Δ C (F)
5
4.5
4
3.5
3
2.5
2
1.5
1
0.5
1
1.5
2
2.5
3
3.5
4
Electrode Width (mm)
Electrode Center Spacing (mm)

Sensitivity Change

For all contaminants simulated.

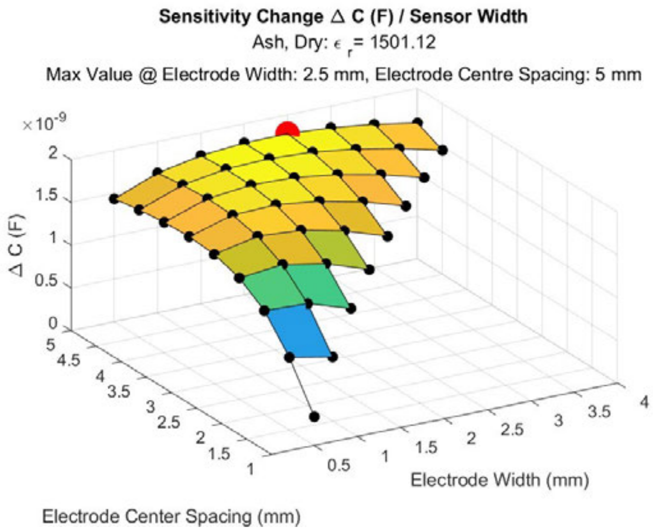

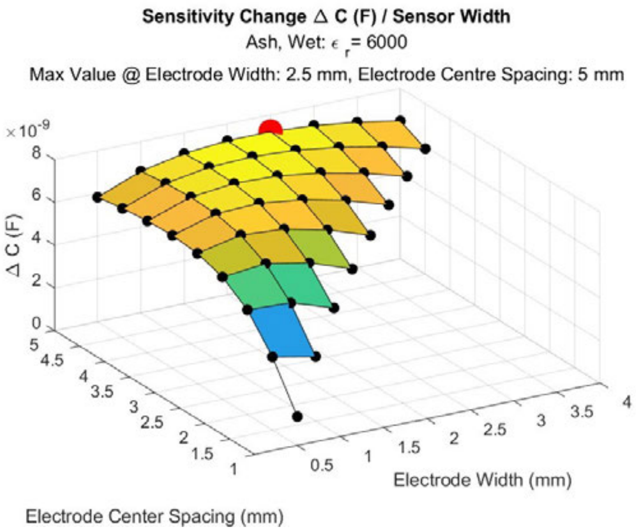

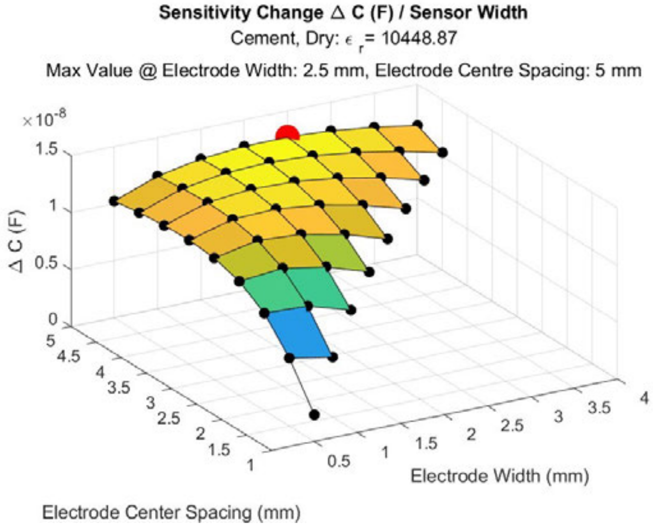

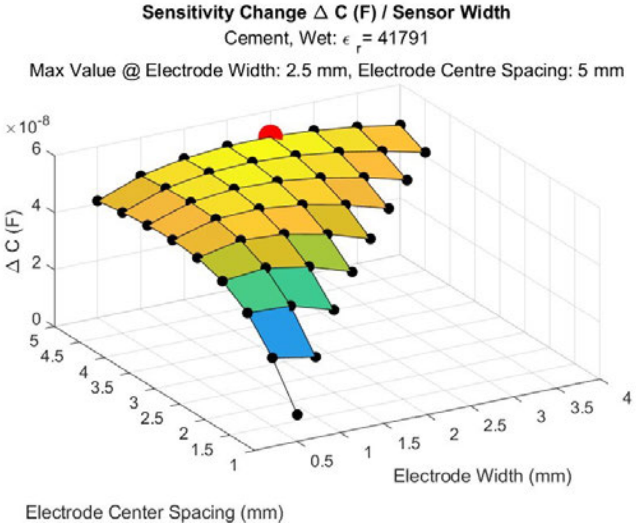

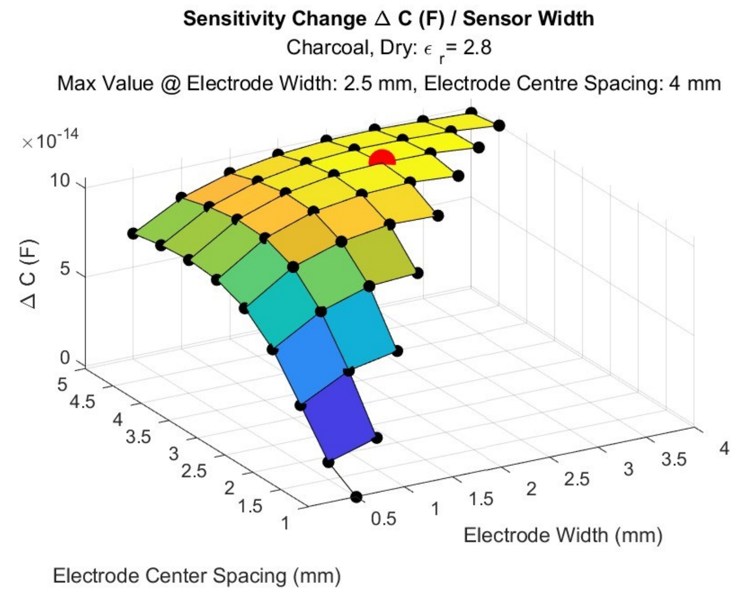

Sensitivity Change △ C (F) / Sensor Width

Charcoal, Dry: $\epsilon_r = 2.8$

Max Value @ Electrode Width: 2.5 mm, Electrode Centre Spacing: 4 mm

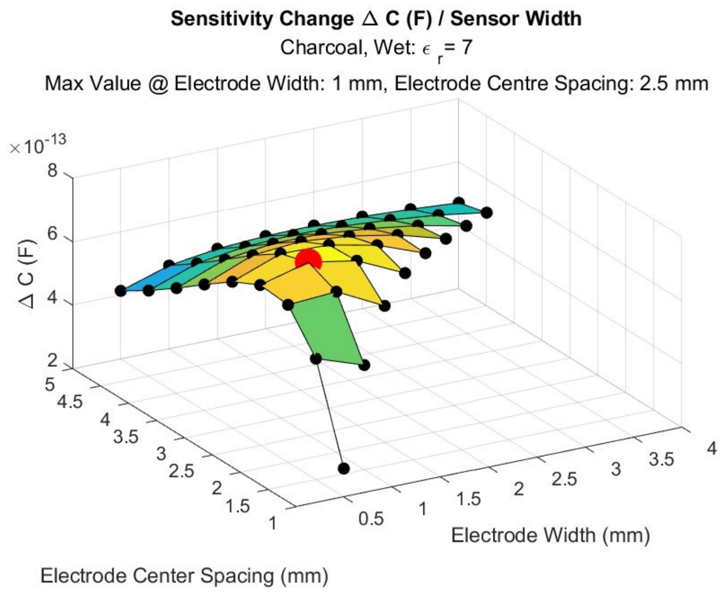

Sensitivity Change △ C (F) / Sensor Width

Charcoal, Wet: $\epsilon_r = 7$

Max Value @ Electrode Width: 1 mm, Electrode Centre Spacing: 2.5 mm

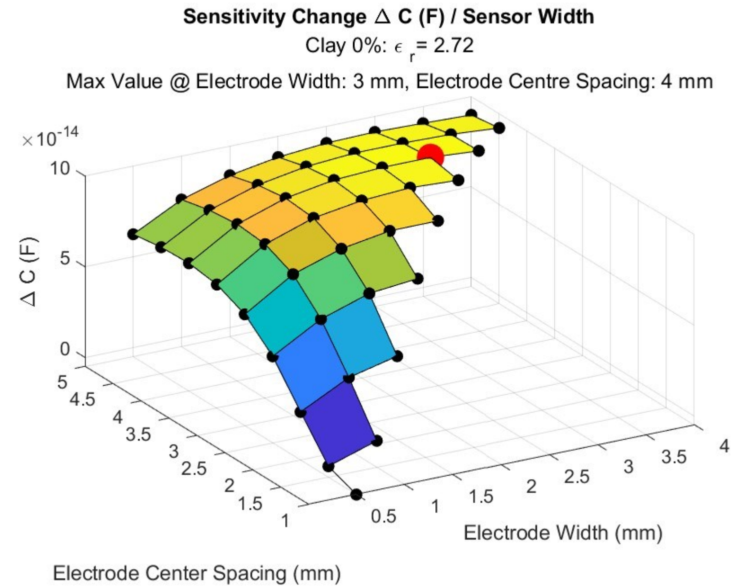

Sensitivity Change △ C (F) / Sensor Width

Clay 0%: $\epsilon_r = 2.72$

Max Value @ Electrode Width: 3 mm, Electrode Centre Spacing: 4 mm

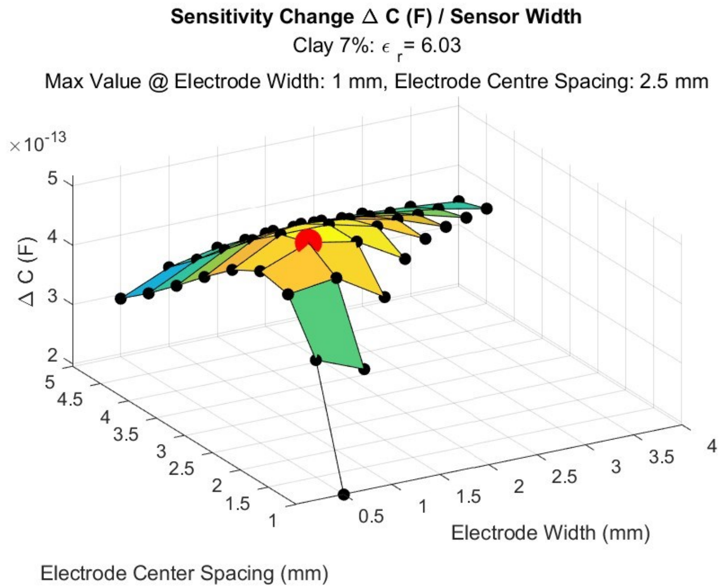

Sensitivity Change △ C (F) / Sensor Width

Clay 7%: $\epsilon_r = 6.03$

Max Value @ Electrode Width: 1 mm, Electrode Centre Spacing: 2.5 mm

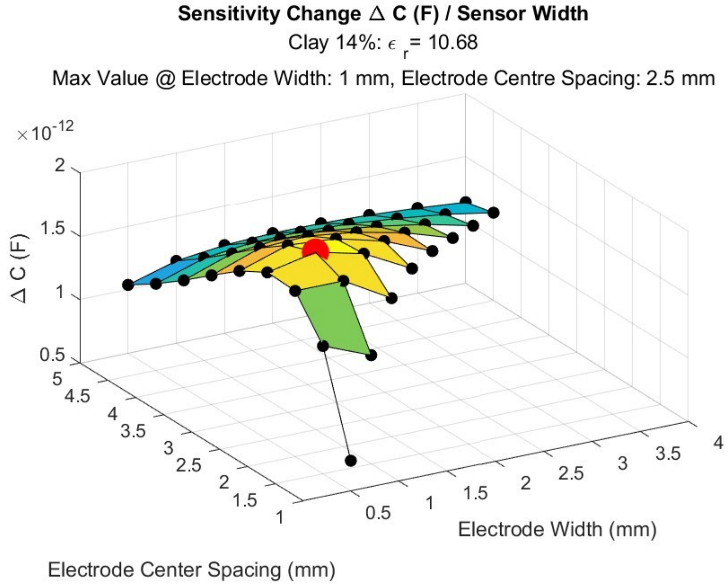
Sensitivity Change △ C (F) / Sensor Width

Clay 14%: ϵ_r= 10.68

Max Value @ Electrode Width: 1 mm, Electrode Centre Spacing: 2.5 mm

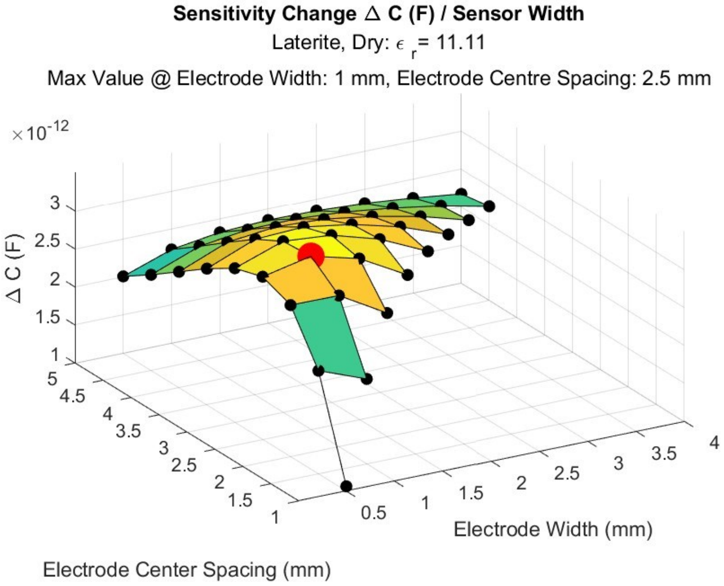
Sensitivity Change △ C (F) / Sensor Width

Laterite, Dry: ϵ_r= 11.11

Max Value @ Electrode Width: 1 mm, Electrode Centre Spacing: 2.5 mm

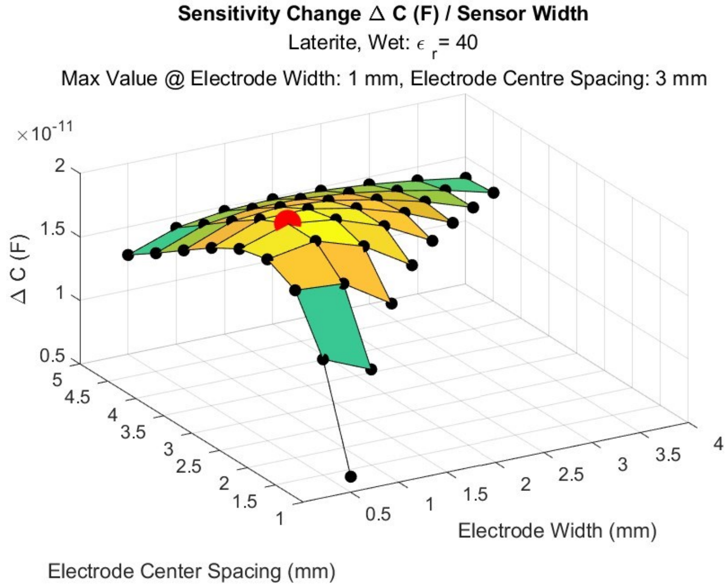
Sensitivity Change △ C (F) / Sensor Width

Laterite, Wet: ϵ_r= 40

Max Value @ Electrode Width: 1 mm, Electrode Centre Spacing: 3 mm

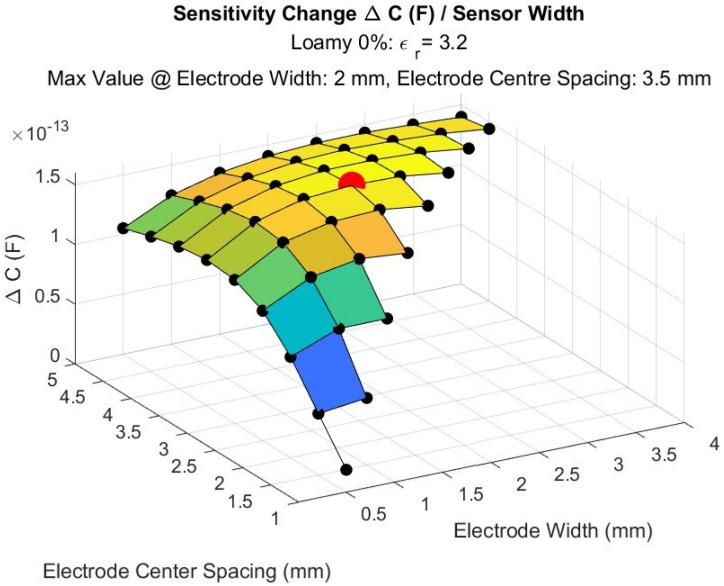
Sensitivity Change △ C (F) / Sensor Width

Loamy 0%: ϵ_r= 3.2

Max Value @ Electrode Width: 2 mm, Electrode Centre Spacing: 3.5 mm

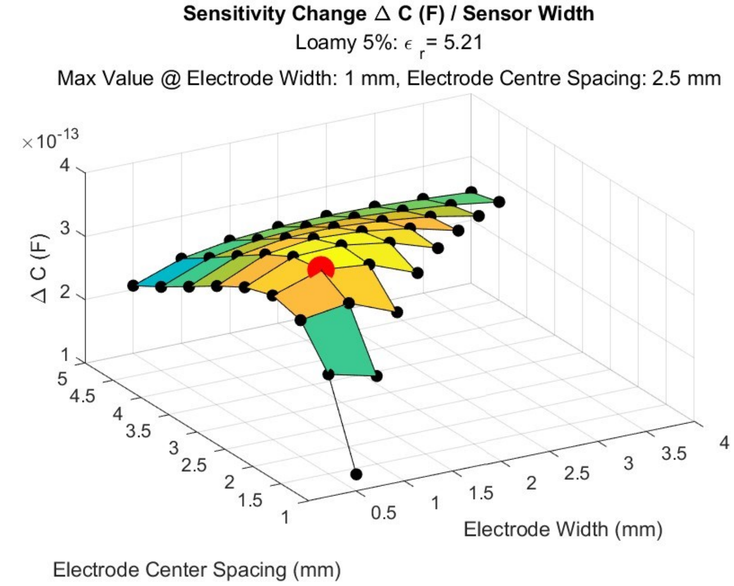

Sensitivity Change △ C (F) / Sensor Width

Loamy 5%: $\epsilon_r = 5.21$

Max Value @ Electrode Width: 1 mm, Electrode Centre Spacing: 2.5 mm

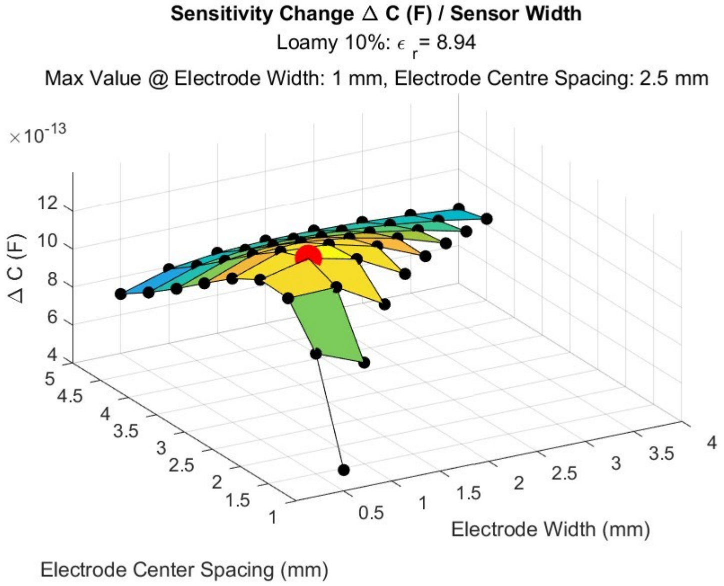

Sensitivity Change △ C (F) / Sensor Width

Loamy 10%: $\epsilon_r = 8.94$

Max Value @ Electrode Width: 1 mm, Electrode Centre Spacing: 2.5 mm

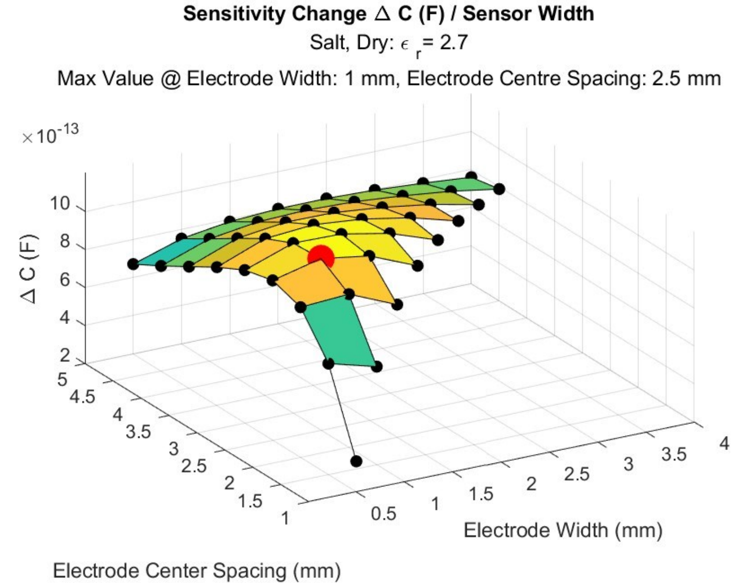

Sensitivity Change △ C (F) / Sensor Width

Salt, Dry: $\epsilon_r = 2.7$

Max Value @ Electrode Width: 1 mm, Electrode Centre Spacing: 2.5 mm

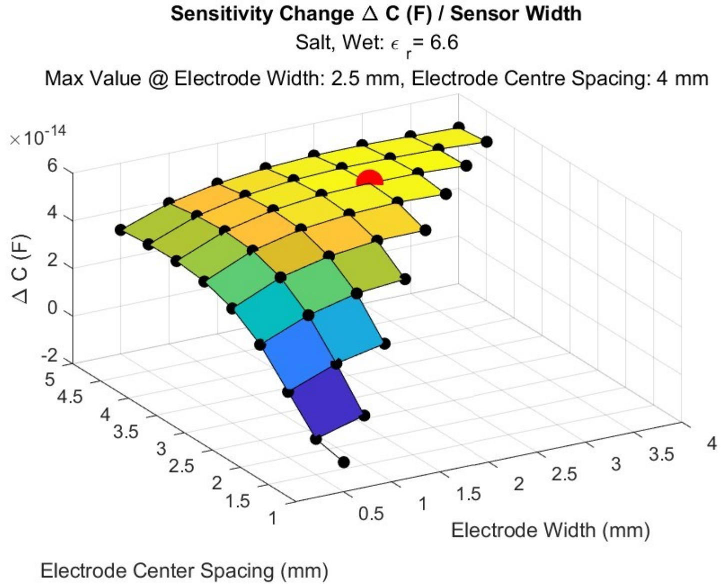

Sensitivity Change △ C (F) / Sensor Width

Salt, Wet: $\epsilon_r = 6.6$

Max Value @ Electrode Width: 2.5 mm, Electrode Centre Spacing: 4 mm

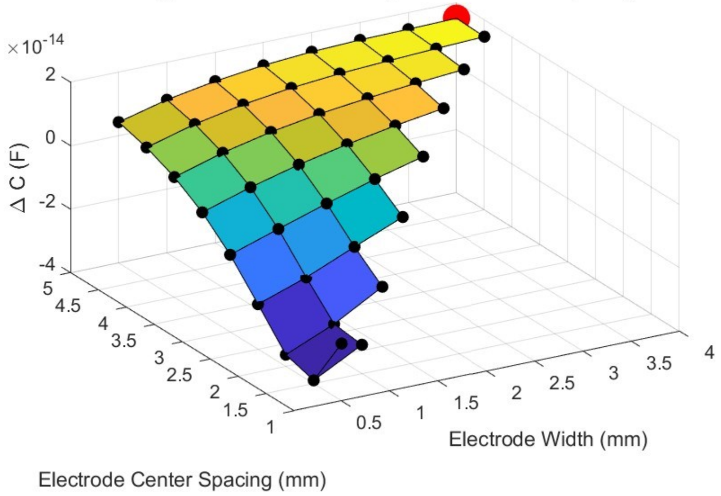
Sensitivity Change △ C (F) / Sensor Width
Sand 0%: ϵ_r= 1.62
Max Value @ Electrode Width: 4 mm, Electrode Centre Spacing: 5 mm

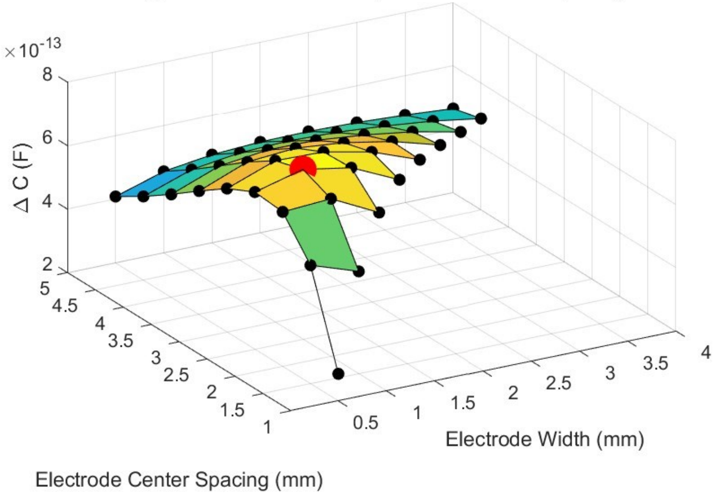
Sensitivity Change △ C (F) / Sensor Width
Sand 8%: ϵ_r= 6.96
Max Value @ Electrode Width: 1 mm, Electrode Centre Spacing: 2.5 mm

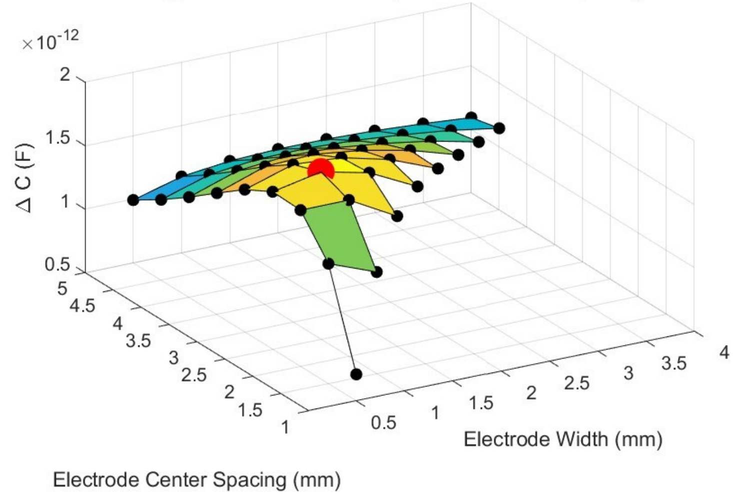
Sensitivity Change △ C (F) / Sensor Width
Sand 14%: ϵ_r= 10.46
Max Value @ Electrode Width: 1 mm, Electrode Centre Spacing: 2.5 mm

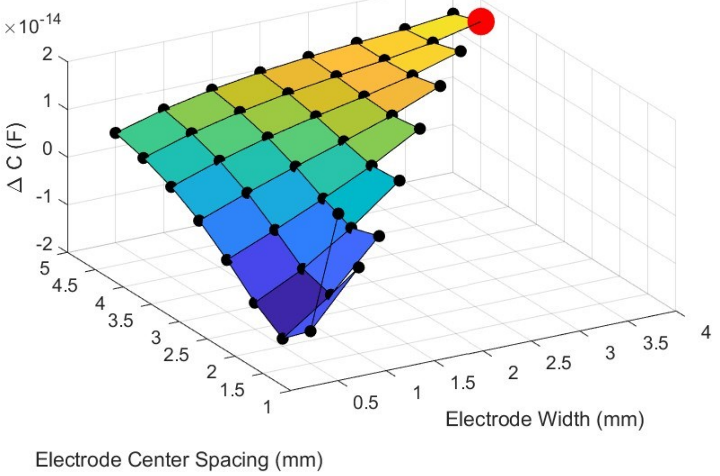
Sensitivity Change △ C (F) / Sensor Width
Wood, Dry: ϵ_r= 1.4
Max Value @ Electrode Width: 4 mm, Electrode Centre Spacing: 4.5 mm

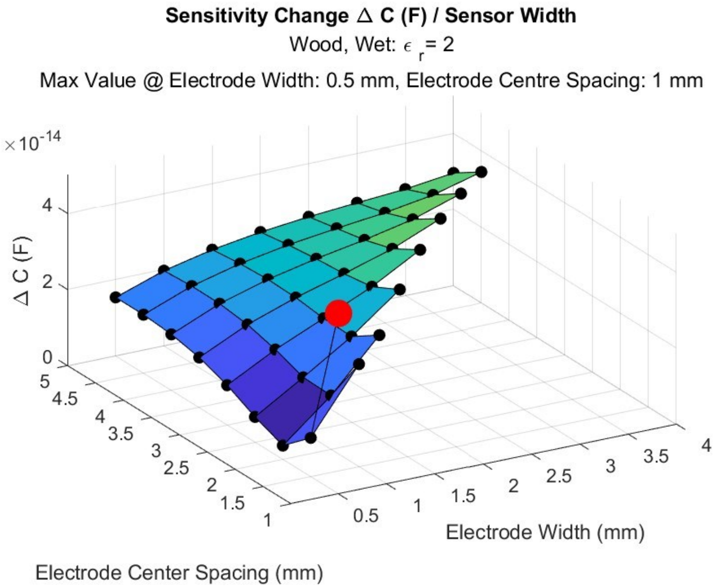

Sensitivity Change △ C (F) / Sensor Width

Wood, Wet: ϵ_r= 2

Max Value @ Electrode Width: 0.5 mm, Electrode Centre Spacing: 1 mm